CONFRONTING THEORIES OF GRAVITY WITH LARGE-SCALE STRUCTURES

Dissertation

zur

Erlangung der naturwissenschaftlichen Doktorwürde
(Dr. sc. nat.)

vorgelegt der

Mathematisch-naturwissenschaftlichen Fakultät

der

Universität Zürich

von

LUCAS LOMBRISER

von

Trun GR

Promotionskommitee

Prof. Dr. Uroš Seljak (Vorsitz)
Prof. Dr. Philippe Jetzer
Prof. Dr. Ben Moore

Zürich, 2011

Lucas Lombriser
Institute for Theoretical Physics
University of Zurich
Winterthurerstrasse 190
CH-8057 Zürich
Switzerland
e-mail: lucas.lombriser@uzh.ch

This dissertation is in copyright.

© Lucas Lombriser 2011

All rights reserved. No part of this document may be reproduced without the written permission of the publisher.

Prepared for print with CreateSpace.com
ISBN: X-XXX-XXXXX-X

Dedicau al pagataglia

"I've been noticing gravity since I was very young."

– *Cameron Diaz*

Preface

The dissertation at hand is the result of my research work of the last three years as a doctoral candidate at the Institute for Theoretical Physics (ITP) at the University of Zurich. The thesis is devoted to studies of modifications of general relativity as an alternative to the dark energy paradigm for describing cosmic acceleration. Four independent analyses have been conducted on generic modifications of gravity, the Dvali-Gabadadze-Porrati braneworld model, as well as on the designer and Hu-Sawicki $f(R)$ gravity models. Thereby, the gravitational aspects on the formation of the largest structures of our universe and the performance of the different theories of gravity in confrontation with the corresponding cosmological observations was in the main focus of interest. The thesis presents the publications made on these studies and complements them with an introductory part for closing possible gaps between the reader's precognition not acquainted with this field of research and the background knowledge required for the full accessibility to the substance of the publications.

Working at the ITP has been a very interesting and enriching experience that was accompanied with many pleasant and instructive discussions. I am very grateful to Uroš Seljak for giving me the opportunity to join his research group and for the support and valuable advise that I got from him over the past years. I also thank all the members of his research group and the people of the ITP for making the time I spent with them such a great experience. In particular, I thank the institute directors Ben Moore and Thomas Gehrmann for making the ITP such an inspiring and enjoyable place of work, Philippe Jetzer for co-examining my dissertation, Esther Meier, Regina Schmid, and Suzanne Wilde for a lot of help with administrative issues, and Doug Potter for outstanding technical support, in particular with the zBox supercomputers. I also thank all of my collaborators on different research projects from whom I have been able to learn a lot and of whom I am, in particular, very grateful to Wayne Hu and Anže Slosar. Furthermore, I thank the Lawrence Berkeley National Laboratory, the Berkeley Center for Cosmological Physics, and Ewha Womans University for hospitality while work on parts of this thesis has been conducted. Last but not least, I am very grateful to my family that has always supported me and Verena Huber for never losing her patience in dealing with a crazy physicist.

Zürich, June 2011 LUCAS LOMBRISER

Table of Contents

Zusammenfassung

Die beobachtete beschleunigte Ausdehnung des Universums deutet auf die Existenz einer unbekannten Energie hin. Alternativ zu dieser *dunklen Energie* lässt sich die kosmische Beschleunigung auch durch eine Modifizierung der allgemeinen Relativitätstheorie erklären. Eine Abänderung der Gravitationstheorie hinterlässt jedoch auch Spuren in den grossen Strukturen des Universums, welche deshalb wertvolle Informationen über die grundlegende Natur der kosmischen Beschleunigung liefern und sich als Laboratorium zur Überprüfung der gravitativen Gesetze anbieten.

Die vorliegende Dissertation fasst vier unabhängige Studien zusammen, welche verschiedene Gravitationstheorien mit den grossen Strukturen des Universums konfrontiert. Generische Abänderungen des kosmologischen Konkordanzmodels ΛCDM basierend auf typischen Modifikationen der allgemeinen Relativitätstheorie werden studiert. Eine Wahrscheinlichkeitsstudie solcher Abweichungen zeigt, dass ΛCDM mit linearen Proben der grossen Strukturen übereinstimmt, wobei aber genug Raum für alternative Modelle übrig bleibt. Es wird darauf hingedeutet, dass die separate Analyse von zusätzlichen Hintergrundparametern und Parametrisierungen des Wachstums der grossen Strukturen *a priori* den Ausschluss von existenzfähigen Abänderungen von ΛCDM bewirken kann. Die hier gesetzten Parametergrenzen für solche phänomenologischen Abweichungen sind die einzigen in der Literatur, welche nicht nur eine Abänderung des Verhältnisses zwischen den skalaren Potentialen und der Poissongleichung auf allen Raumzeitskalen, sondern auch eine zeitabhängige Zustandsfunktion für die, auf die Modifikation der Gravitation beruhende, effektive dunkle Energie zulassen.

In einer zweiten Studie wird eine obere Schranke jenseits der Hubbleskala bei $H_0 r_\mathrm{c} \gtrsim 3$ beim Signifikanzniveau von 95% auf die Übergangsskala r_c gesetzt, welche den Wechsel von einer fünf-dimensionalen Gravitationstheorie zu einer vier-dimensionalen Skalar-Tensor-Theorie im Dvali-Gabadadze-Porrati (DGP) Branenmodell steuert. Dabei werden kosmologische Beobachtungen verwendet, welche mittels linearer Störungstheorie beschrieben werden können. Die dabei gesetzte Schranke deutet auf eine signifikante Ungunst des DGP-Modells zugunsten von ΛCDM hin. Dies ist die erste Studie, welche zeigt, dass dies nicht nur im Fall vom selbstbeschleunigten DGP-Zweig zutrifft, sondern auch für den normalen Zweig und dem selbstbeschleunigten Fall unter Einwirkung einer Branenspannung.

Nichtlineare Proben wie der Galaxienhaufenreichtum und das Halo-Dichteprofil werden in zwei weiteren Analysen benutzt, um Schranken auf den Compton-Wellenlängenparameter B_0 und dem *Skalaron*-Hintergrundwert $|f_{R0}|$ des Designer- und Hu-Sawicki-$f(R)$-Gravitationsmodells zu setzen: $B_0 \lesssim 10^{-3}$ und $|f_{R0}| \lesssim 3 \times 10^{-2}$ beim Signifikanzniveau von 95%. Zusammen mit einer anderen Studie bildet die B_0-Schranke, die zurzeit strengste kosmologische Bedingung für $f(R)$-Gravitationsmodelle in der Literatur, wobei das Halo-Dichteprofil einen neuartigen und unabhängigen Gravitationstest auf zuvor noch nicht untersuchten Skalen stellt.

Um mögliche Wissenslücken zum Anschluss an die Gravitationsstudien zu

überbrücken, wurde die Dissertation mit einer Einführung ergänzt, welche verschiedene theoretische Aspekte der modifizierten Gravitationsmodelle, der entsprechenden kosmischen Störungstheorie, der beobachtbaren grossen Strukturen des Universums und der mathematischen Konzepte für die Erstellung von Wahrscheinlichkeitsverteilungen im kosmologischen Parameterraum beleuchtet.

Abstract

The observed late-time acceleration of the expansion of the universe suggests the existence of an unknown form of energy. Alternatively to this *dark energy*, the cosmic acceleration can be explained by a modification of general relativity. However, deviations in the gravitational interactions leave distinctive imprints in the large-scale structures of the universe, which contain valuable information about the fundamental nature of the cosmic acceleration and provide a great laboratory for testing gravitational theories.

The dissertation at hand comprises four independent analyses confronting different theories of gravity with observations of the largest scales of our universe. Generic departures from the cosmological concordance model ΛCDM based on typical modifications of general relativity are studied. From a likelihood analysis of such deviations, it is found that ΛCDM is consistent with linear probes of the large-scale structure, however, the current constraints leave enough space for alternative models. It is further emphasized that constraining supplementary background parameters and parametrizations of the growth of large-scale structures separately may lead to an *a priori* exclusion of viable departures from ΛCDM. The constraints placed on the phenomenological departures of general relativity are the only ones in the literature including not only deviations on all spacetime scales of the ratio of the scalar potentials and the Poisson equation but also allowing for a time-dependent equation of state for the effective dark energy associated with the modifications of gravity.

In a second study, an upper bound beyond the Hubble scale $H_0 r_\mathrm{c} \gtrsim 3$ at the 95% confidence level is placed on the crossover scale r_c that governs the transition from five-dimensional to four-dimensional scalar-tensor gravity in the Dvali-Gabadadze-Porrati (DGP) braneworld model. Thereby, cosmological observations amenable to linear perturbation theory are employed. The bound placed on DGP gravity disfavours the model at high significance when compared to ΛCDM. This is the first study to show that this is not only true for the self-accelerating branch of DGP but also for the normal branch and for the case of the self-accelerating branch with the inclusion of a brane tension.

Nonlinear probes from the abundance of clusters and the shape of halo density profiles are utilized in two further analyses to obtain constraints on the Compton wavelength parameter B_0 and the *scalaron* background value $|f_{R0}|$ of the designer and Hu-Sawicki $f(R)$ gravity models, obtaining $B_0 \lesssim 10^{-3}$ and $|f_{R0}| \lesssim 3 \times 10^{-2}$ at the 95% confidence level, respectively. Together with another study, the bound on B_0 obtained from the abundance of clusters puts the currently tightest cosmological constraint on $f(R)$ gravity models in the literature, where the halo density profiles provide a new independent test of gravity on scales that have previously not been investigated.

In order to fill possible gaps to the required procognition for the gravitational analyses, the thesis is supplemented with an introductory part on different theo-

retical aspects of modified gravity models, cosmological perturbations conducted therein, the observable large-scale structures of our universe, and mathematical concepts for acquiring probability distributions within the cosmological parameter spaces.

Resumaziun

L'acceleraziun dall'expansiun digl univers constatada entras observaziuns lai supponer l'existenza dad in'energia nunenconuschenta. Alternativamein tier quell'*energia stgira* san modificaziuns dalla teoria dalla relativitad generala declarar quell'acceleraziun. Midadas ella teoria dalla gravitaziun tschentan denton fastitgs ellas pli grondas structuras digl univers, che cuntegnan impurtontas informaziuns sur la natira fundamentala dall'acceleraziun cosmica e porschan in bien laboratori per la verifacaziun dallas interacziuns gravitativas.

Quella dissertaziun cuntegn quater analisas independentas che confronteschan differentas teorias dalla gravitaziun cun observaziuns dallas pli grondas structuras digl univers. Mutaziuns genericas dil model cosmologic da concordanza ΛCDM che sebasan sin tipicas modificaziuns dalla relativitad generala vegnan studegiadas. Ina analisa dalla probabilitat per quellas deviaziuns muossa che ΛCDM ei consistent cun examinaziuns linearas dallas structuras grondas. Quellas laien denton avunda spazi per models alternativs. Ei vegn era mussau che mutaziuns admissiblas da ΛCDM pon esser exludidas a priori cun tschentar limitaziuns sin parameters supplementars per il funs cosmologic e parametrisaziuns per la carschen dallas structuras grondas en separau. Las limitaziuns che vegnan tschentadas sin las mutaziuns fenomenologicas dalla relativitad generala ein las sulettas ella literatura che cuntegnan buca mo deviaziuns sur tuttas scalas dil spazi e dil temps ella relaziun dils potenzials scalars ed ell'equaziun da Poisson, mobein permettan era in'equaziun dil stadi dependent dil temps per l'effectiva energia stgira associatada cun la modificaziun dalla gravitaziun.

En in secund studi vegn tschentau ina limita sura sur la scala da Hubble $H_0 r_\mathrm{c} \gtrsim 3$ al nivel da confidonza da 95% sin la scala da transiziun r_c denter ina teoria da gravitaziun tschun-dimensiunala e teoria da scalars e tensurs quater-dimensiunala el model da branas da Dvali-Gabadadze-Porrati (DGP). Leutier vegn fatg diever dad observaziuns cosmologicas ch'ein admissiblas entras la teoria lineara da perturbaziuns. La limita tschentada sin la gravitaziun da DGP disfavurisescha quei model cun gronda confidonza en cumpregliaziun cun ΛCDM. Quei ei igl emprem studi che muossa che quei constat buca mo sil rom da DGP che s'accelerescha da sez, mobein era sil rom normal ed el cass precedent cun tensiun ella brana.

Observaziuns buca linearas sco la rihezia dil mantun da galaxias ni il profil dalla densitad dil halo vegnan utilisadas en dus studis ulteriurs per obtener limitas sin il parameter per la lunghezia dall'unda da Compton B_0 e sin il *scalaron* alla valur da funs $|f_{R0}|$ el model da designer ed el model da Hu-Sawicki per $f(R)$: $B_0 \lesssim 10^{-3}$ e $|f_{R0}| \lesssim 3 \times 10^{-2}$ al nivel da confidonza da 95%. Ensemen cun in auter studi presenta il cunfin sin B_0 la pli rigurusa limitaziun cosmologica sin las teorias gravitativas dad $f(R)$ ed ils profils dalla densitad dil halo mettan a disposiziun in niev test independent per la gravitaziun sin scalas ch'ein avon buca vegnidas intercuretgas.

Per emplenir largias denter las enconuschientschas gia existentas e las premissas per il studi dallas analisas gravitativas ei la dissertaziun amplificada cun in'introducziun che cumpeglia differents aspects teoretics davart ils models da mod-

ificaziuns dalla gravitaziun, las perturbaziuns cosmologicas correspondentas, las observaziuns dallas structuras grondas digl univers, ed ils concepts matematics per acquirir distribuziuns probabilisticas el spazi dils parameters cosmologics.

1

Introduction

In the concordance model of cosmology ΛCDM, general relativity and the Standard Model of particle physics is supplemented with large amounts of dark matter and dark energy in form of a cosmological constant to accommodate with a considerable number of astrophysical observations. The existence of a small cosmological constant or vacuum energy explains the late-time acceleration of the expansion of our universe, however, given the lack of a complete understanding of its natural origin and magnitude, it is important to repeatedly test the standard cosmological model against observations with the ambition of distinguishing between different explanations for the cosmic acceleration. The dissertation at hand addresses this objective by analyzing specific alternative theories of gravity that produce a late-time acceleration without invoking dark energy.

This introductory chapter is devoted to establishing the basics for the analyses performed in the following chapters. It discusses general relativity as well as motivations and models for modifications thereof in Sec. 1.1. Section 1.2 describes a parametrized post-Friedmann (PPF) framework for the generalized perturbative analysis within the different gravity models. Then, the cosmological probes and computational methods used to constrain the gravitational theories are summarized in Secs. 1.3 and 1.4, respectively. Finally, an outline of the content of the remainder of this dissertation is given in Sec. 1.5, concluding with a discussion of the results presented within this thesis and an outlook for prospective studies.

1.1. Modifications of general relativity

The history of modified gravity is as old as general relativity itself. Therefore, a plethora of modified gravity models can be found in the literature. Rather than presenting a broad discussion of alternative theories, the introduction of this thesis aims at describing in more detail different properties of specific and well-studied models of modified gravity, namely the Dvali-Gabadadze-Porrati (DGP) higher-dimensional braneworld model in Sec. 1.1.2 and $f(R)$ gravity in Sec. 1.1.3. This shall establish the theoretical fundament upon which Chaps. 2 through 4 are based. Note that parts of Sec. 1.1.3, i.e., the discussion about the formal equivalence of $f(R)$ models to a specific scalar-tensor gravity model is taken from Ref. [1]. In order to motivate the modifications of general relativity and inspect their feasibility, Sec. 1.1.1 complements the discussion with a number of mathematical concepts and theoretical constraints on gravity.

1.1.1. General relativity

The fundamental idea in general relativity is to relate the geometry of spacetime, defined by a differentiable manifold $\mathcal{M}$ endowed with a pseudo-Riemannian metric g, to the density and flux of energy and momentum described by the tensor $T_{\mu\nu}$. Moreover, the equivalence principle shall hold, i.e., there shall always exist a local inertial frame of reference in which the metric is Minkowskian, η. Furthermore, the field equations should be generally covariant, i.e., invariant under diffeomorphisms. Hence, they take the form

$$[D^{(2)}(g)]_{\mu\nu} = \kappa^2 T_{\mu\nu}. \tag{1.1}$$

where κ^2 is a constant and $D^{(2)}(g)$ is a tensor of rank two which shall maximally contain second order derivatives of the metric. The speed of light in vacuum is set to unity, $c \equiv 1$, here and throughout the body of this dissertation.

Consider a weak, slowly evolving, gravitational field which perturbs the flat Minkowski background $\eta_{\mu\nu}$ as $\Phi_{\mathrm{N}} = \delta\eta_{\mu\nu}/(2\eta_{\mu\nu})$, where Φ_{N} is the Newtonian gravitational potential. Since Newtonian gravity applies in the regime of weak, slowly evolving, classical gravitational fields, the general relativistic field equations should reproduce the Poisson equation

$$\nabla^2\Phi_{\mathrm{N}} = 4\pi\, G\, \rho \tag{1.2}$$

within this limit. Here, G is the Newton gravitational constant and ρ is the matter distribution. Hence, the field equations should contain second order derivatives of the metric. A perspicuous first choice for $[D^{(2)}(g)]_{\mu\nu}$ is the Ricci tensor $R_{\mu\nu}$, describing the curvature of spacetime: It is a tensor of rank two, includes second-order derivatives of the metric, and, due to the first Bianchi identity, it is symmetric. $R_{\mu\nu} = R^{\rho}{}_{\rho\mu\nu}$, where $R^{\rho}{}_{\sigma\mu\nu}$ are the components of the Riemann curvature operator $\mathcal{R}(\partial_\sigma, \partial_\mu)\partial_\nu = R^{\rho}{}_{\sigma\mu\nu}\partial_\rho$, where

$$R^{\rho}{}_{\sigma\mu\nu} = -\partial_\sigma\Gamma^{\rho}_{\mu\nu} + \partial_\mu\Gamma^{\rho}_{\sigma\nu} - \Gamma^{\rho}_{\sigma\tau}\Gamma^{\tau}_{\mu\nu} + \Gamma^{\rho}_{\mu\tau}\Gamma^{\tau}_{\sigma\nu} \tag{1.3}$$

with Christoffel symbols

$$\Gamma^{\rho}_{\mu\nu} = \frac{1}{2}g^{\rho\sigma}(\partial_\mu g_{\sigma\nu} + \partial_\nu g_{\mu\sigma} - \partial_\sigma g_{\mu\nu}). \tag{1.4}$$

The equivalence principle requires, however, that special relativity holds within any local inertial frame, hence, the energy-momentum conservation $T^{\mu\nu}{}_{,\nu} = 0$ must be formulated covariantly, i.e., $T^{\mu\nu}{}_{;\nu} = 0$, where commas and semicolons denote partial and covariant derivatives, respectively. But $R^{\mu\nu}{}_{;\nu} = 0$ is in general not true. Using metric compatibility, the contracted second Bianchi identity provides a tensor whose covariant derivative vanishes, i.e.,

$$G_{\mu\nu} \equiv R_{\mu\nu} - \frac{1}{2} g_{\mu\nu} R, \tag{1.5}$$

where $R \equiv g^{\mu\nu} R_{\mu\nu}$ is the Ricci scalar. $G_{\mu\nu}$ is commonly referred to as the Einstein tensor [2–5]. The Einstein field equations for general relativity therefore read $G_{\mu\nu} = \kappa^2 T_{\mu\nu}$, where the gravitational coupling constant $\kappa^2 = 8\pi G$ can be determined from requiring that a perfect fluid of energy density ρ and pressure p, described by the energy-momentum tensor

$$T^{\mu}_{\ \nu} = p\, \delta^{\mu}_{\ \nu} + (\rho + p) u^{\mu} u_{\nu}, \tag{1.6}$$

obeys the Poisson equation, Eq. (1.2), in the slowly evolving weak-field limit. Here, u^{μ} is a unit timelike vector field that describes the four-velocity of the fluid.

Note that due to the metric compatibility of the Levi-Civita connection, one can add a constant factor of the metric Λ, the so-called cosmological constant, that still satisfies the requirements made above. Thus, the Einstein field equations become

$$R_{\mu\nu} - \frac{1}{2} g_{\mu\nu} R + \Lambda g_{\mu\nu} = \kappa^2 T_{\mu\nu}. \tag{1.7}$$

One can also use the least-action principle to derive the field equations from the Einstein-Hilbert action

$$S = \frac{1}{2\kappa^2} \int d^4x \sqrt{-g} R + \int d^4x \sqrt{-g} \mathcal{L}_{\mathrm{m}}, \tag{1.8}$$

by variation of S with respect to $g_{\mu\nu}$. Here, g denotes the determinant of $g_{\mu\nu}$, and $\mathcal{L}_{\mathrm{m}}$ is the Lagrangian of the matter fields with $T_{\mu\nu} = -2\, \delta\mathcal{L}_{\mathrm{m}} / \delta g^{\mu\nu} / \sqrt{-g}$. Note that it is this action that provides the source for modifications of general relativity in Secs. 1.1.2 and 1.1.3. However, it is of importance to note that modifications to general relativity automatically break assumptions imposed on $[D^{(2)}(g)]^{\mu\nu}$.

It can be shown [6–8] that the Einstein tensor, Eq. (1.5), with a cosmological constant, $[D^{(2)}(g)]^{\mu\nu} = a\, G^{\mu\nu} + b\, g^{\mu\nu}$, where $a,\ b = \mathrm{const}$, is the only tensor satisfying:

(a) $[D^{(2)}(g)]^{\mu\nu} = [D^{(2)}(g_{\alpha\beta}; g_{\alpha\beta,\rho}; g_{\alpha\beta,\rho\sigma})]^{\mu\nu}$, i.e., the tensor includes maximally second-order derivatives of the metric;

(b) $\nabla^{\mu}[D^{(2)}(g)]_{\mu\nu} = 0$, i.e., the tensor is divergence free;

(c) $[D^{(2)}(g)]^{\mu\nu} = [D^{(2)}(g)]^{\nu\mu}$, i.e., the tensor is symmetric;

(d) linearity of $[D^{(2)}(g)]^{\mu\nu}$ in $g_{\alpha\beta,\rho\sigma}$.

In the four-dimensional case, conditions (c) and (d) are dispensable [9–11]:

Theorem 1.1.1: (**Lovelock**) If for $n = 4$ dimensions, $[D^{(2)}(g)]^{\mu\nu}$ satisfies (a) and (b), then $[D^{(2)}(g)]^{\mu\nu} = a\, G^{\mu\nu} + b\, g^{\mu\nu}$.

A rigorous proof of this theorem shall not be given here but note that the most general $[D^{(2)}(g)]^{\mu\nu}$ satisfying the conditions (a)-(c) is [10]

$$[D^{(2)}(g)]^{\mu\nu} = \sum_{\alpha=1}^{\infty} a_{(\alpha)} g^{\rho\nu} \delta^{\mu\mu_1\cdots\mu_{2\alpha}}_{\rho\rho_1\cdots\rho_{2\alpha}} R^{\rho_2}{}_{\mu_2\mu_1}{}^{\rho_1} \cdots R^{\rho_{2\alpha}}{}_{\mu_{2\alpha}\mu_{2\alpha-1}}{}^{\rho_{2\alpha-1}} + a\, g^{\mu\nu}, \tag{1.9}$$

where $a_{(\alpha)}$, $a =$ const and $\delta^{\mu\mu_1\cdots\mu_{2\alpha}}_{\rho\rho_1\cdots\rho_{2\alpha}}$ is the generalized Kronecker delta defined by the determinant

$$\delta^{\mu\mu_1\cdots\mu_n}_{\rho\rho_1\cdots\rho_n} \equiv \sum_{\sigma\in S_n} \left[\mathrm{sgn}(\sigma) \prod_{i=1}^{n} \delta^{\mu_i}_{\nu_{\sigma(i)}} \right]. \tag{1.10}$$

In four dimensions this reduces to the Einstein tensor, which is the unique tensor even if condition (c) is dropped, as was shown in [11], i.e., (c) and (d) are automatically satisfied. Note furthermore, that for $n = 4$, the most general scalar Lagrange density $\mathcal{L} = \mathcal{L}(g_{\alpha\beta}, g_{\alpha\beta,\rho}, g_{\alpha\beta,\rho\sigma})$, whose Euler-Lagrange equations involve $\sqrt{-g}(a\, G^{\mu\nu} + b\, g^{\mu\nu})$ is [10]

$$\mathcal{L} = \sqrt{-g} \left(\alpha + \beta\, \delta^{\mu\nu}_{\rho\sigma} R^{\sigma}{}_{\nu\mu}{}^{\rho} + \gamma\, \delta^{\mu\nu\xi o}_{\rho\sigma\tau\upsilon} R^{\sigma}{}_{\nu\mu}{}^{\rho} R^{\upsilon}{}_{o\xi}{}^{\tau} \right) + \mu\, R_{\mu\nu\rho\sigma} {}^{*}R^{\mu\nu\rho\sigma}, \tag{1.11}$$

where α, β, γ, $\mu =$ const and ${}^{*}R^{\mu\nu\rho\sigma}$ is dual to $R_{\mu\nu\rho\sigma}$, i.e., ${}^{*}R_{\mu}{}^{\nu\rho}{}_{\sigma} = \epsilon^{\tau\nu\rho\upsilon} R_{\mu\tau\upsilon\sigma}$ with Levi-Civita tensor $\epsilon^{\tau\nu\rho\upsilon}$, which is anti-symmetric under odd permutations.

Even without any gravitational field equations at hand, assumptions imposed on the geometrical properties of the universe constrain the form of its feasible spacetimes. Under the cosmological principle the universe is spatially homogeneous and isotropic, i.e., any spacetime coordinate point looks the same and for any point, different directions look alike. More specifically (cf., e.g., [12]):

Definition 1.1.1: A spacetime $(\mathcal{M}, g)$ is *spatially homogeneous* if $\exists \Sigma_t \mid \forall t \wedge \forall p, q \in \Sigma_t\ \exists f : \Sigma_t \to \Sigma_t, p \mapsto q$ with Σ_t a foliation of spacetime, a one-parameter family of spacelike hypersurfaces, and f an *isometry* of g, i.e., f is a diffeomorphism, $f : (\mathcal{M}, g) \to (\mathcal{N}, h)$, such that the pullback $f^{*}(h) = g$, where $f^{*}(g)_{\mu\nu}(x) = \partial_\mu f^\rho(x) \partial_\nu f^\sigma(x) g_{\rho\sigma}[f(x)]$.

Definition 1.1.2: A spacetime $(\mathcal{M}, g)$ is *spatially isotropic* at each point p if $\forall p\ \exists (u_i)^\mu \in T_p\mathcal{M} \mid (u_i)^\mu (u_i)_\mu = -1 \mid \forall (v_j)^\mu, (v_k)^\mu \in T_p\mathcal{M} \mid (u_i)^\mu (v_l)_\mu = 0 \wedge (v_l)^\mu (v_l)_\mu = 1,\ l = j, k\ \exists f : T_p\mathcal{M} \to T_p\mathcal{M}, p \mapsto p, (u_i)^\mu \mapsto (u_i)^\mu, (v_j)^\mu \mapsto (v_k)^\mu$.

Theorem 1.1.2: (Friedmann-Lemaître-Robertson-Walker – FLRW) Spatial homogeneity and isotropy of a pseudo-Riemannian four-dimensional spacetime $(\hat{\mathcal{M}}, g)$ implies that

$$g_{\mu\nu} dx^\mu dx^\nu = -dt^2 + a^2(t) \left[\frac{1}{1 - K\, r^2} dr^2 + r^2 \left(d\theta^2 + \sin^2\theta\, d\phi^2 \right) \right], \tag{1.12}$$

where $\hat{\mathcal{M}} \cong \mathbb{R} \times \mathcal{M}$ and K is a constant with

$$K = \begin{cases} 1, & \mathcal{M} = \mathcal{S}^3 \\ 0, & \mathcal{M} = \mathbb{R}^3 \\ -1, & \mathcal{M} = \mathcal{PS}^3 \end{cases}, \tag{1.13}$$

i.e., a hyperspherical, flat, and hyperbolic universe at time t.

Proof: An adumbrated proof based on [12] shall be given here: The foliation hypersurfaces are orthogonal to the world lines of isotropic observers, i.e., $\Sigma_t \perp (u_i)^\mu$. The metric g induces a metric $h(t)$ on Σ_t for which (a) (homogeneity) $\exists$ isometry $f : p \mapsto q \ \forall p, q \in \Sigma_t$ and (b) (isotropy) $\nexists$ geometrically preferred vectors on Σ_t. ${}^{(3)}R^{i\ \,k}_{\ j\ \,l}(h_p)$ defines a linear map $L \in C^\infty(T^*\mathcal{M} \otimes T^*\mathcal{M} \otimes T\mathcal{M} \otimes T\mathcal{M})$, $L : \mathcal{W} \to \mathcal{W}$ with $\mathcal{W} = C^\infty(T\mathcal{M}) \times C^\infty(T\mathcal{M})$ at p with orthonormal basis of eigenvectors of L, which due to isotropy must all be equal. Hence, $L = K \cdot \mathbb{1}$ and therefore, ${}^{(3)}R_{ijkl} = K\, h_{l[j}h_{k]i}$, where $K = \text{const}$, which defines a space of constant curvature. The brackets denote the alternating sum over the permutations with signs given by the parity of the permutation. $K > 0$, $K = 0$, and $K < 0$ are locally isometric to $\mathcal{S}^3$, $\mathbb{R}^3$, and $\mathcal{PS}^3$, respectively. Due to $\Sigma_t \perp (u_i)^\mu$, the spacetime is warped and the hypersurface can be assigned the proper time t. □

From the Einstein equations, Eq. (1.7), with the FLRW metric, Eq. (1.12), and for a perfect fluid defined by Eq. (1.6), one obtains the first and second Friedmann equations

$$H^2 = \frac{\kappa^2}{3}\rho - \frac{K}{a^2} + \frac{\Lambda}{3}, \tag{1.14}$$

$$\frac{\ddot{a}}{a} = -\frac{\kappa^2}{6}(\rho + 3p) + \frac{\Lambda}{3}, \tag{1.15}$$

respectively, where $H = \dot{a}/a$ is the Hubble parameter. Note that here and throughout this thesis, where not otherwise indicated, dots denote derivatives with respect to proper time t. From the energy-momentum conservation, one can further derive the fluid equation

$$\dot{\rho} + 3H(\rho + p) = 0, \tag{1.16}$$

which determines the time-dependence of ρ given the equation of state $w = p/\rho$ of the contributing components, i.e.,

$$\rho = \rho_0 a^{-3(1+w)}, \tag{1.17}$$

where w was assumed constant and ρ_0 is the energy density today, $a = a_0 \equiv 1$. For matter, radiation, and the cosmological constant, $w = 0,\ 1/3,\ -1$, respectively. From Eq. (1.15) it is clear how a cosmological constant leads to an acceleration of the universe.

One can move the cosmological constant to the right-hand side of the Einstein field equations, Eq. (1.7), and interpret it as a vacuum energy. Consider the zero-point energy $E = \omega/2 = \sqrt{k^2 + m^2}/2$ of a field with mass m, momentum k, and frequency ω, where $\hbar \equiv 1$. The vacuum energy density is then

$$\rho_{\text{vac}} = \int_0^{k_{\max}} \frac{d^3k}{(2\pi)^3} \frac{\sqrt{k^2 + m^2}}{2} \approx \int_0^{k_{\max}} \frac{dk}{(2\pi)^2} k^3 = \left(\frac{k_{\max}^2}{4\pi}\right)^2 \tag{1.18}$$

with $k \ll m$ and cut-off $k_{\max}$. For a cut-off at the Planck scale with mass m_{P}, one obtains $\rho_{\text{vac}} \simeq 10^{74}$ GeV^4, whereas $\rho_{\text{DE},0} \simeq 10^{-47}$ GeV^4 is the value inferred from observations. This severe discrepancy between the theoretical prediction and the measured value, as well as the fact that the cosmological constant is non-zero, where $\Lambda = 0$ could be due to symmetry conditions, is known as the *cosmological constant problem.* Many attempts have been made to explain the low value of Λ (see, e.g., [13–15] for a review).

Note that it must not necessarily be a cosmological constant that drives the cosmic acceleration. An energy component with equation of state of $w < -1/3$ can also produce this effect [see Eq. (1.15)]. The unknown component used to explain the observed late-time acceleration of the universe [16, 17] is generally dubbed *dark energy.* Dark energy in form of a cosmological constant together with the framework of general relativity, the Standard Model of particle physics [18–23], the flatness of the universe [24], and *dark matter* [25], required to, e.g., explain the clustering of galaxies on large scales [26] and the flattening of rotation curves [27], establishes the concordance model of cosmology ΛCDM. The modifications of gravity analyzed in this thesis are constructed to yield a late-time acceleration of the universe by adopting dark matter but excluding dark energy.

Before continuing by describing such modifications to general relativity, it is worth revisiting assumption (a) made above, i.e., $[D^{(2)}(g)]^{\mu\nu} = [D^{(2)}(g_{\alpha\beta}; g_{\alpha\beta,\rho}; g_{\alpha\beta,\rho\sigma})]^{\mu\nu}$. Since instabilities may arise when going beyond second derivatives of fundamental dynamical quantities in the equations of motion, it is a reasonable condition to impose. More specifically [28]:

Theorem 1.1.3: (Ostrogradsky) The Hamiltonian of a Lagrangian $L\left[q, \dot{q}, \ddot{q}, \dots, q^{(N)}\right]$ with *nondegeneracy* in $q^{(N)}$, i.e., $\partial_{q^{(N)}} L$ depends on $q^{(N)}$, is

$$\begin{aligned} H(Q_1, \dots, Q_N, P_1, \dots P_N) &= \left(\sum_{n=1}^{N-1} P_n Q_{n+1}\right) + P_N a(Q_1, \dots, Q_N, P_N) \\ &\quad - L[Q_1, \dots, Q_N, a(Q_1, \dots, Q_N, P_N)], \end{aligned} \tag{1.19}$$

where the canonical coordinates are

$$Q_n \equiv q^{(n-1)}, \tag{1.20}$$

$$P_n \equiv \sum_{m=n}^{N} \left(-\frac{d}{dt}\right)^{m-n} \frac{\partial L}{\partial q^{(m)}}. \tag{1.21}$$

Here, $n = 1, \dots, N$ and $a(Q_1, \dots, Q_N, P_N)$ with

$$P_N = \partial_{q^{(N)}} L|_{\{q^{(0)}, \dots, q^{(N-1)}, q^{(N)}\} = \{Q_1 \dots, Q_N, a\}}. \tag{1.22}$$

Further, the canonical evolution equations apply.

Proof: The Euler-Lagrange equation of $L\left[q, \dot{q}, \ddot{q}, \dots, q^{(N)}\right]$ is

$$\sum_{m=0}^{N} \left(-\frac{d}{dt}\right)^{m} \frac{\partial L}{\partial q^{(m)}} = 0. \tag{1.23}$$

This implies that $q^{(2N)} = \mathcal{F}\left[q, \dot{q}, \ddot{q}, \dots, q^{(2N-1)}\right]$ and therefore $q(t) = \mathcal{Q}[t, q_0, \dot{q}_0, \ddot{q}_0, \dots, q_0^{(2N-1)}]$, where $q^{(n)}$, $n \in \mathbb{N}|\{q^{(0)} = q, q^{(1)} = \dot{q}, q^{(2)} = \ddot{q}, \dots\}$ and subscripts of 0 indicate initial values. With canonical coordinates defined as above and nondegeneracy of $q^{(N)}$, the phase space transformation can be inverted such that $q^{(N)} = q^{(N)}(Q_1, \ldots, Q_N, P_N)$. Hence, there exists a function $a(Q_1, \ldots, Q_N, P_N)$ with the property described above. The Hamiltonian is obtained through Legendre transformation on $\dot{q}, \ddot{q}, \ldots, q^{(N)}$, i.e., $H(Q_1, \ldots, Q_N, P_1, \ldots, P_N) = \sum_{n=1}^{N} P_n q^{(n)} - L$. $\dot{Q}_n \equiv \partial H / \partial P_n$ and $\dot{P}_n \equiv -\partial H / \partial Q_n$ with $n = 1, \ldots, N$ reproduce the Euler-Lagrange equations and the conditions on P_N. ☐

For $N > 1$, linear terms of the canonical momenta P_n appear in the Hamiltonian H through $\sum_{n=1}^{N-1} P_n Q_{n+1}$. Hence, H does not have a lower bound, which leads to an instability for interacting field theories – the so-called *Ostrogradsky instability.* Note that in the case of general relativity, R contains second-order derivatives of the metric. These are, however, of linear order [see condition (d)], hence, the requirement of nondegeneracy in Thm. (1.1.3) does not apply. The Einstein field equations, Eq. (1.7), contain only second-order derivatives of the metric. A very simple modification of general relativity is the class of the so-called $f(R)$ gravity models discussed in Sec. 1.1.3. $f(R)$ gravity models are, due to the nonlinearity in $g_{\alpha\beta,\rho\sigma}$, higher-order derivative theories. They do, however, not exhibit an Ostrogradsky instability of the kinetic energy as will be shown in Sec. 1.1.3. But first, the following subsection shall be devoted to a higher-dimensional gravitational theory with an additional induced four-dimensional brane metric.

1.1.2. DGP braneworld gravity

Dvali, Gabadadze, and Porrati [29] proposed a gravitational model in which the universe is a $(3+1)$-dimensional brane embedded in a five-dimensional Minkowski space with an infinite size extra dimension. It was shown in [30] that in such a model late-time acceleration can occur without the need of a cosmological constant. The standard model of high-energy physics, including matter fields and a cosmological constant or brane tension, is assumed to be confined to the brane while only gravity is allowed to extend to the full five-dimensional bulk. For now, the more general DGP action shall be considered, i.e.,

$$S = -\frac{1}{2\kappa^2} \int d^5X \sqrt{-\hat{g}} \left(\hat{R} + \mathcal{L}_{\mathrm{M}} \right) - \frac{1}{2\mu^2} \int d^4x \sqrt{-\tilde{g}} \tilde{R}. \tag{1.24}$$

Here the four- and five-dimensional quantities are denoted by tildes and hats, respectively. The five-dimensional bulk metric $\hat{g}_{AB}$ induces the four-dimensional brane metric $\tilde{g}_{\mu\nu}$ by

$$\tilde{g}_{\mu\nu} = \partial_\mu X^A \partial_\nu X^B \hat{g}_{AB}, \tag{1.25}$$

where $X^A(x^\mu)$ are the coordinates of an event x^μ on the brane. The gravitational coupling constants κ^2 and μ^2 are related to the Planck masses M_{bulk} and M_{brane} as $\kappa^2 = M_{\mathrm{bulk}}^{-3}$ and $\mu^2 = M_{\mathrm{brane}}^{-2}$, respectively.

Consider the five-dimensional line element [30]

$$ds^2 = \hat{g}_{AB} dX^A dX^B = \tilde{g}_{\mu\nu} dx^\mu dx^\nu + b^2 dy^2, \tag{1.26}$$

where y represents the extra dimension. The brane shall be the hypersurface located at $y = 0$. For cosmological studies, the FLRW metric is generalized to five-dimensions defined by the line element

$$ds^2 = -n^2(\tau, y)d\tau^2 + a^2(\tau, y)\gamma_{ij}dx^i dx^j + b^2(\tau, y)dy^2, \tag{1.27}$$

where γ_{ij} is the three-dimensional spatial metric with constant curvature K.

Variation of the Einstein-Hilbert action, Eq. (1.24) with respect to $\hat{g}_{AB}$ yields the five-dimensional Einstein equations

$$\hat{G}_{AB} \equiv \hat{R}_{AB} - \frac{1}{2}\hat{R}\,\hat{g}_{AB} = \kappa^2 \hat{S}_{AB}, \tag{1.28}$$

where $\hat{S}$ contains the contributions from $\mathcal{L}_\mathrm{M}$ and $\tilde{R}$, which shall be denoted by the five-dimensional energy-momentum tensor $\hat{T}^A{}_B$ and $\hat{U}^A{}_B$, respectively, i.e., $\hat{S}^A{}_B = \hat{T}^A{}_B + \hat{U}^A{}_B$. Moreover,

$$\begin{aligned}
\hat{T}^A{}_B &= \bar{T}^A{}_B|_\mathrm{bulk} + \tilde{T}^A{}_B|_\mathrm{brane}, && (1.29)\\
\bar{T}^A{}_B|_\mathrm{bulk} &= -\rho_\mathrm{bulk}\mathbb{1}_5, && (1.30)\\
\tilde{T}^A{}_B|_\mathrm{brane} &= \frac{\delta(y)}{b}\mathrm{diag}(-\rho, p, p, p, 0), && (1.31)\\
\hat{T}_{05} &= 0, && (1.32)
\end{aligned}$$

where the assumptions were made that the bulk only contains a tension ρ_bulk in form of a cosmological constant, that the geometry on the brane is homogeneous and isotropic, and that there are no matter flows into the fifth dimension. Furthermore, [30]

$$\begin{aligned}
\hat{U}_{00} &= -\frac{3\delta(y)}{\mu^2 b}\left(\frac{\dot{a}^2}{a^2} + \frac{n^2 K}{a^2}\right), && (1.33)\\
\hat{U}_{ij} &= -\frac{\delta(y)}{\mu^2 b}\gamma_{ij}\left[\frac{a^2}{n^2}\left(-\frac{\dot{a}^2}{a^2} + 2\frac{\dot{a}}{a}\frac{\dot{n}}{n} - 2\frac{\ddot{a}}{a}\right) - K\right], && (1.34)
\end{aligned}$$

where dots represent derivatives with respect to τ and other components of $\hat{U}_{AB}$ vanish.

The relation

$$\left(\frac{a'}{a\,b}\right)^2 - \left(\frac{\dot{a}}{a\,n}\right)^2 - \frac{K}{a^2} + \frac{\kappa^2}{6}\rho_\mathrm{bulk} + \frac{C}{a^4} = 0 \tag{1.35}$$

defines a solution to the Einstein equations in the bulk for any set $\{a, b, n\}$ given $\hat{G}_{05} = \hat{T}_{05} = 0$ [31]. Here and throughout this section primes denote derivatives with respect to y. C is a constant of integration.

The geometry and therefore the metric is required to be continuous across the brane, however, the derivatives of the metric with respect to y may be discontinuous, causing Dirac delta functions in the second derivatives of the metric with respect to y. The extrinsic curvature or second fundamental form is

$$\mathcal{K}_{AB} = h^C{}_A \nabla_C u_B, \tag{1.36}$$

where u^A is the unit vector field normal to the three-brane worldsheet. It is spacelike, $g_{AB}u^Au^B = 1$, with induced metric on the brane worldsheet $h_{AB} = g_{AB} - u_Au_B$. $\mathcal{K}_{AB}$ can be interpreted as the bending of the brane worldsheet in the five-dimensional spacetime. The Israel's junction conditions [32] relate the jump in the extrinsic curvature across the brane to the brane energy-momentum sources $\tilde{T}^A{}_B$. More specifically,

$$[\mathcal{K}^A{}_B - \mathcal{K}\,\delta^A{}_B] = -\kappa^2 \tilde{S}^A{}_B, \tag{1.37}$$

where

$$\tilde{T}^A{}_B|_{\text{brane}} + \hat{U}^A{}_B = \frac{\delta(y)}{b}\tilde{S}^A{}_B. \tag{1.38}$$

With the background above [33]

$$\mathcal{K}^A{}_B = \text{diag}\left(\frac{n'}{n\,b}, \frac{a'}{a\,b}\delta^i{}_j, 0\right) \tag{1.39}$$

and the junction conditions become [30]

$$\begin{aligned} \frac{[a']}{a_0 b_0} &= -\frac{\kappa^2}{3}\rho + \left(\frac{\kappa}{\mu\, n_0}\right)^2 \left\{\left(\frac{\dot{a}_0}{a_0}\right)^2 + K\left(\frac{n_0}{a_0}\right)^2\right\}, && (1.40) \\ \frac{[n']}{n_0 b_0} &= \frac{\kappa^2}{\mu^2 n_0^2}\left\{-\left(\frac{\dot{a}_0}{a_0}\right)^2 - 2\frac{\dot{a}_0}{a_0}\frac{\dot{n}_0}{n_0} + 2\frac{\ddot{a}_0}{a_0} - K\left(\frac{n_0}{a_0}\right)^2\right\} \\ &\quad -\frac{\kappa^2}{3}(3\rho + 2p), && (1.41) \end{aligned}$$

where $q_0 = q(y=0)$ with $q \in \{a, b, n\}$ and $[q] = q(0^+) - q(0^-)$ describes the jump across the brane.

For a $\mathbb{Z}_2$ symmetry in y on the brane, $[a'] = 2a'(0^+)$ and with continuity at $y = 0$, the combination of Eqs. (1.35) and (1.40) yield the first Friedmann equation

$$\sigma\sqrt{H^2 - \frac{\kappa^2}{6}\rho_{\text{bulk}} - \frac{C}{a_0^4} + \frac{K}{a_0^2}} = \frac{\kappa^2}{2\mu^2}\left(H^2 + \frac{K}{a_0^2}\right) - \frac{\kappa^2}{6}\rho, \tag{1.42}$$

where $H = \dot{a}/(a_0 n_0)$ is the Hubble parameter and $\sigma = \text{sgn}([a'])$. With vanishing Schwarzschild mass parameter C and zero bulk tension, this simplifies to

$$H^2 - \frac{\sigma}{r_{\text{c}}}\sqrt{H^2 + \frac{K}{a_0^2}} = \frac{\mu^2}{3}\rho - \frac{K}{a_0^2}, \tag{1.43}$$

where $r_{\text{c}} = \kappa^2/2\mu^2$ is the the crossover distance governing the transition from five-dimensional to four-dimensional effective scalar-tensor gravity. Assuming small spatial curvature K, the standard Friedmann equation is reproduced for $r_{\text{c}} \gg H^{-1}$, otherwise the expansion history is modified and approaches a de Sitter solution for $\sigma = +1$ in the late-time matter-only Universe, i.e., $H \to 1/r_{\text{c}}$. This may mimic cosmic acceleration in the case that $1/r_{\text{c}} \sim H_0$. Hence, the scenario $\sigma = +1$ is referred to as the *self-accelerating* branch of the DGP gravity model. The *normal branch* of the DGP model thus denotes the case where $\sigma = -1$, where a cosmological constant or brane tension is required to yield a late-time acceleration. Gravity on the brane is consequently modified on large scales.

On local scales, modifications of gravity are tightly constrained. However, in DGP, the Vainshtein mechanism [34] applies, i.e., on scales smaller than the Vainshtein radius $r_* = (r_{\rm c}^2 r_{\rm g})^{1/3}$, nonlinear interactions become important [35] and return gravity to general relativity around a point mass with Schwarzschild radius $r_{\rm g}$ (see, e.g., [36]). More specifically, on the brane, in the quasistatic limit of subhorizon perturbations, the brane-bending mode, the effective scalar degree of freedom associated with the brane displacement, is governed by the equation of motion [37]

$$\frac{3\beta(t)}{a^2}\nabla^2\varphi + \frac{r_{\rm c}^2}{a^4}\left[\left(\nabla^2\varphi\right)^2 - \left(\nabla_\mu\nabla_\nu\varphi\right)\left(\nabla^\mu\nabla^\nu\varphi\right)\right] = \mu^2\delta\rho \tag{1.44}$$

with $\delta\rho = -\delta T^0{}_0$ and φ corresponding to the first order of the brane dislocation, where we keep second-order terms of φ. Furthermore,

$$\beta(t) = 1 - 2\sigma\, H\, r_{\rm c}\left(1 + \frac{H'}{3H}\right). \tag{1.45}$$

Applying spherical symmetry, Eq. (1.44) becomes [37]

$$\left(\frac{d^2}{dr^2} + \frac{2}{r}\frac{d}{dr}\right)(3\beta\,\varphi + \Xi) = \mu^2\delta\rho, \tag{1.46}$$

where

$$\Xi = 2r_{\rm c}^2\int\frac{dr}{r}\left(\frac{d\varphi}{dr}\right)^2. \tag{1.47}$$

For a source in a compact region, the solution of Eq. (1.46) is [37]

$$3\beta\,\varphi + \Xi + \frac{r_{\rm g}}{r} = 0, \tag{1.48}$$

where

$$r_{\rm g} = \mu^2\int_0^r dr\, r^2 d\rho \tag{1.49}$$

is the Schwarzschild radius of the source. Assuming a constant $r_{\rm g}$ and taking the derivative of Eq. (1.48), one arrives at [37]

$$\frac{d\varphi}{dr} = \frac{r_{\rm g}}{r^2}\Delta(r), \quad \Delta(r) = \frac{2}{3\beta}\left(\frac{r}{r_*}\right)^3\left[\sqrt{1 + \left(\frac{r_*}{r}\right)^3} - 1\right] \tag{1.50}$$

with

$$r_* = \left(\frac{8r_{\rm c}^2 r_{\rm g}}{9\beta^2}\right), \tag{1.51}$$

the Vainshtein radius in a cosmological background. The metric perturbations $\Psi \equiv \delta g_{00}/(2g_{00})$ and $\Phi \equiv \delta g_{ij}/(2g_{ij})$ are given by [37]

$$\Phi = \frac{r_{\rm g}}{2r} + \frac{\varphi}{2}, \tag{1.52}$$

$$\Psi = -\frac{r_{\rm g}}{2r} + \frac{\varphi}{2}, \tag{1.53}$$

which for $r > r_*$ become [37]

$$\Phi = \frac{r_{\rm g}}{2r}\left(1 - \frac{1}{3\beta}\right), \tag{1.54}$$

$$\Psi = -\frac{r_{\rm g}}{2r}\left(1 + \frac{1}{3\beta}\right), \tag{1.55}$$

and for $r < r_*$ are given by [37]

$$\Phi = \frac{r_{\rm g}}{2r} - \sigma\sqrt{\frac{r_{\rm g} r}{2r_{\rm c}^2}}, \tag{1.56}$$

$$\Psi = -\frac{r_{\rm g}}{2r} + \sigma\sqrt{\frac{r_{\rm g} r}{2r_{\rm c}^2}}, \tag{1.57}$$

respectively. Thus, for scales $r \ll r_*$ modifications to general relativity are suppressed.

1.1.3. $f(R)$ gravity

A simple modification of general relativity is the class of $f(R)$ gravity models, where a free function of the Ricci scalar R is added to the four-dimensional Einstein-Hilbert action such that

$$S = \frac{1}{2\kappa^2}\int dx^4\sqrt{-g}[R + f(R)] + \int d^4x\sqrt{-g}\,\mathcal{L}_{\rm m}(g_{\mu\nu}, \Psi_{\rm m}). \tag{1.58}$$

Here, $\kappa^2 \equiv 8\pi G$ and $\mathcal{L}_{\rm m}$ is the minimally coupled matter Lagrangian, which depends on the metric $g_{\mu\nu}$ and the matter fields $\Psi_{\rm m}$, where we have set $c \equiv 1$. Note that in the case $f(R) = -2\Lambda$, where Λ is a cosmological constant, $f(R)$ gravity returns to ΛCDM. The additional function $f(R)$ can be designed to become important in the low curvature regime and generate cosmic acceleration [38–40].

The standard procedure for the derivation of the Einstein equations is by variation of the Einstein-Hilbert action with respect to the metric. Thereby, the affine connections are of Levi-Civita type, hence, the Christoffel symbols relate to the metric as in Eq. (1.4). This procedure is known as the *metric* formalism. Alternatively, one may consider the metric and the connections as independent variables and vary the action with respect to both, while assuming that the matter Lagrangian is independent of the connection. This approach is commonly referred to as the *Palatini* formalism. For the general relativistic action both formalisms lead to the same Einstein field equations (see, e.g., [41]). This is however not true anymore in $f(R)$ gravity, where one, therefore, distinguishes between metric $f(R)$ and Palatini $f(R)$ gravity. There is even a third, more general kind, dubbed *metric-affine* $f(R)$ gravity, which adopts the Palatini formalism, but does not assume independence of $\mathcal{L}_{\rm m}$ on the connection. This thesis shall concentrate on metric $f(R)$ models only.

In the metric formalism of $f(R)$ gravity, variation of the action, Eq. (1.58), with respect to $g_{\mu\nu}$ yields the modified Einstein equations,

$$G_{\mu\nu} + f_R R_{\mu\nu} - \left(\frac{f}{2} - \Box f_R\right) g_{\mu\nu} - \nabla_\mu\nabla_\nu f_R = \kappa^2 T_{\mu\nu}, \tag{1.59}$$

where $G_{\mu\nu}$ is the Einstein tensor and $T_{\mu\nu}$ is the energy-momentum tensor of the matter content. Subscripts of R denote derivatives with respect to the Ricci scalar.

Eq. (1.59) contains fourth-order derivatives of the metric due to nonlinearities of R and therefore of $g_{\mu\nu,\rho\sigma}$ in $\mathcal{L}$. This seems to satisfy the nondegeneracy-condition of Thm. (1.1.3) at first glance. Hence, one would expect $f(R)$ gravity theories to have an Ostrogradsky instability. However, R contains only second-order derivatives of a single component of $g_{\mu\nu}$. The additional degree of freedom is fixed by the g_{00}-constraint on the Newtonian potentail, thus violating the nondegeneracy-condition [42–44]. The theory does therefore not exhibit an Ostrogradsky instability in the kinetic energy.

The trace of the modified Einstein equations, Eq. (1.59), yields the expression

$$\Box f_R = \frac{1}{3}\left[(1-f_R)R + 2f + \kappa^2 T\right] \equiv \frac{\partial V_{\text{eff}}}{\partial f_R}, \tag{1.60}$$

where $V_{\text{eff}}(f_R)$ is an effective potential of the scalar field f_R. Requiring $|f/R| \ll 1$ and $|f_R| \ll 1$ in high-curvature regimes, $R = -\kappa^2 T$ becomes an extremum of V_{eff}. The mass of f_R is obtained from the second derivative of V_{eff} with respect to f_R, i.e.,

$$m_{f_R}^2 \equiv \frac{\partial^2 V_{\text{eff}}}{\partial f_R^2} = \frac{1}{3}\left(\frac{1+f_R}{f_{RR}} - R\right). \tag{1.61}$$

At high curvatures, this becomes $m_{f_R}^2 \approx 1/f_{RR}$, which constrains f_{RR} to be positive to prevent the scalar field from becoming tachyonic. Furthermore, $f_{RR} > 0$ signifies that the extremum is a minimum, which implies stability against small perturbations [45]. Note that $2\pi/m_{f_R}$ is the Compton wavelength of the scalar field f_R, where $\hbar \equiv 1$.

Sometimes, it is conceptually simpler to perform a conformal transformation on the metric to rewrite the Jordan frame action for $f(R)$ gravity, Eq. (1.58), in the Einstein frame. Thereby, a new scalar degree of freedom emerges, and the matter fields and the conformally transformed metric become minimally coupled. As a consequence of this, freely falling test matter particles no longer follow geodesics of the new metric. The gravitational action of the $f(R)$ model, Eq. (1.58), can be rewritten in a dynamically equivalent form [46–48],

$$S = \frac{1}{2\kappa^2}\int d^4x\sqrt{-g}\left[(\varphi + f(\varphi) + (1+f_\varphi)(R-\varphi)\right] + \int d^4x\sqrt{-g}\mathcal{L}_{\text{m}}(\chi_i, g_{\mu\nu}), \tag{1.62}$$

where φ is a scalar field and $f_\varphi \equiv \partial f/\partial\varphi$. The conformal transformation of the metric is described by $\tilde{g}_{\mu\nu} = e^{2\omega(x^\alpha)}g_{\mu\nu}$, where the function $\omega(x^\alpha)$ is defined by the expression $e^{-2\omega}(1+f_R) = 1$. The action in the Einstein frame then becomes

$$\begin{aligned}\tilde{S} \;=\; & \frac{1}{2\kappa^2}\int d^4x\sqrt{-\tilde{g}}\tilde{R} + \int d^4x\sqrt{-\tilde{g}}\left[-\frac{1}{2}\tilde{g}^{\mu\nu}\left(\tilde{\nabla}_\mu\phi\right)\tilde{\nabla}_\nu\phi - V(\phi)\right] \\ & + \int d^4x\sqrt{-\tilde{g}}e^{-2\beta\kappa\phi}\mathcal{L}_{\text{m}}\left(\chi_i, e^{-\beta\kappa\phi}\tilde{g}_{\mu\nu}\right),\end{aligned} \tag{1.63}$$

where the scalar field is defined as $\phi \equiv 2\omega/(\beta\,\kappa)$ with $\beta \equiv \sqrt{2/3}$. The potential $V(\phi)$ is given by

$$V(\phi) = \frac{1}{2\kappa^2}\frac{R f_R - f}{(1+f_R)^2}. \tag{1.64}$$

There is a formal equivalence of $f(R)$ models with $\omega_{\mathrm{BD}} = 0$ Brans-Dicke scalar-tensor gravity [49], which emanates from the absence of a kinetic term in Eq. (1.62). Such models are found to violate stringent equivalence principle tests, which demand a bound of $\omega > 4 \times 10^4$ [50] for very light Brans-Dicke scalar fields, i.e., for $m_\phi \lesssim 10^{-27}$ GeV [47]. Note that the mass of the field is inferred from the second derivative of the potential, Eq. (1.64), with respect to ϕ.

However, local gravity constraints are obtained within a highly nonlinear region of spacetime. The effective coupling to the fifth force defined by ϕ can severely be suppressed due to nonlinear effects like the chameleon mechanism. Thereby the effective field mass becomes very massive within high density regions, returning the modified gravity theory to general relativity. More specifically, consider a spherically symmetric spacetime within a weak gravitational field. Then the field equation for ϕ obtained from varying the $f(R)$ action in Einstein frame, Eq. 1.63, with respect to ϕ, i.e.,

$$\Box\phi - V_{,\phi} = \frac{\kappa\,\beta}{2} e^{-2\kappa\,\beta\,\phi}\tilde{T}, \tag{1.65}$$

becomes

$$\frac{d^2\phi}{dr^2} + \frac{2}{r}\frac{d\phi}{dr} = \frac{dV_{\mathrm{eff}}}{d\phi}. \tag{1.66}$$

Here, the effective potential is given by

$$V_{\mathrm{eff}} = V(\phi) + e^{-\frac{\kappa}{2}\beta\,\phi}\tilde{\rho}, \qquad \tilde{\rho} = \rho\, e^{-\frac{3\kappa}{2}\beta\,\phi}. \tag{1.67}$$

Let $f(R)$ be such that

$$f(R) \simeq R - \mu\, R_{\mathrm{c}}\left[1 - \left(\frac{R_{\mathrm{c}}}{R}^{2n}\right)\right], \qquad R \gg R_{\mathrm{c}}, \tag{1.68}$$

where the constant $R_{\mathrm{c}} \sim R_0$, i.e., $f(R)$ approaches a cosmological constant in the high-curvature regime. The effective potential V_{eff} for a model satisfying Eq. (1.68) is

$$V_{\mathrm{eff}}(\phi) \simeq \frac{\mu\, R_{\mathrm{c}}}{2\kappa^2} e^{-2\kappa\,\beta\,\phi}\left[1 - (2n+1)\left(-\frac{\kappa\,\beta\,\phi}{2n\mu}\right)^{\frac{2n}{2n+1}}\right] + \tilde{\rho}\, e^{-\frac{\kappa}{2}\beta\,\phi}. \tag{1.69}$$

Let r_{c} be the radius of the spherically symmetric object. The density inside and outside of the body is assumed to be constant, i.e., $\tilde{\rho} = \tilde{\rho}_{\mathrm{A}}$ and $\tilde{\rho} = \tilde{\rho}_{\mathrm{B}}$ for $r < r_{\mathrm{c}}$ and $r > r_{\mathrm{c}}$, respectively. The minimum of V_{eff} inside and outside of the body is [51]

$$\kappa\,\phi_{\mathrm{A,B}} \simeq -\frac{2n\,\mu}{\beta}\left(\frac{R_{\mathrm{c}}}{\kappa^2\tilde{\rho}_{\mathrm{A,B}}}\right)^{2n+1}, \tag{1.70}$$

respectively.

The field can be solved for using the boundary conditions $d\phi/dr(r=0) = 0$ and $\phi(r \to \infty) = \phi_{\mathrm{B}}$. On the inside of the spherically symmetric object the field becomes very heavy, $m_{\mathrm{A}}^2 = V_{\mathrm{eff}}''(\phi_{\mathrm{A}})$, and develops a thin-shell that suppresses the effective coupling to matter outside of the body. The profile of the field on the outside is given by [51]

$$\phi(r) \simeq \phi_{\mathrm{B}} - \frac{2Q_{\mathrm{eff}}}{\kappa}\frac{G\,M_{\mathrm{c}}}{r}, \tag{1.71}$$

where the effective coupling $Q_{\rm eff}$ depends on the thin-shell parameter

$$\epsilon_{\rm th} \equiv \frac{\kappa(\phi_{\rm A} - \phi_{\rm B})}{3\beta\,\Phi_{\rm c}} \tag{1.72}$$

over $Q_{\rm eff} = 3\beta\,\epsilon_{\rm th}/2$. Here, $M_{\rm c} = 4\pi\, r_{\rm c}^3 \rho_{\rm A}/3$ is the mass of the body with gravitational potential $\Phi_{\rm c} = G\,M_{\rm c}/r_{\rm c}$. For $|\phi_{\rm B} \gg \phi_{\rm A}|$, i.e., $\rho_{\rm A} \gg \rho_{\rm B}$, one obtains

$$\epsilon_{\rm th} \simeq n\,\mu \left(\frac{R_{\rm c}}{\kappa^2 \rho_{\rm B}}\right)^{2n+1} \Phi_{\rm c}^{-1}. \tag{1.73}$$

When $\epsilon_{\rm th} \ll 1$, the coupling of the field to the matter is suppressed.

1.2. The parametrized post-Friedmann framework

Many classes of modifications of general relativity with the purpose of producing a late-time acceleration of the universe without invoking dark energy can be described in three regimes of gravitational dynamics, i.e., on superhorizon scales, which are governed by the expansion history, intermediate scales, on which the modification becomes an effective scalar-tensor theory, and the nonlinear regime, where gravity has to return to general relativity in order to not violate stringent observational constraints on local scales. The PPF [52, 53] formalism provides a framework that describes the three regimes of modifications. Using three functions and one parameter, it admits a mapping of the perturbations in modified gravity theories into the PPF perturbations. Since in this thesis, predictions made for the cosmic microwave background (CMB) anisotropies rely on this framework, it shall briefly be reviewed here. Thereby, for simplicity, radiation shall be neglected.

The extra terms appearing in the Einstein field equations due to modifications of gravity may be viewed as en effective dark energy component, hence,

$$T^{\mu\nu}_{\rm eff} \equiv \kappa^2 G^{\mu\nu} - T^{\mu\nu}_{\rm m}, \tag{1.74}$$

with energy-momentum conservation, $\nabla_\mu T^{\mu\nu}_{\rm eff} = 0$. Thus, the usual cosmological perturbation theory may be applied.

Linear scalar metric perturbations on the FLRW background metric, Eq. (1.12), can be described by [52, 54, 55]

$$\begin{aligned} g^{00} &= -a^{-2}(1 - 2A\,Y), && (1.75)\\ g^{0i} &= -a^{-2} B\,Y^i, && (1.76)\\ g^{ij} &= a^{-2}\left(\gamma^{ij} - 2H_L Y \gamma^{ij} - 2H_T Y^{ij}\right), && (1.77) \end{aligned}$$

where the superscripts of zero represent conformal time. The spatial metric γ is assumed flat in contrast to the wavelengths such that one can assume plane waves for Y, hence,

$$\begin{aligned} Y &= e^{i\mathbf{k}\cdot\mathbf{x}}, && (1.78)\\ Y_i &= -k\nabla_i Y, && (1.79)\\ Y_{ij} &= \left(\frac{1}{k^2}\nabla_i\nabla_j + \frac{\gamma_{ij}}{3}\right) Y. && (1.80) \end{aligned}$$

The total energy-momentum tensor, $T^{\mu\nu} = T^{\mu\nu}_{\mathrm{m}} + T^{\mu\nu}_{\mathrm{eff}}$, is described by [52]

$$\begin{aligned} T^0_{\ 0} &= -\rho - \delta\rho, && (1.81)\\ T_0^{\ i} &= -(\rho + p) v Y^i, && (1.82)\\ T^i_{\ j} &= (p + \delta p Y)\delta^i_{\ j} + p\Pi Y^i_{\ j}. && (1.83) \end{aligned}$$

and the Einstein field equations read [52, 56]

$$\begin{aligned} H_L + \frac{1}{3}H_T + \frac{B}{k_H} - \frac{H_T'}{k_H^2} - \frac{\kappa^2}{2H^2k_H^2}\left[\delta\rho + 3(\rho+p)\frac{v-B}{k_H}\right] &= 0, && (1.84)\\ A + H_L + \frac{H_T}{3} + \frac{B'+2B}{k_H} - \left[\frac{H_T''}{k_H^2} + \left(3 + \frac{H'}{H}\right)\frac{H_T'}{k_H^2}\right] + \frac{\kappa^2}{H^2k_H^2}p\Pi &= 0, && (1.85)\\ A - H_L' - \frac{H_T'}{3} - \frac{\kappa^2}{2H^2}(\rho+p)\frac{v-B}{k_H} &= 0, && (1.86)\\ A' + \left(2 + \frac{2H'}{H} - \frac{k_H^2}{3}\right)A - \frac{k_H(B'+B)}{3} - H_L'' - \left(2+\frac{H'}{H}\right)H_L' & \\ + \frac{\kappa^2}{H^2}\left(\delta p + \frac{\delta\rho}{3}\right) &= 0, && (1.87) \end{aligned}$$

where $k_H = k/(aH)$ and primes denote derivatives with respect to $\ln a$. Energy-momentum conservation requires

$$\begin{aligned} \delta\rho' + 3(\delta\rho + \delta p) &= -(\rho+p)(k_H v + 3H_L'), && (1.88)\\ \frac{1}{a^4 k_H}\left[a^4(\rho+p)(v-B)\right]' &= \delta p - \frac{2p\Pi}{3} + (\rho+p)A. && (1.89) \end{aligned}$$

The matter comoving gauge is defined by $B = v_{\mathrm{m}}$ and $H_T = 0$, where further the notations $\zeta \equiv H_L$, $\xi \equiv A$, $\rho\Delta \equiv \delta\rho$, $\Delta_p \equiv \delta p$, and $V \equiv v$ shall be used. The Newtonian gauge is specified by $B = 0 = H_T = 0$, employing the further notations $\Phi \equiv H_L$ and $\Psi \equiv A$. The velocities in the two gauges correspond.

Note that the four metric perturbations in Eqs. (1.75) through (1.77) and the four matter perturbations in Eqs. (1.81) through (1.83) amount to a total of eight degrees of freedom. The Einstein field equations and the conservation equations fix only four of them, given that the Bianchi identities are already satisfied. Two degrees of freedom can further be removed by fixing to a gauge. The remaining two fluctuations are constrained by the closure relations defining the PPF formalism.

In Newtonian gauge, assuming that there is no anisotropic stress for matter, $\Pi_{\mathrm{m}} = 0$, two of the Einstein equations become

$$\begin{aligned} \Phi_+ &= -\frac{\kappa^2}{2H^2k_H^2}p_{\mathrm{eff}}\Pi_{\mathrm{eff}}, && (1.90)\\ \Phi_- &= \frac{\kappa^2}{2H^2k_H^2}\left[\rho_{\mathrm{m}}\Delta_{\mathrm{m}} + \rho_{\mathrm{eff}}\Delta_{\mathrm{eff}} + 3(\rho_{\mathrm{eff}} + p_{\mathrm{eff}})\frac{V_{\mathrm{eff}} - V_{\mathrm{m}}}{k_H} + p_{\mathrm{eff}}\Pi_{\mathrm{eff}}\right], && (1.91) \end{aligned}$$

where $\Phi_+ = (\Phi + \Psi)/2$ and $\Phi_- = (\Phi - \Psi)/2$. From the Einstein equations in the matter comoving gauge one obtains

$$V_{\mathrm{eff}} = V_{\mathrm{m}} - k_H\frac{2H^2}{\kappa^2 a^2(\rho_{\mathrm{eff}} + p_{\mathrm{eff}})}\zeta' \qquad (1.92)$$

and the stress-energy conservation for the effective dark energy component implies

$$\Delta_{p,\mathrm{eff}} = p_{\mathrm{eff}}\Delta_{\mathrm{eff}} - \frac{1}{3}\rho_{\mathrm{eff}}\Delta'_{\mathrm{eff}} - (\rho_{\mathrm{eff}} - p_{\mathrm{eff}})\left(\frac{k_H V_{\mathrm{eff}}}{3} + \zeta'\right), \tag{1.93}$$

where the perturbation variables can be related using, e.g., the variable transforms and energy-momentum conservation equations in the matter comoving gauge, i.e., $\zeta = \Phi - V_{\mathrm{m}}/k_H$, $\xi = \Psi - (V'_{\mathrm{m}} + V_{\mathrm{m}})/k_H$, $\Delta'_{\mathrm{m}} = -k_H V_{\mathrm{m}} - 3\zeta'$, and $\xi = 0$, respectively. Finally, the PPF closure relations are

$$\begin{aligned} p_{\mathrm{eff}}\Pi_{\mathrm{eff}} &= -\frac{2H^2k_H^2}{\kappa^2}g(a,k)\Phi_-, & (1.94)\\ \rho_{\mathrm{eff}}\Delta_{\mathrm{eff}} + 3(\rho_{\mathrm{eff}} + p_{\mathrm{eff}})\frac{V_{\mathrm{eff}} - V_{\mathrm{m}}}{k_H} + p_{\mathrm{eff}}\Pi_{\mathrm{eff}} &= -\frac{2k^2}{\kappa^2a^2}\Gamma(a,k), & (1.95)\end{aligned}$$

where g and Γ are PPF functions that are defined by the particular gravitational theory.

On superhorizon scales, it can be shown that [52, 54]

$$\Phi'' - \Psi' + \frac{H''}{H'}\Phi' - \left(\frac{H'}{H} - \frac{H''}{H'}\right) = \mathcal{O}(k_H^2\zeta). \tag{1.96}$$

This equation holds in specific for general relativity [56], DGP gravity [57], and $f(R)$ models [58]. The perturbations are completely characterized by the expansion history H and the relation of the two metric perturbations, which defines the first PPF function

$$g(a,k) \equiv \frac{\Phi_+}{\Phi_-} = \frac{\Phi + \Psi}{\Phi - \Psi}, \tag{1.97}$$

the metric ratio. In the quasistatic regime of subhorizon scales, the modifications of general relativity are characterized by a modification of the Poisson equation through $f_G(a)$,

$$k^2\Phi_- = \frac{\kappa^2}{2(1+f_G)}a^2\rho_{\mathrm{m}}\Delta_{\mathrm{m}}. \tag{1.98}$$

More generally, the Poisson equation may be written as [cf. Eqs. (1.91) and (1.95)]

$$k^2(\Phi_- + \Gamma) = \frac{\kappa^2}{2}a^2\rho_{\mathrm{m}}\Delta_{\mathrm{m}} \tag{1.99}$$

to interpolate between the super- and subhorizon scales, where Γ is determined by the evolution equation [52]

$$(1 + c_\Gamma k_H^2)[\Gamma' + \Gamma + c_\Gamma^2 k_H^2(\Gamma - f_G\Phi_-)] = S. \tag{1.100}$$

$S(a,k)$ is the source function defined by

$$S = -\left[\frac{1}{g+1}\frac{H'}{H} + \frac{3}{2}\frac{H_0^2\Omega_{\mathrm{m}}}{H^2a^3}(1+f_\zeta)\right]\frac{V_{\mathrm{m}}}{k_H} + \left[\frac{g' - 2g}{g+1}\right]\Phi_-, \tag{1.101}$$

where c_Γ relates the transition scale between the super- and subhorizon scales to the Hubble scale and the function $f_\zeta(a)$ determines

$$\lim_{k_H \to 0} \zeta' = \frac{1}{3} f_\zeta k_H V_{\mathrm{m}}. \tag{1.102}$$

Hence, the PPF formalism completely defines the linear perturbations given the expansion history H, the metric ratio g that quantifies the effective anisotropic stress of the modifications, f_ζ that relates the matter to the metric on superhorizon scales, and f_G, which defines this relationship in the linearized Newtonian regime, as well as the parameter c_Γ. These functions can be described for modified gravity theories, e.g., for DGP and $f(R)$ gravity [52], to obtain the linear fluctuations for the specific model. This thesis utilizes implementations of this framework in particular for deriving the anisotropies in the cosmic microwave background (CMB) (see Sec. 1.3.1).

In the nonlinear regime, the PPF formalism is not completely developed yet. However, the idea is that viable modifications of gravity should reduce to general relativity on small scales. Based on this postulation, Ref. [52] provides a fitting formula for the nonlinear power spectrum,

$$P(a,k) = \frac{P_{\mathrm{non-GR}}(a,k) + c_{\mathrm{nl}} \Sigma^2(a,k) P_{\mathrm{GR}}(a,k)}{1 + c_{\mathrm{nl}} \Sigma^2(a,k)}, \tag{1.103}$$

where $P_{\mathrm{non-GR}}(a,k)$ is the nonlinear power spectrum of the modified gravity theory neglecting nonlinear interactions such as the chameleon or Vainshtein mechanism and $P_{\mathrm{GR}}(a,k)$ is the nonlinear general relativistic power spectrum with an equivalent expansion history to the modified model. $\Sigma^2(a,k)$ describes the degree of nonlinearity and is modeled by $\Sigma^2(k) = k^3 P_{\mathrm{L}}(k)/(2\pi^2)$ in [52]. For extensions of the nonlinear PPF framework the reader is referred to, e.g., [59, 60].

In this thesis only the linear PPF formalism is implemented to compare cosmological perturbations of gravitational theories to the large-scale structures of the universe.

1.3. Large-scale structures

Different gravitational theories yield distinctive structures on the largest scales of the universe. A number of observables can be used to quantify and measure these structures to subsequently test the underlying nature of gravity. This section shall be devoted to the observables of the large-scale structure utilized in the MCMC analyses of Chaps. 2 to 4. Note that parts of Sec. 1.3.1 and 1.3.5 are taken from [1] and Sec. 1.3.1 is to a large part based on the discussions in [61].

1.3.1. Cosmic microwave background anisotropies

Before recombination, photons are tightly coupled to electrons via Compton scattering and electrons to protons via Coulomb scattering. Photons are detained from freely propagating through space and form a primordial cosmic plasma together with the baryons that mainly consist of protons coexisting to other ionized light elements such as ^{4}He and traces of deuterium, ^{3}He, and lithium. As the universe is expanding, the temperature decreases and eventually drops well below the ionization energy of hydrogen. This is when recombination occurs. Electrons and protons combine to form neutral hydrogen. Roughly as the expansion rate grows larger than the rate for Compton scattering, decoupling takes place and photons begin to freely stream through space, producing today's black body CMB radiation. At the time of decoupling, the universe is extremely homogeneous and isotropic in accordance to the cosmological principle (see Sec. 1.1.1). Inflationary theories provide an explanation for why the heterogeneous, anisotropic, and strongly curved universe at his birth impropriates a smooth and flat structure as it grows older. The key idea is that the universe undergoes a period of rapid expansion such that the observable universe today originates from a small causally connected patch. Quantum fluctuations of the inflationary field provide the seed for cosmic structure and predict a nearly scale-invariant spectrum of primordial inhomogeneities at the end of the inflationary epoch. As the universe develops, these initial inhomogeneities evolve to the local clumpiness of matter distributions observed today.

The CMB anisotropies can mainly be divided into two categories – in primary and late-time or secondary types. The first kind is due to effects occurring before and at the time of last scattering. Late-time anisotropies, on the contrary, are produced through interactions of the photons with hot gases or gravitational potentials which the photons encounter while propagating through the universe. Secondary anisotropies like the thermal and kinetic Sunyaev Zel'dovich (tSZ & kSZ) effects [62, 63], caused by the interaction of the CMB photons with highly energetic electrons, gravitational lensing, as well as the integrated Sachs-Wolfe (ISW) effect [64] are best observed in cross correlations of the CMB with tracers of the large-scale structure. The galaxy-ISW (gISW) angular cross correlation is of particular interest in this thesis and shall be discussed in Sec. 1.3.5 in more detail.

In the following a short recapitulation of the basic ingredients in the derivation of the CMB anisotropy power spectra shall be given. A more detailed derivation of the alluded relations may be found, e.g., in [61]. For simplicity a ΛCDM universe shall be assumed.

In general relativity, Liouville's theorem still holds, i.e., the phase volume of a Hamiltonian system is conserved under canonical transformations. For noninteracting identical particles the collisionless Boltzmann equation reads

$$\frac{D}{D\eta} f(x^i, p_i, \eta) \equiv \frac{\partial f}{\partial \eta} + \frac{dx^i}{d\eta}\frac{\partial f}{\partial x^i} + \frac{dp_i}{d\eta}\frac{\partial f}{\partial p_i} = 0 \tag{1.104}$$

with $dx^i/d\eta$ and $dp_i/d\eta$ taken along the geodesics. The frequency of the thermal radiation at the location of an observer x^i has the Planckian spectrum

$$f\left(\frac{\omega}{T}\right) \equiv \frac{2}{e^{\omega/T(x^\alpha, l^i)} - 1}, \tag{1.105}$$

where the factor of two is due to the two polarizations of the photon, the incoming direction is denoted by $l^i \equiv -p_i/(\sum p_i^2)$ with p_α being the four-momentum of the photon, and $\omega = p_\alpha u^\alpha$ with u^α being the four-velocity of the observer. Under the assumption of a nearly isotropic universe, the temperature is $T(x^\alpha, l^i) = T_0(\eta) + \delta T(x^\alpha, l^i)$, given $\delta T \ll T_0$. Note that in a multipole expansion, the monopole and dipole terms of δT depend on the coordinate system of the rest frame of the observer. The monopole determined by an observation from a single location is degenerate with the background temperature and the dipole depends on the relative motion of the observer to the background frame. Hence, the higher multipole orders are more informative.

The slightly perturbed FLRW metric for a nearly spatially isotropic and homogeneous flat universe in the Newtonian conformal gauge is defined by the line element[1]

$$ds^2 = a^2(\eta)\left[(1+2\Phi)d\eta^2 - (1-2\Phi)\delta_{ik}dx^i dx^k\right]. \tag{1.106}$$

Using the geodesic equations in this metric, the Boltzmann equation becomes

$$\frac{\partial f}{\partial \eta} + l^i(1+2\Phi)\frac{\partial f}{\partial x^i} + 2p\frac{\partial \Phi}{\partial x^j}\frac{\partial f}{\partial p_j} = 0, \tag{1.107}$$

where $p \equiv a^2 p^0$. Further, $\omega/T \simeq p(1+\Phi-\delta T/T_0)/(a\,T_0)$ and the zeroth and first order Boltzmann equation becomes

$$\begin{aligned}\frac{\partial}{\partial \eta}(a\,T_0) &= 0, & (1.108)\\ 2\frac{\partial}{\partial \eta}\Phi &= \left(\frac{\partial}{\partial \eta} + l^i\frac{\partial}{\partial x^i}\right)\left(\frac{\delta T}{T} + \Phi\right), & (1.109)\end{aligned}$$

respectively. Hence, to zeroth order, T_0 scales as a^{-1}. To first order, matter dominates and Φ is constant in time, thus, $(\delta T/T + \Phi) = \text{const}$. The contribution of Φ is referred to as the Sachs-Wolfe (SW) effect. The early ISW effect is due to the radiation field affecting the potential in a time-dependent manner and consequently contributes to the temperature fluctuations. At later times, when dark energy begins to contribute more dominantly, Φ regains a temporal dependence, which also affects the temperature fluctuations. This is referred to as the late ISW effect. Both phenomena shall be neglected in the following relations and reintroduced at a later point (see Sec. 1.3.5). Therefore, assuming that $\partial\Phi/\partial\eta = 0$, the temperature fluctuation today is

$$\left.\frac{\delta T}{T}\right|_{\eta_0} = \left.\frac{\delta T}{T}\right|_{\eta_\mathrm{r}} + \Phi|_{\eta_\mathrm{r}} - \Phi|_{\eta_0}, \tag{1.110}$$

where η_r is the conformal time at recombination, taken to be instantaneous here. The last term, contributing to the monopole, can be ignored due to its degeneracy with the background temperature. Matching the time-time-components and divergences of ${T_0}^i$ from the hydrodynamic energy-momentum tensor for the radiation prior to decoupling to the kinetic energy-momentum tensor for the gas of free photons following decoupling, the temperature fluctuation at the spatial location $\mathbf{x}_0$ and from

---

[1] Note that here sign conventions differ from Sec. 1.1, Sec. 1.2, and the rest of the thesis. They are chosen to match the notation of [61]. Further, $\Psi = \delta g_{00}/(2g_{00}) = -\delta g_{ii}/(2g_{ii}) = \Phi$ corresponds to a general relativistic universe in the absence of anisotropic stress.

the direction $\mathbf{l}$ is given by the spatial Fourier transform [61]

$$\frac{\delta T(\eta_0, \mathbf{x}_0, \mathbf{l})}{T} = \frac{1}{(2\pi)^{3/2}} \int \left[\left(\Phi + \frac{\delta_\gamma}{4} \right)_{\mathbf{k}} - \frac{3\delta'_{\gamma,\mathbf{k}}}{4k^2} \frac{\partial}{\partial \eta_0} \right]_{\eta_\mathrm{r}} e^{i\mathbf{k}[\mathbf{x}_0 + (\eta_\mathrm{r} - \eta_0)\mathbf{l}]} d^3k, \tag{1.111}$$

where $k \equiv |\mathbf{k}|$, $\mathbf{k} \cdot \mathbf{l} \equiv k_m l^m$, $\mathbf{k} \cdot \mathbf{l} \equiv k_n x_0^n$, and δ_γ is the photon energy density.

The temperature fluctuations across the sky can be described by correlation functions, e.g., the autocorrelation function

$$C(\theta) \equiv \left\langle \frac{\delta T(\mathbf{l}_1)}{T_0} \frac{\delta T(\mathbf{l}_2)}{T_0} \right\rangle, \tag{1.112}$$

where the average is taken for all $\mathbf{l}_1$ and $\mathbf{l}_2$ with $\mathbf{l}_1 \cdot \mathbf{l}_2 = \cos\theta$. For Gaussian fluctuations, only the even order correlation functions are nonzero. Deviations from zero in, e.g., the bispectrum – the three-point correlation function – indicate non-Gaussian contributions to the fluctuations. $C(\theta)$ can be expanded in Legendre polynomials, hence, [61]

$$\begin{aligned} C(\theta) &= \frac{1}{4\pi} \sum_{l=2}^{\infty} (2l+1) C_l P_l(\cos\theta), && (1.113) \\ C_l &= \frac{2}{\pi} \int \left| \left[\Phi_k(\eta_\mathrm{r}) + \frac{\delta_{\gamma,k}(\eta_\mathrm{r})}{4} \right] j_l(k\,\eta_0) - \frac{3\delta'_{\gamma,k}(\eta_\mathrm{r})}{4k} \frac{dj_l(k\,\eta_0)}{d(k\,\eta_0)} \right|^2 k^2 dk, && (1.114) \end{aligned}$$

where j_l are the spherical Bessel functions of order l and the monopole and dipole contributions have been removed for the reasons stated above. In spherical harmonics, the temperature fluctuations can be written as

$$\frac{\delta T(\theta, \phi)}{T_0} = \sum_{l,m} a_{lm} Y_{lm}(\theta, \phi) \tag{1.115}$$

with $\langle a^*_{l'm'} a_{lm} \rangle = \delta_{l'l} \delta_{m'm} C_l$ for a homogeneous and isotropic universe. Note that observations are done on a local basis and $C(\theta)$ corresponds to an average for all observers. For the variance between the two quantities, one commonly uses the terminology *cosmic variance*. It is an inevitable uncertainty, which on the large scales of the CMB anisotropies dominates over the measurement error.

In Eq. (1.111) recombination was assumed to happen instantaneously. However, this approximation becomes inaccurate at small angular scales, where the so-called finite thickness effect that is due to a finite duration of recombination suppresses the temperature fluctuations. Taking into account this effect, one obtains [61]

$$\frac{\delta T}{T} = \frac{1}{(2\pi)^{3/2}} \int \left(\Phi + \frac{\delta_\gamma}{4} - \frac{3\delta'_\gamma}{4k^2} \frac{\partial}{\partial \eta_0} \right)_{\eta_\mathrm{r}} e^{-(\sigma\, k\, \eta_\mathrm{r})^2} e^{i\mathbf{k}[\mathbf{x}_0 + (\eta_\mathrm{r} - \eta_0)\mathbf{l}]} d^3k, \tag{1.116}$$

where $\sigma \equiv (\sqrt{6}\kappa\, \mathcal{H}\, \eta)^{-1}|_{\eta_\mathrm{r}}$, $\mathcal{H} = a^{-1} da/d\eta$, and $\kappa \propto z|_{\eta_\mathrm{r}}$. The new term in Eq. (1.116) comes from an approximation of the visibility function. Further, note that the Silk photon diffusion damping of the early anisotropies is also stronger for finite-time recombination.

The source function $(\Phi_k + \delta_{\gamma,k}/4)$ at recombination η_{r} depends on transfer functions T_i, which relate $\Phi_k(\eta_{\mathrm{r}})$ and $\delta_{\gamma,k}(\eta_{\mathrm{r}})$ to an initial Φ_k^0 of the primordial spectrum, i.e., [61]

$$\begin{aligned}\left(\Phi_k + \frac{\delta_k}{4}\right)\bigg|_{\eta_{\mathrm{r}}} \simeq \; & \left[T_{\mathrm{p}}(k\,\eta_{\mathrm{eq}})\left(1 - \frac{1}{3c_{\mathrm{s}}^2}\right)\right. \\ & \left. + T_0(k\,\eta_{\mathrm{eq}})\sqrt{c_{\mathrm{s}}}\cos\left(k\int_0^{\eta_{\mathrm{r}}} c_{\mathrm{s}} d\eta\right) e^{-\left(\frac{k}{k_{\mathrm{D}}}\right)^2}\right]\Phi_k^0, \qquad (1.117)\end{aligned}$$

where k_{D} is the comoving damping scale and η_{eq} is the conformal time at matter-radiation equality. The transfer functions are usually calculated numerically or may be approximated by relations given in [65–67].

From a measurement of the CMB temperature anisotropies, one can extract important information about the parameter values of a cosmological model. First, at low multipoles ℓ, a nearly scale-invariant spectrum predicts that the anisotropy power spectrum is almost flat. The slope and amplitude of the measurement can be used to constrain the scalar tilt and amplitude of the primordial spectrum. The height of the first peak scales with the relation of the baryon to the dark matter energy density, whereas the height of the second peak contains information about the magnitudes of the densities. At given peak heights, the location of the first peak is sensitive to the spatial curvature of the universe. In combination, they indicate a lack of energy density and the existence of dark energy to compensate for that. The height of the third peak is sensitive to the scalar tilt and the full power spectrum contains further information on the Hubble constant and optical depth to reionization. The multipole moments of the locations of the peaks and troughs in the CMB anisotropy angular power spectrum are given by $\ell_m = \ell_{\mathrm{A}}(m - \phi_m)$, where for $n \in \mathbb{N}$, $m = n$ and $m = n + 1/2$ corresponds to the n-th peak and the n-th through, respectively, and ϕ_m is a phase shift introduced by the decay of the gravitational potential during the radiation dominated era [68]. ℓ_A corresponds to the characteristic angle of the CMB acoustic peaks, $\theta_{\mathrm{A}} \equiv r_{\mathrm{s}}(z_{\mathrm{d}})d_{\mathrm{A}}^{-1}(z_{\mathrm{d}})(1 + z_{\mathrm{d}})^{-1}$ [69], where z_{d} is the redshift at decoupling, i.e., [70, 71]

$$\ell_{\mathrm{A}} = \frac{\pi}{\theta_{\mathrm{A}}} = \pi\frac{d_{\mathrm{A}}(z_{\mathrm{d}})(1 + z_{\mathrm{d}})}{r_{\mathrm{s}}(z_{\mathrm{d}})} \qquad (1.118)$$

$$= \frac{3\pi}{4}\sqrt{\frac{\Omega_{\mathrm{b}}h^2}{\Omega_\gamma h^2}}\left[\ln\left(\frac{\sqrt{R_{\mathrm{s}}(a_{\mathrm{d}}) + R_{\mathrm{s}}(a_{\mathrm{eq}})} + \sqrt{1 + R_{\mathrm{s}}(a_{\mathrm{d}})}}{1 + \sqrt{R_{\mathrm{s}}(a_{\mathrm{eq}})}}\right)\right]^{-1}\mathcal{R}. \qquad (1.119)$$

Here r_{s} is the comoving sound horizon, $R_{\mathrm{s}} = 3a\,\Omega_{\mathrm{b}}h^2/(4\Omega_\gamma h^2)$, and [72]

$$\mathcal{R} \equiv \sqrt{\frac{\Omega_{\mathrm{m}}}{\Omega_K}}\sinh\left(\Omega_K\int_0^{z_{\mathrm{d}}}\frac{H_0 dz}{H(z)}\right) \qquad (1.120)$$

is the CMB shift parameter.

Although the CMB temperature anisotropy data yields a powerful probe for constraining cosmologies, when introducing new degrees of freedom, e.g., from modifications of gravity or time-dependent dark energy models, parameter degeneracies may become more severe and can only be broken by the addition of data from supplementary observables.

Since recombination is not instantaneous, the CMB radiation exhibits polarizations due to Thomson scattering of the photons on electrons. This process does not produce any circular polarization. Hence, the tensor

$$\mathcal{P}_{ab} \equiv \frac{1}{I}\left(\langle E_a E_b\rangle - \frac{1}{2} g_{ab}\langle E_c E^c\rangle\right) \tag{1.121}$$

can be used to fully describe the polarization. Here, the electric field is decomposed into $\boldsymbol{E} = E^a \boldsymbol{e}_a$ with $a = 1, 2$, where $\boldsymbol{e}_1$ and $\boldsymbol{e}_2$ are linearly independent and perpendicular to the direction of propagation $\boldsymbol{n}$. Further, $g_{ab} = \boldsymbol{e}_a \cdot \boldsymbol{e}_b$ and $I \equiv \langle E_c E^c\rangle$ is proportional to the radiation intensity. The temperature fluctuations measured through a polarizer depend on the orientation $\boldsymbol{m} = m^a \boldsymbol{e}_a$ as $\delta T(\boldsymbol{m}) \propto \mathcal{P}_{ab} m^a m^b$. For an orthonormal basis, the Stokes parameters are defined as $Q \equiv 2I\mathcal{P}_{11} = -2I\mathcal{P}_{22}$ and $U \equiv -2I\mathcal{P}_{12}$. Further, one can define the E and B mode, i.e., $E(\boldsymbol{n}) \equiv \mathcal{P}_{ab}{}^{;ab}$ and $B(\boldsymbol{n}) \equiv \mathcal{P}_a{}^{b;ac}\epsilon_{cb}$, respectively, where semicolons indicate covariant derivatives and ϵ_{cb} is the skew-symmetric Levi-Civita tensor defined as

$$\epsilon_{cb} \equiv \sqrt{g}\begin{pmatrix} 0 & 1 \\ -1 & 0 \end{pmatrix}. \tag{1.122}$$

Note that E is a scalar and B is a pseudo-scalar that can be produced by gravitational waves but not by scalar perturbations. They can also be expanded in spherical harmonics and cross correlated with each other and the temperature fluctuations to extract further information from the CMB radiation. Finally, note that late-time structures within the universe can reionize the neutral hydrogen at which photons can scatter. This produces a smearing out of the cross correlations at scales smaller than the reionization horizon scale.

The CMB anisotropies may also be used to test for primordial gravitational waves predicted by inflation, which appear in the traceless, divergence-free part of the tensor perturbations h_{ik}, where[2]

$$ds^2 = a^2[d\eta^2 - (\delta_{ik} + h_{ik} dx^i dx^k)], \tag{1.123}$$

through blueshifts or redshifts in the photon spectra. The effects of gravity waves on the power spectra shall, however, not be explained here in more detail. The reader is referred to, e.g., [61].

The thesis at hand employs the CAMB code [73], based on CMBFAST [74], for calculating the transfer functions and deriving the CMB power spectra. It utilizes the five- [75] and seven-year [76] data of the Wilkinson Microwave Anisotropy Probe (WMAP) in Chaps. 3 as well as in 4, and 2, respectively. To calculate the CMB anisotropies for modified gravity theories, the PPF framework (see Sec. 1.2) is adopted and the PPF modifications to CAMB by [77, 78] are employed.

---

[2] Note again the difference in sign convention in Eq. (1.123) with respect to the metric used in other parts of the thesis.

1.3.2. Supernovae Ia

Assuming that the universe is spatially homogeneous and isotropic, the FLRW metric and the time-time-component of the Einstein equations can be used to derive the first Friedmann equation expressing the Hubble expansion in terms of the effective energy density (see Sec. 1.1.1)

$$H^2 = \frac{\kappa^2}{3}\rho_{\mathrm{eff}} - \frac{K}{a^2}, \tag{1.124}$$

where ρ_{eff} may include contributions from nonrelativistic and relativistic matter, as well as a dark energy component or terms from a modification of gravity.

Supernovae of the category type Ia are assumed to be standard candles, meaning that their absolute magnitude at the peak of brightness is always $M \simeq -19$ [16, 17]. With this characteristic, supernovae Ia can be utilized to yield a relative distance probe by relating the apparent magnitudes m of high-redshift to low-redshift objects. The quantity of interest is the luminosity distance $d_L(z)$ at different redshifts $z = \lambda_{\mathrm{em}}/\lambda_{\mathrm{obs}} - 1 = 1/a - 1$, where λ_{em} is the wavelength of a photon emitted by an object in its rest frame and λ_{obs} is the wavelength of the photon in the rest frame of the observer. It is defined as

$$d_L^2 \equiv \frac{L_{\mathrm{s}}}{4\pi\mathcal{F}}, \tag{1.125}$$

where $\mathcal{F}$ is the flux and L_{s} the absolute luminosity of a source. The apparent magnitude is

$$m = 5\log_{10} d_L + M + 25, \tag{1.126}$$

where d_L is in units of Mpc. Theoretically, the luminosity distance is determined by the relation $d_L(z) = (1+z)r(z)$, where $r(z)$ is the comoving angular diameter distance defined by

$$r(z) = \begin{cases} \sin\left[H_0\sqrt{-\Omega_K}\chi(z)\right]/H_0\sqrt{|\Omega_K|}, & \Omega_K < 0, \\ \chi(z), & \Omega_K = 0, \\ \sinh\left[H_0\sqrt{\Omega_K}\chi(z)\right]/H_0\sqrt{|\Omega_K|}, & \Omega_K > 0, \end{cases} \tag{1.127}$$

with comoving radial distance

$$\chi(z) = \int_0^z \frac{dz'}{H(z')}. \tag{1.128}$$

It relates to the angular diameter distance by the distance duality $d_L(z) = (1+z)^2 d_{\mathrm{A}}(z)$, which, given that the photon number is conserved, can be applied to any metric theory (see, e.g., [79] and references therein). Note that there is a degeneracy between M and H_0. Hence observations of supernovae Ia at different redshifts yield a relative distance measure.

Measurements of $d_L(z)$ [16, 17] suggest a late-time acceleration of the universe. This thesis will make use of supernovae Ia data from different surveys, namely, the Supernovae Legacy Survey (SNLS) [80] in Chap. 3, the Supernovae Cosmology Project (SCP) Union [81] compilation in Chap. 4, and Union2 [82] in Chap. 2.

1.3.3. The Hubble constant

The Hubble law, $v = H_0 D$, relates the recessional velocity v of an object to its proper distance D when v is large compared to peculiar velocities. The Hubble constant H_0 gives the proportionality and $v = dD/dt$ indicates the velocity with respect to cosmological time t. In practice, for low-redshift objects, one can estimate v through the redshifts of transition spectra and D by, e.g., determining the distance to a nearby supernova. Cepheid stars exhibit a variation of the apparent magnitude over time with a well-defined relation between its pulsation period and its luminosity. Hence, they serve as very useful standard candles for measuring the local Hubble constant and provide an absolute distance probe for the geometry produced by a cosmological model by constraining the luminosity distance $d_L(z_{\mathrm{eff}})$ at an effective redshift z_{eff} defined by the Cepheid star and the supernova. In the analyses conducted in this thesis the Hubble constant measurement from the Supernovae and H_0 for the Equation of State (SHOES) [83] program is employed.

1.3.4. Baryon acoustic oscillations

In the early universe photons and baryons are strongly coupled through Thomson scattering and form a hot primordial plasma. An overdense region of this plasma is gravitationally attractive while photon-baryon interactions produce an outward pressure creating oscillations in the fluid, which propagate like acoustic waves. The sound speed of a single spherical density perturbation is $c_{\mathrm{s}} = c/\sqrt{3(1+R)}$, where $R \equiv 3\rho_{\mathrm{b}}/4\rho_\gamma \propto \Omega_{\mathrm{b}}(1+z)$ [84]. As the universe expands, it cools and enters a phase of recombination, wherein electrons and protons combine to neutral hydrogen atoms. Since the cross section of the photon-hydrogen interaction is small, the pressure on the baryons is disengaged and photons begin to propagate freely through the universe. The phase at which this free-streaming of the photons begins is commonly referred to as the time of decoupling. The baryon wave, with the only gravitationally interacting dark matter at the center of the density perturbation, stagnates at the sound horizon. Such overdensities are imprinted in the sky as wave patterns within which the likelihood of galaxy formation is increased. This characteristic structure caused by BAO is therefore an important probe for the underlying gravitational physics.

The preferred clustering scale of galaxies from the BAO measured at different redshifts provides a statistical standard ruler. The scale along the line-of-sight and perpendicular to it gives a measurement of the Hubble parameter and the angular diameter distance, respectively [79]. The combination of these measurements can be used to constrain the ratio [85]

$$d_z \equiv \frac{r_{\mathrm{s}}(z_{\mathrm{d}})}{d_{\mathrm{V}}(z)} = \frac{r_{\mathrm{s}}(z_{\mathrm{d}}) H(z)^{1/3}}{(1+z)^{2/3} d_{\mathrm{A}}(z)^{2/3} z^{1/3}}, \tag{1.129}$$

where $r_{\mathrm{s}}(z_{\mathrm{d}})$ denotes the comoving sound horizon at the baryon drag epoch z_{d}. The theoretical prediction of this quantity involves linear theory only and its measurement provides a useful complementary probe of cosmic acceleration to the previous ones. Chapters 2 and 4 use the BAO distance measurement of [85] to place constraints on phenomenological departures of the standard cosmological model and $f(R)$ gravity, respectively.

1.3.5. Cross correlations of the integrated Sachs-Wolfe effect with foreground galaxies

Prior to the epoch of last scattering, the baryons were clustered together in gravitational wells. The tight coupling between photons and baryons present at that time also confined the photons to potential wells, causing them to undergo a redshift before leaving the well. This primary anisotropy is the SW effect (see Sec. 1.3.1) and can be observed through a rise in the CMB power spectrum at low angular scales ℓ. A photon propagating through space may cross several gravitational potentials. When passing through the well while the magnitude of the potential increases or decreases, the photon loses or gains energy, hence, is redshifted or blueshifted, respectively. Additionally, a variation in the potential well comprehends a change in space and time and enhances these wavelength shifts. More precisely, the increase or decrease that is accompanied by stretching or contracting of the space-time grid subsequently causes the wavelength of the photon to elongate, thus being redshifted, or shorten and therefore undergo a blueshift, respectively. The net effect along the line of sight to the observer is the ISW effect and is a secondary anisotropy of the CMB. It is determined by

$$\frac{\delta T}{T}(\boldsymbol{e}_n) = \int_{t_\mathrm{r}}^{t_0} dt(\dot{\Psi} - \dot{\Phi}), \tag{1.130}$$

where $\boldsymbol{e}_n$ indicates the direction of the photon. Here dots denote derivatives with respect to proper time t, where the metric perturbations in longitudinal gauge are of the form presented in Sec. 1.2. The present time and the time at recombination are denoted by t_0 and t_r, respectively. Further, the effect is divided into two types: the early ISW and the late ISW.

The process causing the early ISW effect commenced during the radiation dominated epoch succeeding recombination and ended at matter-radiation equality. At scales which are in causal contact with each other via sound or pressure, i.e., at a relative scale of the sound horizon, gravitational potentials are decaying, including an energy gain to the traversing photons. The late ISW effect occurs at the end of the matter dominated epoch. As matter ceases to dominate, gravitational potentials decay. At this time, however, photons are equally likely to reside in regions of low matter density as in high matter density areas, causing a severe damping in the overall wavelength shift of the propagating photon. Nevertheless, it serves as an excellent direct probe of cosmological density parameters.

The ISW effect in the CMB can be isolated by using cross correlations thereof with galaxy number densities. Such a measurement yields further insights into the nature of cosmic acceleration and is a useful test for modifications of general relativity. In the Limber and quasistatic approximation, the gISW cross correlation may be written as

$$C_\ell^{\mathrm{g}T} \simeq \frac{3\Omega_\mathrm{m} H_0^2 T_\mathrm{CMB}}{(\ell+1/2)^2} \int dz\, f(z) H(z) \left[D(z,k) \frac{d}{dz} G(z,k) \right] P(k) \bigg|_{k=\frac{\ell+1/2}{\chi(z)}}, \tag{1.131}$$

where $P(k)$ is the matter power spectrum today, $D(z,k)$ is the linear density growth rate defined by the matter density perturbation $\Delta_{\mathrm{m}}(z,k) = \Delta_{\mathrm{m}}(0,k)D(z,k)/D(0,k)$ and

$$G(z,k) = \frac{\Phi_-(z,k)}{\Phi_-(z_{\mathrm{i}},k)} \frac{\Delta_{\mathrm{m}}(z_{\mathrm{i}},k)}{\Delta_{\mathrm{m}}(0,k)(1+z_{\mathrm{i}})} \tag{1.132}$$

is the linear potential growth rate with initial redshift z_{i}. The Limber approximation becomes accurate at the percent level for $\ell \gtrsim 10$ and drops approximately as ℓ^2 at higher ℓ (see, e.g., [86–88]). The function $f(z)$ relates the matter density to the observed projected galaxy overdensity with $f(z) = b(z)\Pi(z)$ in the absence of magnification bias. $\Pi(z)$ is the redshift distribution of the galaxies and the bias $b(z)$ is assumed independent of scale but dependent on redshift. For quasars from the Sloan Digital Sky Survey (SDSS) [89–92], magnification bias has to be taken into account for $f(z)$, which in the concordance model, is given by [93]

$$f(z) = b(z)\Pi(z) + \int_z^\infty W(z,z')[\alpha(z') - 1]\Pi(z')dz'. \tag{1.133}$$

Here $\alpha(z')$ describes the slope of the number counts of the galaxy density in dependence on flux. The lensing window function is (cf. [93])

$$W(z,z') = \frac{3H_0^2(1+z)}{2H(z)} r(z)^2 \left[\frac{d\ln r(z'')}{d\chi(z'')} \bigg|_{z'}^{z} \right]. \tag{1.134}$$

This thesis employs the ISWWLL code [93, 94] comprising nine different galaxy samples correlated with the ISW anisotropy to derive constraints on several alternative theories of gravity in Chaps. 2 and 3, as well as in Sec. 4.1.

1.3.6. Weak gravitational lensing and galaxy flows

The relationship of weak gravitational lensing around galaxies to their large-scale velocities yields an important probe of gravity. The advantage of such a measurement lies in its insensitivity to galaxy bias and initial matter fluctuations. The expectation value of the ratio of galaxy-galaxy to galaxy-velocity cross correlations of the same galaxies yields the estimator

$$E_G \equiv \left[\frac{\nabla^2(\Psi - \Phi)}{3H_0^2 a^{-1} \frac{d\ln\Delta_{\mathrm{m}}}{d\ln a} \Delta_{\mathrm{m}}} \right]_{k=\frac{\ell}{\bar{\chi}}, \bar{z}}. \tag{1.135}$$

Galaxy-galaxy lensing can be measured by stacking the lensing signals from the shapes of source galaxies distorted by foreground galaxies to obtain the projected mass distribution of the foreground object. The differential excess surface mass density is determined by [95]

$$\Delta\Sigma_{\mathrm{gm}}(R) = \bar{\Sigma}_{\mathrm{gm}}(R) - \Sigma_{\mathrm{gm}}(R) = \Sigma_{\mathrm{crit}} \langle \gamma_{\mathrm{t}}(R,\phi) \rangle_\phi, \tag{1.136}$$

where γ_{t} is the average tangential shear on the background galaxy images, Σ_{gm} is the projected surface mass density of the foreground objects, and $R \approx \theta D_l$, the comoving transverse distance between lens and source galaxies with angular separation θ. The indices $\mathcal{I} = \{\mathrm{g}, \mathrm{m}\}$ refer to galaxies and mass, respectively. The mean surface mass density within a circular aperture is given by

$$\bar{\Sigma}_{\mathrm{gm}}(R) = \frac{2}{R^2}\int_0^R \Sigma_{\mathrm{gm}}(R')R'dR', \tag{1.137}$$

and the critical surface mass density is

$$\Sigma_{\mathrm{crit}}(R) = \frac{2c^2}{\kappa^2}\frac{D_{\mathrm{s}}}{D_{\mathrm{ls}}D_{\mathrm{l}}(1+z_{\mathrm{l}})^2}, \tag{1.138}$$

where D_{s}, D_{l}, and D_{ls} denote the angular diameter distance to the source, the lens, and between the lens and the source, respectively. Note that Σ_{crit} is an effective quantity obtained from the stacking of a large amount of foreground and background objects and is dependent on the specific cosmological model. Finally, the projected surface mass density is determined by

$$\Sigma_{\mathrm{gm}}(R) = \frac{2H^2\Omega_{\mathrm{m}}}{\kappa^2}\int_{\mathbb{R}} g_{\mathrm{l}}(\chi)\left[1+\xi_{\mathrm{gm}}\left(\sqrt{R^2+\chi^2}\right)\right]d\chi, \tag{1.139}$$

where H indicates the Hubble parameter, χ denotes the line of sight, and ξ_{gm} is the galaxy-matter correlation function. The dependence of the lensing strength on the distribution of the lens mass is contained in the window function $g_{\mathrm{l}}(\chi)$. It is a function of the positions of the lens and the source. The inhomogeneous mass distribution in between contributes to the final distortion. Therefore, $g_{\mathrm{l}}(\chi)$ is taken to be very broad and is defined by the radial distribution of the lens and source samples.

The distribution of galaxies yields another useful probe of the cosmological model. The clustering between two tracer fields A and B may be described by the projected two-point correlation function [96]

$$w_{\mathrm{AB}}(R) = \int_{\mathbb{R}} g_{\mathrm{g}}(\chi)\xi_{\mathrm{AB}}\left(\sqrt{R^2+\chi^2}\right)d\chi, \tag{1.140}$$

where $A \in \mathcal{I}$ and $B \in \mathcal{I}$ and $g_{\mathrm{g}}(\chi)$ is a window function for which a narrow top-hat filter of thickness $\Delta\chi \approx 100h^{-1}$ Mpc is taken around the lens positions. In particular, $\Sigma_{\mathrm{gg}} = 3H_0^2 w_{\mathrm{gg}}/\kappa^2$.

The excess surface mass density $\Delta\Sigma$ contains information from small and large, i.e., nonlinear and linear, scales. In order to alleviate the incoherence induced by the nonlinear clustering process, the Annular Differential Surface Density (ADSD), $\Upsilon(R)$, was introduced in [97, 98] and is defined by

$$\Upsilon(R) \equiv \Delta\Sigma(R) - \frac{R_0^2}{R^2}\Delta\Sigma(R_0). \tag{1.141}$$

The $\Upsilon(R)$ statistic removes contributions to $\Delta\Sigma(R)$ from small scales and reduces to the differential excess surface mass density when the cutoff radius is set to $R_0 = 0$. The statistic is adopted to circumvent statistical and systematical uncertainties about the inner halo profiles.

With these definitions at hand, E_G is the probe of the relation

$$E_G = \frac{1}{\beta}\frac{\Upsilon_{\rm gm}(R)}{\Upsilon_{\rm gg}(R)}, \tag{1.142}$$

where $\beta = b^{-1} d\ln\Delta_{\rm m}/d\ln a$. A measurement of E_G by [99] is utilized to constrain departures from the concordance model and modifications from $f(R)$ gravity in Chaps. 2 and 4, respectively.

1.3.7. Cluster density profiles and abundance

The shape of halo density profiles and the abundance of massive clusters are informative quantities of cosmological structure formation with strong sensitivity to modifications of gravity. Hence, their measurements yield powerful tests of gravity. However, to accurately predict these observables, N-body simulations have to be employed, solving the Poisson equation,

$$k^2\Psi(\boldsymbol{k}) = -\frac{\kappa^2}{2}a^2\delta\rho_{\rm m}(\boldsymbol{k}), \tag{1.143}$$

in the case of standard gravity, where $k = |\boldsymbol{k}|$ and $\delta\rho_{\rm m} = \rho_{\rm m} - \bar{\rho}_{\rm m}$ with the overbar denoting the background quantity. For modified gravity scenarios an additional field equation coupled to the Poisson equation has to be solved (see, e.g. [100, 101]), which makes the simulations computationally more expensive. There exist, however, a number of fitting formulae calibrated to simulation outputs and theoretical models for describing the halo profiles and the abundance of clusters produced in the simulations. The most important ideas incorporated in this thesis shall be adumbrated here. For a more detailed derivation of the following relations the reader shall be referred to [102] and references therein or to the appendix of Secs. 4.1 and 4.2.

The continuity and Euler equation for a pressureless fluid of nonrelativistic matter,

$$\dot{\delta} + \frac{1}{a}\nabla\cdot(1+\delta)\mathbf{v} = 0, \tag{1.144}$$

$$\dot{\mathbf{v}} + \frac{1}{a}(\mathbf{v}\cdot\nabla)\mathbf{v} + H\mathbf{v} = -\frac{1}{a}\nabla\Psi, \tag{1.145}$$

respectively, can be combined to yield a second-order differential equation for the overdensity δ. Here, $\mathbf{v}$ is the velocity field and Ψ is the Newtonian potential, where spatial coordinates are comoving. The density shall be approximated by a top-hat distribution for determining the velocity field. Appending mass conservation and the Poisson equation yields a nonlinear differential equation for δ describing the evolution of a spherical overdensity, which will expand, undergo a turn-around and eventually collapse. The collapse density $\delta_{\rm c}$ is the overdensity determined from the linear differential equation for δ combined from Eqs. (1.144) and (1.145) extrapolated to the collapse epoch ascertained through its nonlinear correspondent.

The virial theorem and energy conservation relates the kinetic and potential energies at turn-around $r_{\rm max}$ to their counterparts at the virial radius $r_{\rm v}$. The virial density is defined as the ratio between the overdensity at the virial radius and the average density at the end of collapse, i.e., $\Delta_{\mathrm{v}} = \rho_{\mathrm{m}}(r_{\mathrm{v}})/\bar{\rho}_{\mathrm{m}}(r=0)$. The parameters δ_{c} and Δ_{v} are subsequently used to model the profile of a cluster and the abundance of clusters in form of a halo mass function. If gravitational forces are modified, the differential equations for δ are as well, which leads to deviations in δ_{c} and Δ_{v}. Adhering to this effect or not is what gives rise to the classification of the *standard spherical collapse* and *modified spherical collapse* cases when modeling the observables in alternative theories of gravity [102].

Consider the variance $\sigma(M)$ of the linear density field convolved with a top-hat filter of radius R, where $M = 4\pi\, r^3 \bar{\rho}_{\mathrm{m}}/3$,

$$\sigma^2(R) = \int \frac{d^3k}{(2\pi)^3} \left|\hat{W}(k\,R)\right|^2 P_{\mathrm{L}}(k) \tag{1.146}$$

with the Fourier transform of the real-space top-hat window function of radius R,

$$\hat{W}(k\,R) = 3\left[\frac{\sin(k\,R)}{(k\,R)^3} - \frac{\cos(k\,R)}{(k\,R)^2}\right], \tag{1.147}$$

and linear matter power spectrum $P_{\mathrm{L}}(k)$. The peak threshold is defined by $\nu = \delta_{\mathrm{c}}/\sigma(M_{\mathrm{v}})$, where M_{v} is the virial mass. The Sheth-Tormen prescription [103] can be used to describe the mass function, which defines the comoving number density of halos per logarithmic interval in the virial mass M_{v} by

$$n_{\ln M_{\mathrm{v}}} \equiv \frac{dn}{d\ln M_{\mathrm{v}}} = \frac{\bar{\rho}_{\mathrm{m}}}{M_{\mathrm{v}}} f(\nu) \frac{d\nu}{d\ln M_{\mathrm{v}}}, \tag{1.148}$$

where

$$\nu\, f(\nu) = A\sqrt{\frac{2}{\pi} a\,\nu^2}\left[1 + (a\,\nu^2)^{-p}\right] e^{-a\,\nu^2/2}. \tag{1.149}$$

Within the concordance model, $a \simeq 0.75$, $p \simeq 0.3$, $\delta_{\mathrm{c}} \simeq 1.673$, and A is chosen such that $\int d\nu f(\nu) = 1$.

The halo mass function may also be obtained from fitting formulae motivated by Eq. (1.148) and calibrated to N-body simulations, such as, e.g., the Tinker *et al.* [104] formula, which is described by

$$\frac{dn}{dM} = f(\sigma)\frac{\bar{\rho}_{\mathrm{m}}}{M}\frac{d\ln\sigma^{-1}}{dM}, \tag{1.150}$$

where the distribution $f(\sigma)$ is given by

$$f(\sigma) = A\left[\left(\frac{\sigma}{b}\right)^{-a} + 1\right] e^{-c/\sigma^2}. \tag{1.151}$$

The free parameters A, a, b, and c are fitted to ΛCDM simulations in [104].

The cluster density profile or halo-matter correlation function $\xi_{\mathrm{hm}}(r)$ can be modeled by a two- and one-halo contribution yielding

$$\xi_{\mathrm{hm}}(r) = b_{\mathrm{L}}(M_{\mathrm{v}}) \int \frac{d^3k}{(2\pi)^3} I(k) P_{\mathrm{L}}(k) e^{-i\mathbf{k}\cdot\mathbf{x}} + \frac{\rho_{\mathrm{NFW}}(r)}{\bar{\rho}_{\mathrm{m}}}, \tag{1.152}$$

where $b_{\rm L}(M_{\rm v})$ is the linear bias given by

$$b_{\rm L}(M_{\rm v}) = 1 + \frac{a\,\nu^2 - 1}{\delta_{\rm c}} + \frac{2p}{\delta_{\rm c}\,[1 + (a\,\nu^2)^p]} \tag{1.153}$$

and $\rho_{\rm NFW}(r)$ is the Navarro-Frenk-White (NFW) [105] profile with

$$\rho_{\rm NFW}(r) = \frac{\rho_{\rm s}}{\frac{r}{r_{\rm s}}\left(1 + \frac{r}{r_{\rm s}}\right)^2}. \tag{1.154}$$

Here, $r_{\rm s}$ is the scale radius of the halo defined through the concentration $c_{\rm v} \equiv r_{\rm v}/r_{\rm s} = 9(M_{\rm v}/M_*)^{-0.13}$ and $M_\star$ is given by $\sigma(M_*) = \delta_{\rm c}$. The normalization $\rho_{\rm s}$ is determined by

$$M_{\rm v} = 4\pi \int_0^{r_{\rm v}} \rho_{\rm NFW}(r) r^2 dr, \tag{1.155}$$

i.e., $\rho_{\rm s}^{-1} = 4\pi\, M_{\rm v}^{-1} r_{\rm s}^3\, [\ln(1 + c_{\rm v}) - c_{\rm v}/(1 + c_{\rm v})]$. Finally,

$$I(k) = \int d\ln M_{\rm v}\; n_{\ln M_{\rm v}} \frac{M_{\rm v}}{\bar{\rho}_{\rm m}} y(k, M_v) b_{\rm L}(M_{\rm v}), \tag{1.156}$$

with $y(k, M) = \hat{\rho}_{\rm NFW}(k)/N$, where $\hat{\rho}_{\rm NFW}(k)$ is the Fourier transform of a NFW density profile truncated at $r_{\rm v}$, i.e.,

$$\begin{aligned} \hat{\rho}_{\rm NFW}(k) &= \frac{\rho_{\rm s} r_{\rm s}^3}{2\pi^2} \Big[\cos(r_{\rm s}k)\, \{ {\rm Ci}[k(r_{\rm s} + r_{\rm v})] - {\rm Ci}(r_{\rm s}k) \} \\ &\qquad + \sin(r_{\rm s}k)\, \{ {\rm Si}[k(r_{\rm s} + r_{\rm v})] - {\rm Si}(r_{\rm s}k) \} - \frac{\sin(k\, r_{\rm v})}{k(r_{\rm s} + r_{\rm v})} \Big], \end{aligned} \tag{1.157}$$

with Si and Ci being the sine and cosine trigonometric integrals, respectively, and

$$N \equiv \lim_{k\to 0} \hat{\rho}_{\rm NFW}(k) = \frac{\rho_{\rm s} r_{\rm s}^3}{2\pi^2} \left[\ln\left(\frac{r_{\rm s} + r_{\rm v}}{r_{\rm s}} \right) - \frac{r_{\rm v}}{r_{\rm s} + r_{\rm v}} \right]. \tag{1.158}$$

Section 4.1 employs a preliminary version of the likelihood code of [106], which utilizes constraints from the most massive halos ($M > 10^{13}\ M_\odot/h$) inferred from SDSS data measuring the galaxy-galaxy lensing signal from clusters and groups from the MaxBCG catalog [107] to put constraints on $f(R)$ gravity from the abundance of clusters. Section 4.2 utilizes galaxy-galaxy lensing probes around the maxBCG sample, a selection of MaxBCG clusters from the SDSS, measuring the excess surface mass density $\Delta\Sigma_{\rm gm}$ given in Eq. (1.136) to constrain modifications of gravity induced by $f(R)$ models.

1.4. The Markov chain Monte Carlo method

An important task addressed in this thesis is to determine how the different gravitational theories specified in Sec. 1.1 perform in explaining the observations on the largest cosmological scales, presented in Sec. 1.3. The specific cosmological model can be depicted by the parameter vector $\boldsymbol{\theta}$, describing the degrees of freedom of the theory. The object of interest is then the probability distribution of $\boldsymbol{\theta}$ given the data $\boldsymbol{D}$, in other words the *conditional probability* $P(\boldsymbol{\theta}|\boldsymbol{D})$. For the *parameter estimation* in this thesis a *Baysian* viewpoint shall be adopted. More specifically, the following mathematical descriptions define the probabilistic framework (cf., e.g., [108]):

Definition 1.4.3: The conditional probability of event A given event B is

$$P(A|B) = \frac{P(A \cap B)}{P(B)}. \tag{1.159}$$

Definition 1.4.4: $(B_i)_{i \in I}$ is a *disjunct decomposition* of the space of all possible events or *state space* $\mathcal{S}$ if

(i) $\mathcal{S} = \bigcup_{i \in I} B_i$,

(ii) $B_i \cap B_j = \emptyset$, $i \neq j \; \forall \, i, j \in I$.

Proposition 1.4.1: (Total probability) Let $(B_i)_{i \in I}$ be a disjunct decomposition. Then

$$P(A) = \sum_{i \in I} P(A|B_i) P(B_i). \tag{1.160}$$

Proof: This can be seen from

$$P(A) = P\left(\bigcup_{i \in I} [A \cap B_i] \right) = \sum_{i \in I} P(A \cap B_i) = \sum_{i \in I} P(A|B_i) P(B_i).$$

$\square$

Theorem 1.4.4: (Bayes) Let $(B_i)_{i \in I}$ be a disjunct decomposition. Then

$$P(B_i|A) = \frac{P(A|B_i) P(B_i)}{\sum_{j \in I} P(A|B_j) P(B_j)} \tag{1.161}$$

Proof: The theorem follows from

$$P(B_i|A) = \frac{P(B_i \cap A)}{P(A)} = \frac{P(A|B_i) P(B_i)}{P(A)} = \frac{P(A|B_i) P(B_i)}{\sum_{j \in I} P(A|B_j) P(B_j)}.$$

$\square$

Markov chain Monte Carlo (MCMC) algorithms provide a framework for efficient estimation of the probability distribution $P(\boldsymbol{\theta}, \boldsymbol{D})$. In general, Monte Carlo methods summarize a class of computational techniques based on random sampling algorithms that are employed for acquiring numerical solutions to mathematical or statistical problems. A Markov chain is a discrete-time chainlike random process that satisfies the Markov property, where the proceeding state is only dependent on the current state but not on previous ones. The transition from one state of the system to the next is governed by the *transition probability.* The Markov chain is then defined by the set of all states of the system and transition probabilities. For clarity the following definitions shall be given (cf., e.g., [109, 110]):

Definition 1.4.5: A *random process* $\mathcal{B}$ is a sequence of random states B_t at time t, i.e.,

$$\mathcal{B} := \{\{B_t\}_{t\geq 1} | B_t \in \mathcal{S}\}\,. \tag{1.162}$$

Definition 1.4.6: A random process $\mathcal{B}$ is called a *Markov chain* if it satisfies the *Markov property,* i.e., $\forall\ \{\{A_t\}_{t\geq 1}|A_t \in \mathcal{S}\}$ and $\forall\, t$,

$$P(B_{t+1} = A_{t+1}|B_t = A_t) = P(B_{t+1} = A_{t+1}|B_t = A_t, B_{t-1} = A_{t-1}, \ldots, B_1 = A_1). \tag{1.163}$$

Definition 1.4.7: The transition probability from A_i to A_j at time t is the conditional probability

$$T_{ij}(t) := P(B_{t+1} = A_j|B_t = A_i), \tag{1.164}$$

where $\mathcal{B}$ is a Markov chain and $A_i, A_j \in \mathcal{S}$. If the transition is time-independent the Markov chain is said to be *time-homogeneous.*

According to Bayes' theorem, the conditional probability for the model parameters given the data, which is also referred to as the *posterior distribution*, is $P(\boldsymbol{\theta}|\boldsymbol{D}) = P(\boldsymbol{D}|\boldsymbol{\theta})P(\boldsymbol{\theta})/P(\boldsymbol{D})$, where $P(\boldsymbol{D}|\boldsymbol{\theta})$ is the *likelihood*, $P(\boldsymbol{\theta})$ the *prior*, and $P(\boldsymbol{D})$ the *evidence.*

A MCMC method of particular interest in this thesis is the so-called Metropolis-Hastings [111, 112] algorithm used to generate a sequence of random samples from the posterior distribution. The transition probability is designed so that the Markov chain asymptotically approaches the stationary posterior distribution (see, e.g., [113, 114]):

$$T(\boldsymbol{\theta}_{n+1}, \boldsymbol{\theta}_n) = \alpha(\boldsymbol{\theta}_{n+1}, \boldsymbol{\theta}_n)q(\boldsymbol{\theta}_{n+1}, \boldsymbol{\theta}_n), \tag{1.165}$$

where $q(\boldsymbol{\theta}_{n+1}, \boldsymbol{\theta}_n)$, is an, in principle, arbitrary *proposal density* for a new state $\boldsymbol{\theta}_{n+1}$ given $\boldsymbol{\theta}_n$ and

$$\alpha(\boldsymbol{\theta}_{n+1}, \boldsymbol{\theta}_n) = \min\left\{1, \frac{P(\boldsymbol{\theta}_{n+1})q(\boldsymbol{\theta}_n, \boldsymbol{\theta}_{n+1})}{P(\boldsymbol{\theta}_n)q(\boldsymbol{\theta}_{n+1}, \boldsymbol{\theta}_n)}\right\} \tag{1.166}$$

is the *acceptance probability.* If q is symmetric, this reduces to the Metropolis algorithm. Since

$$P(\boldsymbol{\theta}_{n+1})T(\boldsymbol{\theta}_n, \boldsymbol{\theta}_{n+1}) = P(\boldsymbol{\theta}_n)T(\boldsymbol{\theta}_{n+1}, \boldsymbol{\theta}_n), \tag{1.167}$$

the posterior distribution is an equilibrium.

One can run multiple independent Markov chains, all approximating the posterior distribution. The Gelman-Rubin [115] criterion can then be applied to determine whether the chains have converged (see, e.g., [114]). Consider M independent

Markov chains of which each has $2N$ entries. The first N entries of each chain shall be removed to ensure *burn-in*, i.e., equilibrium sampling. The Gelman-Rubin criterion compares the average of the combined samples to the average of the means of each sample. More specifically, let $\boldsymbol{\theta}_{ij}$ be the entry $i \in I = \{N+1, \ldots, 2N\}$ of the chain $j \in J = \{1, 2, \ldots, M\}$. The relations

$$\bar{\boldsymbol{\theta}}_j = \frac{1}{N} \sum_{i \in I} \boldsymbol{\theta}_{ij}, \tag{1.168}$$

$$\bar{\boldsymbol{\theta}} = \frac{1}{NM} \sum_{i \in I,\, j \in J} \boldsymbol{\theta}_{ij}, \tag{1.169}$$

define the mean of the samples for each chain and for the combined chains, respectively. The variance of the mean of every chain to the mean of the combined chains and the average of the variance of each chain are

$$\sigma_J^2 = \frac{1}{M-1} \sum_{j \in J} (\bar{\boldsymbol{\theta}}_j - \bar{\boldsymbol{\theta}})^2, \tag{1.170}$$

$$\bar{\sigma}_J^2 = \frac{1}{M(N-1)} \sum_{i \in I,\, j \in J} (\boldsymbol{\theta}_{ij} - \bar{\boldsymbol{\theta}}_j)^2, \tag{1.171}$$

respectively. The weighted variance [115]

$$\sigma_+^2 = \frac{N-1}{N} \bar{\sigma}_J^2 + \sigma_J^2 \left(1 + \frac{1}{M}\right) \tag{1.172}$$

overestimates the true variance, whereas $\bar{\sigma}_J^2$ is an underestimate. The ratio of the two estimates defines the Gelman-Rubin statistic [115]

$$R = \frac{\sigma_+^2}{\bar{\sigma}_J^2} \frac{f}{f-2}, \tag{1.173}$$

where f is the number of degrees of freedom with $f \to \infty$ as $n \to \infty$. The chains have converged when $|R-1| \to 0$.

The cosmological Monte Carlo (cosmomc) code of [113] incorporates the techniques described in this section and is the tool utilized in this thesis for parameter estimation of the cosmological models described in Sec. 1.1 given the large-scale cosmological data presented in Sec. 1.3 (see Chaps. 2 to 4).

1.5. Thesis outline and paper list

This thesis comprises two journal publications, a publication on an online platform currently in referee process with a journal, and a paper draft, as well as the introductory part at hand. The publications are organized into three chapters: Chapter 2 describes a test of the standard cosmological model ΛCDM based on modifications of general relativity using cosmological data. Chapter 3 presents constraints on the five-dimensional DGP braneworld gravity model from linear probes of the large-scale structure. Finally, Cha. 4 describes constraints on $f(R)$ gravity from nonlinear probes such as the abundance of clusters and halo profiles measured around the virial radius of clusters.

1.5.1. General relativity

Chapter 2 analyzes departures from assumptions made in the standard model of cosmology based on typical deviations exhibited in modified gravity scenarios. The study conservatively restricts to cosmological probes amenable to linear perturbation theory since the nonlinear behavior of such phenomenological modifications has not been studied in full extent. Standard scaling relations do not apply and may lead to illusive conclusions.

Sec. 2.1 Consistency check of ΛCDM phenomenology

General relativity, the assumption of a flat spatial geometry of the universe, and the presence of a positive cosmological constant are cornerstones of the standard model of cosmology ΛCDM. Motivated by modifications to general relativity, this paper introduces five phenomenological parameters in addition to spatial curvature that describe departures from ΛCDM: a time-dependent effective dark energy equation of state, modifications of the Poisson equation for the lensing potential, and modifications of the growth of linear density perturbations. Deviations from the standard parameter values expected in ΛCDM do however not necessarily originate from modifications of general relativity but might as well describe properties of a nonstandard dark energy component. MCMC likelihood analyses are performed on the parameter spaces introduced by the addition of alternate combinations of the extra parameters to the basic cosmological parameters of the concordance model. Utilizing CMB anisotropies, cross correlations thereof with high-redshift galaxies through the ISW effect, the Hubble constant, supernovae and baryon acoustic oscillation distances, as well as the relation between weak gravitational lensing and galaxy flows, the paper checks ΛCDM against departures in these parameters from their standard values. Although the concordance model yields consistent predictions for these observables at the 95% confidence level, the constraints on the parameters leave enough space for nonstandard cosmological theories and the results suggest that constraining supplementary background parameters and parametrizations of the growth of large-scale structure separately may lead to an *a priori* exclusion of viable departures from the concordance model.

1.5.2. DGP braneworld gravity

Chapter 3 is devoted to tests of the self-accelerating and normal branch of the DGP model using various probes of large-scale structure that can accurately be described within linear perturbation theory. Of particular importance here are the cross correlations of the ISW effect with foreground galaxies that help to break parameter degeneracies on the normal branch of DGP gravity.

Sec. 3.1 Cosmological constraints on DGP braneworld gravity with brane tension

In the DGP model the universe is a four-dimensional brane embedded in a five-dimensional Minkowski bulk. While matter fields, including a cosmological constant or brane tension, are confined to the brane, gravitational fields extend to the full five-dimensional bulk. This leads to a modification of gravity on large scales that can be characterized by the crossover distance r_c that is proportional to the ratio of the gravitational coupling constants in the bulk and the brane, respectively. There are two branches of DGP cosmologies. In principle, a late-time acceleration can be achieved on the so-called self-accelerating branch without the need of a cosmological constant, however, it cannot consistently amount to a simultaneous combination of cosmological observations [77] without the introduction of a brane tension. A cosmological constant or brane tension is also required on the normal branch of the DGP model in order to produce cosmic acceleration. This paper derives constraints on both branches of the DGP model, where in the self-accelerating case both scenarios are studied, when including a cosmological constant and when omitting it. Thereby, a MCMC analysis is conducted on the DGP parameter spaces utilizing CMB data, its correlation with foreground galaxies, supernovae distances, and the Hubble constant. No signatures are found in support of the unique DGP modifications of gravity with strong preferences of a brane tension or cosmological constant on both DGP branches.

This paper is the result of a study performed with three co-authors: Wayne Hu, Wenjuan Fang, and Uroš Seljak. Wayne Hu provided the normal branch DGP fitting formulae within the PPF framework based on preliminary calculations of [116]. He also considerably contributed in editing the paper. Wenjuan Fang adapted her PPF module in the CAMB code for the self-accelerating DGP model [77] to be compatible with the inclusion of a cosmological constant, which I subsequently configured to yield predictions for the normal branch and self-accelerating plus brane tension DGP scenarios. Uroš Seljak initiated the project and motivated the use of the gISW cross correlation measurements of [93, 94] to put strong constraints on the DGP model. My contribution to this paper was also the modification of the ISWWLL code for predicting the gISW cross correlations and the corresponding likelihoods within DGP and to combine the different contributions of my co-authors to conduct a MCMC likelihood analysis for deriving the constraints, as well as the largest part in writing the paper.

1.5.3. $f(R)$ gravity models

Chapter 4 presents two tests of $f(R)$ gravity models using both linear and nonlinear probes of the large-scale structure, i.e., for latter, the abundance of clusters, which yields the currently strongest cosmological constraints on $f(R)$ gravity models, and the analysis of halo density profiles around the virial radius of clusters.

Sec. 4.1 Constraints on $f(R)$ gravity from probing the large-scale structure

In $f(R)$ gravity an arbitrary function $f(R)$ of the the Ricci scalar is added to the Einstein-Hilbert action. A suitable choice of this function may yield late-time modifications of gravity and provide an alternative explanation for the cosmic acceleration. This paper considers $f(R)$ modifications that exactly reproduce the ΛCDM expansion history and characterizes the class of solutions by the Compton wavelength parameter B_0. This approach is known as the designer model of $f(R)$ gravity [58]. A MCMC likelihood analysis is performed on the cosmological parameter space of such $f(R)$ gravity models, placing an upper limit on the viable values of B_0 by utilizing the geometrical constraints from supernovae, baryon acoustic oscillation distances, and the Hubble constant, as well as the CMB anisotropy data, along with its correlations with foreground galaxies, and a probe of the relation between weak gravitational lensing and galaxy flows. A further measurement of the abundance of clusters from the galaxy-galaxy lensing signal inferred from the MaxBCG catalog from the SDSS data is added. The abundance of clusters places the currently tightest constraints on $f(R)$ gravity models (cf. [117]) from large-scale structures.

The study presented in this paper was conducted along with three co-authors: Anže Slosar, Uroš Seljak, and Wayne Hu. Uroš Seljak initiated this project and suggested the use of gISW cross correlations and cluster abundance data for obtaining tight constraints on $f(R)$ gravity. Together with Anže Slosar he contributed a preliminary analysis of the cluster abundance data from the SDSS, for which Anže Slosar provided a module for the calculation of the model likelihood inferred from the galaxy-galaxy lensing signal within the MaxBCG catalog. Wayne Hu contributed with valuable advice in the initial and final phases of this project regarding the theoretical frameworks of $f(R)$ gravity and the PPF formalism. My contribution to the project was the adaption of the PPF module within CAMB to provide accurate predictions from $f(R)$ gravity for the CMB anisotropies and the matter power spectrum that is also used in the cluster abundance likelihood and ISWWLL codes, as well as the modification of the ISWWLL code for calculating the gISW cross correlations and the corresponding likelihoods for the $f(R)$ models. This involved numerically solving the full linear perturbation theory within $f(R)$ gravity to justify approximations made for efficient computation of the gISW cross correlations. Furthermore, I combined the different contributions of my co-authors to conduct a MCMC likelihood analysis for deriving the constraints on B_0 and wrote the large fraction of the paper.

Sec. 4.2 Cluster density profiles as a test of modified gravity

This paper draft presents a new test of modifications of gravity on scales around the virial radius of dark matter clusters measuring the halo profiles through the differential excess surface mass density from galaxy-galaxy lensing around the maxBCG sample from the SDSS data. Thereby the focus lies on the Hu-Sawicki $f(R)$ gravity model [118] with $n = 1$ and constraints are placed on the background scalar field amplitude $|f_{R0}|$, where $f_R \equiv df/dR$, the free degree of the model. For the correct description of the halo density profiles, N-body dark-matter-only simulations of ΛCDM and $f(R)$ cosmologies are employed. The paper shows that strong limits can be placed on $f(R)$ gravity modifications at the $(0.2 - 20)$ Mpc scale independent from solar-system and large-scale cosmological constraints, i.e., $|f_{R0}| < 0.027$ at the 95% confidence level. Moreover, the increase in fit observed in a phenomenological approach to modifications of gravity motivated by $f(R)$ models suggests that employing dark matter particles only in a ΛCDM simulation is not sufficient to correctly describe halo profiles around the virial radius of the cluster and that additional effects have to be taken into account.

This paper draft summarizes the results of a study performed with five co-authors: Fabian Schmidt, Tobias Baldauf, Rachel Mandelbaum, Uroš Seljak, and Robert Smith. So far the different contributions to this paper are as follows: Fabian Schmidt provided the predictions for the ratios of $f(R)$ gravity to ΛCDM halo profiles calibrated with N-body simulations and halo model predictions. Tobias Baldauf evaluated the high-precision ZHORIZON N-body simulations within ΛCDM performed by Robert Smith to determine the halo profiles within ΛCDM that I subsequently rescaled to $f(R)$ gravity predictions using the ratios determined by Fabian Schmidt and integrated to obtain the excess surface mass density with modified versions of a code written by Tobias Baldauf. Tobias Baldauf and I also designed the phenomenological description that yields the best fit to the galaxy-galaxy lensing data. Uroš Seljak initiated this project and suggested the use of the galaxy-galaxy lensing data that he prepared together with Rachel Mandelbaum as a new test of gravity. I combined the different efforts of my co-authors in a likelihood code to perform a MCMC analysis for deriving the constraints on $|f_{R0}|$ as well as on the phenomenological degree of freedom, and wrote the large fraction of the presented paper draft.

1.5.4. List of publications

The work described in the previous subsection is the result of different collaborations where I figured as the project leader or performed an analysis on my own. The presented projects are, however, related to further studies with smaller contributions from my part. The following is a complete list of publications were I was involved as (co-)author during my doctoral studies:

- L. Lombriser, F. Schmidt, T. Baldauf, R. Mandelbaum, U. Seljak, R. Smith, "Cluster density profiles as a test of modified gravity", in preparation.

- L. Lombriser, "Consistency check of ΛCDM phenomenology", Phys. Rev. **D83**, 063519 (2011), [arXiv:1101.0594].

- L. Lombriser, A. Slosar, U. Seljak, W. Hu, "Constraints on $f(R)$ gravity from probing the large-scale structure", submitted to Phys. Rev. **D**, [arXiv:1003.3009].

- R. Reyes, R. Mandelbaum, U. Seljak, T. Baldauf, J. Gunn, L. Lombriser, R. Smith, “Confirmation of general relativity on large scales from weak lensing and galaxy velocities”, Nature **464**, 256 (2010), [arXiv:1003.2185].
- S. Daniel, E. Linder, T. Smith, R. Caldwell, A. Cooray, A. Leauthaud, L. Lombriser, “Testing general relativity with current cosmological data”, Phys. Rev. **D81**, 123508 (2010) [arXiv:1002.1962].
- L. Lombriser, W. Hu, W. Fang, U. Seljak, “Cosmological constraints on DGP braneworld gravity with brane tension”, Phys. Rev. **D80**, 063536 (2009), [arXiv:0905.1112].
- R. Reyes, R. Mandelbaum, U. Seljak, J. Gunn, L. Lombriser, “Test of gravity on large scales with weak gravitational lensing and clustering measurements of SDSS luminous red galaxies”, American Astronomical Society Meeting Abstracts #213, Bulletin of the American Astronomical Society **41**, 425 (2009).

1.6. Conclusion

General relativity and the Standard Model of particle physics cannot amount to a large set of observations in astrophysics unless one is willing to supplement it with dark matter and dark energy. The observed late-time acceleration of the universe may be explained by introducing a cosmological constant or vacuum energy in the Einstein field equations, along with large amounts of dark matter. The resulting concordance model provides a simple but successful description for the observed universe. Given the lack of a complete understanding, however, it is important to repeatedly test this model against observations with the ambition of distinguishing between different explanations for the observed cosmic acceleration, e.g., a cosmological constant, dynamical dark energy, or a modification of gravity, and rule out or constrain the different models.

The DGP braneworld theory and $f(R)$ gravity are only two models of a class of models that adopt dark matter, but offer an alternative to dark energy. These theories make unique predictions in both the linear and nonlinear regimes of gravitational dynamics and can be probed with current and future observations. A large class of modified gravity models that provide an alternative explanation for the late-time acceleration can be parametrized by departures from the general relativistic relations in the Poisson equation and the ratio of the scalar metric perturbations along with an effective dark energy equation of state that may deviate from the cosmological constant. Although such parametrizations are motivated by modified gravity models, they may as well describe properties of a dark energy component. These parametrizations provide a framework to search for phenomena within cosmological observations which may indicate new physical effects, not describable by the concordance model.

1.6.1. Discussion

The dissertation at hand is the result of my personal efforts in the past three years as a doctoral candidate at the Institute for Theoretical Physics at the University of Zurich, where I worked intensively with modified gravity theories and conducted several tests on different models. In specific, linear probes of the large-scale structure were used to put stringent constraints on the crossover scale that governs the transition from five- to four-dimensional scalar-tensor gravity on the normal branch of the DGP model [119]. This work also concentrated on the self-accelerating branch of DGP gravity with and without a brane tension, its predictions for cosmological observables, and constraints obtained from current cosmological data. Using the enhanced abundance of clusters in designer models of $f(R)$ gravity, tight limits were put on the present background value of the additional scalar degree of freedom of the model [120]. Moreover, effects on halo density profiles from modified gravity theories motivated by the Hu-Sawicki $f(R)$ gravity model were studied and used to constrain modifications with gravitational lensing measurements [121]. Parameter spaces of phenomenological parametrizations that allow degrees of freedom in both the growth of structure and the background geometry were explored in [122]. Further collaborations included tests of phenomenological modifications of general relativity using gravitational lensing data [123] and the first measurement of E_G combining measures of large-scale gravitational lensing, galaxy clustering, and the growth rate of structure [99], which are, however, not presented here.

1.6.2. Outlook

Cosmological probes amenable to linear perturbation theory can efficiently be utilized as tests of modified gravity by adopting parametrizations such as the PPF framework and similar generalizations of the gravitational dynamics (see, e.g., [124]). Although they are very useful, they usually only comprise the description of a subset of the proposed modifications to gravity and are not completely developed in the nonlinear regime, where often observations contain more information and nonlinear mechanisms prohibit simple scaling relations from standard gravity. The extension and application of such formalisms to derive linear and nonlinear predictions of various modifications of gravity is subjct to future research with the goal of providing a framework for efficient cosmological tests of gravity. It involves numerical evaluation and calibration of N-body simulations of different gravitational models and the development of codes for this purpose.

On solar-system scales, gravity is very well tested and a potentially viable alternative theory of gravity, where modifications are introduced to explain and produce the late-time acceleration of the universe, must essentially reduce to general relativity. DGP gravity and some scalar-tensor theories, including $f(R)$ models, exhibit such a nonlinear feature through the Vainshtein and chameleon mechanisms, respectively. These unique features have to be incorporated when performing tests of gravity. While such a mechanism can considerably weaken constraints on the extra degrees of freedom introduced in the modifications from an observable, it provides a unique scale-dependent signature around dense objects, which can itself be utilized as a test of the gravitational theory.

In modified gravity models, masses inferred from the dynamics of galaxies and clusters may differ from the masses derived from gravitational lensing. This is attributed to a difference in the dynamical and lensing potentials that determine the propagation of massive and massless particles, respectively. In general relativity the two potentials correspond and the discrepancy predicted from modifications offers a great opportunity to probe gravity. An inconsistency between these two masses may point toward a modification of gravity, whereas independent and consistent measurements can be utilized to put constraints on the modifications of gravity.

Future research should continue with the exposure of specific and phenomenological modifications of gravity as well as other models of dark energy and dark matter to current and future cosmological data sets, and the study of their effects on the large-scale structure. In connection with this, it is also worth searching for or developing models that access the sensitive regions in the posterior distributions of the phenomenological parameter spaces obtained from data analysis. Instrumentalizing the discrepancies in the masses inferred from gravitational lensing and the dynamics of clusters, as well as the predicted signature of nonlinear mechanisms that return an alternative theory of gravity to general relativity on solar-system scales, one can generate new powerful probes of gravity. One may expect work in this direction to contribute further pieces in the understanding of gravity and the dark components of the universe.

References

[1] L. Lombriser, "Testing Modifications of General Relativity with Cosmological Observations" (ETHZ Diploma Thesis, 2008).

[2] A. Einstein, “Die formale Grundlage der allgemeinen Relativitätstheorie”, Sitzungsberichte der Königlich Preußischen Akademie der Wissenschaften (Berlin), 1030–1085 (1914).

[3] A. Einstein, “Zur allgemeinen Relativitätstheorie”, Sitzungsberichte der Königlich Preußischen Akademie der Wissenschaften (Berlin), 778–786 (1915).

[4] A. Einstein, “Die Feldgleichungen der Gravitation”, Sitzungsberichte der Königlich Preußischen Akademie der Wissenschaften (Berlin), 844–847 (1915).

[5] A. Einstein, “Die Grundlage der allgemeinen Relativitätstheorie”, Annalen der Physik **354**, 769 (1916).

[6] H. Vermeil, “Notiz über das mittlere Krümmungsmass einer n-fach ausgedehnten Riemannschen Mannigfaltigkeit”, Nachr. Ges. Wiss. Göttingen, 334–343 (1917).

[7] E. J. Cartan, “Sur les équations de la gravitation d'Einstein”, J. Math. Pures Appl. **1**, 141 (1922).

[8] H. Weyl, "Space-Time-Matter" (Dover, New York, 1922).

[9] D. Lovelock, “The uniqueness of the Einstein field equations in a four-dimensional space”, Archive for Rational Mechanics and Analysis **33**, 54 (1969).

[10] D. Lovelock, “The Einstein Tensor and Its Generalizations”, Journal of Mathematical Physics **12**, 498 (1971).

[11] D. Lovelock, “The Four-Dimensionality of Space and the Einstein Tensor”, Journal of Mathematical Physics **13**, 874 (1972).

[12] R. M. Wald, ”General relativity” (University of Chicago Press, Chicago, 1984).

[13] S. Weinberg, “The cosmological constant problem”, Rev. Mod. Phys. **61**, 1 (1989).

[14] S. M. Carroll, “The cosmological constant”, Living Rev. Rel. **4**, 1 (2001), [arXiv:astro-ph/0004075].

[15] S. Nobbenhuis, “Categorizing Different Approaches to the Cosmological Constant Problem”, Found. Phys. **36**, 613 (2006), [arXiv:gr-qc/0411093].

[16] Supernova Search Team, A. G. Riess *et al.*, “Observational Evidence from Supernovae for an Accelerating Universe and a Cosmological Constant”, Astron. J. **116**, 1009 (1998), [arXiv:astro-ph/9805201].

[17] Supernova Cosmology Project, S. Perlmutter *et al.*, “Measurements of Omega and Lambda from 42 High-Redshift Supernovae”, Astrophys. J. **517**, 565 (1999), [arXiv:astro-ph/9812133].

[18] S. L. Glashow, “Partial Symmetries of Weak Interactions”, Nucl. Phys. **22**, 579 (1961).

[19] S. Weinberg, “A Model of Leptons”, Phys. Rev. Lett. **19**, 1264 (1967).

[20] A. Salam, ”Elementary Particle Physics” (Almquist and Wiksell, Stockholm, 1968).

[21] S. L. Glashow, J. Iliopoulos, and L. Maiani, “Weak Interactions with Lepton-Hadron Symmetry”, Phys. Rev. **D2**, 1285 (1970).

[22] G. ’t Hooft and M. J. G. Veltman, “Regularization and Renormalization of Gauge Fields”, Nucl. Phys. **B44**, 189 (1972).

[23] H. Fritzsch, M. Gell-Mann, and H. Leutwyler, “Advantages of the Color Octet Gluon Picture”, Phys. Lett. **B47**, 365 (1973).

[24] R. H. Dicke, ”Gravitation and the universe” (American Philosophical Society, Philadelphia, 1969).

[25] F. Zwicky, “Die Rotverschiebung von extragalaktischen Nebeln”, Helvetica Physica Acta **6**, 110 (1933).

[26] F. Zwicky, “On the Masses of Nebulae and of Clusters of Nebulae”, Astrophys. J. **86**, 217 (1937).

[27] V. C. Rubin, N. Thonnard, and W. K. Ford, Jr., “Extended rotation curves of high-luminosity spiral galaxies. IV - Systematic dynamical properties, SA through SC”, Astrophys. J. **225**, L107 (1978).

[28] M. V. Ostrogradsky, “Mémoires sur les équations différentielles relatives au problème des isopérimetres”, Mém. Acad. Imp. Sci. St. Pétersbourg **VI**, 385 (1850).

[29] G. R. Dvali, G. Gabadadze, and M. Porrati, “4D gravity on a brane in 5D Minkowski space”, Phys. Lett. **B485**, 208 (2000), [arXiv:hep-th/0005016].

[30] C. Deffayet, “Cosmology on a brane in Minkowski bulk”, Phys. Lett. **B502**, 199 (2001), [arXiv:hep-th/0010186].

[31] P. Binetruy, C. Deffayet, U. Ellwanger, and D. Langlois, “Brane cosmological evolu-

tion in a bulk with cosmological constant", Phys. Lett. **B477**, 285 (2000), [arXiv:hep-th/9910219].

[32] W. Israel, "Singular hypersurfaces and thin shells in general relativity", Nuovo Cim. **B44S10**, 1 (1966).

[33] P. Binetruy, C. Deffayet, and D. Langlois, "Non-conventional cosmology from a brane-universe", Nucl. Phys. **B565**, 269 (2000), [arXiv:hep-th/9905012].

[34] A. I. Vainshtein, "To the problem of nonvanishing gravitation mass", Phys. Lett. **B39**, 393 (1972).

[35] C. Deffayet, G. R. Dvali, G. Gabadadze, and A. I. Vainshtein, "Nonperturbative continuity in graviton mass versus perturbative discontinuity", Phys. Rev. **D65**, 044026 (2002), [arXiv:hep-th/0106001].

[36] A. Lue and G. Starkman, "Gravitational leakage into extra dimensions: Probing dark energy using local gravity", Phys. Rev. **D67**, 064002 (2003), [arXiv:astro-ph/0212083].

[37] K. Koyama and F. P. Silva, "Non-linear interactions in a cosmological background in the DGP braneworld", Phys. Rev. **D75**, 084040 (2007), [arXiv:hep-th/0702169].

[38] S. Capozziello, S. Carloni, and A. Troisi, "Quintessence without scalar fields", Recent Res. Dev. Astron. Astrophys. **1**, 625 (2003), [arXiv:astro-ph/0303041].

[39] S. M. Carroll, V. Duvvuri, M. Trodden, and M. S. Turner, "Is Cosmic Speed-Up Due to New Gravitational Physics?", Phys. Rev. **D70**, 043528 (2004), [arXiv:astro-ph/0306438].

[40] S. Nojiri and S. D. Odintsov, "Modified gravity with negative and positive powers of the curvature: Unification of the inflation and of the cosmic acceleration", Phys. Rev. **D68**, 123512 (2003), [arXiv:hep-th/0307288].

[41] T. P. Sotiriou and V. Faraoni, "f(R) Theories Of Gravity", Rev. Mod. Phys. **82**, 451 (2010), [arXiv:0805.1726].

[42] R. P. Woodard, "Avoiding dark energy with 1/R modifications of gravity", Lect. Notes Phys. **720**, 403 (2007), [arXiv:astro-ph/0601672].

[43] R. Durrer and R. Maartens, "Dark Energy and Dark Gravity", Gen. Rel. Grav. **40**, 301 (2008), [arXiv:0711.0077].

[44] R. P. Woodard, "How Far Are We from the Quantum Theory of Gravity?", Rept. Prog. Phys. **72**, 126002 (2009), [arXiv:0907.4238].

[45] I. Sawicki and W. Hu, "Stability of Cosmological Solution in f(R) Models of Gravity", Phys. Rev. **D75**, 127502 (2007), [arXiv:astro-ph/0702278].

[46] G. Magnano and L. M. Sokolowski, "On physical equivalence between nonlinear gravity theories and a general relativistic selfgravitating scalar field", Phys. Rev. **D50**, 5039 (1994), [arXiv:gr-qc/9312008].

[47] T. Chiba, "1/R gravity and scalar-tensor gravity", Phys. Lett. **B575**, 1 (2003), [arXiv:astro-ph/0307338].

[48] R. Bean, D. Bernat, L. Pogosian, A. Silvestri, and M. Trodden, "Dynamics of Linear Perturbations in f(R) Gravity", Phys. Rev. **D75**, 064020 (2007), [arXiv:astro-ph/0611321].

[49] C. Brans and R. H. Dicke, “Mach’s principle and a relativistic theory of gravitation”, Phys. Rev. **124**, 925 (1961).

[50] C. M. Will, “The confrontation between general relativity and experiment”, Living Rev. Rel. **9**, 3 (2005), [arXiv:gr-qc/0510072].

[51] S. Tsujikawa, “Dark energy: investigation and modeling”, (2010), [arXiv:1004.1493].

[52] W. Hu and I. Sawicki, “A Parameterized Post-Friedmann Framework for Modified Gravity”, Phys. Rev. **D76**, 104043 (2007), [arXiv:0708.1190].

[53] W. Hu, “Parametrized Post-Friedmann Signatures of Acceleration in the CMB”, Phys. Rev. **D77**, 103524 (2008), [arXiv:0801.2433].

[54] J. M. Bardeen, “Gauge Invariant Cosmological Perturbations”, Phys. Rev. **D22**, 1882 (1980).

[55] H. Kodama and M. Sasaki, “Cosmological Perturbation Theory”, Prog. Theor. Phys. Suppl. **78**, 1 (1984).

[56] W. Hu and D. J. Eisenstein, “The Structure of structure formation theories”, Phys. Rev. **D59**, 083509 (1999), [arXiv:astro-ph/9809368].

[57] I. Sawicki, Y.-S. Song, and W. Hu, “Near-Horizon Solution for DGP Perturbations”, Phys. Rev. **D75**, 064002 (2007), [arXiv:astro-ph/0606285].

[58] Y.-S. Song, W. Hu, and I. Sawicki, “The large scale structure of f(R) gravity”, Phys. Rev. **D75**, 044004 (2007), [arXiv:astro-ph/0610532].

[59] K. Koyama, A. Taruya, and T. Hiramatsu, “Non-linear Evolution of Matter Power Spectrum in Modified Theory of Gravity”, Phys. Rev. **D79**, 123512 (2009), [arXiv:0902.0618].

[60] E. Beynon, D. J. Bacon, and K. Koyama, “Weak lensing predictions for modified gravities at non- linear scales”, Mon. Not. Roy. Astron. Soc. **403**, 353 (2010), [arXiv:0910.1480].

[61] V. Mukanov, ”Physical Foundations of Cosmology” (Cambridge University Press, New York, 2005).

[62] R. A. Sunyaev and Y. B. Zeldovich, “The Velocity of clusters of galaxies relative to the microwave background. The Possibility of its measurement”, Mon. Not. Roy. Astron. Soc. **190**, 413 (1980).

[63] R. A. Sunyaev and Y. B. Zeldovich, “Microwave background radiation as a probe of the contemporary structure and history of the universe”, Ann. Rev. Astron. Astrophys. **18**, 537 (1980).

[64] R. K. Sachs and A. M. Wolfe, “Perturbations of a cosmological model and angular variations of the microwave background”, Astrophys. J. **147**, 73 (1967).

[65] J. M. Bardeen, J. R. Bond, N. Kaiser, and A. S. Szalay, “The Statistics of Peaks of Gaussian Random Fields”, Astrophys. J. **304**, 15 (1986).

[66] D. J. Eisenstein and W. Hu, “Baryonic Features in the Matter Transfer Function”, Astrophys. J. **496**, 605 (1998), [arXiv:astro-ph/9709112].

[67] D. J. Eisenstein and W. Hu, “Power Spectra for Cold Dark Matter and its Variants”, Astrophys. J. **511**, 5 (1997), [arXiv:astro-ph/9710252].

[68] W. Hu, M. Fukugita, M. Zaldarriaga, and M. Tegmark, "CMB Observables and Their Cosmological Implications", Astrophys. J. **549**, 669 (2001), [arXiv:astro-ph/0006436].

[69] WMAP, L. Page *et al.*, "First Year Wilkinson Microwave Anisotropy Probe (WMAP) Observations: Interpretation of the TT and TE Angular Power Spectrum Peaks", Astrophys. J. Suppl. **148**, 233 (2003), [arXiv:astro-ph/0302220].

[70] W. Hu and N. Sugiyama, "Anisotropies in the Cosmic Microwave Background: An Analytic Approach", Astrophys. J. **444**, 489 (1995), [arXiv:astro-ph/9407093].

[71] W. Hu and N. Sugiyama, "Small scale cosmological perturbations: An Analytic approach", Astrophys. J. **471**, 542 (1996), [arXiv:astro-ph/9510117].

[72] G. Efstathiou and J. R. Bond, "Cosmic Confusion: Degeneracies among Cosmological Parameters Derived from Measurements of Microwave Background Anisotropies", Mon. Not. Roy. Astron. Soc. **304**, 75 (1999), [arXiv:astro-ph/9807103].

[73] A. Lewis, A. Challinor, and A. Lasenby, "Efficient Computation of CMB anisotropies in closed FRW models", Astrophys. J. **538**, 473 (2000), [arXiv:astro-ph/9911177].

[74] U. Seljak and M. Zaldarriaga, "A Line of Sight Approach to Cosmic Microwave Background Anisotropies", Astrophys. J. **469**, 437 (1996), [arXiv:astro-ph/9603033].

[75] WMAP, J. Dunkley *et al.*, "Five-Year Wilkinson Microwave Anisotropy Probe (WMAP) Observations: Likelihoods and Parameters from the WMAP data", Astrophys. J. Suppl. **180**, 306 (2009), [arXiv:0803.0586].

[76] D. Larson *et al.*, "Seven-Year Wilkinson Microwave Anisotropy Probe (WMAP) Observations: Power Spectra and WMAP-Derived Parameters", Astrophys. J. Suppl. **192**, 16 (2011), [arXiv:1001.4635].

[77] W. Fang *et al.*, "Challenges to the DGP Model from Horizon-Scale Growth and Geometry", Phys. Rev. **D78**, 103509 (2008), [arXiv:0808.2208].

[78] W. Fang, W. Hu, and A. Lewis, "Crossing the Phantom Divide with Parameterized Post-Friedmann Dark Energy", Phys. Rev. **D78**, 087303 (2008), [arXiv:0808.3125].

[79] B. A. Bassett and R. Hlozek, "Baryon Acoustic Oscillations", (2009), [arXiv:0910.5224].

[80] The SNLS, P. Astier *et al.*, "The Supernova Legacy Survey: Measurement of Ω_M, Ω_Λ and w from the First Year Data Set", Astron. Astrophys. **447**, 31 (2006), [arXiv:astro-ph/0510447].

[81] Supernova Cosmology Project, M. Kowalski *et al.*, "Improved Cosmological Constraints from New, Old and Combined Supernova Datasets", Astrophys. J. **686**, 749 (2008), [arXiv:0804.4142].

[82] R. Amanullah *et al.*, "Spectra and Light Curves of Six Type Ia Supernovae at $0.511 < z < 1.12$ and the Union2 Compilation", Astrophys. J. **716**, 712 (2010), [arXiv:1004.1711].

[83] A. G. Riess *et al.*, "A Redetermination of the Hubble Constant with the Hubble Space Telescope from a Differential Distance Ladder", Astrophys. J. **699**, 539 (2009), [arXiv:0905.0695].

[84] D. J. Eisenstein, H.-J. Seo, and M. J. White, “On the Robustness of the Acoustic Scale in the Low-Redshift Clustering of Matter”, Astrophys. J. **664**, 660 (2007), [arXiv:astro-ph/0604361].

[85] W. J. Percival *et al.*, “Baryon Acoustic Oscillations in the Sloan Digital Sky Survey Data Release 7 Galaxy Sample”, Mon. Not. Roy. Astron. Soc. **401**, 2148 (2010), [arXiv:0907.1660].

[86] N. Afshordi, “Integrated Sachs-Wolfe effect in Cross-Correlation: The Observer’s Manual”, Phys. Rev. **D70**, 083536 (2004), [arXiv:astro-ph/0401166].

[87] M. LoVerde and N. Afshordi, “Extended Limber Approximation”, Phys. Rev. **D78**, 123506 (2008), [arXiv:0809.5112].

[88] R. E. Smith, C. Hernandez-Monteagudo, and U. Seljak, “Impact of Scale Dependent Bias and Nonlinear Structure Growth on the ISW Effect: Angular Power Spectra”, Phys. Rev. **D80**, 063528 (2009), [arXiv:0905.2408].

[89] SDSS, D. G. York *et al.*, “The Sloan Digital Sky Survey: technical summary”, Astron. J. **120**, 1579 (2000), [arXiv:astro-ph/0006396].

[90] SDSS, D. J. Eisenstein *et al.*, “Spectroscopic Target Selection for the Sloan Digital Sky Survey: The Luminous Red Galaxy Sample”, Astron. J. **122**, 2267 (2001), [arXiv:astro-ph/0108153].

[91] SDSS, J. K. Adelman-McCarthy *et al.*, “The Sixth Data Release of the Sloan Digital Sky Survey”, Astrophys. J. Suppl. **175**, 297 (2008), [arXiv:0707.3413].

[92] SDSS, K. N. Abazajian *et al.*, “The Seventh Data Release of the Sloan Digital Sky Survey”, Astrophys. J. Suppl. **182**, 543 (2009), [arXiv:0812.0649].

[93] S. Ho, C. Hirata, N. Padmanabhan, U. Seljak, and N. Bahcall, “Correlation of CMB with large-scale structure: I. ISW Tomography and Cosmological Implications”, Phys. Rev. **D78**, 043519 (2008), [arXiv:0801.0642].

[94] C. M. Hirata, S. Ho, N. Padmanabhan, U. Seljak, and N. A. Bahcall, “Correlation of CMB with large-scale structure: II. Weak lensing”, Phys. Rev. **D78**, 043520 (2008), [arXiv:0801.0644].

[95] G. Squires and N. Kaiser, “Unbiased Cluster Lens Reconstruction”, Astrophys. J. **473**, 65 (1996), [arXiv:astro-ph/9512094].

[96] M. Davis and P. J. E. Peebles, “A Survey of galaxy redshifts. V - The Two point position and velocity correlations”, Astrophys. J. **267**, 465 (1982).

[97] T. Baldauf, R. E. Smith, U. Seljak, and R. Mandelbaum, “An algorithm for the direct reconstruction of the dark matter correlation function from weak lensing and galaxy clustering”, Phys. Rev. **D81**, 063531 (2010), [arXiv:0911.4973].

[98] R. Mandelbaum, U. Seljak, T. Baldauf, and R. E. Smith, “Precision cluster mass determination from weak lensing”, Mon. Not. Roy. Astron. Soc. **405**, 2078 (2010), [arXiv:0911.4972].

[99] R. Reyes *et al.*, “Confirmation of general relativity on large scales from weak lensing and galaxy velocities”, Nature **464**, 256 (2010.), [arXiv:1003.2185].

[100] H. Oyaizu, “Non-linear evolution of f(R) cosmologies I: methodology”, Phys. Rev. **D78**, 123523 (2008), [arXiv:0807.2449].

[101] F. Schmidt, “Cosmological Simulations of Normal-Branch Braneworld Gravity”, Phys. Rev. **D80**, 123003 (2009), [arXiv:0910.0235].

[102] F. Schmidt, M. V. Lima, H. Oyaizu, and W. Hu, “Non-linear Evolution of f(R) Cosmologies III: Halo Statistics”, Phys. Rev. **D79**, 083518 (2009), [arXiv:0812.0545].

[103] R. K. Sheth and G. Tormen, “Large scale bias and the peak background split”, Mon. Not. Roy. Astron. Soc. **308**, 119 (1999), [arXiv:astro-ph/9901122].

[104] J. L. Tinker *et al.*, “Toward a halo mass function for precision cosmology: the limits of universality”, (2008), [arXiv:0803.2706].

[105] J. F. Navarro, C. S. Frenk, and S. D. M. White, “The Structure of Cold Dark Matter Halos”, Astrophys. J. **462**, 563 (1996), [arXiv:astro-ph/9508025].

[106] U. Seljak, A. Slosar, and R. Mandelbaum *et al.*, in preparation.

[107] SDSS, B. Koester *et al.*, “A MaxBCG Catalog of 13,823 Galaxy Clusters from the Sloan Digital Sky Survey”, Astrophys. J. **660**, 239 (2007), [arXiv:astro-ph/0701265].

[108] H. Föllmer and H. R. Künsch, ”Wahrscheinlichkeitsrechnung und Statistik” (ETHZ lecture notes, 2000).

[109] S. P. Meyn and R. L. Tweedie, ”Markov chains and stochastic stability” (Springer-Verlag, London, 1993).

[110] D. Ocone, ”Discrete and Probabilistic Models in Biology” (Rutgers University lecture notes, 2005).

[111] N. Metropolis, A. W. Rosenbluth, M. N. Rosenbluth, A. H. Teller, and E. Teller, “Equation of state calculations by fast computing machines”, J. Chem. Phys. **21**, 1087 (1953).

[112] W. K. Hastings, “Monte Carlo sampling methods using Markov chains and their applications”, Biometrika **57**, 97 (1970).

[113] A. Lewis and S. Bridle, “Cosmological parameters from CMB and other data: a Monte-Carlo approach”, Phys. Rev. **D66**, 103511 (2002), [arXiv:astro-ph/0205436].

[114] A. Heavens, “Statistical techniques in cosmology”, (2009), [arXiv:0906.0664].

[115] A. Gelman and D. B. Rubin, “Inference from Iterative Simulation Using Multiple Sequences”, Statist. Sci. **7**, 457 (1992).

[116] S. S. Seahra and W. Hu, “Analytic Description of DGP Perturbations on All Scales”, Phys. Rev. **D82**, 124015 (2010), [arXiv:1007.4242].

[117] F. Schmidt, A. Vikhlinin, and W. Hu, “Cluster Constraints on f(R) Gravity”, Phys. Rev. **D80**, 083505 (2009), [arXiv:0908.2457].

[118] W. Hu and I. Sawicki, “Models of f(R) Cosmic Acceleration that Evade Solar-System Tests”, Phys. Rev. **D76**, 064004 (2007), [arXiv:0705.1158].

[119] L. Lombriser, W. Hu, W. Fang, and U. Seljak, “Cosmological Constraints on DGP Braneworld Gravity with Brane Tension”, Phys. Rev. **D80**, 063536 (2009), [arXiv:0905.1112].

[120] L. Lombriser, A. Slosar, U. Seljak, and W. Hu, “Constraints on f(R) gravity from probing the large-scale structure”, (2010), [arXiv:1003.3009].

[121] L. Lombriser, F. Schmidt, R. Mandelbaum, T. Baldauf, and U. Seljak, "Cluster density profiles as a test of modified gravity", in preparation.

[122] L. Lombriser, "Consistency check of ΛCDM phenomenology", Phys. Rev. **D83**, 063519 (2011), [arXiv:1101.0594].

[123] S. F. Daniel *et al.*, "Testing General Relativity with Current Cosmological Data", Phys. Rev. **D81**, 123508 (2010), [arXiv:1002.1962].

[124] L. Amendola, M. Kunz, and D. Sapone, "Measuring the dark side (with weak lensing)", JCAP **0804**, 013 (2008), [arXiv:0704.2421].

2

General relativity

2.1. Consistency check of ΛCDM phenomenology

Lucas Lombriser[1]

Published in Physical Review D 83, 063519 (2011), [arXiv:1101.0594]

Abstract

The standard model of cosmology ΛCDM assumes general relativity, flat space, and the presence of a positive cosmological constant. We relax these assumptions allowing spatial curvature, a time-dependent effective dark energy equation of state, as well as modifications of the Poisson equation for the lensing potential, and modifications of the growth of linear matter density perturbations in alternate combinations. Using six parameters characterizing these relations, we check ΛCDM for consistency utilizing cosmic microwave background anisotropies, cross correlations thereof with high-redshift galaxies through the integrated Sachs-Wolfe effect, the Hubble constant, supernovae, and baryon acoustic oscillation distances, as well as the relation between weak gravitational lensing and galaxy flows. In all scenarios, we find consistency of the concordance model at the 95% confidence level. However, we emphasize that constraining supplementary background parameters and parametrizations of the growth of large-scale structure separately may lead to an a priori exclusion of viable departures from the concordance model.

2.1.1. Introduction

The detection of the late-time acceleration of our universe [125, 126] challenges the known laws of physics. General relativity and the standard model of particle physics cannot amount to the observed cosmic expansion unless we are willing to accept a seemingly random constant in the Einstein field equations or the presence of an unknown form of energy, along with large amounts of dark matter. The concordance model assumes such a cosmological constant or vacuum energy and provides a simple but successful description for the observed universe. Given the lack of a complete understanding, it is important to repeatedly test this model against observations with the ambition of distinguishing between different explanations of the observed cosmic acceleration, e.g., a cosmological constant, dynamical dark energy, or a modification of gravity, and rule out or constrain the different models. See [127–129] for recent reviews on tests of nonstandard cosmologies.

Phenomenological parametrizations for departures from the concordance model have been studied in [130–139]. In this paper, we shall mainly adopt the parametrization and notation of [136, 137]. In addition to the usual cosmological parameters, including spatial curvature, we use five phenomenological parameters quantifying modifications of the Poisson equation for the lensing potential, modifications of the

---

[1] Institute for Theoretical Physics, University of Zurich, Winterthurerstrasse 190, CH-8057 Zürich, Switzerland

growth of linear matter density perturbations, as well as a time-dependent effective dark energy equation of state. The parameters are based on models of modified gravity, but may also describe properties of dark energy and provide a framework to search for phenomena which may indicate new physical effects in current and future cosmological observations.

We conduct a Markov chain Monte Carlo (MCMC) study of this parameter space using data from the cosmic microwave background (CMB) anisotropies, supernovae distances, the baryon acoustic oscillations (BAO) distances, and the Hubble constant. We also utilize information from the cross correlation between high-redshift galaxies and the CMB through the integrated Sachs-Wolfe (ISW) effect, as well as a probe of the relation between weak gravitational lensing and galaxy flows. For the predictions of the CMB anisotropies, we connect our phenomenological parameters to the parametrized post-Friedmann (PPF) framework [138, 140] and use its implementation into a standard Einstein-Boltzmann linear theory solver [141].

In Sec. 2.1.2, we define the phenomenological parametrization of the modifications to standard cosmology and explain their implications on various cosmological probes in Sec. 2.1.3.1. Modifications to the ISWWLL [142, 143] code used for the galaxy-ISW (gISW) cross correlation observations are specified in Sec. 2.1.3.1. For the connection of our parametrization to the PPF formalism, we refer to the appendix. We present the results of our MCMC study in Sec. 2.1.3.2 and discuss them in Sec. 2.1.4.

2.1.2. Phenomenological modifications

We consider scalar linear perturbations of the Friedmann-Lemaître-Robertson-Walker background in the longitudinal gauge, hence

$$ds^2 = -(1+2\Psi)dt^2 + a^2(1+2\Phi)d\mathbf{x}^2, \tag{2.1}$$

where $d\mathbf{x}^2$ is the unperturbed spatial line element with curvature K and $c \equiv 1$. Motivated by modified gravity models, effects from a nonstandard cosmology may introduce the following three time- and scale-dependent phenomenological modifications on the background and at quasistatic scales of linear perturbations (see, e.g., [134–136, 138, 144, 145]; cf. [133]):

- A deviation from the ΛCDM expansion history, parametrized by an effective dark energy equation of state $w_{\rm eff}(a)$,

$$\left(\frac{H}{H_0}\right)^2 = \Omega_{\rm m}a^{-3} + \Omega_K a^{-2} + (1-\Omega_{\rm m}-\Omega_K)a^{-3[w_{\rm eff}(a)+1]}. \tag{2.2}$$

- An effective change of the Newton's constant, which we can parametrize by a free function $Q(k,a)$, yielding a generalized Poisson equation,

$$k^2\Phi = 4\pi\, G\, a^2 Q\, \rho_{\rm m}\Delta_{\rm m}. \tag{2.3}$$

- A difference in the scalar linear potentials Ψ and Φ parametrized by the free function $\eta(k,a)$,

$$\Psi = -(1+\eta)\Phi. \tag{2.4}$$

Deviations from $Q = 1$ and $\eta = 0$, the standard values, do not necessary indicate modifications of general relativity but might, for instance, also originate from contributions of nonmatter fluids to the Poisson equation ($Q \neq 1$), e.g., from clustering of dark energy or interactions between the dark components (see, e.g., [146]), or nonvanishing anisotropic stress ($\eta \neq 0$) (see, e.g., [133, 147]). Dark energy models other than the cosmological constant also predict departures from $w_{\mathrm{eff}}(a) = -1$. Note that a dark energy model can always be constructed to be formally equivalent to a modification of gravity through an effective dark energy stress-energy tensor. The parameters introduced here cannot distinguish between the two descriptions. Consideration of microphysical aspects may, however, indicate which is the more reasonable picture (see, e.g., [138, 148]).

We can combine Eqs. (2.3) and (2.4) to obtain [136]

$$k^2\Phi_- = \frac{3H_0^2\Omega_{\mathrm{m}}}{2a}\Sigma\,\Delta_{\mathrm{m}}, \tag{2.5}$$

where $\Sigma = Q(1+\eta/2)$ and $\Phi_- = (\Phi - \Psi)/2$. This relation is in particular sensitive to weak lensing measurements and the ISW effect can be used to probe its time evolution. Modifications as in Eqs. (2.3) and (2.4) lead to changes in the growth of the linear matter overdensity perturbation Δ_{m}, which we parametrize via the growth index γ [132, 137],

$$\frac{d\ln\Delta_{\mathrm{m}}}{d\ln a} = \Omega_{\mathrm{m}}(a)^{\gamma}(1+\xi), \tag{2.6}$$

where $\Omega_{\mathrm{m}}(a) = H_0^2\Omega_{\mathrm{m}}a^{-3}H^{-2}$. We also introduce here the parameter ξ to account for growth rates beyond unity, given $\gamma > 0$ and $0 \leq \Omega_{\mathrm{m}} \leq 1$, as can be observed in scalar-tensor theories [137]. Hence, detection of $\xi > 0$ may indicate the presence of an additional attractive force.

We decide to use the quantities defined in Eqs. (2.5) and (2.6) to scan the cosmological data for departures from standard theory and replace the two free functions Q and η by Σ and (γ, ξ). Note that ξ should not be interpreted as a new parameter in the gravitational dynamics like Q and η, but rather as the separation $\gamma \to \gamma + \Gamma$, where we assume the specific form $\Gamma = \ln(1+\xi)/\ln\Omega_{\mathrm{m}}(a)$.

From the ordinary differential equation which describes the correct behavior of the linear matter overdensity perturbations in the quasistatic regime,

$$\Delta_{\mathrm{m}}'' + \left(2 + \frac{H'}{H}\right)\Delta_{\mathrm{m}}' - \frac{3}{2}\frac{H_0^2\Omega_{\mathrm{m}}}{a^3H^2}\mathcal{F}\,\Delta_{\mathrm{m}} = 0, \tag{2.7}$$

where $\mathcal{F} = Q(1+\eta) = 2\Sigma(1+\eta)/(2+\eta)$ and primes denote derivatives with respect to $\ln a$, we derive

$$\begin{aligned}\mathcal{F} &= \frac{2}{3}\Omega_{\mathrm{m}}(a)^{2\gamma-1}(1+\xi)^2 - \frac{2}{3}\left\{\gamma\left[2\frac{H'}{H}+3\right]\right.\\ &\quad \left. - \left[\frac{H'}{H}+2\right]\right\}\Omega_{\mathrm{m}}(a)^{\gamma-1}(1+\xi),\end{aligned} \tag{2.8}$$

where we assumed constant γ and ξ. Given Σ and (γ, ξ), we can use Eq. (2.8) to derive Q and η and thus define our modifications to ΛCDM in the framework of

Eqs. (2.2) through (2.4). Note that

$$\mathcal{F} = \frac{2}{3}(1+\xi)^2 + \frac{1}{3}(1+\xi), \tag{2.9}$$

whenever $a^{w_{\rm eff}(a)} \gg 1$ and $w'_{\rm eff}(\ln a) \ll 1$ as $a \ll 1$. If $|\xi| \ll 1$ at $a \ll 1$, standard gravity is reproduced. Otherwise, modifications to gravity persist up to high redshifts.

2.1.2.1. Parametrization

It is a difficult task to find general functions with a minimal set of free parameters that are flexible enough to capture the wealth of possible modifications in Eqs. (2.2) through (2.4) or equivalently in Eqs. (2.2), (2.5), and (2.6). Rather than to construct such a function for each relation, we decide to use a low number of five parameters, in addition to spatial curvature, and examine the combinational aspects of introducing modifications in each of the relations. We restrict to constant and time-dependent modifications and choose the parametrization in a way that ΛCDM is contained in the parameter space.

For the expansion history we consider the parametrization

$$\begin{aligned} H(a)^2 \;=\;& H_0^2\Omega_{\rm m}a^{-3} + H_0^2\Omega_K a^{-2} + H_0^2(1-\Omega_{\rm m}-\Omega_K) \\ & \times a^{-3(1+w_0+w_a)}\exp\left[3w_a(a-1)\right], \end{aligned} \tag{2.10}$$

where the dark energy equation of state is given by [130, 131]

$$w_{\rm DE}(a) = w_0 + (1-a)w_a, \tag{2.11}$$

$$a^{-3[1+w_{\rm eff}(a)]} = \exp\left[3\int_a^1 \frac{1+w_{\rm DE}(a')}{a'}da'\right]. \tag{2.12}$$

Note that this parametrization does not always provide a good fit to model predictions. We adopt the approach primarily due to its simplicity and wide usage. In the limit $(w_0, w_a) \to (-1, 0)$, the effective dark energy term in Eq. (2.10) reduces to a cosmological constant. The parametrization is less successful, e.g., in the case of Dvali-Gabadadze-Porrati (DGP) gravity [149]. It provides a good approach for distance measures [132] and the quasistatic regime for the self-accelerated branch, but it fails for the normal branch due to the appearance of a divergence in $w_{\rm DE}(a)$. Also note that choosing a specific form for $w_{\rm DE}$ may have a nontrivial effect on the constraints inferred for it (see, e.g., [150] for a model-independent approach).

Next, we need to define modifications to the rate of growth and the Poisson equation. We decide to use a constant growth index γ_0, which is a good approximation to general relativity, where $\gamma_0 \approx 0.55$, or the quasistatic regime of self-accelerating DGP gravity [151], where $\gamma_0 \approx 0.68$ [132, 152, 153]. We further use a constant $\xi = \xi_0$, which was found to provide a good fit to scalar-tensor theories where the scalar field couples to dark matter [137]. Equation (2.6) relates to the parametrization of [139] as $d\ln g_\star/d\ln a = \xi\,\Omega_{\rm m}(a)^\gamma$, which was introduced to describe effects from early dark energy, modified gravity at high redshifts, or early acceleration. For these models,

$g_\star$ was found to be well-described by a constant [139]. Therefore, there is only limited correspondence to a constant $\xi = \xi_0 = 0$. For Σ we use a parametrization that reduces to its general relativistic value $\Sigma \rightarrow 1$ at early times. Hence, for our consistency test, we furthermore set

$$\gamma = \gamma_0, \tag{2.13}$$

$$\xi = \xi_0 \tag{2.14}$$

$$\Sigma = 1 + \Sigma_0 a. \tag{2.15}$$

For reference, we denote our nonstandard cosmologies by the extra parameters we allow to be free. Hence, when, e.g., taking Ω_K and γ_0, as well as w_0 and w_a, to be free parameters deviating from their standard values, we denote the according model by $\gamma w K$. Note that in the limit where $\{w_0,\ w_a,\ \gamma_0,\ \xi_0,\ \Sigma_0) \rightarrow \{-1,\ 0,\ 0.55,\ 0,\ 0)$, Eqs. (2.2), (2.5), and (2.6) reduce to general relativity with cold dark matter and a cosmological constant. From Eqs. (2.6) and (2.10), it is clear that when $w_a \approx -w_0$, there is a degeneracy between w_a and ξ_0, which manifests itself, in particular, at high redshifts. To explore the parameter space unclosed by free w_0, w_a, and ξ_0, we furthermore study three models where we fix $\gamma_0 = 0.55$ and $\Sigma_0 = 0$ while allowing the following degrees of freedom:

(A) ξ_0, $w_{\rm DE} = w_0 + (1-a)w_a$,

(B) ξ_0, $w_{\rm DE} = -1 + (1-a)w_a$,

(C) ξ_0, $w_{\rm DE} = -1 + \lambda_0(1 - 1.15a)$,

such that ΛCDM is a limiting case in all of the three models. The slope of $w_{\rm DE}(a)$ in model (C) is motivated by the best-fit values derived in Sec. 2.1.3.2. For numerical predictions, we connect our parametrizations to the linear PPF framework as described in App. 2.1.A.

Note that we have ignored scale dependence of the parameters, which is a good approximation within ΛCDM. Modifications of gravity such as $f(R)$ gravity models [154–156], however, may introduce a strong scale dependence in these relations. The same holds for DGP gravity, where the deficiency is, however, restricted to near-horizon and superhorizon scales [157]. Although for these cases the parametrization is not very descriptive, it still serves as a useful tracer of nonstandard phenomenologies. Departures from the standard parameter values may indicate inconsistencies in the concordance model and point toward new physical effects, which in turn have to be addressed with more developed theories. It has been pointed out, by conducting a principal component analysis [158], that such inconsistencies in Eqs. (2.3) through (2.5) are more likely to be detected in scale-dependent modifications due to weaker sensitivity in the data to time-dependent deviations [159, 160]. A parametrization like the one described in this section is still capable of tracing trends in the observations and disclosing new regions in the parameter space of possible modifications, especially when simultaneously allowing for time-dependent modifications in the effective dark energy equation of state.

2.1.3. Consistency check

We use a variety of cosmological data sets to check against nonstandard cosmology. First we use the CMB anisotropy data from the seven-year Wilkinson Microwave Anisotropy Probe (WMAP) [161], the Arcminute Cosmology Bolometer Array Receiver (ACBAR) [162], the Balloon Observations Of Millimetric Extragalactic Radiation and Geophysics (BOOMERanG) flight in 2003 (B03) [163], and the Cosmic Background Imager (CBI) [164]. Next we employ data from the Supernova Cosmology Project (SCP) Union2 [165] compilation, the measurement of the Hubble constant from the Supernovae and H_0 for the Equation of State (SHOES) [166] program generalized by [167], and the BAO distance measurements of [168]. Furthermore, we take gISW cross correlation observations using the ISWWLL code of [142, 143], and the E_G measurement, probing the relation between weak gravitational lensing and galaxy flows, of [169].

Note that we restrict to data sets amenable to linear perturbation theory. Nonlinear probes such as from the abundance of clusters and the full range of scales of weak gravitational lensing yield tight constraints on the parameters that quantify modifications to general relativity (see, e.g., [170–175]). In the case of $f(R)$ gravity models or DGP gravity, nonlinear effects have been studied in [171, 176–184] and spherical collapse within various dark energy models in, e.g., [185, 186]. However, for phenomenological parametrizations like the one we use, nonlinear behavior has not been examined in full extent. Hence, applying standard scaling relations may lead to illusive conclusions. Furthermore, note that the inclusion of gISW cross correlations, along with the ISW effect in the CMB, and E_G, yield competitive results to constraints from nonlinear probes (cf., e.g., [187]).

In Sec. 2.1.3.1, we discuss the predictions for some of these observables for specific parameter values. In Sec. 2.1.3.2, we present the results of a MCMC likelihood analysis, which is conducted with the publicly available COSMOMC [188] package.

2.1.3.1. Cosmological observables

In this section, we illustrate model predictions of various cosmological observables we use to derive our results. We chose the parameters of the various models that highlight results from the MCMC analysis.

As our basic set, we choose a parametrization that separates high-redshift and low-redshift constraints. Specifically we take six high-redshift parameters: the physical baryon and cold dark matter density $\Omega_\mathrm{b}h^2$ and $\Omega_\mathrm{c}h^2$, the ratio of sound horizon to angular diameter distance at recombination $\theta/100$, the optical depth to reionization τ, the scalar tilt n_s, and amplitude A_s at $k_* = 0.002$ Mpc^{-1}. We extend this parameter set with alternate combinations of the six additional parameters, describing departures from the concordance model: the spatial curvature density Ω_K, two parameters for the evolution of the effective dark energy equation of state, w_0 and w_a, the growth index γ_0 and the scaling of the growth rate ξ_0, as well as the first-order of a time-dependent modification of the Poisson equation for the lensing potential Σ_0.

We illustrate predictions from the maximum-likelihood ΛCDM model, as well as from the overall best-fit model (see Sec. 2.1.3.2). Hereby, we derive the parame-

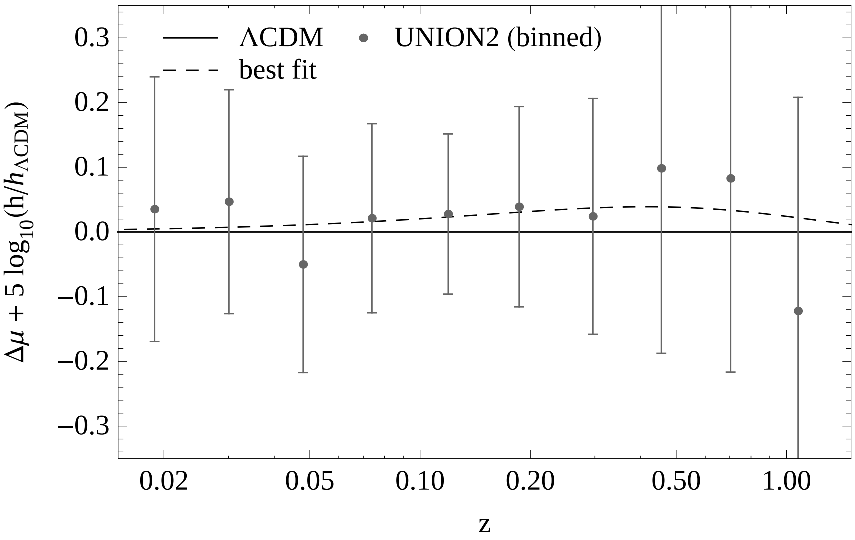

Figure 2.1: Overall best-fit distance modulus with respect to the best-fit ΛCDM distance modulus. For illustration, the UNION2 data are binned into ten data bands with logarithmic spacing.

ter values using the full set of cosmological data. To demonstrate effects from the variation of a specific basic cosmological parameter on the observables, we use the corresponding 1D-marginalized 68% confidence limits from the ΛCDM model while setting the complementary parameters to their best-fit values. For a supplementary parameter, we use its 1D-marginalized 68% confidence boundary, when including it as the sole extra parameter while setting the basic parameters to their ΛCDM best-fit values. Note, however, that for the nonstandard cases, γ_0 is always simultaneously varied with any of the extra parameters. Hereby, (w_0, w_a) should be counted as one parameter, i.e., w_0 and w_a are always either fixed to $(-1, 0)$ or both considered free.

Distance measures

The comparison of the magnitudes of high-redshift to low-redshift supernovae yields a relative distance measure. Theoretical predictions for the distance modulus are related to the luminosity distance, $d_L(z) = (1+z)r(z)$, where $r(z)$ is the comoving angular diameter distance defined by

$$r(z) = \begin{cases} \sin\left[H_0\sqrt{-\Omega_K}\chi(z)\right]/H_0\sqrt{|\Omega_K|}, & \Omega_K < 0, \\ \chi(z), & \Omega_K = 0, \\ \sinh\left[H_0\sqrt{\Omega_K}\chi(z)\right]/H_0\sqrt{|\Omega_K|}, & \Omega_K > 0 \end{cases} \tag{2.16}$$

with comoving radial distance

$$\chi(z) = \int_0^z \frac{dz'}{H(z')}. \tag{2.17}$$

The supernovae magnitudes, once standardized, are related to the distance by

$$m \equiv \mu + M = 5\log_{10} d_L + M + 25, \tag{2.18}$$

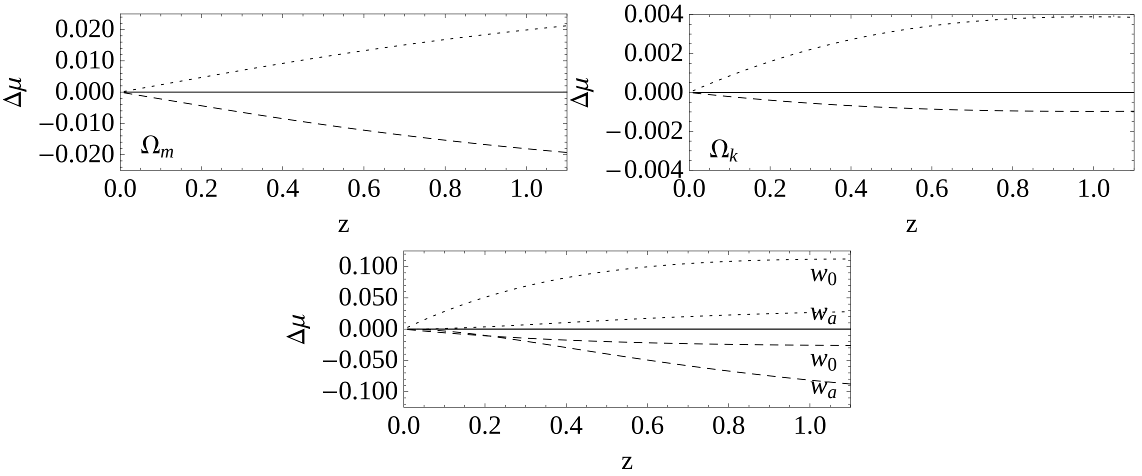

Figure 2.2: Deviation of the distance modulus with respect to the overall best-fit ΛCDM model. The dashed and dotted lines indicate upper and lower 1D-marginalized 68% confidence limits of the according parameters, respectively, while other parameters are fixed to their ΛCDM best-fit values.

where d_L is in units of Mpc. The unknown absolute magnitude M of the supernovae is a nuisance parameter in the fit and is degenerate with H_0. Hence supernovae measure relative distances within the set. In Fig. 2.1, we plot the prediction for the distance modulus from the overall best-fit model with respect to its counterpart from the best-fit ΛCDM model. The effect of varying parameters in the expansion history is illustrated in Fig. 2.2.

The acoustic peaks in the CMB and the measurement of the local Hubble constant additionally provide absolute distance probes, which complement the relative distance measure of the supernovae. For the Hubble constant, we utilize the SHOES measurement, $H_0 = 74.2 \pm 3.6 \text{ km s}^{-1} \text{ Mpc}^{-1}$, which employs Cepheid measurements to link the low-redshift supernovae to the distance scale established by the maser galaxy NGC 4258. In the analysis, we use the generalization of this measurement as a constraint on the inverse luminosity distance at $z_{\rm eff} = 0.04$, i.e., [167]

$$\begin{aligned} d_A\left(z_{\rm eff}\right)^{-1} &= \left(1+z_{\rm eff}\right) r\left(z_{\rm eff}\right)^{-1} \\ &= \left(1+z_{\rm eff}\right)^2 d_L\left(z_{\rm eff}\right)^{-1} \\ &\simeq (6.49 \pm 0.32) \times 10^{-3} \text{ Mpc}^{-1}, \end{aligned} \tag{2.19}$$

where d_A is the angular diameter distance and the fiducial cosmology is $h = 0.742$, $\Omega_{\rm m} = 0.3$, $\Omega_K = 0$, $w_0 = -1$, $w_a = 0$. Figure 2.3 demonstrates predictions for $d_A(z_{\rm eff})^{-1}$ and effects on the observable from varying parameters in the expansion history. The gray band corresponds to the 1σ region of the SHOES measurement, where the solid gray line indicates the mean value.

Further, we apply the BAO distance measurement of [168] that is obtained from analyzing the clustering of galaxies from the Sloan Digital Sky Survey (SDSS) [189] and the 2-degree Field Galaxy Redshift Survey (2dFGRS) [190], constraining the ratio

$$d_z \equiv \frac{r_{\rm s}\left(z_{\rm d}\right)}{d_V(z)} \equiv \frac{r_{\rm s}\left(z_{\rm d}\right) H(z)^{1/3}}{(1+z)^{2/3} d_A(z)^{2/3} z^{1/3}} \tag{2.20}$$

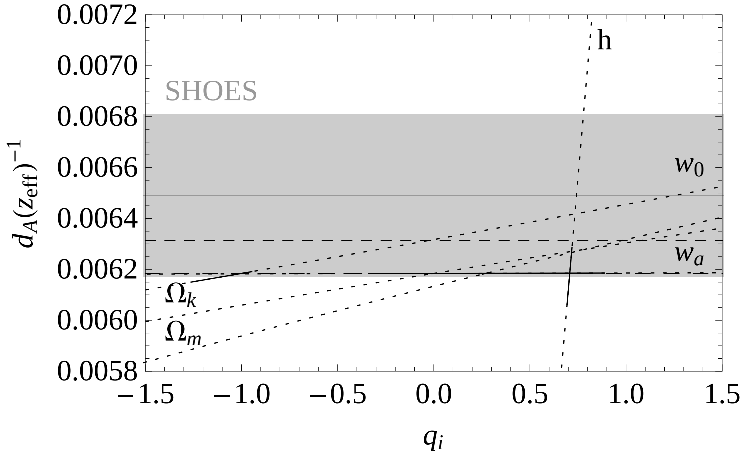

Figure 2.3: Inverse angular diameter distance $d_A\left(z_{\mathrm{eff}}=0.04\right)^{-1}$ for the parameters $q_i \in \{\Omega_{\mathrm{m}}, \Omega_K, h, w_0, w_a\}$. The solid segments of the curves correspond to the 1D-marginalized 68% confidence limits of the respective parameter. Only the according parameter is varied while other parameters are fixed to their best-fit ΛCDM values. The long-dashed line is the overall best-fit ΛCDM prediction and the dashed line corresponds to the prediction of the overall best-fit model. Note that due to the low effective redshift $z_{\mathrm{eff}}=0.04$, predictions for different values of w_a nearly overlap with the best-fit ΛCDM prediction. For Ω_{m} and Ω_K 1D-marginalized 68% confidence intervals are too narrow to be distinguishable in the plot, i.e., $\Omega_{\mathrm{m}} \in (0.255, 0.282)$ and $\Omega_K \in (-8.35 \times 10^{-3}, 2.10 \times 10^{-3})$, respectively.

at $z=0.2$ and $z=0.35$. Here $r_{\mathrm{s}}\left(z_{\mathrm{d}}\right)$ denotes the comoving sound horizon at the baryon drag epoch z_{d}. In Fig. 2.4, we plot predictions for d_z at $z=0.2$ and $z=0.35$ and effects on the observables from varying parameters in the expansion history. The gray bands correspond to the 1σ region of the BAO distance measurement, where the solid gray lines indicate the mean values.

These probes place tight constraints on the background parameters in Eq. (2.10) and help to identify sources for the growth of structure and break degeneracies.

The cosmic microwave background

The CMB probes the geometry of the background history as well as the formation of large-scale structure. The latter manifests itself on the largest scales through the ISW effect from the evolution of the gravitational potential. To predict these effects we connect our parametrization to the PPF formalism and utilize the PPF modifications to CAMB [191] implemented in [141]. We configure the PPF parameters as described in App. 2.1.A. This connection and the incorporation of the PPF formalism into a standard Einstein-Boltzmann linear theory solver yields an efficient way to obtain predictions from our parametrization for the CMB. It also prevents violations of energy-momentum conservation and avoids gauge artifacts in our results.

In Fig. 2.1.3.1, we plot the CMB angular temperature anisotropy power spectrum for the overall best-fit model with respect to the prediction of the best-fit ΛCDM model. Effects from varying chain parameters are illustrated in Figs. 2.6 and 2.7.

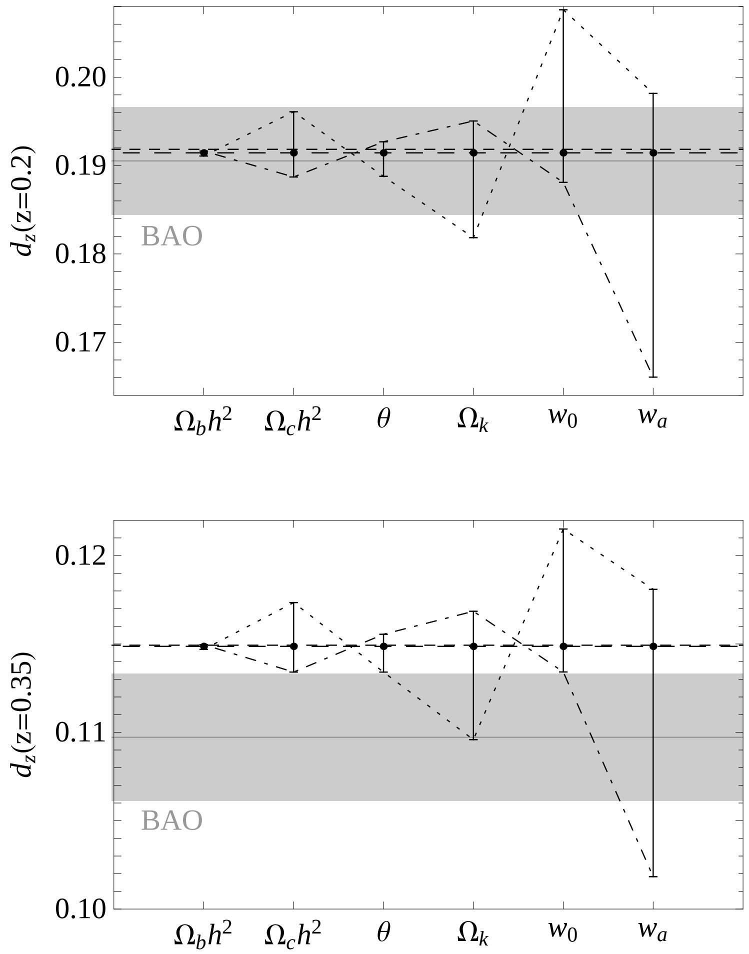

Figure 2.4: The ratio d_z of the BAO measurement at redshifts $z = 0.2$ (upper panel) and $z = 0.35$ (lower panel) for different parameter values. The horizontal dashed and long-dashed line corresponds to the overall best-fit model and best-fit ΛCDM prediction, respectively. They nearly overlap. The dot-dashed and dotted lines indicate upper and lower 1D-marginalized 68% confidence limits, respectively. These lines do not have any relevance in between the discrete parameter abscissae and only serve to indicate relative enhancement or suppression due to parameter variations with respect to the best-fit ΛCDM model.

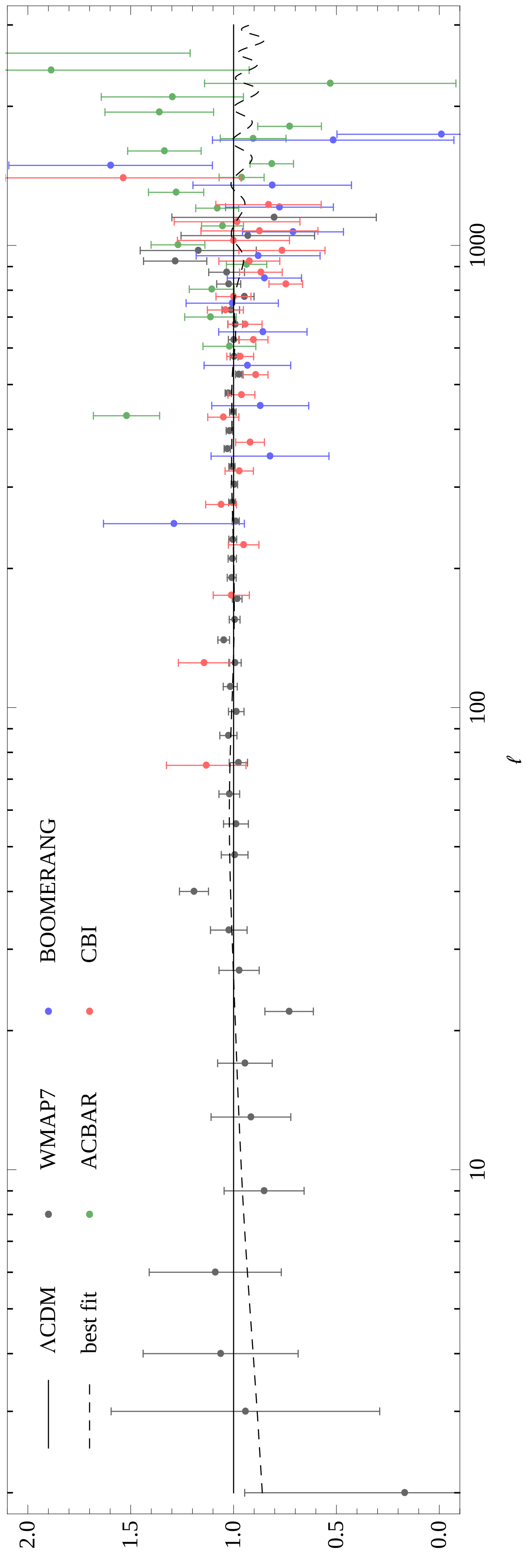

Figure 2.5: Ratio of the prediction of the CMB temperature anisotropy power spectrum of the overall best-fit model (dashed line) with respect to its best-fit ΛCDM counterpart.

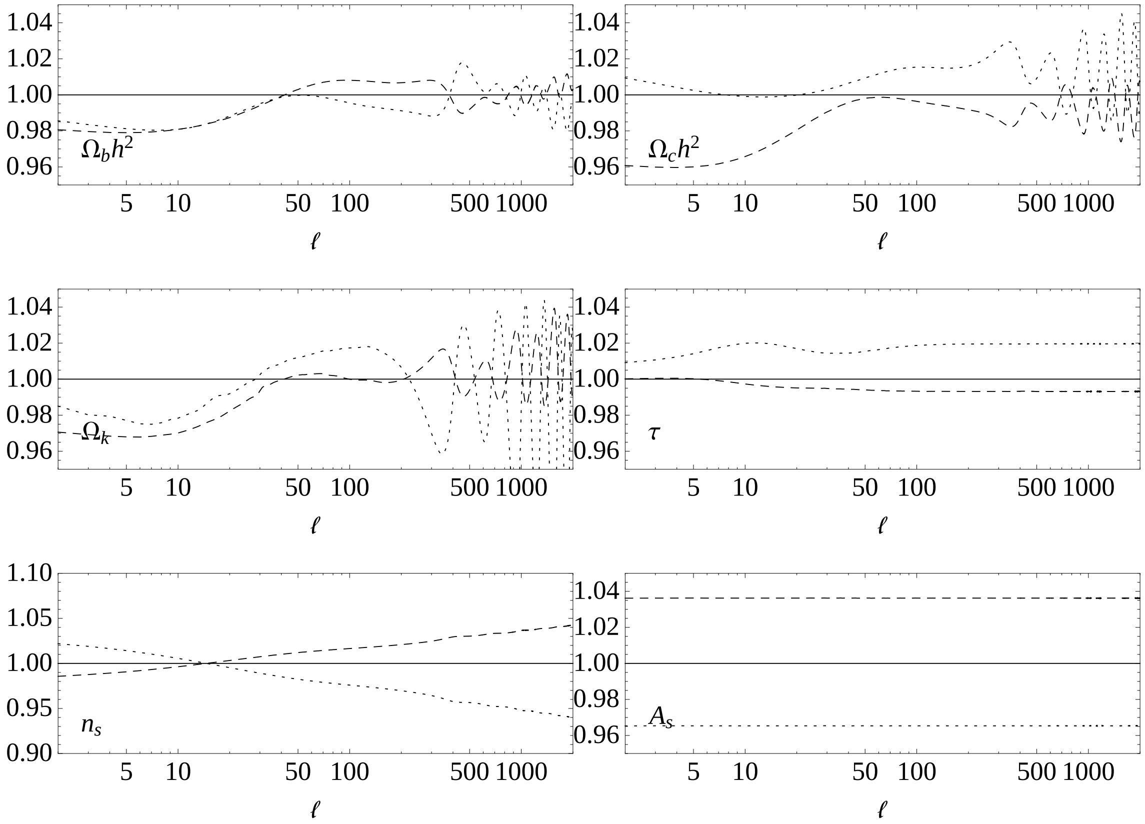

Figure 2.6: Ratio of the prediction of the 1D-marginalized 68% confidence limits of cosmological parameters with respect to the overall best-fit ΛCDM prediction for the CMB temperature anistropies. Only the respective parameter is varied. Other parameters are fixed to their best-fit ΛCDM values. Upper limits are indicated by dashed lines, lower limits by dotted lines. Oscillatory behavior at the acoustic peaks indicate shifts of peak position. Note that the first acoustic peak is located at $\ell \simeq 220$ and the second at $\ell \simeq 540$.

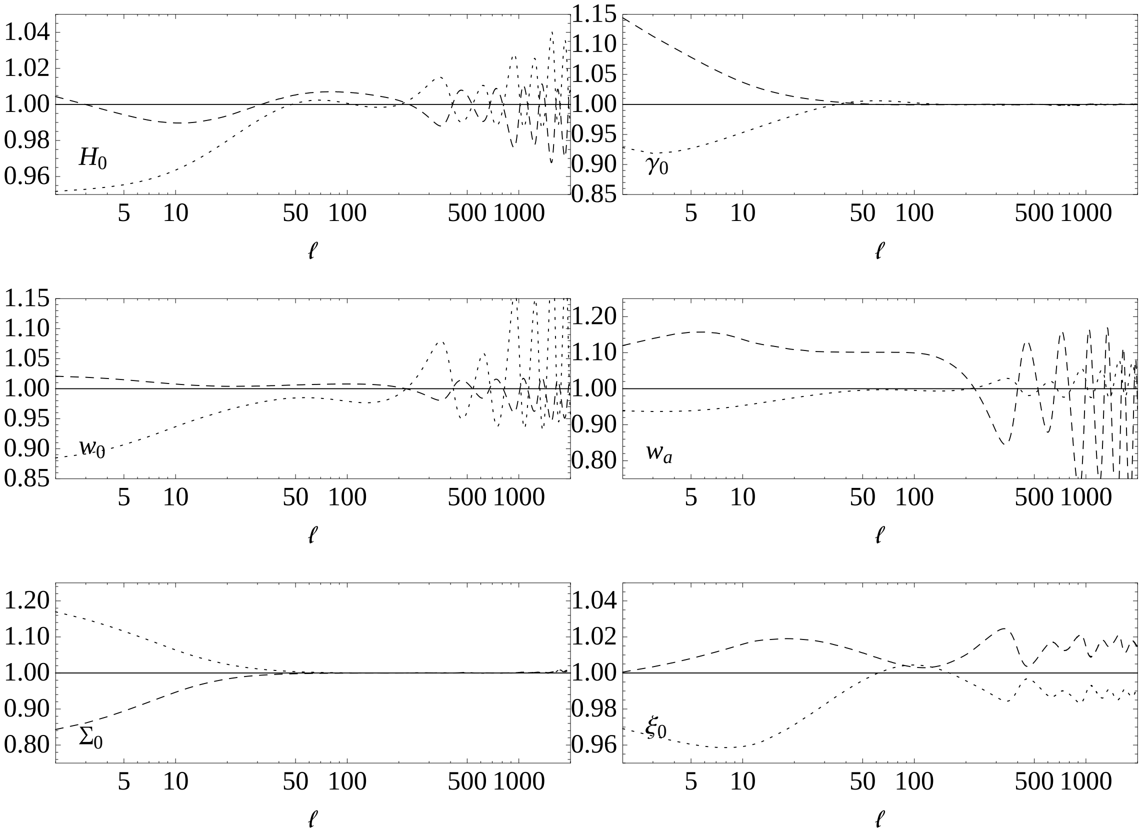

Figure 2.7: The same as in Fig. 2.6 for further parameters. Various degeneracies between parameters and sets of parameters are clearly identifiable.

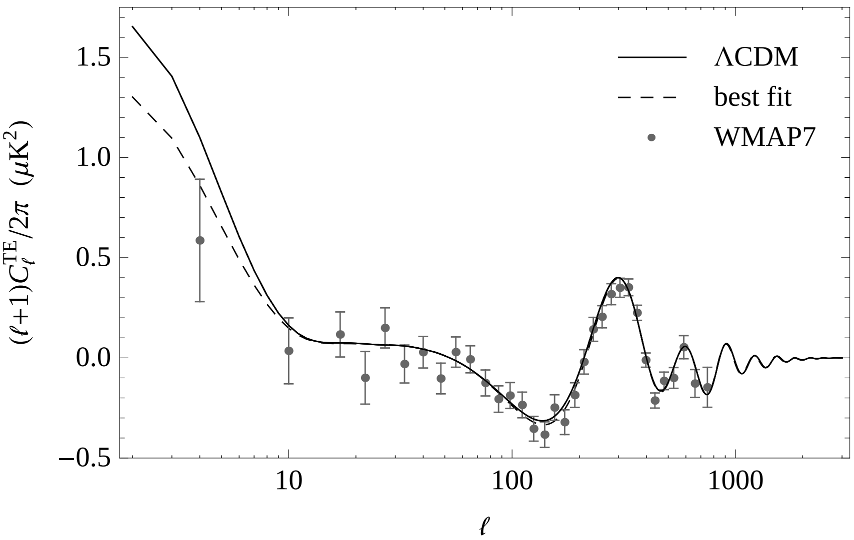

Figure 2.8: CMB temperature-polarization cross power spectrum of the overall best-fit model (dashed line) and the best-fit ΛCDM counterpart (solid line).

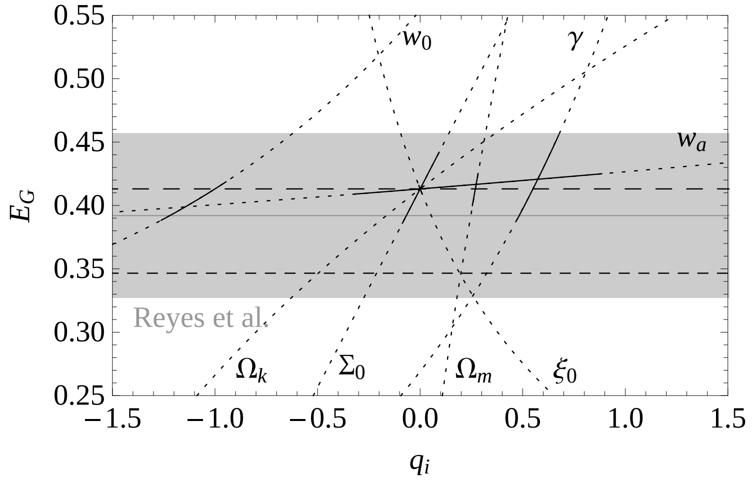

Figure 2.9: E_G at $z = 0.32$ for the parameters $q_i \in \{\Omega_\mathrm{m}, \Omega_K, \gamma_0, w_0, w_a, \Sigma_0, \xi_0\}$. The solid segments of the curves correspond to the 1D-marginalized 68% confidence limits of the respective parameter. Only the according parameter is varied. Other parameters are fixed to their best-fit ΛCDM values. The long-dashed line is the overall best-fit ΛCDM prediction and the dashed line indicates the overall best fit. For Ω_K and ξ_0, 1D-marginalized 68% confidence intervals are too narrow to be distinguishable in the plot, i.e., $\Omega_K \in (-8.35 \times 10^{-3}, 2.10 \times 10^{-3})$ and $\xi_0 \in (-6.41 \times 10^{-3}, 8.66 \times 10^{-3})$, respectively.

Figure 2.8 illustrates the CMB temperature-polarization (TE) cross power spectrum for ΛCDM and the overall best-fit model. The errors denote diagonal elements of the covariance matrix and include cosmic variance and instrumental noise. The overall best-fit model provides a better fit to all of the CMB data sets. This has to be attributed not only to the relative suppression of the power spectra at large scales with respect to the best-fit ΛCDM model but also to deviations at large angular multipoles.

Weak gravitational lensing and galaxy flows

The relationship of weak gravitational lensing around galaxies to their large-scale velocities has been proposed as a smoking gun of gravity [135]. The advantage of such a probe lies in its insensitivity to galaxy bias and initial matter fluctuations. The expectation value of the ratio of galaxy-galaxy to galaxy-velocity cross correlations of the same galaxies yields an estimator E_G [135]. We have

$$E_G \equiv \left[\frac{\nabla^2(\Psi - \Phi)}{3H_0^2 a^{-1} \frac{d\ln\Delta_\mathrm{m}}{d\ln a} \Delta_\mathrm{m}}\right]_{k=\frac{\ell}{\bar{\chi}}, \bar{z}} = \frac{\Omega_\mathrm{m}}{\Omega_\mathrm{m}(a)^\gamma} \frac{\Sigma}{1+\xi}. \tag{2.21}$$

Recently this quantity has been measured analyzing 70 205 luminous red galaxies (LRGs) [192] from the SDSS [193], yielding $E_G = 0.392 \pm 0.065$ [169] at the redshift $z = 0.32$ by averaging over scales $R = (10 - 50)h^{-1}$ Mpc.

Figure 2.9 illustrates predictions for E_G for different parameter values of $q_i \in \{\Omega_\mathrm{m}, \Omega_K, \gamma_0, w_0, w_a, \Sigma_0, \xi_0\}$, when varying only one parameter at a time and fixing

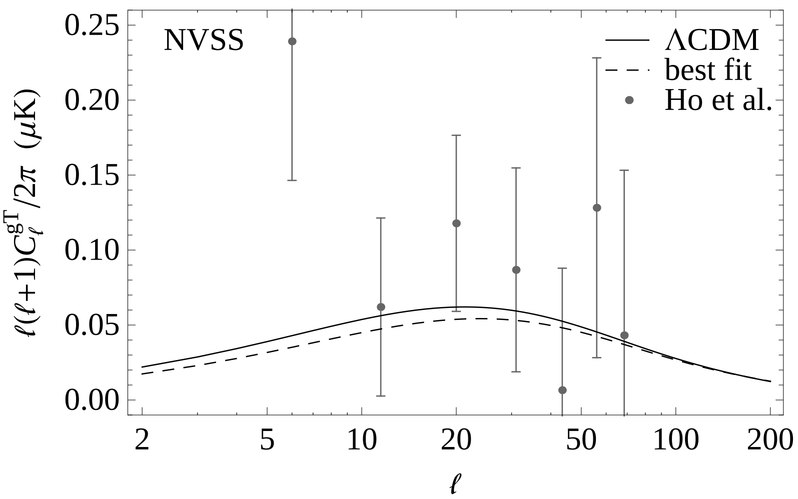

Figure 2.10: gISW cross correlations for the NVSS sample. The solid line is the prediction from the best-fit ΛCDM model, whereas the dashed line corresponds to its counterpart from the overall best-fit model.

the others to their overall best-fit ΛCDM values. 1D-marginalized 68% confidence limits are obtained from the MCMC analysis in Sec. 2.1.3.2. The gray shaded band corresponds to the 1σ region of the E_G measurement with the gray solid line being the mean value.

Galaxy-ISW cross correlations

The correlation between galaxy number densities and the CMB anisotropies can be used to isolate the ISW effect in the CMB and has proven to be a useful probe for constraining modifications to standard cosmology (see, e.g., [175, 187, 194, 195]). We utilize the publicly available ISWWLL code [142, 143], where we turn off weak lensing contributions to the likelihood, focusing only on the gISW constraints. The galaxies in this probe are collected from the Two Micron All Sky Survey (2MASS) extended source catalog (XSC) [196, 197], the LRG samples and photometric quasars (QSO) of the SDSS [198], and the National Radio Astronomy Observatory (NRAO) Very Large Array (VLA) Sky Survey (NVSS) [199] and correlated with the five-year WMAP [200] CMB anisotropies. The resulting 42 data points of gISW cross correlations are divided into nine galaxy sample bins j (2MASS0-3, LRG0-1, QSO0-1, and NVSS) based on flux (2MASS) or redshift (LRG and QSO). These data points are a selection of multipole bins from all samples, where the selection is based on the avoidance of nonlinearities and systematic effects from dust extinction, galaxy foregrounds, the thermal Sunyaev-Zel'dovich effect, and point source contamination to affect the gISW cross correlations [142].

We evaluate the gISW cross correlation in the Limber and quasistatic approximation, as it is done in the ISWWLL code used for the data analysis. The gISW cross

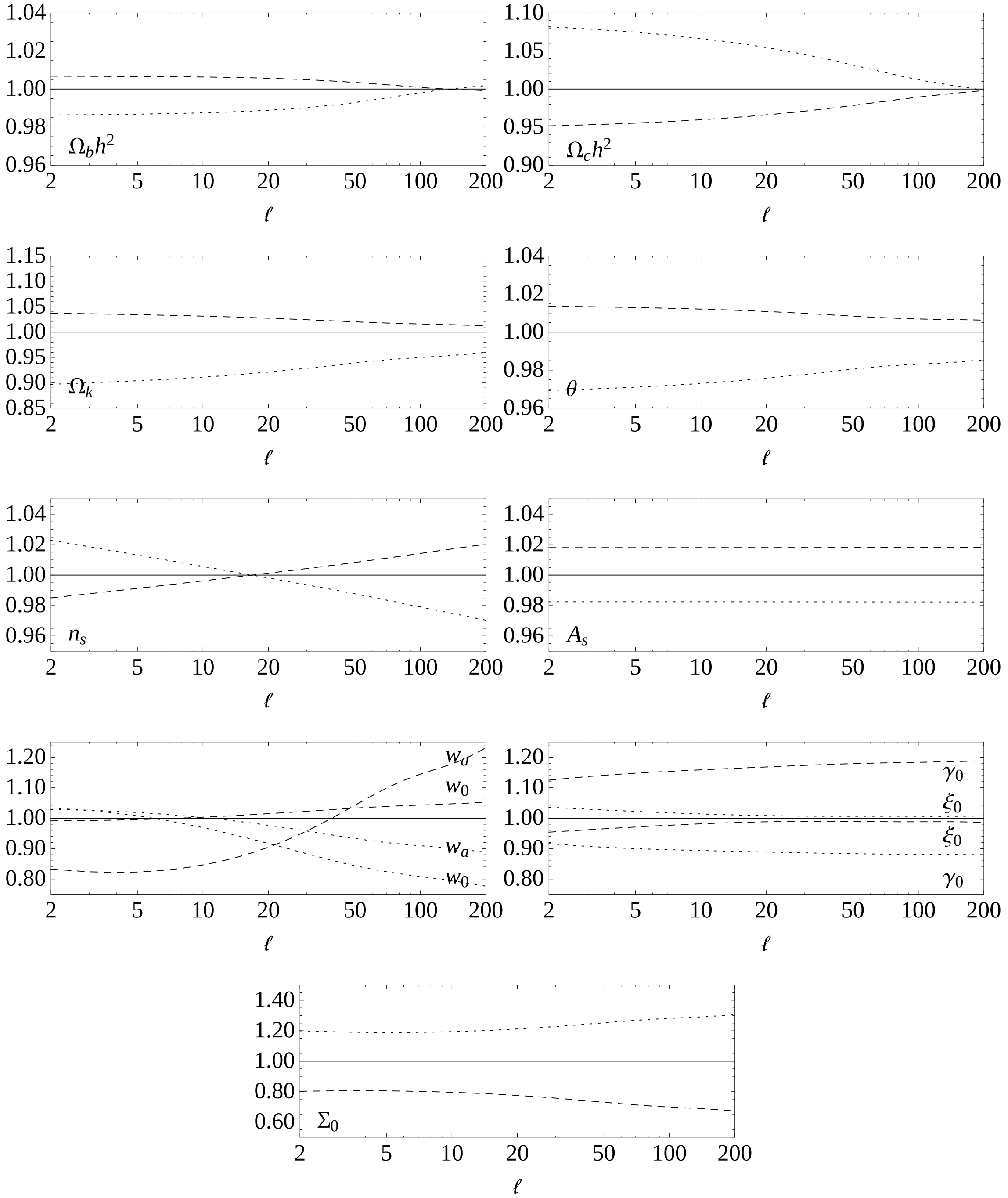

Figure 2.11: Ratio of the prediction of the 1D-marginalized 68% confidence limits of cosmological parameters with respect to the overall best-fit ΛCDM prediction for the gISW cross correlation in the NVSS sample. Other parameters are fixed to their best-fit ΛCDM values. Upper limits are indicated by dashed lines, lower limits by dotted lines.

correlation in this approximation reads

$$C_\ell^{g_j T} \simeq \frac{3\Omega_{\rm m} H_0^2 T_{\rm CMB}}{(\ell+1/2)^2} \int dz\, f_j(z) H(z) \left[D \frac{d}{dz} G\right] P \left[\frac{\ell+1/2}{\chi(z)}\right] . \qquad (2.22)$$

Here, $P(k)$ is the matter power spectrum today. D is the linear density growth rate defined by $\Delta_{\rm m}(k,z) = \Delta_{\rm m}(k,0) D/D|_{z=0}$ and $G = \Sigma\, D(1+z)/\Sigma_{\rm i}$ is the linear potential growth rate, where $\Sigma_{\rm i} = \Sigma|_{a=a_{\rm i}}$ and $a_{\rm i} \ll 1$.

In ΛCDM, the Limber approximation becomes accurate at the percent level for $\ell \gtrsim 10$ and drops approximately as ℓ^2 at higher ℓ (see, e.g., [201–203]). This condition is satisfied by about 90% of the total 42 data points that are used in the ISWWLL code. The approximation is also valid for, e.g., DGP and $f(R)$ gravity [175, 195]. Apart from the multipole ℓ, the error depends also on the width of the redshift distribution, which changes only little with modifications. Given the large errors of the currently available data points at low ℓ, we conclude that it is safe to apply the Limber approximation and furthermore that it is very useful since it is numerically faster than an exact integration.

The function $f_j(z)$ relates the matter density to the observed projected galaxy overdensity with $f_j(z) = b_j(z)\Pi_j(z)$ in the absence of magnification bias. $\Pi_j(z)$ is the redshift distribution of the galaxies and the bias $b_j(z)$ is assumed independent of scale (cf. [201]) but dependent on redshift.

The term in brackets in Eq. (2.22), parametrized by Eqs. (2.5) and (2.6), can be rewritten as

$$D \frac{d}{dz} G = \left\{ \left[1 - \Omega_{\rm m}(z)^\gamma (1+\xi)\right] \Sigma + (1+z) \frac{d\Sigma}{dz} \right\} D^2, \qquad (2.23)$$

where

$$D = \exp\left[- \int_0^z \frac{\Omega_{\rm m}(z)^\gamma (1+\xi)}{z+1} dz \right] . \qquad (2.24)$$

For SDSS quasars, the derivation of $f_j(z)$ involves the modified linear growth factor given through Eq. (2.23) and magnification bias, for which we use a modification of the lensing window function of [142]

$$W(z,z') = \frac{3\Sigma\, H_0^2 (1+z)}{2H(z)} r(z)^2 \left[\frac{d \ln r(z'')}{d\chi(z'')} \bigg|_{z'}^{z} \right] . \qquad (2.25)$$

Note that the gISW analysis uses photometric LRG samples, whereas the E_G measurement is based on spectroscopic LRG samples that do not overlap in redshift. Furthermore, the gISW signal is dominated by large scales and most of the error is caused by sampling variance and shot noise of galaxies. The error on E_G is dominated by uncertainties in lensing and redshift space distortions and most of the signal comes from small scales around $10h^{-1}$ Mpc. Therefore, we can safely neglect correlations between the gISW and E_G data sets.

We plot predictions from the overall best-fit model and the best-fit ΛCDM model for the gISW cross correlation in the NVSS sample in Fig. 2.10 and illustrate effects of varying the chain parameters in Fig. 2.11.

Parameter	*Flat*		*Nonflat*	
γ_0	0.57 ± 0.10	0.53	0.59 ± 0.10	0.60
$100\,\Omega_K$	$\cdots$		-0.32 ± 0.53	-0.81
γ_0	0.59 ± 0.11	0.56	0.62 ± 0.12	0.60
w_0	-1.10 ± 0.16	-1.12	-1.05 ± 0.18	-1.18
w_a	$(-0.19, 1.03)$	0.44	$(-0.79, 0.99)$	0.58
$100\,\Omega_K$	$\cdots$		-0.54 ± 0.77	-0.21
γ_0	0.57 ± 0.12	0.62	0.58 ± 0.11	0.60
$10\,\Sigma_0$	0.02 ± 0.93	0.12	-0.03 ± 0.95	0.24
$100\,\Omega_K$	$\cdots$		-0.30 ± 0.58	-0.30
γ_0	0.58 ± 0.10	0.57	0.60 ± 0.10	0.56
$100\,\xi_0$	0.11 ± 0.76	0.52	0.83 ± 1.08	0.47
$100\,\Omega_K$	$\cdots$		-0.73 ± 0.75	-0.59
γ_0	0.58 ± 0.12	0.55	0.60 ± 0.15	0.59
w_0	-1.11 ± 0.15	-1.13	-1.05 ± 0.18	-1.18
w_a	$(-0.99, 1.05)$	0.48	$(-0.78, 1.13)$	0.48
$10\,\Sigma_0$	0.09 ± 0.92	-0.08	-0.14 ± 0.94	-0.20
$100\,\Omega_K$	$\cdots$		-0.52 ± 0.93	-0.25
γ_0	0.57 ± 0.12	0.51	0.60 ± 0.11	0.56
$10\,\Sigma_0$	0.07 ± 0.97	-0.27	0.01 ± 0.94	0.18
$100\,\xi_0$	0.15 ± 0.80	0.33	0.79 ± 1.07	0.57
$100\,\Omega_K$	$\cdots$		-0.71 ± 0.77	-0.47
γ_0	0.60 ± 0.11	0.67	0.63 ± 0.12	0.60
w_0	$(-1.31, -1.03)$	-1.13	$(-1.30, -0.93)$	-1.29
w_a	$(0.36, 1.45)$	1.17	$(-0.46, 1.36)$	1.29
$100\,\xi_0$	$(-1.46, 3.17)$	10.06	$(-0.58, 2.16)$	3.72
$100\,\Omega_K$	$\cdots$		-0.64 ± 0.93	0.23
γ_0	0.60 ± 0.11	0.60	0.61 ± 0.13	0.66
w_0	$(-1.29, -1.01)$	-1.15	$(-1.30, -0.94)$	-1.24
w_a	$(0.37, 1.43)$	1.17	$(-0.37, 1.42)$	1.26
$10\,\Sigma_0$	0.27 ± 0.99	-0.38	0.06 ± 0.96	0.50
$100\,\xi_0$	$(-1.29, 3.14)$	6.33	$(-0.67, 2.35)$	7.19
$100\,\Omega_K$	$\cdots$		-0.54 ± 1.02	-0.41

Table 2.1: Mean, standard deviations, and best-fit values for the extra degrees of freedom in the $\gamma[w][\Sigma][\xi][K]$ models from using the WMAP7, ACBAR, B03, CBI, UNION2, BAO, SHOES, gISW, and E_G data sets. Values in brackets denote the 1D-marginalized 68% minimal credible intervals [204] quoted for parameter directions in the posterior distribution with distinctive skewness.

Parameter	ΛCDM		$\gamma w\xi$		(A)	
$100\,\Omega_{\mathrm{b}}h^2$	2.229 ± 0.050	2.244	2.237 ± 0.056	2.246	2.231 ± 0.056	2.196
$\Omega_{\mathrm{c}}h^2$	0.1114 ± 0.0030	0.1121	0.1066 ± 0.0075	0.0995	0.1058 ± 0.0077	0.0935
θ	1.0397 ± 0.0024	1.0406	1.0443 ± 0.0063	1.0510	1.0453 ± 0.0068	1.0560
τ	0.085 ± 0.014	0.087	0.086 ± 0.015	0.090	0.086 ± 0.015	0.091
n_{s}	0.960 ± 0.012	0.962	$(0.947, 0.991)$	1.016	$(0.948, 0.992)$	1.011
$\ln\,[10^{10}A_{\mathrm{s}}]$	3.199 ± 0.036	3.199	$(3.034, 3.270)$	2.810	$(3.009, 3.271)$	2.744
γ_0	...		0.60 ± 0.11	0.67	...	
w_0	...		$(-1.31, -1.03)$	-1.13	$(-1.29, -1.02)$	-1.07
w_a	...		$(0.36, 1.45)$	1.17	$(0.38, 1.47)$	1.09
$100\,\xi_0$	...		$(-1.46, 3.17)$	10.06	$(-1.42, 3.63)$	9.67
Ω_{m}	0.268 ± 0.014	0.269	0.258 ± 0.018	0.233	0.256 ± 0.019	0.224
σ_8	0.806 ± 0.021	0.812	0.779 ± 0.077	0.749	0.800 ± 0.063	0.769
H_0	70.6 ± 1.3	70.7	70.7 ± 1.7	72.3	70.7 ± 1.8	71.8

Table 2.2: The same as in Table 2.1, but for the ΛCDM, $\gamma w\xi$, and (A) models and including the basic cosmological parameters along with matter density, power spectrum normalization σ_8, and the Hubble constant.

Parameter	(B)		(C)		(C)*	
$100\,\Omega_{\mathrm{b}}h^2$	2.236 ± 0.056	2.230	2.229 ± 0.056	2.189	2.232 ± 0.055	2.201
$\Omega_{\mathrm{c}}h^2$	0.1097 ± 0.0059	0.1150	0.1041 ± 0.0073	0.0976	0.1023 ± 0.0067	0.0986
θ	1.0413 ± 0.0048	1.0395	$(1.0474, 1.0559)$	1.0550	1.0489 ± 0.0066	1.0544
τ	0.085 ± 0.014	0.086	0.086 ± 0.015	0.081	0.087 ± 0.014	0.085
n_{s}	0.963 ± 0.014	0.959	$(0.953, 1.002)$	0.996	$(0.970, 1.018)$	0.998
$\ln\,[10^{10}A_{\mathrm{s}}]$	3.179 ± 0.059	3.221	$(2.830, 2.958)$	2.841	$(2.775, 2.982)$	2.864
w_a	$(-0.23, 0.53)$	-0.20	...		...	
$100\,\xi_0$	$(-0.81, 1.41)$	-0.18	$(5.07, 7.64)$	7.88	$(4.19, 8.59)$	7.68
λ_0	...		$(0.31, 1.22)$	1.02	$(0.71, 1.25)$	1.02
Ω_{m}	0.267 ± 0.015	0.274	0.253 ± 0.021	0.227	0.248 ± 0.021	0.232
σ_8	0.809 ± 0.060	0.829	0.811 ± 0.062	0.818	0.788 ± 0.062	0.805
H_0	70.4 ± 1.7	70.9	70.7 ± 1.8	72.5	71.0 ± 2.0	72.0

Table 2.3: The same as in Table 2.1, but for the (B) and (C) models, where (C)* denotes the case where no gISW data are used. The best-fit values quoted here for the (C) model define the overall highest maximum-likelihood model found for the combination of all of the data sets studied in this paper and are used to derive predictions for illustrations in Sec. 2.1.3.1. For the (C) models, the 1D-marginalized minimal credible intervals correspond to the mode with larger mean likelihood.

Statistic	ΛCDM	$\gamma w\xi$	$\gamma w\xi K$	$\gamma w\Sigma\xi$	$\gamma w\Sigma\xi K$	(A)	(C)	*Others*	(C)*
$-2\Delta\ln\mathcal{L}_{\max}$	0	-5.2	-2.2	-3.8	-3.4	-4.9	-7.3	> -0.5	-6.8
$-2\Delta\langle\ln\mathcal{L}\rangle_{\mathrm{s}}$	0	0.9	2.9	2.2	3.4	0.0	-0.9	> 0	-2.9
$\overline{\langle\mathcal{L}\rangle_{\mathrm{s}}}$	1	2.6	0.6	1.0	0.6	2.3	6.5	< 1	11.3

Table 2.4: Comparison of the goodness of fit of the models with respect to ΛCDM, where $\ln\mathcal{L}_{\max}^{\Lambda\mathrm{CDM}} = -4049.6$, $\langle\ln\mathcal{L}_{\Lambda\mathrm{CDM}}\rangle_{\mathrm{s}} = -4052.8$, and $\ln\langle\mathcal{L}_{\Lambda\mathrm{CDM}}\rangle_{\mathrm{s}} = -4051.9$. $\overline{\langle\mathcal{L}\rangle_{\mathrm{s}}} > 1$ suggests that the adoption of the extra parameters might be justified. (C)* denotes the case where no gISW data are used.

2.1.3.2. MCMC likelihood analysis

We turn to the likelihood analysis of the cosmological parameter space. As our elementary set of parameters we use $\mathcal{C} = \{\Omega_\mathrm{b}h^2, \Omega_\mathrm{c}h^2, \theta, \tau, n_\mathrm{s}, \ln\left[10^{10}A_\mathrm{s}\right], \gamma_0\}$, where for the concordance model $\mathcal{C}_{\Lambda\mathrm{CDM}} \approx \mathcal{C} \cap \{\gamma_0 = 0.55\}$. We implement the following flat priors: $\Omega_\mathrm{b}h^2 \in (0.01, 0.1)$, $\Omega_\mathrm{c}h^2 \in (0.045, 0.99)$, $\theta \in (0.5, 10)$, $\tau \in (0.01, 0.8)$, $n_\mathrm{s} \in (0.5, 1.5)$, $\ln\left[10^{10}A_\mathrm{s}\right] \in (2.7, 4)$, and $\gamma_0 \in (-5, 5)$.[2] In addition we use all the sets of combinations between the phenomenological parameters and spatial curvature $p_i \in \mathcal{P}$, where $\mathcal{P} = \{W, \Sigma_0, \xi_0, \Omega_K\}$ and $W = \{w_0, w_a\}$, being free and taking on their ΛCDM values $\{w_0 = -1, w_a = 0, \Sigma_0 = 0, \xi_0 = 0, \Omega_K = 0\}$. We assign the following flat priors to them: $w_0 \in (-5, 5)$, $w_a \in (-10, 10)$, $\Sigma_0 \in (-5, 5)$, $\xi_0 \in (-0.5, 0.5)$, and $\Omega_K \in (-0.3, 0.3)$. As starting centers for $p_i \in \mathcal{P}$ we use the ΛCDM values. For the (C) model, we use $\lambda_0 \in (-20, 20)$ with starting center $\lambda_0 = 0.5$.

The COSMOMC package employs the Metropolis-Hastings algorithm [205, 206] for the sampling and the Gelman and Rubin statistic R [207] for testing the convergence. We require $R - 1 < 0.01$ for our runs with two or fewer extra degrees of freedom and $R - 1 < 0.02$ for three or more extra degrees of freedom.[3]

The chain samples are used to infer marginalized probabilities and mean likelihoods of the posterior. The marginalized distribution is obtained from projecting the samples to the reduced dimensions of a subspace, ignoring information about the goodness of fit and skewness of the distribution in the marginalized directions. Averaging the likelihood for each point of a subspace produces the mean likelihood. If the two curves do not overlap, the distribution is not Gaussian or the priors are not flat. It is important to note that in this case, marginalized probabilities may be amplified due to a larger parameter volume rather than by a better fit to the data. Furthermore, for skew distributions, we quote our 1D-marginalized constraints in terms of minimal credible intervals [204] rather than by marginalized confidence limits. The former indicate where the tails occupy equal fractions of the probability distribution, whereas the latter are constructed in such a way that any point inside of the interval has a larger posterior than a point outside of it, being the more meaningful selection in the case of skew or multimodal distributions.

We summarize our results in Table 2.1 through 2.4. For comparison of the goodness of fit between the different models, we quote

$$
\begin{aligned}
-2\Delta\ln\mathcal{L}_\mathrm{max} &= 2\ln\left(\mathcal{L}_\mathrm{max}^{\Lambda\mathrm{CDM}}/\mathcal{L}_\mathrm{max}\right), && (2.26)\\
-2\Delta\langle\ln\mathcal{L}\rangle_\mathrm{s} &= 2\left(\langle\ln\mathcal{L}_{\Lambda\mathrm{CDM}}\rangle_\mathrm{s} - \langle\ln\mathcal{L}\rangle_\mathrm{s}\right), && (2.27)\\
\overline{\langle\mathcal{L}\rangle_\mathrm{s}} &= \langle\mathcal{L}\rangle_\mathrm{s}/\langle\mathcal{L}_{\Lambda\mathrm{CDM}}\rangle_\mathrm{s} && (2.28)
\end{aligned}
$$

in Table 2.4, where $\mathcal{L}_\mathrm{max}$ is the maximum likelihood of a model and $\langle\cdot\rangle_\mathrm{s}$ denotes the average over the Monte-Carlo samples. Note that MCMC sampling may not provide very accurate best-fit estimates (see, e.g., [188]). The best-fit values may also have a much higher likelihood than the mean, but simultaneously be confined to a very

---

[2] Parameter constraints on $\ln\left[10^{10}A_\mathrm{s}\right]$ are close to its prior boundary, suggesting a non-negligible influence of the prior. We have checked that using a flat top-hat prior with the lower boundary set at 2 instead of 2.7 does not alter our results in a significant manner.

[3] Note that the $\gamma w\Sigma\xi[K]$ models did not acquire the desired accuracy and reached only a convergence of $R - 1 \lesssim 0.1$.

small region of the parameter space. We also give the mean likelihood of the samples $\overline{\langle \mathcal{L} \rangle_{\rm s}}$, which corresponds to taking the posterior distribution as prior in calculating the evidence and in contrary to the maximum likelihood is a quantity that penalizes fine-tuning. If $\overline{\langle \mathcal{L} \rangle_{\rm s}}$ is greater than unity, this usually suggests that, on average, the extra parameters improve the goodness of fit to the data. This, however, has to be interpreted only as a rule of thumb (see, e.g., [188]). We only give constraints on the parameters $c_i \in C \backslash \{\gamma_0\}$ for the $\gamma w \xi$, (A), (B), and (C) models in addition to ΛCDM (see Tables 2.1 through 2.3). These models, except for the (B) model, exhibit an improved goodness of fit in terms of maximum and averaged likelihoods over the ΛCDM model. We numerically evaluate Eqs. (2.26) through (2.28) and quote the numbers for the $\gamma w[\Sigma]\xi[K]$, (A), and (C) models in Table 2.4. For all other models, $\overline{\langle \mathcal{L} \rangle_{\rm s}}$ is smaller than unity, $-2\Delta\langle \ln \mathcal{L}\rangle_{\rm s}$ is positive, and $-2\Delta \ln \mathcal{L}_{\rm max} > -0.5$.

Under the assumptions made in Sec. 2.1.2.1, our results show that constraints on the growth index parameter γ_0 are only weakly affected by the introduction of the other extra degrees of freedom with consistency of ΛCDM, i.e., $\gamma_0 \approx 0.55$, at the 68% confidence level. The constraints on γ_0 are dominated by the gISW data and are competitive to existing results in the literature derived from linear and nonlinear probes (cf., e.g., [170, 172, 187, 208]).

In every scenario studied here, the standard values of all extra parameters, corresponding to the concordance model, lie within their 1D-marginalized 95% confidence limits. Thus, we conclude that the ΛCDM model is consistent with the joint set of WMAP7, ACBAR, B03, CBI, UNION2, BAO, SHOES, gISW, and E_G data under the assumption of the existence of extra degrees of freedom of the kind described in Sec. 2.1.2.1 and form of priors given above. Note that constraints on a parameter direction depend a lot on the prior assumed for it or for the parameters used to derive it (see, e.g., [188]). Identifying adequate priors on extra degrees of freedom in the gravitational dynamics based on theoretical contemplations is the object of current research (see, e.g., [146, 209]).

For the maximum-likelihood ΛCDM model we obtain a fit of $-2 \ln \mathcal{L}_{\rm max}^{\Lambda\rm CDM} = 8099.3$ using all of the data described above. The overall best-fit to the data was obtained in the chains of model (C) with $-2\Delta \ln \mathcal{L}_{\rm max} = -7.3$ with respect to the best-fit ΛCDM model. Note that in principle the best-fit values of model (C) are also contained in the parameter spaces of the $\gamma w[\Sigma]\xi[K]$ and (A) models. The fact that none of these models accessed the best-fit point can be attributed to sampling errors in the chains. However, for the maximum-likelihood values of the $\gamma w[\Sigma]\xi[K]$ and (A) models, we also obtain increases in fit of $-2\Delta \ln \mathcal{L}_{\rm max} \lesssim -2$ over the best-fit ΛCDM model (see Table 2.4). In terms of p values this translates to 3%, 18%, and 27% for consistency with ΛCDM in the (C), (A), and $\gamma w \xi$ scenarios, respectively, where for all other models this number is greater than 50%. However, several best-fit parameter values of the $\gamma w[\Sigma]\xi[K]$, (A), and (C) models lie beyond their corresponding 1D-marginalized 68% confidence limits. In the case of, e.g., the $\gamma w \xi$ model with parameter space $\mathcal{C} \cup \{w_0, w_a, \xi_0\}$, the best fit of ξ_0 lies even beyond the 1D-marginalized 99% confidence level, indicating that the best-fit model occupies only a very small subspace of the parameter space.

Remarkably, this increase in maximum likelihood ($\Delta\chi^2_{\rm max} \lesssim -2$) seems to appear only in cases where we allow a free, positive, ξ_0, phantom crossing in $w_{\rm DE}$, and $w_0 \approx$

$-w_a$, i.e., an effective dark energy equation of state that drives toward a matterlike equation of state at early times. We further observe that in these scenarios, there is no signature of $n_{\mathrm{s}} \neq 1$. Quite to the contrary, the overall best fit obtained in model (C), i.e., $n_{\mathrm{s}} = 0.996$, portrays an almost perfect scale-invariant Harrison-Zel'dovich spectrum [210, 211]. Moreover, we observe a slight preference for smaller dark matter densities, smaller amplitudes for the primordial superhorizon power of the curvature perturbation, and larger ratios of sound horizon to angular diameter distance at recombination with respect to parameter values inferred for the concordance model. If we additionally assume a flat universe and matter density perturbations that relate to lensing potentials as in ΛCDM, i.e., $\Sigma_0 = 0$, these scenarios induce values for $\overline{\langle \mathcal{L} \rangle_{\mathrm{s}}}$ beyond unity, suggesting an increase of the goodness of fit through the inclusion of their extra parameters.

The increase in maximum likelihood observed for models with $\xi_0 > 0$ and $w_a \approx -w_0 > 1$ is mainly attributed to slightly better fits of the CMB anisotropy data on all scales and to a smaller extent also to marginally better fits in distance measures, as can be perceived from the figures in Sec. 2.1.3.1. Merely the gISW data counteracts this trend in favor of ΛCDM and when removed from the joint data set for, e.g., the (C) model, here denoted by (C)*, we obtain the most extreme values for our statistics, Eqs. (2.26) through (2.28) (see Table 2.4), while ΛCDM parameter values remain consistent at the 95% confidence level (cf. Table 2.3).

Figures 2.12 and 2.13 show the marginalized likelihoods for the extra parameters and the parameters that exhibit a distinctive skewness or multiple modes in the case of the $\gamma w \xi$ and (C) model, respectively. In Fig. 2.14, we plot 2D-marginalized contours of the extra parameters w_0, w_a, γ_0, and ξ_0 within the $\gamma w \xi$ model. We also indicate the 1D-marginalized minimal credible intervals on λ_0 and ξ_0 obtained in model (C). Note that the best-fit points lie outside the 2D-marginalized 68% confidence level contours of ξ_0 and γ_0, as well as of ξ_0 and w_a, which is due to the fact that the best-fit model occupies only a small parameter subspace and a distinctive skewness of the posterior distribution in the parameter directions. Note that there is a strong degeneracy between the parameters ξ_0 and w_a as we expected from Eq. (2.6). Figure 2.15 illustrates the overall best-fit parameter values from model (C) and $\gamma w \xi$ for the modifications in the dark energy equation of state $w_{\mathrm{DE}}(a)$, the factor $\mathcal{F}$ that enters the ordinary differential equation of quasistatic matter overdensity perturbations, the scaling of the effective Newton's constant Q, and η that modifies the ratio of the scalar potentials. Also shown are the standard values for these quantities.

We find consistency of the ΛCDM values at the 95% confidence level for all extra parameters in all scenarios. We, therefore, do not claim detection of nonstandard cosmological effects or the necessity of extra degrees of freedom based on the increases in the maximum and mean likelihoods (see Table 2.4). This would require a physically better-motivated model with well-understood priors and a more sophisticated analysis of the goodness of fit with, e.g., efficient exploration of the different modes and determination of the Bayes factor for model comparison (see, e.g., [212–215]). Note that even for a hypothetical, theoretically well-motivated model that would naturally access the best-fit region in the parameter space, there would only be a moderate preference over the concordance model, i.e., $\Delta\chi^2_{\max} \simeq -7$. It is not clear

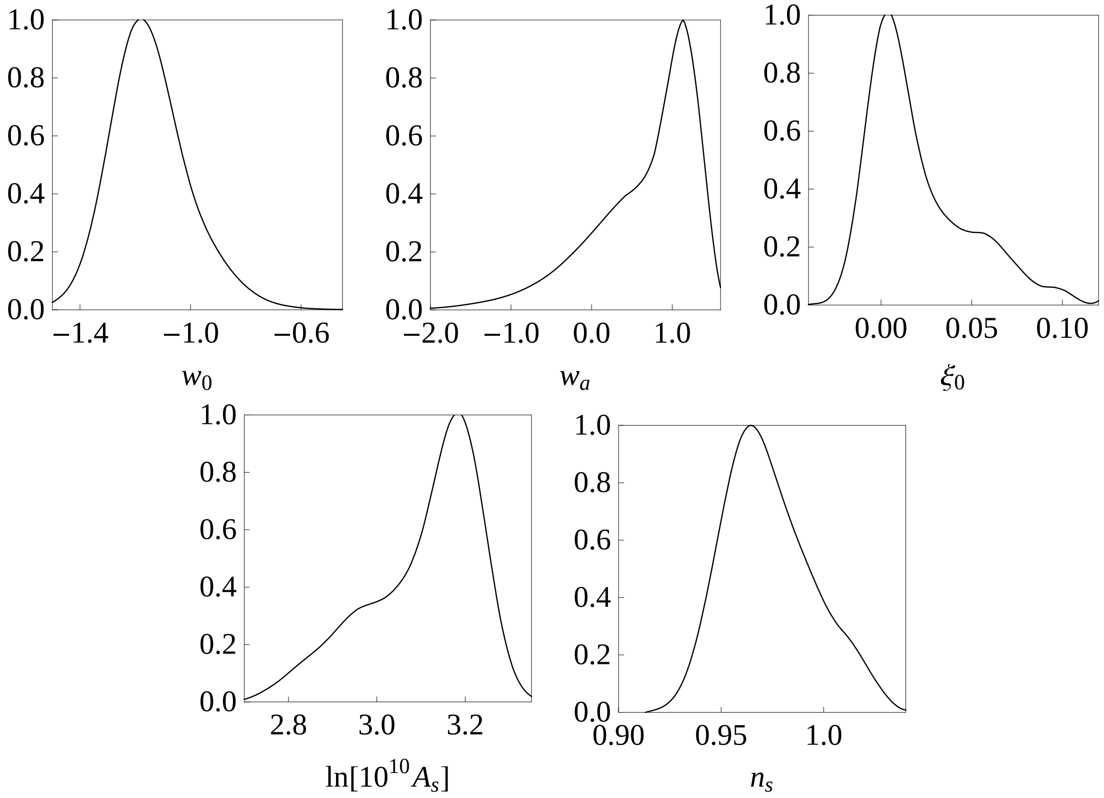

Figure 2.12: Marginalized likelihoods for different parameters of the $\gamma w \xi$ model that exhibit skew distributions.

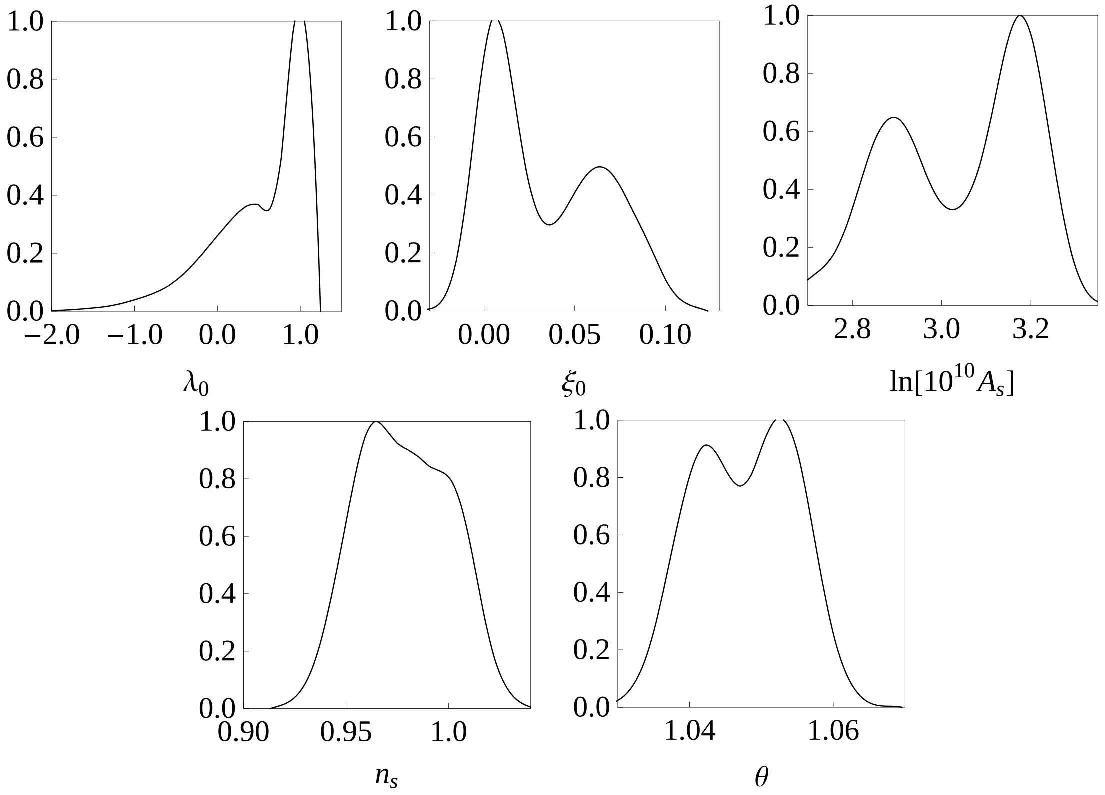

Figure 2.13: The same as Fig. 2.12 but for the (C) model. The posterior distribution is bimodal.

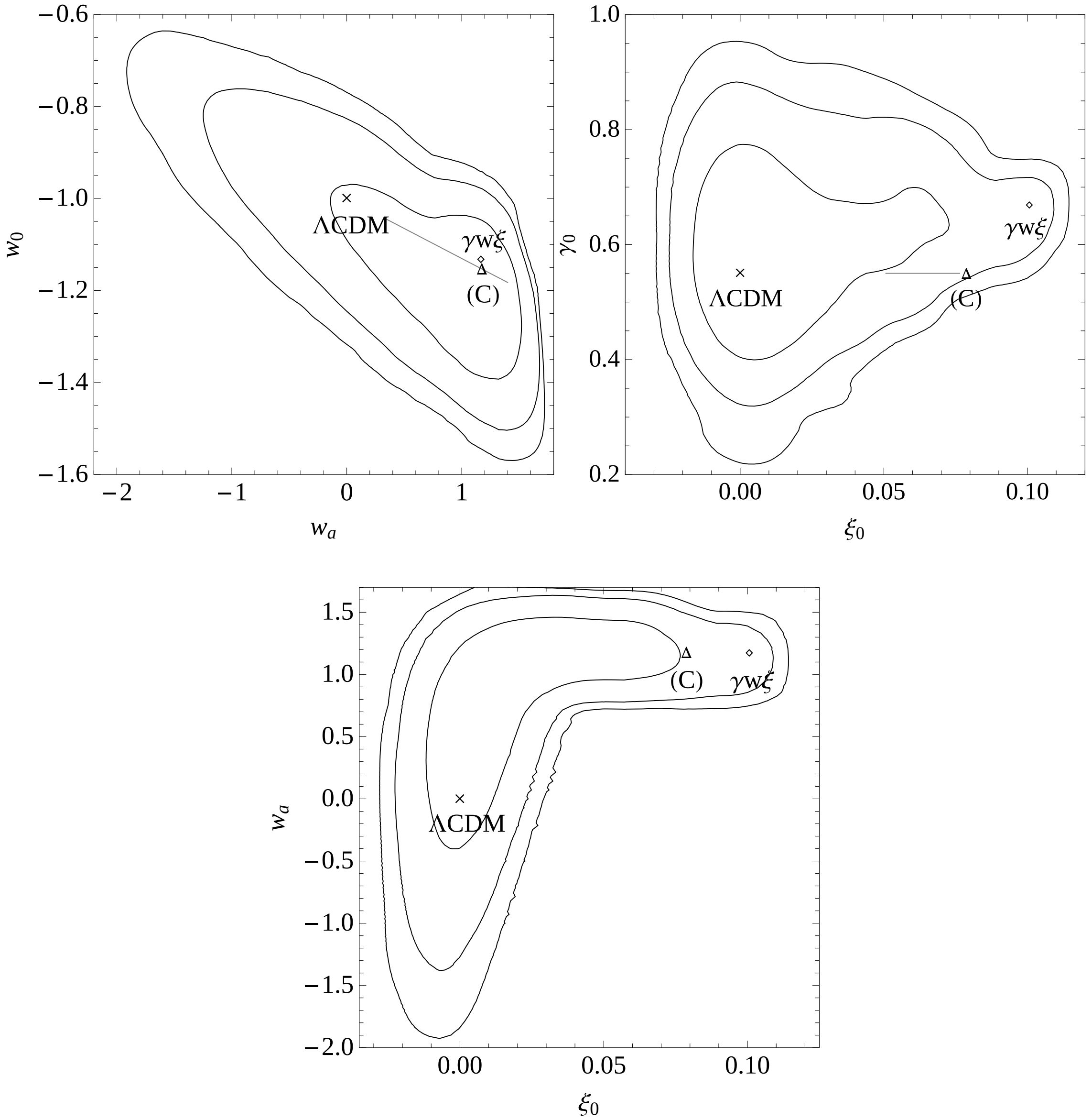

Figure 2.14: 2D-marginalized contours for the background parameters (w_a, w_0) (upper left panel), the growth rate parameters (ξ_0, γ_0) (upper right panel), and (ξ_0, w_a) (lower panel), respectively. The boundaries indicate the 68%, 95%, and 99% confidence limits, respectively. Also shown are the best-fit values for the ΛCDM, $\gamma w \xi$, and (C) models. The solid gray line indicates the 1D-marginalized 68% minimal credible interval for λ_0 (upper left panel) and ξ_0 (upper right panel), respectively.

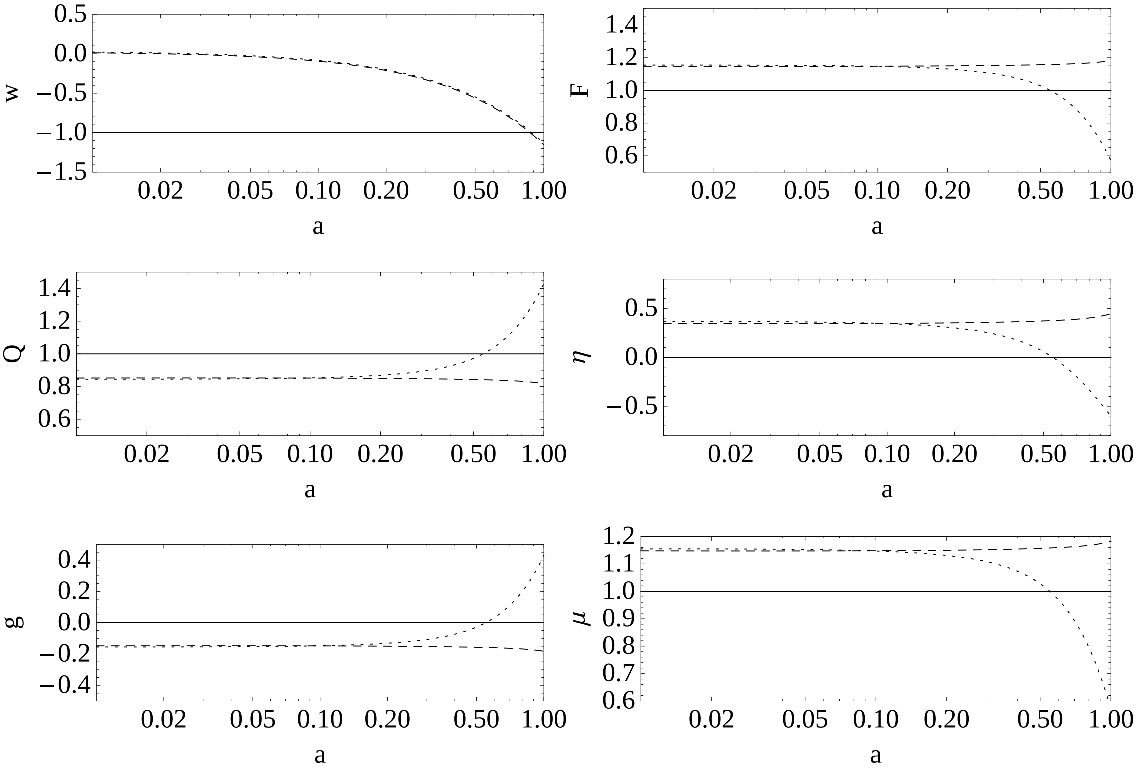

Figure 2.15: Best-fit predictions for the parameters that quantify departures from the concordance model (see Sec. 2.1.2) in the $\gamma w \xi$ (dotted lines) and (C) (dashed lines) models. Solid lines indicate the ΛCDM predictions. We also show predictions for the metric ratio $g = -\eta/(\eta+2)$ [138] and the parameter $\mu = Q(1+\eta)$ [146]. Note that $w_{\mathrm{DE}}(a)$ approaches a matterlike equation of state at early times. Predictions for $w_{\mathrm{DE}}(a)$ from the $\gamma w \xi$ and (C) models overlap.

if such a model exists or may be developed, but we emphasize that we may *a priori* be excluding viable departures from the concordance model when constraining supplementary parameters for the background and growth of structure separately.

2.1.4. Discussion

We allowed departures from the concordance model by introducing six additional degrees of freedom parametrizing a time-dependent effective dark energy equation of state, modifications of the Poisson equation for the lensing potential, and modifications of the growth of linear matter density perturbations, as well as spatial curvature. We constrained alternate combinations of these parameters by performing MCMC likelihood analyses on cosmological data amenable to linear perturbation theory. In particular, we utilized all of the CMB data, including the lowest multipoles, its correlation with galaxies and the comparison of weak lensing to large-scale velocities in addition to geometrical probes from supernovae and BAO distances, as well as from the Hubble constant.

We find consistency of the concordance model at the 95% confidence level. For specific combinations of the supplementary free parameters, we, however, find an increase in the maximum likelihood of up to $\Delta\chi^2_{\mathrm{max}} \simeq -7$ over the maximum-likelihood ΛCDM model in the joint data. We observe that this increase in maximum likelihood only appears in cases where we allow a free, positive, ξ_0, phantom crossing in $w_{\mathrm{DE}}(a)$, and $w_0 \approx -w_a$, i.e., an effective dark energy equation of state that drives toward a matterlike equation of state at early times. Moreover, we find that in these scenarios there is no preference for $n_{\mathrm{s}} \neq 1$. For scenarios where we adopt the assumptions of a flat universe and a standard relation of matter density perturbations to lensing potentials, both maximum and mean likelihoods are greater than in ΛCDM, with a maximal ratio of mean likelihoods of the samples of $\overline{\langle\mathcal{L}\rangle}_{\mathrm{s}} \simeq 6$, suggesting that the introduction of their extra parameters might be justified. The increase in maximum likelihood can be attributed to better fits of the CMB anisotropy data on all scales and to a smaller extent also to better fits in distance measures. We therefore expect future CMB data from, e.g., the Planck mission [216] to yield more decisive constraints on our modifications (cf., e.g., [217]). The gISW data sets counteract this trend in favor of the ΛCDM model and when removed, we obtain $\Delta\chi^2_{\mathrm{max}} \simeq -7$ and $\overline{\langle\mathcal{L}\rangle}_{\mathrm{s}} \simeq 11$ for the (C) model.

Given the consistency of ΛCDM parameter values with their marginalized constraints, also under removal of gISW data, and the lack of a better-motivated theory and priors, we do, however, not claim detection of nonstandard cosmological effects or the necessity of the introduction of extra degrees of freedom, but we emphasize that when constraining the background parameters and growth parameters separately, we may *a priori* be excluding viable departures from ΛCDM. We leave the search for a well-motivated model that matches the above requirements and the analysis of its performance in confrontation with new data, as well as the study of effects from scale-dependent deviations from the concordance model on our results to future work. We also point out that more sophisticated sampling methods may significantly improve our statistical analysis and offer more information through efficient exploration of the different modes and the determination of the Bayes factor for model comparison.

Acknowledgments

I thank Uroš Seljak, Anže Slosar, Tristan Smith, Eric Linder, David Rapetti, Scott Daniel, Dragan Huterer, and Gregory Martinez for useful discussions and comments. Computational resources were provided on the Schrödinger and zBox2 supercomputers at the University of Zurich. This work was supported by the Swiss National Foundation under Contract No. 2000_124835/1.

2.1.A. Connecting our parametrization to the linear PPF framework

Given the expansion history, the PPF framework [138, 140] is defined by three functions and one parameter. From these quantities, the dynamics are determined by conservation of energy and momentum and the Bianchi identities. The defining quantities are $g(a, k)$, which quantifies the effective anisotropic stress of the modifications and distinguishes the two gravitational potentials, $f_\zeta(a)$, which describes the relationship between the matter and the metric on superhorizon scales, and $f_G(a)$, which defines it in the linearized Newtonian regime. The additional parameter c_Γ is the transition scale between the superhorizon and Newtonian behaviors.

From the relations defined in Sec. 2.1.2, we infer $g = -\eta/(\eta + 2) = 1 - \mathcal{F}/\Sigma$ and $f_G = (1 - \Sigma)/\Sigma$ in the quasistatic regime. At superhorizon scales, we impose $f_\zeta = 0$ and we set the transition at the horizon, $c_\Gamma = 1$. Given that $g \to 0$ sufficiently fast for $a \ll 1$, if $|\xi| \ll 1$ and $\Sigma \to 1$, we apply the relation $g = 1 - \mathcal{F}/\Sigma$ to all scales.

We implement these relations and the definitions in Sec. 2.1.2 into the PPF modified CAMB code [141]. This procedure produces the correct power spectra for ΛCDM and self-accelerating DGP gravity. The latter, however, only when restricting to its subhorizon effects. In connecting our parametrization to the PPF linear theory, we can take advantage of a fully consistent framework for modifications in the gravitational dynamics. In this way, we can also prevent implicit violations of the conservation of energy and momentum and avoid gauge artifacts in our parametrization.

References

[125] Supernova Search Team, A. G. Riess *et al.*, “Observational Evidence from Supernovae for an Accelerating Universe and a Cosmological Constant”, Astron. J. **116**, 1009 (1998), [arXiv:astro-ph/9805201].

[126] Supernova Cosmology Project, S. Perlmutter *et al.*, “Measurements of Omega and Lambda from 42 High-Redshift Supernovae”, Astrophys. J. **517**, 565 (1999), [arXiv:astro-ph/9812133].

[127] S. Tsujikawa, “Dark energy: investigation and modeling”, (2010), [arXiv:1004.1493].

[128] B. Jain and J. Khoury, “Cosmological Tests of Gravity”, Annals Phys. **325**, 1479 (2010), [arXiv:1004.3294].

[129] D. Sapone, “Dark Energy in Practice”, Int. J. Mod. Phys. **A25**, 5253 (2010), [arXiv:1006.5694].

[130] M. Chevallier and D. Polarski, “Accelerating universes with scaling dark matter”, Int. J. Mod. Phys. **D10**, 213 (2001), [arXiv:gr-qc/0009008].

[131] E. V. Linder, “Exploring the expansion history of the universe”, Phys. Rev. Lett. **90**, 091301 (2003), [arXiv:astro-ph/0208512].

[132] E. V. Linder, “Cosmic growth history and expansion history”, Phys. Rev. **D72**, 043529 (2005), [arXiv:astro-ph/0507263].

[133] T. Koivisto and D. F. Mota, “Dark Energy Anisotropic Stress and Large Scale Structure Formation”, Phys. Rev. **D73**, 083502 (2006), [arXiv:astro-ph/0512135].

[134] R. Caldwell, A. Cooray, and A. Melchiorri, “Constraints on a New Post-General Relativity Cosmological Parameter”, Phys. Rev. **D76**, 023507 (2007), [arXiv:astro-ph/0703375].

[135] P. Zhang, M. Liguori, R. Bean, and S. Dodelson, “Probing Gravity at Cosmological Scales by Measurements which Test the Relationship between Gravitational Lensing and Matter Overdensity”, Phys. Rev. Lett. **99**, 141302 (2007), [arXiv:0704.1932].

[136] L. Amendola, M. Kunz, and D. Sapone, “Measuring the dark side (with weak lensing)”, JCAP **0804**, 013 (2008), [arXiv:0704.2421].

[137] C. Di Porto and L. Amendola, “Observational constraints on the linear fluctuation growth rate”, Phys. Rev. **D77**, 083508 (2008), [arXiv:0707.2686].

[138] W. Hu and I. Sawicki, “A Parameterized Post-Friedmann Framework for Modified Gravity”, Phys. Rev. **D76**, 104043 (2007), [arXiv:0708.1190].

[139] E. V. Linder, “Extending the Gravitational Growth Framework”, Phys. Rev. **D79**, 063519 (2009), [arXiv:0901.0918].

[140] W. Hu, “Parametrized Post-Friedmann Signatures of Acceleration in the CMB”, Phys. Rev. **D77**, 103524 (2008), [arXiv:0801.2433].

[141] W. Fang, W. Hu, and A. Lewis, “Crossing the Phantom Divide with Parameterized Post-Friedmann Dark Energy”, Phys. Rev. **D78**, 087303 (2008), [arXiv:0808.3125].

[142] S. Ho, C. Hirata, N. Padmanabhan, U. Seljak, and N. Bahcall, “Correlation of CMB with large-scale structure: I. ISW Tomography and Cosmological Implications”, Phys. Rev. **D78**, 043519 (2008), [arXiv:0801.0642].

[143] C. M. Hirata, S. Ho, N. Padmanabhan, U. Seljak, and N. A. Bahcall, “Correlation of CMB with large-scale structure: II. Weak lensing”, Phys. Rev. **D78**, 043520 (2008), [arXiv:0801.0644].

[144] T. Koivisto and D. F. Mota, “Accelerating Cosmologies with an Anisotropic Equation of State”, Astrophys. J. **679**, 1 (2008), [arXiv:0707.0279].

[145] T. S. Koivisto and D. F. Mota, “Vector Field Models of Inflation and Dark Energy”, JCAP **0808**, 021 (2008), [arXiv:0805.4229].

[146] Y.-S. Song, L. Hollenstein, G. Caldera-Cabral, and K. Koyama, “Theoretical Priors On Modified Growth Parametrisations”, JCAP **1004**, 018 (2010), [arXiv:1001.0969].

[147] D. F. Mota, J. R. Kristiansen, T. Koivisto, and N. E. Groeneboom, “Constraining Dark Energy Anisotropic Stress”, Mon. Not. Roy. Astron. Soc. **382**, 793 (2007), [arXiv:0708.0830].

[148] W. Hu, “Acceleration from Modified Gravity: Lessons from Worked Examples”, Nucl. Phys. Proc. Suppl. **194**, 230 (2009), [arXiv:0906.2024].

[149] G. R. Dvali, G. Gabadadze, and M. Porrati, “4D gravity on a brane in 5D Minkowski space”, Phys. Lett. **B485**, 208 (2000), [arXiv:hep-th/0005016].

[150] S. Nesseris and A. Shafieloo, “A model independent null test on the cosmological constant”, Mon. Not. Roy. Astron. Soc. **408**, 1879 (2010), [arXiv:1004.0960].

[151] C. Deffayet, “Cosmology on a brane in Minkowski bulk”, Phys. Lett. **B502**, 199 (2001), [arXiv:hep-th/0010186].

[152] A. Lue, R. Scoccimarro, and G. D. Starkman, “Probing Newton’s constant on vast scales: DGP gravity, cosmic acceleration and large scale structure”, Phys. Rev. **D69**, 124015 (2004), [arXiv:astro-ph/0401515].

[153] E. V. Linder and R. N. Cahn, “Parameterized Beyond-Einstein Growth”, Astropart. Phys. **28**, 481 (2007), [arXiv:astro-ph/0701317].

[154] S. M. Carroll, V. Duvvuri, M. Trodden, and M. S. Turner, “Is cosmic speed-up due to new gravitational physics?”, Phys. Rev. **D70**, 043528 (2004), [arXiv:astro-ph/0306438].

[155] S. Nojiri and S. D. Odintsov, “Modified gravity with negative and positive powers of the curvature: Unification of the inflation and of the cosmic acceleration”, Phys. Rev. **D68**, 123512 (2003), [arXiv:hep-th/0307288].

[156] S. Capozziello, S. Carloni, and A. Troisi, “Quintessence without scalar fields”, Recent Res. Dev. Astron. Astrophys. **1**, 625 (2003), [arXiv:astro-ph/0303041].

[157] S. S. Seahra and W. Hu, “Analytic Description of DGP Perturbations on All Scales”, Phys. Rev. **D82**, 124015 (2010), [arXiv:1007.4242].

[158] G.-B. Zhao, L. Pogosian, A. Silvestri, and J. Zylberberg, “Cosmological tests of GR – a look at the principals”, Phys. Rev. Lett. **103**, 241301 (2009), [arXiv:0905.1326].

[159] L. Pogosian, A. Silvestri, K. Koyama, and G.-B. Zhao, “How to optimally parametrize deviations from General Relativity in the evolution of cosmological perturbations?”, Phys. Rev. **D81**, 104023 (2010), [arXiv:1002.2382].

[160] G.-B. Zhao *et al.*, “Probing modifications of General Relativity using current cosmological observations”, Phys. Rev. **D81**, 103510 (2010), [arXiv:1003.0001].

[161] D. Larson *et al.*, “Seven-Year Wilkinson Microwave Anisotropy Probe (WMAP) Observations: Power Spectra and WMAP-Derived Parameters”, Astrophys. J. Suppl. **192**, 16 (2011), [arXiv:1001.4635].

[162] C.-L. Kuo *et al.*, “Improved Measurements of the CMB Power Spectrum with ACBAR”, Astrophys. J. **664**, 687 (2007), [arXiv:astro-ph/0611198].

[163] C. J. MacTavish *et al.*, “Cosmological parameters from the 2003 flight of BOOMERANG”, Astrophys. J. **647**, 799 (2006), [arXiv:astro-ph/0507503].

[164] A. C. S. Readhead *et al.*, “Extended Mosaic Observations with the Cosmic Background Imager”, Astrophys. J. **609**, 498 (2004), [arXiv:astro-ph/0402359].

[165] R. Amanullah *et al.*, “Spectra and Light Curves of Six Type Ia Supernovae at $0.511 < z < 1.12$ and the Union2 Compilation”, Astrophys. J. **716**, 712 (2010), [arXiv:1004.1711].

[166] A. G. Riess *et al.*, “A Redetermination of the Hubble Constant with the Hubble Space Telescope from a Differential Distance Ladder”, Astrophys. J. **699**, 539 (2009), [arXiv:0905.0695].

[167] B. A. Reid, L. Verde, R. Jimenez, and O. Mena, “Robust Neutrino Constraints by Combining Low Redshift Observations with the CMB”, JCAP **1001**, 003 (2010), [arXiv:0910.0008].

[168] W. J. Percival *et al.*, “Baryon Acoustic Oscillations in the Sloan Digital Sky Survey Data Release 7 Galaxy Sample”, Mon. Not. Roy. Astron. Soc. **401**, 2148 (2010), [arXiv:0907.1660].

[169] R. Reyes *et al.*, “Confirmation of general relativity on large scales from weak lensing and galaxy velocities”, Nature **464**, 256 (2010.), [arXiv:1003.2185].

[170] D. Rapetti, S. W. Allen, A. Mantz, and H. Ebeling, “Constraints on modified gravity from the observed X-ray luminosity function of galaxy clusters”, Mon. Not. Roy. Astron. Soc. **400**, 699 (2009), [arXiv:0812.2259].

[171] F. Schmidt, A. Vikhlinin, and W. Hu, “Cluster Constraints on f(R) Gravity”, Phys. Rev. **D80**, 083505 (2009), [arXiv:0908.2457].

[172] D. Rapetti, S. W. Allen, A. Mantz, and H. Ebeling, “The observed growth of massive galaxy clusters - III. Testing general relativity on cosmological scales”, Mon. Not. Roy. Astron. Soc. **406**, 1796 (2010), [arXiv:0911.1787].

[173] S. F. Daniel *et al.*, “Testing General Relativity with Current Cosmological Data”, Phys. Rev. **D81**, 123508 (2010), [arXiv:1002.1962].

[174] S. F. Daniel and E. V. Linder, “Confronting General Relativity with Further Cosmological Data”, Phys. Rev. **D82**, 103523 (2010), [arXiv:1008.0397].

[175] L. Lombriser, A. Slosar, U. Seljak, and W. Hu, “Constraints on f(R) gravity from probing the large-scale structure”, (2010), [arXiv:1003.3009].

[176] H. Oyaizu, “Non-linear evolution of f(R) cosmologies I: methodology”, Phys. Rev. **D78**, 123523 (2008), [arXiv:0807.2449].

[177] H. Oyaizu, M. Lima, and W. Hu, “Non-linear evolution of f(R) cosmologies II: power spectrum”, Phys. Rev. **D78**, 123524 (2008), [arXiv:0807.2462].

[178] F. Schmidt, M. V. Lima, H. Oyaizu, and W. Hu, “Non-linear Evolution of f(R) Cosmologies III: Halo Statistics”, Phys. Rev. **D79**, 083518 (2009), [arXiv:0812.0545].

[179] F. Schmidt, “Self-Consistent Cosmological Simulations of DGP Braneworld Gravity”, Phys. Rev. **D80**, 043001 (2009), [arXiv:0905.0858].

[180] F. Schmidt, W. Hu, and M. Lima, “Spherical Collapse and the Halo Model in Braneworld Gravity”, Phys. Rev. **D81**, 063005 (2010), [arXiv:0911.5178].

[181] K. Koyama, A. Taruya, and T. Hiramatsu, “Non-linear Evolution of Matter Power Spectrum in Modified Theory of Gravity”, Phys. Rev. **D79**, 123512 (2009), [arXiv:0902.0618].

[182] E. Beynon, D. J. Bacon, and K. Koyama, “Weak lensing predictions for modified gravities at non-linear scales”, Mon. Not. Roy. Astron. Soc. **403**, 353 (2010), [arXiv:0910.1480].

[183] S. Ferraro, F. Schmidt, and W. Hu, “Cluster Abundance in f(R) Gravity Models”,

Phys. Rev. **D83**, 063503 (2011), [arXiv:1011.0992].

[184] G.-B. Zhao, B. Li, and K. Koyama, "N-body Simulations for f(R) Gravity using a Self-adaptive Particle-Mesh Code", Phys. Rev. **D83**, 044007 (2011), [arXiv:1011.1257].

[185] F. Pace, J. Waizmann, and M. Bartelmann, "Spherical collapse model in dark-energy cosmologies", Mon. Not. Roy. Astron. Soc. **406**, 1865 (2010), [arXiv:1005.0233].

[186] N. Wintergerst and V. Pettorino, "Clarifying spherical collapse in coupled dark energy cosmologies", Phys. Rev. **D82**, 103516 (2010), [arXiv:1005.1278].

[187] R. Bean and M. Tangmatitham, "Current constraints on the cosmic growth history", Phys. Rev. **D81**, 083534 (2010), [arXiv:1002.4197].

[188] A. Lewis and S. Bridle, "Cosmological parameters from CMB and other data: a Monte- Carlo approach", Phys. Rev. **D66**, 103511 (2002), [arXiv:astro-ph/0205436].

[189] SDSS, K. N. Abazajian *et al.*, "The Seventh Data Release of the Sloan Digital Sky Survey", Astrophys. J. Suppl. **182**, 543 (2009), [arXiv:0812.0649].

[190] The 2dFGRS, S. Cole *et al.*, "The 2dF Galaxy Redshift Survey: Power-spectrum analysis of the final dataset and cosmological implications", Mon. Not. Roy. Astron. Soc. **362**, 505 (2005), [arXiv:astro-ph/0501174].

[191] A. Lewis, A. Challinor, and A. Lasenby, "Efficient Computation of CMB anisotropies in closed FRW models", Astrophys. J. **538**, 473 (2000), [arXiv:astro-ph/9911177].

[192] SDSS, D. J. Eisenstein *et al.*, "Spectroscopic Target Selection for the Sloan Digital Sky Survey: The Luminous Red Galaxy Sample", Astron. J. **122**, 2267 (2001), [arXiv:astro-ph/0108153].

[193] SDSS, D. G. York *et al.*, "The Sloan Digital Sky Survey: technical summary", Astron. J. **120**, 1579 (2000), [arXiv:astro-ph/0006396].

[194] T. Giannantonio, M. Martinelli, A. Silvestri, and A. Melchiorri, "New constraints on parametrised modified gravity from correlations of the CMB with large scale structure", JCAP **1004**, 030 (2010), [arXiv:0909.2045].

[195] L. Lombriser, W. Hu, W. Fang, and U. Seljak, "Cosmological Constraints on DGP Braneworld Gravity with Brane Tension", Phys. Rev. **D80**, 063536 (2009), [arXiv:0905.1112].

[196] T. H. Jarrett *et al.*, "2MASS Extended Source Catalog: Overview and Algorithms", Astron. J. **119**, 2498 (2000), [arXiv:astro-ph/0004318].

[197] M. F. Skrutskie *et al.*, "The Two Micron All Sky Survey (2MASS)", Astron. J. **131**, 1163 (2006).

[198] SDSS, J. K. Adelman-McCarthy *et al.*, "The Sixth Data Release of the Sloan Digital Sky Survey", Astrophys. J. Suppl. **175**, 297 (2008), [arXiv:0707.3413].

[199] J. J. Condon *et al.*, "The NRAO VLA Sky survey", Astron. J. **115**, 1693 (1998).

[200] WMAP, J. Dunkley *et al.*, "Five-Year Wilkinson Microwave Anisotropy Probe (WMAP) Observations: Likelihoods and Parameters from the WMAP data", Astrophys. J. Suppl. **180**, 306 (2009), [arXiv:0803.0586].

[201] R. E. Smith, C. Hernandez-Monteagudo, and U. Seljak, "Impact of Scale Dependent

Bias and Nonlinear Structure Growth on the ISW Effect: Angular Power Spectra", Phys. Rev. **D80**, 063528 (2009), [arXiv:0905.2408].

[202] M. LoVerde and N. Afshordi, "Extended Limber Approximation", Phys. Rev. **D78**, 123506 (2008), [arXiv:0809.5112].

[203] N. Afshordi, "Integrated Sachs-Wolfe effect in Cross-Correlation: The Observer's Manual", Phys. Rev. **D70**, 083536 (2004), [arXiv:astro-ph/0401166].

[204] J. Hamann, S. Hannestad, G. G. Raffelt, and Y. Y. Y. Wong, "Observational bounds on the cosmic radiation density", JCAP **0708**, 021 (2007), [arXiv:0705.0440].

[205] N. Metropolis, A. W. Rosenbluth, M. N. Rosenbluth, A. H. Teller, and E. Teller, "Equation of state calculations by fast computing machines", J. Chem. Phys. **21**, 1087 (1953).

[206] W. K. Hastings, "Monte Carlo sampling methods using Markov chains and their applications", Biometrika **57**, 97 (1970).

[207] A. Gelman and D. B. Rubin, "Inference from Iterative Simulation Using Multiple Sequences", Statist. Sci. **7**, 457 (1992).

[208] J. Dossett, M. Ishak, J. Moldenhauer, Y. Gong, and A. Wang, "Constraints on growth index parameters from current and future observations", JCAP **1004**, 022 (2010), [arXiv:1004.3086].

[209] P. G. Ferreira and C. Skordis, "The linear growth rate of structure in Parametrized Post Friedmannian Universes", Phys. Rev. **D81**, 104020 (2010), [arXiv:1003.4231].

[210] E. R. Harrison, "Fluctuations at the threshold of classical cosmology", Phys. Rev. **D1**, 2726 (1970).

[211] Y. B. Zeldovich, "A hypothesis, unifying the structure and the entropy of the Universe", Mon. Not. Roy. Astron. Soc. **160**, 1P (1972).

[212] F. Feroz and M. P. Hobson, "Multimodal nested sampling: an efficient and robust alternative to Markov Chain Monte Carlo methods for astronomical data analyses", Mon. Not. Roy. Astron. Soc. **384**, 449 (2008), [arXiv:0704.3704].

[213] F. Feroz, M. P. Hobson, and M. Bridges, "MULTINEST: an efficient and robust Bayesian inference tool for cosmology and particle physics", Mon. Not. Roy. Astron. Soc. **398**, 1601 (2009), [arXiv:0809.3437].

[214] P. Mukherjee, D. Parkinson, and A. R. Liddle, "A Nested Sampling Algorithm for Cosmological Model Selection", Astrophys. J. **638**, L51 (2006), [arXiv:astro-ph/0508461].

[215] R. Shaw, M. Bridges, and M. P. Hobson, "Clustered nested sampling: efficient Bayesian inference for cosmology", Mon. Not. Roy. Astron. Soc. **378**, 1365 (2007), [arXiv:astro-ph/0701867].

[216] J. A. Tauber *et al.*, "Planck pre-launch status: The Planck mission", Astron. & Astrophys. **520**, A1+ (2010).

[217] M. J. Mortonson, W. Hu, and D. Huterer, "Falsifying Paradigms for Cosmic Acceleration", Phys. Rev. **D79**, 023004 (2009), [arXiv:0810.1744].

3

DGP Braneworld Gravity

3.1. Cosmological constraints on DGP braneworld gravity with brane tension

Lucas Lombriser[1], *Wayne Hu*[2], *Wenjuan Fang*[3], *Uroš Seljak*[4]

Published in Physical Review D 80, 063536 (2009), [arXiv:0905.1112]

Abstract

We perform a Markov chain Monte Carlo analysis of the self-accelerating and normal branch of Dvali-Gabadadze-Porrati braneworld gravity. By adopting a parametrized post-Friedmann description of gravity, we utilize all of the cosmic microwave background data, including the largest scales, and its correlation with galaxies in addition to the geometrical constraints from supernovae distances and the Hubble constant. We find that on both branches brane tension or a cosmological constant is required at high significance with no evidence for the unique Dvali-Gabadadze-Porrati modifications. The crossover scale must therefore be substantially greater than the Hubble scale $H_0 r_\mathrm{c} > 3$ *and* 3.5 *at the* 95% *confidence level with and without uncertainties from spatial curvature. With spatial curvature, the limit from the normal branch is substantially assisted by the galaxy cross correlation which highlights its importance in constraining infrared modifications to gravity.*

3.1.1. Introduction

Cosmological tests of the acceleration of the expansion offer unique opportunities to test gravity on large scales and low curvature. Dvali, Gabadadze, and Porrati (DGP) [218] proposed that such infrared modifications to gravity might arise in a braneworld model where our universe is a 4D brane embedded in a 5D bulk.

The two branches of cosmological solutions in the DGP model have distinct properties. In the so-called self-accelerating branch, late-time acceleration of the universe occurs without the need of a cosmological constant [219]. Unfortunately without a cosmological constant, the self-accelerating branch predicts cosmological observables that are now in substantial conflict with the data (e.g. [220–222]). Moreover, the linearized theory implies the presence of ghost degrees of freedom (e.g. [223, 224]). The former problem can be alleviated with the restoration of a cosmological constant or

---

[1] Institute for Theoretical Physics, University of Zurich, Winterthurerstrasse 190, CH-8057 Zürich, Switzerland

[2] Kavli Institute for Cosmological Physics, Department of Astronomy and Astrophysics, Enrico Fermi Institute, University of Chicago, Chicago, Illinois 60637, USA

[3] Department of Physics, Columbia University, New York, New York 10027, USA; Brookhaven National Laboratory, Upton, New York 11973, USA

[4] Institute for Theoretical Physics, University of Zurich, Winterthurerstrasse 190, CH-8057 Zürich, Switzerland; Physics and Astronomy Department, University of California, and Lawrence Berkeley National Laboratory, Berkeley, California 94720, USA; Ewha University, Seoul 120-750, Korea

brane tension. A definitive assessment of the latter problem awaits nonlinear solutions [225, 226]. On the second or normal branch, self-acceleration does not occur but interestingly phantom effective equations of state with $p/\rho < -1$ can be achieved without ghosts with the help of brane tension [227]. In both cases, brane tension is required but substantial modifications to large-scale gravitational dynamics can still persist.

In this paper, we conduct a Markov chain Monte Carlo (MCMC) study of both branches of the DGP model using data from cosmic microwave background (CMB) anisotropies, supernovae distances, and the Hubble constant. For observables in the linear regime, we adopt the parametrized post-Friedmann (PPF) framework [228, 229] and its implementation into a standard Einstein-Boltzmann linear theory solver [222, 230] for the theoretical predictions. This framework allows us to include information from the near horizon scales which are crucial for assessing the viability of the self-accelerating branch. We also utilize information from the cross correlation between high-redshift galaxies and the CMB, which has been proposed as an interesting test of both the self-accelerating and normal branches [231–233].

In Sec. 3.1.2, we review the theory of the normal and self-accelerating branches of DGP gravity and their approximation through the PPF formalism. We present the results of our MCMC study in Sec. 3.1.3 and discuss them in Sec. 3.1.4. Finally, the details about the modifications to the ISWWLL code [234, 235] used for the galaxy-ISW cross-correlation observations are specified in the appendix.

3.1.2. Normal and self-accelerating branches

In the DGP model [218] our universe is a (3+1)-brane embedded in a 5D Minkowski space described by the action

$$S = -\frac{1}{2\kappa^2}\int d^5x\sqrt{-\hat{g}}\hat{R} - \frac{1}{2\mu^2}\int d^4x\sqrt{-\tilde{g}}\tilde{R} + \int d^4x\sqrt{-\tilde{g}}L_{\rm T}, \qquad (3.1)$$

where 5D quantities are denoted by hats and 4D quantities are denoted by tildes. Matter fields, including a cosmological constant or brane tension and represented by $L_{\rm T}$, are confined to the brane while only gravity extends to the full 5D bulk. We assume that there is no bulk tension. The constants κ^2 and μ^2 are proportional to the inverse Planck masses in the bulk and brane, respectively.

Gravity on the brane is consequently modified at large scales. In particular, the crossover distance $r_{\rm c} = \kappa^2/2\mu^2$ governs the transition from 5D to 4D scalar-tensor gravity. On scales smaller than the Vainshtein radius $r_* = (r_{\rm c}^2 r_{\rm g})^{1/3}$, nonlinear interactions return gravity to general relativity around a point mass with Schwarzschild radius $r_{\rm g}$. In the following sections we describe the evolution of the background and linear density perturbations in the two branches of cosmological solutions.

3.1.2.1. Background expansion

Variation of the action yields the modified Einstein equations on the brane, which reduce to the modified Friedmann equation in a homogeneous and isotropic metric

$$H^2 - \frac{\sigma}{r_{\rm c}}\sqrt{H^2 + \frac{K}{a^2}} = \frac{\mu^2}{3}\sum_i \rho_i - \frac{K}{a^2}, \qquad (3.2)$$

where $H = \dot{a}/a$ is the Hubble parameter, K is the spatial curvature, a is the scale factor, and ρ_i are the energy densities of the various components on the brane. Here $\sigma = \pm 1$ and designates the branch of the cosmological solutions.

For $\sigma = +1$, late-time acceleration occurs even without a cosmological constant Λ [219] and so this branch is referred to as self-accelerating DGP (sDGP). In order to separate tests of gravity from explanations of acceleration, we will also study the sDGP branch supplemented by a nonvanishing ρ_Λ which we denote as sDGP+Λ where confusion might arise. For $\sigma = -1$, DGP modifications slow the expansion rate and the branch is referred to as normal DGP (nDGP). Here, a cosmological constant is required in order to achieve late-time acceleration.

With the usual definitions $\Omega_i = \mu^2 \rho_i(a=1)/3H_0^2$ and $\Omega_K = -K/H_0^2$, the modified Friedmann equation becomes

$$\left(\frac{H}{H_0}\right)^2 = \left(\sqrt{\frac{\Omega_{\rm m}}{a^3} + \frac{\Omega_{\rm r}}{a^4} + \Omega_\Lambda + \Omega_{r_{\rm c}}} + \sigma\sqrt{\Omega_{r_{\rm c}}}\right)^2 + \frac{\Omega_K}{a^2}, \tag{3.3}$$

where we have assumed that the energy density components include nonrelativistic matter, radiation, and possibly a cosmological constant. Here

$$\sqrt{\Omega_{r_{\rm c}}} \equiv \frac{1}{2H_0 r_{\rm c}} = \sigma \frac{\Omega_{\rm DGP}}{2\sqrt{1-\Omega_K}}, \tag{3.4}$$

where

$$\Omega_{\rm DGP} = 1 - \Omega_{\rm m} - \Omega_{\rm r} - \Omega_\Lambda - \Omega_K \tag{3.5}$$

represents the effective contribution of the DGP modification to the energy density assuming the ordinary Friedmann equation. Specifically,

$$\rho_{\rm DGP} \equiv \frac{3}{\mu^2}\left(H^2 + \frac{K}{a^2}\right) - \sum_i \rho_i. \tag{3.6}$$

As with any real energy density component, it obeys the conservation equation

$$\rho'_{\rm DGP} = -3(1 + w_{\rm DGP})\rho_{\rm DGP}. \tag{3.7}$$

Using Eqs. (3.2) and (3.7), we derive

$$1 + w_{\rm DGP} = \frac{\frac{\mu^2}{3}\sum_i (1+w_i)\rho_i}{H^2 + \frac{K}{a^2} + \frac{\mu^2}{3}\sum_i \rho_i}. \tag{3.8}$$

For cases with a cosmological constant it is also useful to define the total effective dark energy

$$\rho_{\rm e} = \rho_{\rm DGP} + \rho_\Lambda \tag{3.9}$$

and its equation of state

$$1 + w_{\rm e} = (1 + w_{\rm DGP})\frac{\rho_{\rm DGP}}{\rho_{\rm DGP} + \rho_\Lambda}. \tag{3.10}$$

In nDGP this quantity diverges when the DGP and Λ density terms are equal and opposite at which point the value of $1 + w_{\rm e}$ switches sign. In particular, its value today is given by

$$w_0 = -\frac{1-\Omega_K}{1-\Omega_K-\Omega_{\rm m}} \frac{1-\Omega_K-\Omega_{\rm m}+\Omega_\Lambda}{1-\Omega_K+\Omega_{\rm m}+\Omega_\Lambda}, \tag{3.11}$$

where we have neglected the small radiation contribution. With realistic cosmological parameters $w_0 > -1$ and $w_0 < -1$ for sDGP and nDGP, respectively, with $w_0 = -1$ being the limit of cosmological constant domination in either case.

3.1.2.2. PPF linear theory

Unlike the background, the evolution of density and metric perturbations on the brane require solutions for the bulk metric equations. The parametrized post-Friedmann framework was introduced in Refs. [228, 229] to encapsulate these effects in an effective 3+1 description. Fits to the bulk calculation in sDGP without Λ or curvature from [236] were given in [228] and incorporated into the linear theory code CAMB [237] in [222]. We extrapolate these fits to cases with Λ and curvature here though we caution the reader that these have not been tested by explicit bulk calculations. For nDGP, we utilize a description from [238] based on bulk calculations from [232] and [239] with Λ but no curvature. We again extrapolate these results for spatial curvature. The errors induced by these extrapolations are controlled given the well-defined limits of Λ domination and the small dynamical effects of curvature in the regime we consider.

Given the expansion history, the PPF framework is defined by three functions and one parameter. From these quantities, the dynamics are determined by conservation of energy and momentum and the Bianchi identities. The defining quantities are $g(a,k)$ which quantifies the effective anisotropic stress of the modifications and distinguishes the two gravitational potentials, $f_\zeta(a)$, which defines the relationship between the matter and the metric on superhorizon scales, and $f_G(a)$, which defines it in the linearized Newtonian regime. The additional parameter defines the transition scale between the superhorizon and Newtonian behaviors.

More specifically,

$$g(a,k) \equiv \frac{\Phi+\Psi}{\Phi-\Psi}, \tag{3.12}$$

where the scalar linear perturbations are represented in longitudinal gauge

$$ds^2 = -(1+2\Psi)dt^2 + a^2(1+2\Phi)d\mathbf{x}^2, \tag{3.13}$$

where $d\mathbf{x}^2$ is the unperturbed spatial line element with constant curvature K. In the quasistatic high k limit, the DGP model predicts

$$g_{\rm QS} = -\frac{1}{3}\left[1 - \frac{2\sigma H r_{\rm c}}{\sqrt{1-\Omega_K(a)}}\left(1+\frac{H'}{3H}-\frac{2}{3}\Omega_K(a)\right)\right]^{-1}, \tag{3.14}$$

where $\Omega_K(a) = H_0^2\Omega_K/H^2a^2$. On superhorizon scales, we take for sDGP [228]

$$\begin{aligned} g_{\rm SH,sDGP}(a) &= \frac{9}{8H\,r_{\rm c}\sqrt{1-\Omega_K(a)}-1} \\ &\quad\times\left(1+\frac{0.51}{H\,r_{\rm c}\sqrt{1-\Omega_K(a)}-1.08}\right). \end{aligned} \tag{3.15}$$

We exclude models $\sqrt{1-\Omega_K}H_0r_{\rm c} > 1.08$ from consideration as they are not within the domain of applicability of the fit nor are they cosmologically viable. For nDGP we take [238] (*cf.* [240])

$$g_{\rm SH,nDGP}(a) = -\frac{1}{2H\,r_{\rm c}\sqrt{1-\Omega_K(a)}+1}. \tag{3.16}$$

The corrections for curvature have not been verified by a bulk calculation for the superhorizon cases. For the curvatures that we will consider, the total impact is small as can be verified by omitting the correction. We expect therefore that corrections on the correction have negligible impact.

At intermediate scales, g is fitted by the interpolating function

$$g(a,k) = \frac{g_{\rm SH} + g_{\rm QS}(c_gk_H)^{n_g}}{1+(c_gk_H)^{n_g}}, \tag{3.17}$$

where $k_H = k/(aH)$, $c_g = 0.14$ for sDGP and $c_g = 0.4$ for nDGP, respectively. Furthermore, we set $n_g = 3$.

The function $f_\zeta(\ln a)$ relates the metric to the density at superhorizon scales and is well described by $f_\zeta(\ln a) = 0.4g_{\rm SH}(\ln a)$. In the quasistatic regime, the analogous relationship between $\Phi - \Psi$ and the density is the Poisson equation and that is unmodified from ordinary gravity for DGP. Hence $f_G(\ln a) = 0$.

Finally the parameter c_Γ relates the transition scale in the dynamical equations from superhorizon to quasistatic behavior. For sDGP we take $c_\Gamma = 1$ following [228] and we employ this value for cases that include Λ. In nDGP, $c_\Gamma \sim 0.15$ from [238] implying a delayed approach to quasistatic behavior.

3.1.3. Constraints on the models

We will use a variety of cosmological data sets to constrain the two branches of the DGP models. First we use the CMB anisotropy data from the five-year Wilkinson Microwave Anisotropy Probe (WMAP) [241], the Arcminute Cosmology Bolometer Array Receiver (ACBAR) [242], the Cosmic Background Imager (CBI) [243], and the Very Small Array (VSA) [244]. Next we employ data from the Supernovae Legacy Survey (SNLS) [245] and the measurement of the Hubble constant from the Supernovae and H_0 for the Equation of State (SHOES) [246] program. Finally we take galaxy-ISW (gISW) correlation observations using the likelihood code of [234, 235]. We quote results with and without the gISW constraint to highlight its impact on the results.

In Sec. 3.1.3.1, we discuss the predictions for these observables in the two branches of the DGP model. In Secs. 3.1.3.2 and 3.1.3.3, we present the results of a

MCMC-likelihood analysis for flat and nonflat universes, respectively. The MCMC analysis is conducted with the publicly available COSMOMC [247] package.

3.1.3.1. Model predictions

In this section we illustrate model predictions of the various cosmological observables we use in the constraints. We chose the parameters of the various models that highlight results from the MCMC analysis.

At high redshifts the DGP modifications become negligible on either branch [see Eq. (3.3)], and so we choose a parametrization that separates high-redshift and low-redshift constraints. Specifically we take 6 high-redshift parameters: the physical baryon and cold dark matter energy density $\Omega_\mathrm{b}h^2$ and $\Omega_\mathrm{c}h^2$, the ratio of sound horizon to angular diameter distance at recombination multiplied by a factor of 100 θ, the optical depth to reionization τ, the scalar tilt n_s, and amplitude A_s at $k_* = 0.002$ Mpc^{-1}.

The low-redshift parameters differ in the various classes of models. For flat ΛCDM and sDGP without Λ there are no additional degrees of freedom. Note that θ carries information on H_0. For flat sDGP+Λ and nDGP, Ω_Λ is an extra degree of freedom. For the open versions of all models Ω_K is the final degree of freedom.

For ΛCDM and sDGP, we illustrate predictions from the nonflat maximum likelihood models found in the next section (see Tables 3.6 and 3.7). Since the large-scale behavior of nDGP is new to this work, we highlight the dependence of observables on Ω_Λ and Ω_K while keeping the high-redshift cosmological parameters fixed (see Table 3.1). Note in the $r_\mathrm{c} \to 0$ limit where $\Omega_{r_\mathrm{c}} = 0$, both nDGP and sDGP+Λ become ΛCDM. We therefore choose to illustrate the maximum likelihood sDGP model with $\Lambda = 0$.

nDGP	A	B	C	D	E	F	G
Ω_Λ	0.77	1.00	1.25	1.50	1.50	1.25	1.00
Ω_K	–	–	–	–	-0.025	-0.015	-0.010
Ω_{r_c}	0.000	0.012	0.049	0.114	0.132	0.057	0.015
H_0	73	77	82	86	71	72	71

Table 3.1: Different choices of nDGP models for illustration. Note that nDGP-A is the best-fit (with gISW) flat nDGP model, corresponding to ΛCDM. Other chain parameters are fixed to values in Table 3.5.

Cosmic microwave background

The CMB probes the geometry of the background expansion as well as the formation of large-scale structure. The latter manifests itself on the largest scales through the integrated Sachs-Wolfe (ISW) effect from the evolution of the gravitational potential. To predict these effects we implement the PPF modifications from Sec. 3.1.2.2. The incorporation of the PPF formalism into a standard Einstein-Boltzmann linear theory solver yields an efficient way to obtain predictions of the DGP model for the CMB. We utilize the PPF modifications to CAMB [237] implemented in

Refs. [222, 230], which we can apply directly for sDGP and figure as a starting point for the implementation of nDGP and sDGP+Λ. In Fig. 3.1, we plot the CMB temperature anisotropy power spectrum with respect to angular multipoles ℓ for the best-fit models of ΛCDM and sDGP, as well as the nDGP parameter choices given in Table 3.1.

Relative to ΛCDM, the growth of structure is suppressed in the sDGP model, yielding an ISW enhancement at the lowest multipoles. This enhancement is sufficiently large to bring the sDGP model without Λ into serious conflict with the joint data [222]. The opposite effect occurs in the nDGP model and leads to predictions that are compatible with the CMB data. Here raising Ω_Λ at fixed Ω_K enhances the low multipoles through the ISW effect. However, compensating effects from curvature can lead to parameter degeneracies.

At high redshifts the contribution of Ω_{r_c} to the Hubble parameter, Eq. (3.3), becomes negligible in either branch. The CMB acoustic peaks can therefore be utilized as usual to infer constraints on the high-redshift parameters, in particular, the physical energy densities of baryonic matter and dark matter as well as the angular diameter distance to recombination.

Distances to the supernovae and H_0

The comparison of the magnitudes of high-redshift to low-redshift supernovae yields a relative distance measure. Theoretical predictions for the distance modulus are related to the luminosity distance, $d_L(z) = (1+z)r(z)$, where $r(z)$ is the comoving angular diameter distance defined by

$$r(z) = \begin{cases} \sin\left[H_0\sqrt{-\Omega_K}\chi(z)\right]/H_0\sqrt{|\Omega_K|}, & \Omega_K < 0, \\ \chi(z), & \Omega_K = 0, \\ \sinh\left[H_0\sqrt{\Omega_K}\chi(z)\right]/H_0\sqrt{|\Omega_K|}, & \Omega_K > 0, \end{cases} \tag{3.18}$$

where the comoving radial distance χ is

$$\chi(z) = \int_0^z \frac{dz'}{H(z')}. \tag{3.19}$$

The supernovae magnitudes, once standardized, are related to the distance by

$$m \equiv \mu + M = 5\log_{10} d_L + M + 25, \tag{3.20}$$

where d_L is in units of Mpc. The unknown absolute magnitude M of the supernovae is a nuisance parameter in the fit and is degenerate with H_0. Hence supernovae measure relative distances within the set.

In Fig. 3.2, we plot the predictions for the distance modulus for the SNLS data in sDGP gravity, nDGP-B, nDGP-F, and in the ΛCDM model.

The acoustic peaks in the CMB and the measurement of the local Hubble constant additionally provide absolute distance probes which complement the relative distance measure of the supernovae. For the Hubble constant, we take the SHOES measurement of $H_0 = 74.2 \pm 3.6$ km s^{-1} Mpc^{-1} which employs Cepheid measurements to link the low-redshift supernovae to the distance scale established by the maser galaxy NGC 4258.

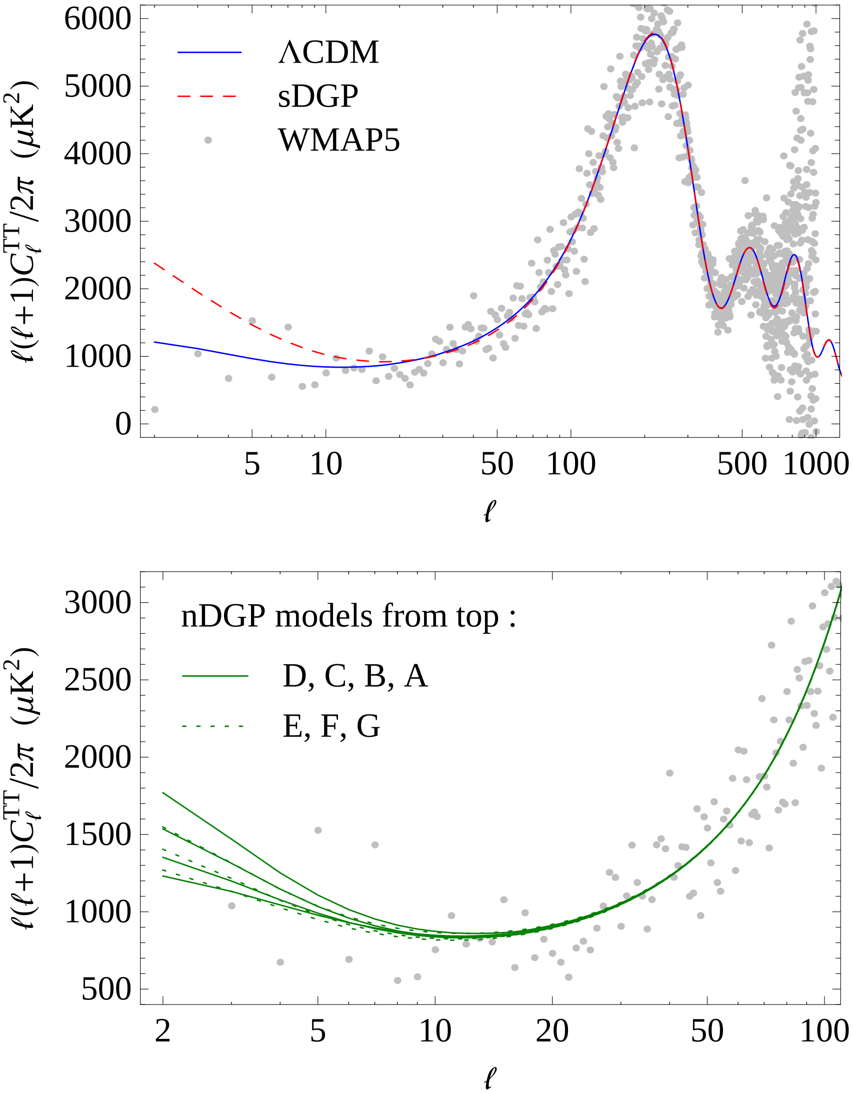

Figure 3.1: Best-fit CMB temperature anisotropy power spectrum for ΛCDM and sDGP (upper panel). Examples of nDGP models (lower panel) illustrate the degeneracy between Ω_Λ and Ω_K corresponding to models in Table 3.1.

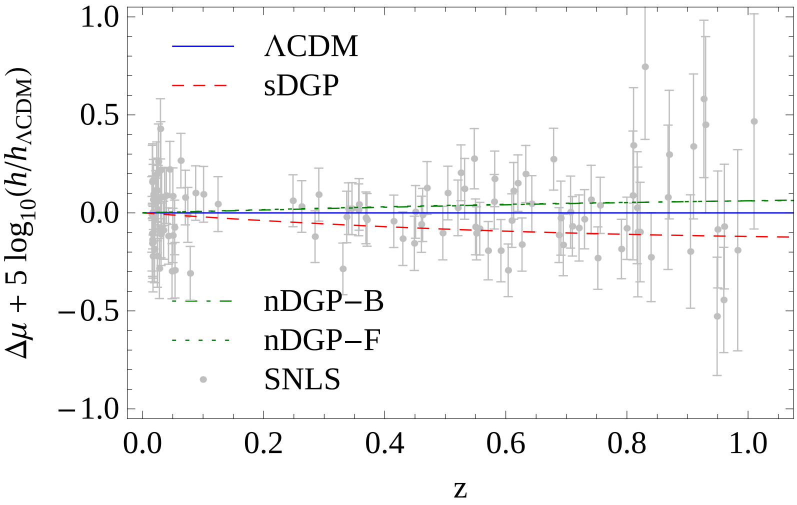

Figure 3.2: Best-fit distance modulus for sDGP, as well as the overlapping predictions for nDGP-B and nDGP-F with respect to ΛCDM.

Galaxy-ISW cross correlations

The correlation between galaxy number densities and the CMB anisotropies can be used to isolate the ISW effect in the CMB. The enhanced ISW effect exhibited in the sDGP model without Λ leaves a strong imprint on the large scales of the CMB temperature anisotropy. As pointed out by Song *et al.* [231], an interesting consequence of this is a considerable correlation of high-redshift galaxies with the CMB.

For nDGP gravity, whereas the ISW effect does not exhibit a substantial impact on the largest scales in the CMB, useful signatures remain in the correlations with galaxies that can break parameter degeneracies [233].

We evaluate the gISW cross correlations in the Limber and quasistatic approximation, as it is done in the ISWWLL code [234, 235] used for the data analysis. Therefore, we write

$$\begin{aligned} C_\ell^{\mathrm{g}_j T} \simeq & \frac{3\Omega_{\mathrm{m}} H_0^2 T_{\mathrm{CMB}}}{(\ell+1/2)^2} \int dz\, f_j(z) H(z) D(z) \\ & \times \frac{d}{dz}[D(z)(1+z)] P\left[\frac{\ell+1/2}{\chi(z)}\right]. \end{aligned} \tag{3.21}$$

Here, $D(z)$ is the linear growth rate in the quasistatic regime defined by $\Delta_{\mathrm{m}}(k,z) = \Delta_{\mathrm{m}}(k,0)D(z)/D(0)$, where $\Delta_{\mathrm{m}}(k,z)$ is the matter density perturbation. $P(k)$ is the matter power spectrum today.

The approximations in Eq. (3.21) become accurate at the percent level for $\ell \gtrsim 10$. This condition is satisfied by about 90% of the total 42 data points that are used in the ISWWLL code. We discuss details about the approximations and the data in the appendix. The data are divided into nine galaxy sample bins j, i.e., 2MASS0-3, LRG0-1, QSO0-1, and NVSS. The function $f_j(z)$ relates the matter density to the observed projected galaxy overdensity with $f_j(z) = b_j(z)\Pi_j(z)$ in the absence of magnification bias. $\Pi_j(z)$ is the redshift distribution of the galaxies and the bias

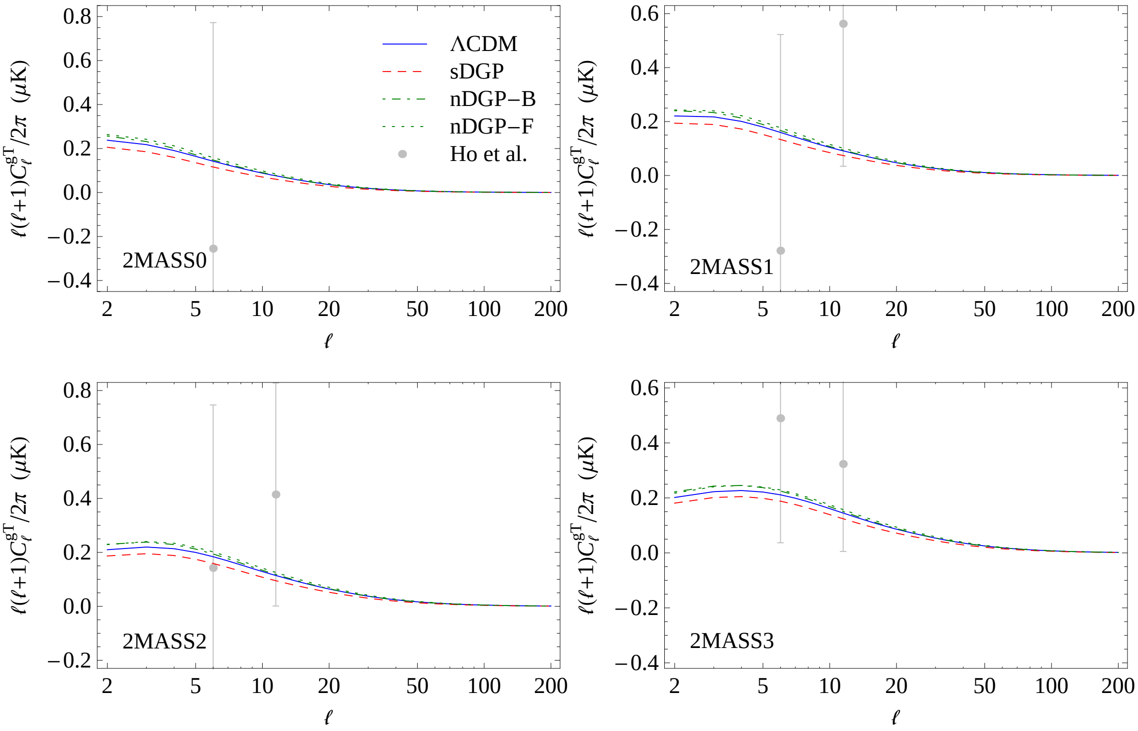

Figure 3.3: Best-fit ΛCDM and sDGP 2MASS galaxy-ISW cross correlations for the different galaxy samples, roughly ordered in increasing effective, bias-weighted, redshift.

factor $b_j(z)$ is assumed independent of scale, but dependent on redshift. The code determines $f_j(z)$, among other things, from fitting autopower spectra and cross-power spectra between the samples.

We modify the above calculations in the ISWWLL code with the appropriate DGP quantities such that the correct predictions for the cross correlations are obtained. We refer to the appendix for details. The predictions for the best-fit values, combining all data, of ΛCDM and sDGP for the different samples are shown in Figs. 3.3 and 3.4. We also plot the curves for nDGP-B and nDGP-F to illustrate the breaking of the degeneracy between Ω_Λ and Ω_K. Notice that the model with larger curvature has reduced correlation especially at high redshift. We shall see that models with significantly larger curvature can be excluded by the gISW data.

3.1.3.2. Flat universe constraints

We begin by studying a universe without spatial curvature, where the basic cosmological parameter set is $P = \{\Omega_b h^2, \Omega_c h^2, \theta, \tau, n_s, \ln[10^{10} A_s]\}$. We implement the following flat priors on them: $\Omega_b h^2 \in (0.01, 0.1)$, $\Omega_c h^2 \in (0.05, 0.99)$, $\theta \in (0.5, 10)$, $\tau \in (0.01, 0.8)$, $n_s \in (0.5, 1.5)$, and $\ln[10^{10} A_s] \in (2.7, 4)$. For nDGP and sDGP with nonvanishing Λ, we use $\Omega_\Lambda \in (0.0, 2.5)$.

We begin with the analysis of flat ΛCDM without DGP modifications in Table 3.2. We show constraints with and without the gISW data and the maximum likelihood parameters and value. Horizontal lines divide the chain parameters from

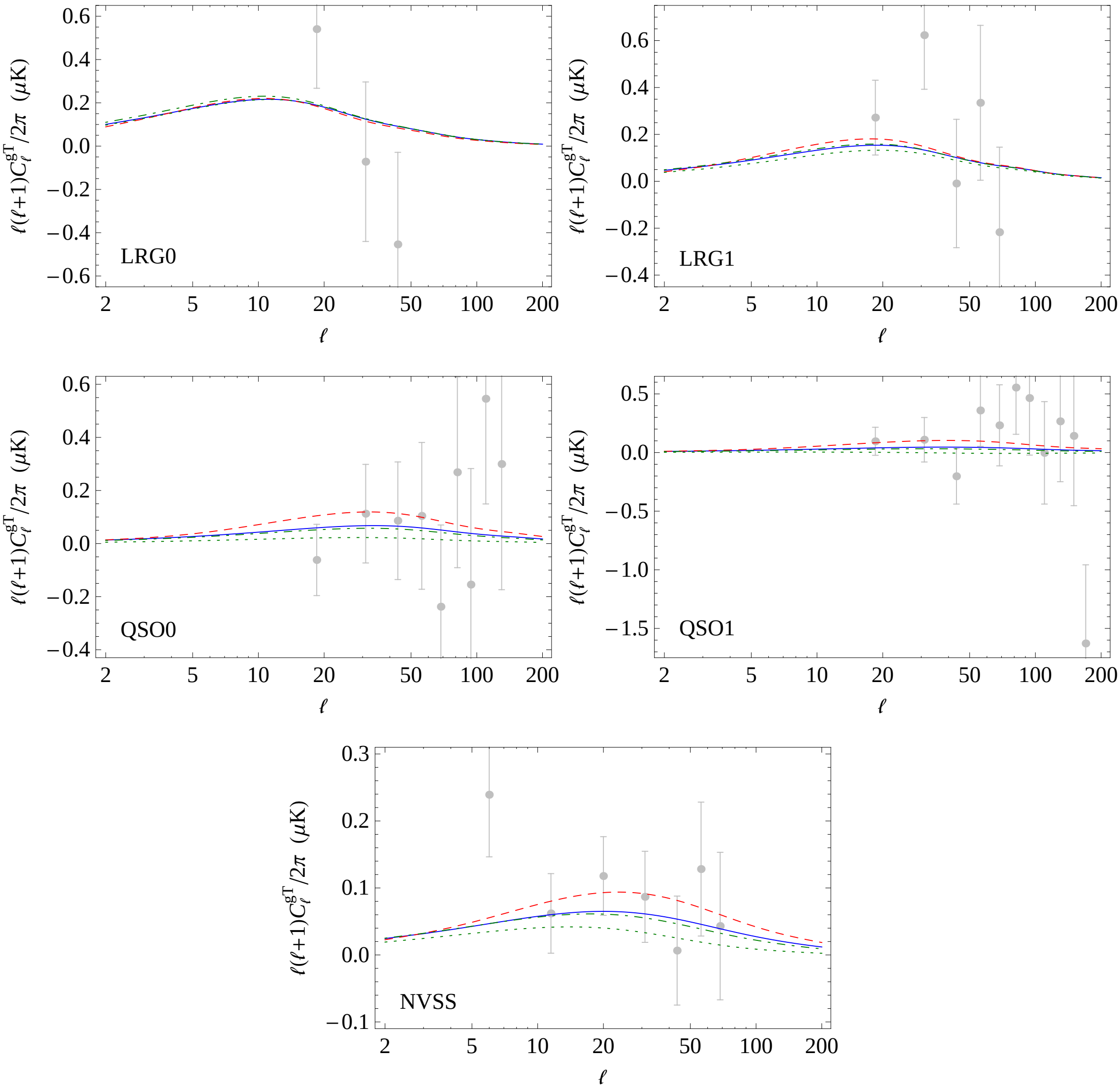

Figure 3.4: Continuation of Fig. 3.3 illustrating the galaxy-ISW cross correlations for the LRG0, LRG1, QSO0, QSO1, and NVSS galaxy samples. Note the distinct predictions for the previously degenerate nDGP-B and nDGP-F models.

Parameters	ΛCDM		ΛCDM (with gISW)	
$100\Omega_{\rm b}h^2$	2.248 ± 0.055	2.240	2.251 ± 0.055	2.258
$\Omega_{\rm c}h^2$	0.1080 ± 0.0043	0.1072	0.1075 ± 0.0042	0.1071
θ	1.0410 ± 0.0027	1.0404	1.0411 ± 0.0027	1.0417
τ	0.086 ± 0.017	0.086	0.087 ± 0.017	0.089
$n_{\rm s}$	0.963 ± 0.013	0.961	0.963 ± 0.013	0.965
$\ln[10^{10}A_{\rm s}]$	3.176 ± 0.041	3.177	3.174 ± 0.041	3.173
Ω_Λ	0.751 ± 0.019	0.754	0.754 ± 0.019	0.758
$\Omega_{\rm m}$	0.249 ± 0.019	0.246	0.246 ± 0.019	0.242
H_0	72.6 ± 1.8	72.6	72.8 ± 1.8	73.2
$-2\ln L$	2834.29		2867.99	

Table 3.2: Means, standard deviations (left subdivision of columns), and best-fit values (right subdivision of columns) with likelihood for the flat ΛCDM model using data from WMAP, ACBAR, CBI, VSA, SNLS, and SHOES without (left column) and with the gISW data (right column).

Parameters	sDGP		sDGP (with gISW)	
$100\Omega_{\rm b}h^2$	2.390 ± 0.066	2.393	2.390 ± 0.065	2.376
$\Omega_{\rm c}h^2$	0.0884 ± 0.0042	0.0873	0.0889 ± 0.0041	0.0899
θ	1.0448 ± 0.0028	1.0447	1.0449 ± 0.0028	1.0452
τ	0.105 ± 0.021	0.110	0.105 ± 0.021	0.103
$n_{\rm s}$	1.011 ± 0.015	1.013	1.011 ± 0.015	1.007
$\ln[10^{10}A_{\rm s}]$	3.001 ± 0.045	2.998	3.003 ± 0.044	3.015
$\Omega_{r_{\rm c}}$	0.1410 ± 0.0075	0.1430	0.1403 ± 0.0075	0.1384
$\Omega_{\rm m}$	0.249 ± 0.020	0.244	0.251 ± 0.020	0.256
H_0	67.2 ± 1.7	67.6	67.1 ± 1.7	66.7
$-2\Delta\ln L$	32.70		33.06	

Table 3.3: Same as Table 3.2, but for the flat sDGP model. $-2\Delta\ln L$ is quoted with respect to the maximum likelihood flat ΛCDM model.

the derived parameters and the best-fit (maximum) likelihood. In the case of ΛCDM, the inclusion of the gISW data does not yield noticeable improvement on the parameter constraints [234]. This analysis sets the baseline by which adding the DGP degrees of freedom should be measured.

In the flat sDGP model without Λ, there is no choice of parameters that can satisfy the joint requirements of geometrical measurements from the CMB, supernovae, and H_0 and the dynamical requirements from the ISW effect. For sDGP, we find $-2\Delta\ln L = 32.7$ with respect to ΛCDM and $-2\Delta\ln L = 33.1$ (5.8σ) when including the gISW likelihood. In this case, the ISW effect is so large at low multipoles that the CMB alone rules out such contributions [222] and the gISW constraint adds only an insignificant amount of extra information (see Tables 3.3). The strengthening of the constraint when compared to Ref. [222] comes from the improved Hubble constant measurements.

In the sDGP+Λ and nDGP models, the cosmological constant becomes a free parameter and we have to add it to the parameter set, hence, $P \to P \cup \{\Omega_\Lambda\}$. $\Omega_{r_{\rm c}}$ is

Parameters	sDGP+Λ		sDGP+Λ (with gISW)	
$100\Omega_\mathrm{b}h^2$	2.265 ± 0.058	2.245	2.265 ± 0.058	2.257
$\Omega_\mathrm{c}h^2$	0.1050 ± 0.0046	0.1071	0.1048 ± 0.0046	0.1070
θ	1.0415 ± 0.0028	1.0405	1.0415 ± 0.0027	1.0415
τ	0.089 ± 0.017	0.080	0.089 ± 0.017	0.083
n_s	0.969 ± 0.014	0.961	0.969 ± 0.014	0.968
$\ln[10^{10}A_\mathrm{s}]$	3.153 ± 0.044	3.165	3.152 ± 0.044	3.154
Ω_Λ	$0.590 - 0.752$	0.733	$0.588 - 0.751$	0.719
Ω_{r_c}	< 0.0178	0.0001	< 0.0186	0.0003
Ω_m	0.248 ± 0.019	0.248	0.247 ± 0.018	0.247
H_0	71.9 ± 1.9	72.3	71.9 ± 1.9	72.5
$-2\Delta \ln L$	0.20		0.13	

Table 3.4: Same as Table 3.3, but for the flat sDGP+Λ model, quoting one-sided 1D marginalized upper 95% confidence levels for Ω_{r_c} and 68% MCI for Ω_Λ.

Parameters	nDGP		nDGP (with gISW)	
$100\Omega_\mathrm{b}h^2$	2.237 ± 0.054	2.245	2.238 ± 0.056	2.254
$\Omega_\mathrm{c}h^2$	0.1109 ± 0.0049	0.1095	0.1100 ± 0.0046	0.1076
θ	1.0406 ± 0.0027	1.0410	1.0407 ± 0.0027	1.0409
τ	0.084 ± 0.016	0.084	0.085 ± 0.017	0.092
n_s	0.958 ± 0.012	0.961	0.959 ± 0.013	0.961
$\ln[10^{10}A_\mathrm{s}]$	3.196 ± 0.043	3.182	3.191 ± 0.043	3.190
Ω_Λ	$0.754 - 0.934$	0.765	$0.753 - 0.924$	0.772
Ω_{r_c}	< 0.0228	0.0001	< 0.0203	0.0001
Ω_m	0.247 ± 0.019	0.253	0.243 ± 0.018	0.244
H_0	73.6 ± 2.0	72.2	73.9 ± 2.0	73.0
$-2\Delta \ln L$	0.05		0.23	

Table 3.5: Same as Table 3.4, but for the flat nDGP model.

a derived parameter and in particular we get $\Omega_{r_\mathrm{c}} \to 0$ in the limit $\Omega_\Lambda \to (1-\Omega_\mathrm{m})$. In this limit, the phenomenology of ΛCDM is recovered for all observables. Preference for a finite Ω_{r_c} indicates evidence for the DGP modification in these cases.

In both the nDGP and sDGP+Λ cases the maximum likelihood models differ insignificantly from ΛCDM (see Tables 3.4 and 3.5) and there is no preference for finite Ω_{r_c}. Conversely, both branches require a finite Ω_Λ at high significance.

Since ΛCDM is the $\Omega_{r_\mathrm{c}} \to 0$ limit of both branches with Λ, the slightly poorer fit for nDGP and sDGP+Λ should be attributed to sampling error in the MCMC. The one-sided 1D marginalized upper 95% confidence limits for Ω_{r_c} are $\Omega_{r_\mathrm{c}} < 0.0178(0.0186)$ for sDGP+Λ and $\Omega_{r_\mathrm{c}} < 0.0228(0.0203)$ for nDGP where the values in parentheses include the gISW constraint. These values indicate that the crossover scale is at least substantially greater than the Hubble scale $H_0 r_\mathrm{c} \gtrsim 3.5$.

In this ΛCDM limit, the modifications to the gISW predictions do not affect the constraints. The slight weakening of the constraints with the inclusion of gISW in sDGP+Λ does not indicate a statistically significant tension but does suggest that future improvement in constraints can tighten the bounds on $H_0 r_\mathrm{c}$. In particular, sDGP modifications tend to enhance correlations at high redshift relative to low redshift. The current data have a marginal preference for increased correlation with redshift relative to ΛCDM (see Figs. 3.3 and 3.4).

Note that due to the distinctive skewness of the posterior distribution, we give the 1D marginalized 68% minimum credible intervals (MCI) (see Ref. [248]) for the brane tension Ω_Λ as opposed to the standard deviations given for the other parameters.

Finally, in the context of these flat models the possibility of phantom equations of state currently is highly constrained. For nDGP $1 + w_0 > -0.039$ at the 95% confidence level.

3.1.3.3. Nonflat universe constraints

In a universe with spatial curvature, we include Ω_K as a parameter in the chain for each of the model classes. We use the prior $\Omega_K \in (-0.1, 0.1)$, which we weaken to $\Omega_K \in (-1, 1)$ in nDGP since we expect degeneracies between Ω_K and Ω_Λ. We also implement latter prior for sDGP+Λ. For ΛCDM, Ho *et al.* [234] have found an improvement of the constraints on Ω_K by a factor of 3.2, with respect to WMAP3 data *alone*, due to the inclusion of the gISW and weak lensing data. However, we find that the inclusion of the other data, specifically the supernova and H_0 data, make curvature constraints only marginally improved by the gISW inclusion. We again use these ΛCDM results shown in Table 3.6 as a baseline for comparison with sDGP, sDGP+Λ, and nDGP in Tables 3.7, 3.8, and 3.9.

For sDGP without Λ, adding curvature alleviates the tension between CMB and supernova distance measures. However, it cannot reduce the ISW contributions [222, 231] and so we obtain $-2\Delta \ln L = 23.3(23.8)$, with respect to ΛCDM, where values in parentheses include the gISW constraint. Utilizing all of the data, the significance of the exclusion of sDGP without Λ is $\sim 5\sigma$.

Similar to the flat case, we find no preference for a finite Ω_{r_c} in nDGP and sDGP+Λ and consequently no indications of DGP modifications to gravity (see Fig. 3.1.3.3). With sDGP+Λ, we are again driven to the limiting case of ΛCDM with the slightly poorer best fit reflecting a sampling error in the chain. Allowance for curvature on the other hand weakens the upper limit on the DGP modifications: $\Omega_{r_c} < 0.0248(0.0244)$ and $H_0 r_c > 3.18(3.20)$ at the 95% confidence level.

For nDGP, the addition of curvature introduces a degeneracy with the cosmological constant. As was pointed out by Giannantonio *et al.* [233], this degeneracy can be broken by the use of gISW cross correlations since high curvature solutions underpredict the correlation especially at high redshift. Figure 3.6 illustrates this degeneracy and the effect of gISW measures. The result of marginalizing curvature in nDGP is again a weakening of the DGP constraints $\Omega_{r_c} < 0.0501(0.0300)$ and $H_0 r_c > 2.23(2.89)$ at the 95% confidence level.

In summary with the gISW constraint, the limit on either branch implies $H_0 r_c \gtrsim 3$ and only a small weakening from the flat case of 3.5. Furthermore due to the curvature degeneracy in nDGP, restrictions on phantomlike equations of state are also somewhat weakened to $w_0 + 1 < -0.049$.

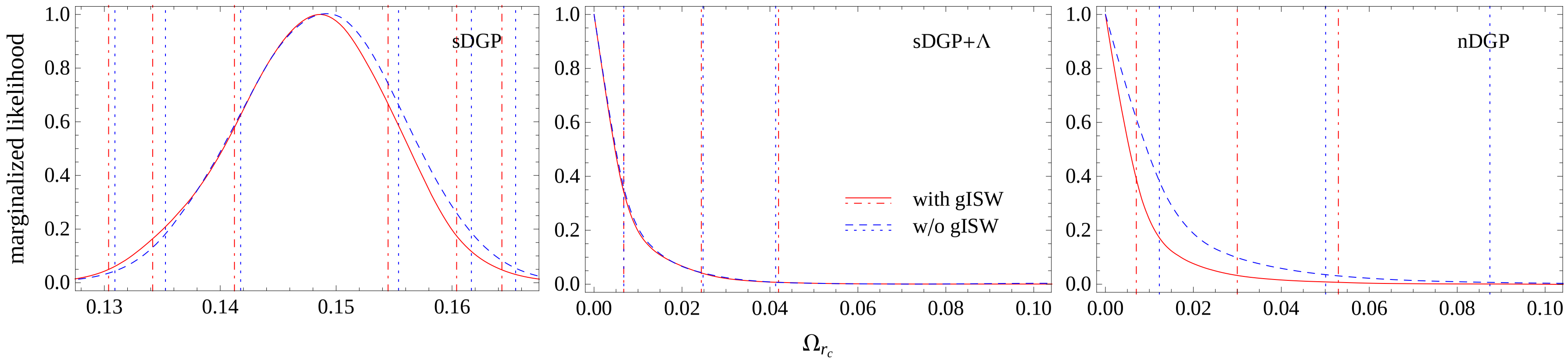

Figure 3.5: Marginalized likelihood for Ω_{r_c} in the nonflat nDGP and sDGP models. The vertical lines indicate the 68%, 95%, and 99% confidence level.

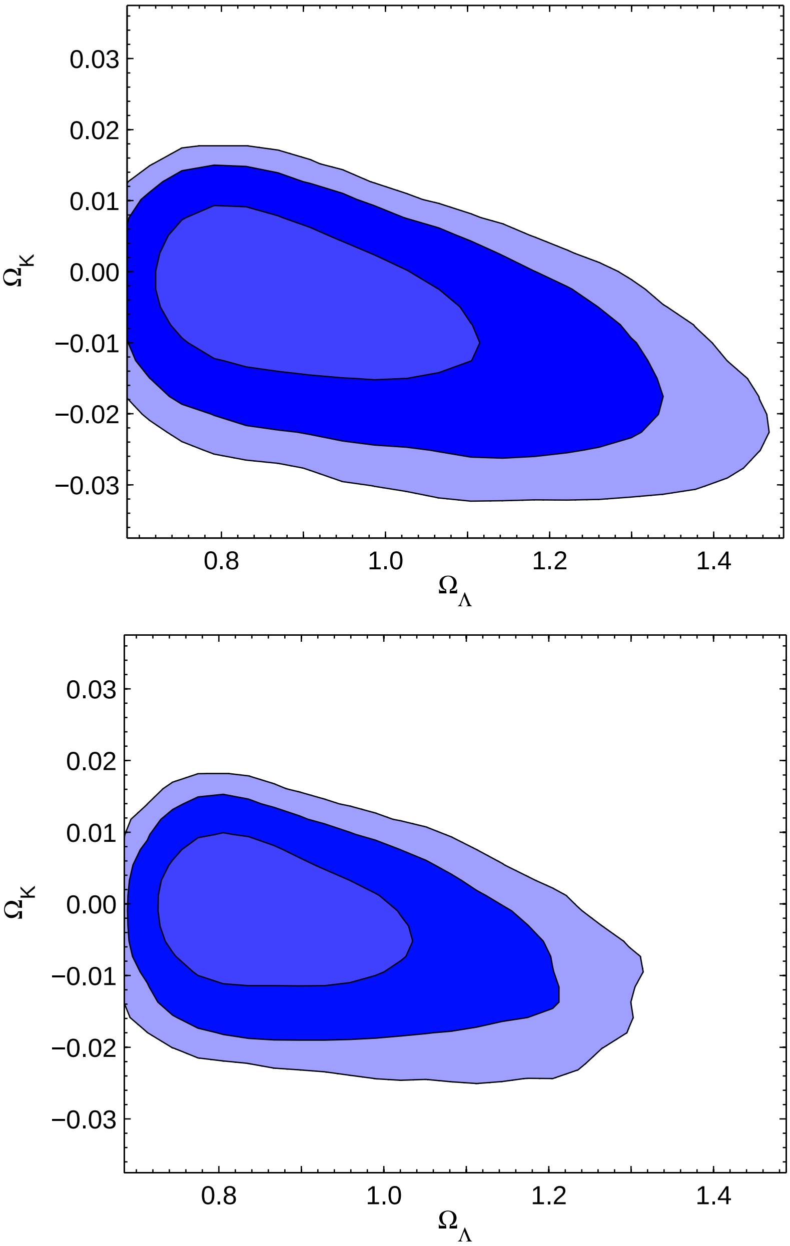

Figure 3.6: Contours of 2D marginalized 68%, 95%, and 99% confidence boundaries using WMAP5, ACBAR, CBI, VSA, SNLS, and SHOES (upper panel), including gISW (lower panel) for nDGP.

Parameters	ΛCDM		ΛCDM (with gISW)	
$100\Omega_{\rm b}h^2$	2.250 ± 0.056	2.246	2.249 ± 0.055	2.238
$\Omega_{\rm c}h^2$	0.1084 ± 0.0052	0.1095	0.1084 ± 0.0051	0.1085
θ	1.0412 ± 0.0027	1.0412	1.0411 ± 0.0027	1.0419
τ	0.086 ± 0.017	0.090	0.087 ± 0.017	0.083
$n_{\rm s}$	0.963 ± 0.013	0.960	0.963 ± 0.013	0.962
$\ln[10^{10}A_{\rm s}]$	3.176 ± 0.044	3.196	3.179 ± 0.043	3.174
Ω_K	-0.0001 ± 0.0063	0.0020	0.0007 ± 0.0062	0.0021
Ω_Λ	0.751 ± 0.020	0.751	0.753 ± 0.019	0.758
$\Omega_{\rm m}$	0.249 ± 0.022	0.246	0.246 ± 0.022	0.240
H_0	72.6 ± 3.0	73.2	73.0 ± 3.0	73.8
$-2\ln L$	2834.01		2867.74	

Table 3.6: ΛCDM as in Table 3.2, except allowing spatial curvature.

Parameters	sDGP		sDGP (with gISW)	
$100\Omega_{\rm b}h^2$	2.377 ± 0.061	2.365	2.376 ± 0.062	2.352
$\Omega_{\rm c}h^2$	0.0951 ± 0.0041	0.0970	0.0952 ± 0.0039	0.0979
θ	1.0441 ± 0.0028	1.0451	1.0441 ± 0.0028	1.0439
τ	0.091 ± 0.020	0.084	0.092 ± 0.019	0.084
$n_{\rm s}$	1.004 ± 0.014	1.002	1.004 ± 0.014	0.997
$\ln[10^{10}A_{\rm s}]$	3.018 ± 0.043	3.019	3.021 ± 0.043	3.037
Ω_K	0.0186 ± 0.0055	0.0212	0.0182 ± 0.0055	0.0220
$\Omega_{r_{\rm c}}$	0.1486 ± 0.0068	0.1486	0.1479 ± 0.0067	0.1467
$\Omega_{\rm m}$	0.218 ± 0.019	0.216	0.220 ± 0.019	0.220
H_0	74.0 ± 3.0	74.7	73.7 ± 2.9	74.2
$-2\Delta\ln L$	23.32		23.79	

Table 3.7: sDGP without Λ as in Table 3.3, except allowing spatial curvature. $-2\Delta\ln L$ is quoted with respect to the maximum likelihood ΛCDM model with curvature here and in the following tables.

3.1.4. Discussion

We have performed the first Markov chain Monte Carlo analysis of the nDGP and sDGP branches of DGP braneworld gravity to utilize all of the CMB data, including the lowest multipoles, and its correlation with galaxies (gISW). We also include supernovae and Hubble constant data in the constraint.

We find no preference for DGP modifications to gravity on either branch. Indeed, on the self-accelerating branch without Λ, the model is excluded at the 4.9σ and 5.8σ levels with and without curvature respectively [222]. While the gISW data do not substantially improve this constraint, they do additionally disfavor sDGP.

With the inclusion of Λ on either branch, the DGP model cannot be entirely excluded but its modifications are strongly limited. We find that the crossover scale, which measures the strength of the modifications, must be substantially above the Hubble scale $H_0 r_{\rm c} > 3$ with curvature and 3.5 without curvature. The robustness of this constraint is substantially assisted by the gISW data. In nDGP, it breaks

Parameters	sDGP+Λ		sDGP+Λ (with gISW)	
$100\Omega_{\rm b}h^2$	2.266 ± 0.058	2.252	2.266 ± 0.0059	2.251
$\Omega_{\rm c}h^2$	0.1065 ± 0.0051	0.1066	0.1064 ± 0.0051	0.1095
θ	1.0416 ± 0.0028	1.0406	1.0415 ± 0.0028	1.0414
τ	0.087 ± 0.017	0.077	0.088 ± 0.017	0.090
$n_{\rm s}$	0.968 ± 0.014	0.962	0.968 ± 0.014	0.960
$\ln[10^{10}A_{\rm s}]$	3.157 ± 0.046	3.153	3.158 ± 0.046	3.197
Ω_K	0.0032 ± 0.0068	0.0022	0.0036 ± 0.0065	0.0018
Ω_Λ	$0.557 - 0.745$	0.711	$0.561 - 0.746$	0.737
$\Omega_{r_{\rm c}}$	< 0.0248	0.0006	< 0.0244	0.0000
$\Omega_{\rm m}$	0.245 ± 0.022	0.240	0.243 ± 0.021	0.248
H_0	72.8 ± 3.0	73.3	73.1 ± 2.9	72.9
$-2\Delta \ln L$	0.07		0.04	

Table 3.8: sDGP with Λ as in Table 3.4, but allowing spatial curvature.

Parameters	nDGP		nDGP (with gISW)	
$100\Omega_{\rm b}h^2$	2.239 ± 0.056	2.245	2.242 ± 0.056	2.239
$\Omega_{\rm c}h^2$	0.1099 ± 0.0054	0.1076	0.1094 ± 0.0054	0.1099
θ	1.0409 ± 0.0027	1.0412	1.0409 ± 0.0027	1.0409
τ	0.084 ± 0.017	0.084	0.085 ± 0.017	0.091
$n_{\rm s}$	0.959 ± 0.013	0.960	0.960 ± 0.013	0.960
$\ln[10^{10}A_{\rm s}]$	3.189 ± 0.045	3.176	3.188 ± 0.045	3.205
Ω_K	-0.0055 ± 0.0080	-0.0056	-0.0029 ± 0.0069	0.0021
Ω_Λ	$0.749 - 1.009$	0.801	$0.749 - 0.953$	0.764
$\Omega_{r_{\rm c}}$	< 0.0501	0.0008	< 0.0300	0.0000
$\Omega_{\rm m}$	0.255 ± 0.023	0.261	0.248 ± 0.022	0.247
H_0	72.1 ± 3.0	70.6	73.0 ± 3.0	73.1
$-2\Delta \ln L$	0.09		0.41	

Table 3.9: nDGP as in Table 3.5, but allowing spatial curvature.

the geometric degeneracy between Λ and spatial curvature. In sDGP, the relatively large correlation at high redshift offers opportunities in the future for improving the limits on $H_0r_{\rm c}$. These abilities highlight the importance of obtaining improved gISW data for constraining infrared modifications to gravity.

Acknowledgments

We would like to thank Kazuya Koyama, Sanjeev Seehra, Fabian Schmidt, and Yong-Seon Song for useful discussions and Anže Slosar for helpful insights into the COSMOMC and ISWWLL codes. Computational resources were provided on the zBox2 supercomputer at the University of Zurich. This work was partially supported by the Swiss National Foundation under Contract No. 200021-116696/1 and WCU Grant No. R32-2008-000-10130-0. W.H. was supported by the Kavli Institute for Cosmological Physics (KICP) at the University of Chicago through Grants NSF No. PHY-0114422 and NSF No. PHY-0551142, U.S. Department of Energy Contract

No. DE-FG02-90ER-40560, and the David and Lucile Packard Foundation. W.F. was supported by the U.S. Department of Energy Contract No. DE-AC02-98CH10886.

3.1.A. Modifications to the ISWWLL code

We use the publicly available ISWWLL code [234, 235] for our analysis. Note that we have turned off weak lensing likelihood contributions in the code, focusing only on the gISW constraints. The 42 data points of gISW cross correlations that are used in the likelihood analysis are collected from the Two Micron All Sky Survey (2MASS) extended source catalog (XSC) [249, 250], the luminous red galaxies (LRG) and photometric quasars (QSO) of the Sloan Digital Sky Survey (SDSS) [251], and the National Radio Astronomy Observatory (NRAO) Very Large Array (VLA) Sky Survey (NVSS) [252]. They are divided into nine galaxy sample bins j (2MASS0-3, LRG0-1, QSO0-1, NVSS) based on flux (2MASS) or redshift (LRG, QSO). These data points are a selection of multipole bins from all samples, where the selection is based on the avoidance of nonlinearities and systematic effects from dust extinction, galaxy foregrounds, the thermal Sunyaev-Zel'dovich effect, and point source contamination to affect the gISW cross correlations [234].

In the remainder of this appendix, we discuss the details of the modifications implemented in the ISWWLL code. First, we describe the calculation of the quasistatic linear growth rate $D(z)$ in the gISW cross correlation, Eq. (3.21), and analyze the validity of the Limber and the quasistatic approximation. We then discuss the function $f_j(z)$ that carries information about the redshift distribution and bias.

3.1.A.1. gISW cross correlations

It has been argued that for nDGP and sDGP the gISW cross correlations are well described within the quasistatic regime [231, 233, 236, 253]. Here, this can easily be seen from the substitution $k \to (\ell + 1/2)/\chi(z)$ considering the relevant redshifts. In this limit, we solve the ordinary differential equation [254]

$$\Delta_{\mathrm{m}}'' + \left(2 + \frac{H'}{H}\right)\Delta_{\mathrm{m}}' - \frac{3}{2}\left(1 - g_{\mathrm{QS}}\right)\frac{H_0^2\Omega_{\mathrm{m}}}{a^3H^2}\Delta_{\mathrm{m}} = 0 \tag{3.22}$$

for the linear matter density perturbation Δ_{m}. Note that for nDGP, in the limit $r_{\mathrm{c}} \to \infty$, we have $g_{\mathrm{QS}} \to 0$ and $H(z)$ approaches the expansion history of ΛCDM. Therefore, in this limit, Eq. (3.22) recovers the quasistatic ordinary differential equation for the matter overdensity in ΛCDM. We solve Eq. (3.22) with initial conditions at $a_{\mathrm{i}} \ll 1$, in a regime where general relativity is expected to hold, i.e., $\Delta_{\mathrm{m}}'(a_{\mathrm{i}}) = \Delta_{\mathrm{m}}(a_{\mathrm{i}})$ with a normalization set by the initial power spectrum.

The accuracy of the Limber approximation in the case of ΛCDM is at the order of 10% at $\ell = 2$ and drops approximately as ℓ^2 at higher ℓ (see e.g. [255–257]). The error depends further on the width of the redshift distribution, which changes only little with DGP effects. The relative deviation from the exact result at $\ell = 6$ does not exceed $\sim 3\%$ for the samples and typical models considered in Figs. 3.3 and 3.4. Given the large errors of the currently available data points at low ℓ, we conclude that the Limber approximation is applicable and furthermore very useful since it is numerically faster than an exact integration.

3.1.A.2. Redshift distribution and bias

A further modification to the code that we need to conduct is in the determination of the function $f_j(z)$. In the Markov chain, $f_j(z)$ is recomputed when changing the cosmological parameter values. The methods by which this function is determined differ for each sample, but they are all based on galaxy clustering data.

The 2MASS galaxies are matched with SDSS galaxies in order to identify their redshifts. To obtain the nonlinear power spectrum, the Q model for nonlinearities [258] is applied. Then, the code computes the galaxy power spectrum and fits it to measurements, thereby determining the bias $b(z)$ and Q. Since the required accuracy for the estimation of bias is only at the order of a few tens of percent [234], this processing is also applicable to DGP. The Q model is also adopted for LRG galaxies, where the redshift probability distribution is inferred with methods described in Ref. [259]. For QSO, first, a preliminary estimate for the redshift distribution is deduced by locating a region of sky with high spectroscopic completeness, but simultaneously maintaining a large area. Taking into account magnification bias and fitting $b_j(z)\Pi_j(z)$ using the quasar power spectrum and quasar-LRG cross power yields the desired shape of $f_j(z)$. Finally, the effective redshift distribution of NVSS is obtained from cross-correlating with the other samples and $f_j(z)$ is fitted with a Γ distribution.

The part of the ISWWLL code that is devoted to this processing is configured for a parametrization of the expansion history by $w_{\mathrm{e}} = w_0 + (1-a)w_a$. This approach gives a good approximation to sDGP in the domain of interest, but it fails for nDGP and sDGP+Λ due to the appearance of a divergence in $w_{\mathrm{e}}(a)$. Therefore, instead of taking w_0 and w_a to describe the expansion history, we utilize Ω_{r_c} and Ω_Λ, where only the latter really is a necessary, free parameter.

In case of the SDSS quasars, the derivation of $f_j(z)$ involves the linear growth factor, which we need to replace by its DGP counterpart. This implies solving Eq. (3.22). A further contribution for the QSO samples is due to magnification bias. In the quasistatic regime of DGP the relationship between the metric combination sensitive to gravitational redshifts and lensing $(\Phi - \Psi)$ and the density perturbations is unmodified so the expression of the lensing window function for magnification effects given in Ref. [234] is unchanged.

References

[218] G. R. Dvali, G. Gabadadze, and M. Porrati, “4D gravity on a brane in 5D Minkowski space”, Phys. Lett. **B485**, 208 (2000), [arXiv:hep-th/0005016].

[219] C. Deffayet, “Cosmology on a brane in Minkowski bulk”, Phys. Lett. **B502**, 199 (2001), [arXiv:hep-th/0010186].

[220] M. Fairbairn and A. Goobar, “Supernova limits on brane world cosmology”, Phys. Lett. **B 642**, 432 (2006), [arXiv:astro-ph/0511029].

[221] R. Maartens and E. Majerotto, “Observational constraints on self-accelerating cosmology”, Phys. Rev. **D 74**, 023004 (2006), [arXiv:astro-ph/0603353].

[222] W. Fang *et al.*, “Challenges to the DGP Model from Horizon-Scale Growth and Geometry”, Phys. Rev. **D78**, 103509 (2008), [arXiv:0808.2208].

[223] M. A. Luty, M. Porrati, and R. Rattazzi, “Strong interactions and stability in the DGP model”, JHEP **09**, 029 (2003), [arXiv:hep-th/0303116].

[224] C. Charmousis, R. Gregory, N. Kaloper, and A. Padilla, “DGP specteroscopy”, JHEP **10**, 066 (2006), [arXiv:hep-th/0604086].

[225] G. Dvali, “Predictive Power of Strong Coupling in Theories with Large Distance Modified Gravity”, New J. Phys. **8**, 326 (2006), [arXiv:hep-th/0610013].

[226] K. Koyama, “Ghosts in the self-accelerating universe”, Class. Quant. Grav. **24**, R231 (2007), [arXiv:0709.2399].

[227] V. Sahni and Y. Shtanov, “Braneworld models of dark energy”, JCAP **0311**, 014 (2003), [arXiv:astro-ph/0202346].

[228] W. Hu and I. Sawicki, “A Parameterized Post-Friedmann Framework for Modified Gravity”, Phys. Rev. **D76**, 104043 (2007), [arXiv:0708.1190].

[229] W. Hu, “Parametrized Post-Friedmann Signatures of Acceleration in the CMB”, Phys. Rev. **D77**, 103524 (2008), [arXiv:0801.2433].

[230] W. Fang, W. Hu, and A. Lewis, “Crossing the Phantom Divide with Parameterized Post-Friedmann Dark Energy”, Phys. Rev. **D78**, 087303 (2008), [arXiv:0808.3125].

[231] Y.-S. Song, I. Sawicki, and W. Hu, “Large-Scale Tests of the DGP Model”, Phys. Rev. **D75**, 064003 (2007), [arXiv:astro-ph/0606286].

[232] Y.-S. Song, “Large Scale Structure Formation of normal branch in DGP brane world model”, Phys. Rev. **D77**, 124031 (2008), [arXiv:0711.2513].

[233] T. Giannantonio, Y.-S. Song, and K. Koyama, “Detectability of a phantom-like braneworld model with the integrated Sachs-Wolfe effect”, Phys. Rev. **D78**, 044017 (2008), [arXiv:0803.2238].

[234] S. Ho, C. Hirata, N. Padmanabhan, U. Seljak, and N. Bahcall, “Correlation of CMB with large-scale structure: I. ISW Tomography and Cosmological Implications”, Phys. Rev. **D78**, 043519 (2008), [arXiv:0801.0642].

[235] C. M. Hirata, S. Ho, N. Padmanabhan, U. Seljak, and N. A. Bahcall, “Correlation of CMB with large-scale structure: II. Weak lensing”, Phys. Rev. **D78**, 043520 (2008), [arXiv:0801.0644].

[236] I. Sawicki, Y.-S. Song, and W. Hu, “Near-Horizon Solution for DGP Perturbations”, Phys. Rev. **D75**, 064002 (2007), [arXiv:astro-ph/0606285].

[237] A. Lewis, A. Challinor, and A. Lasenby, “Efficient Computation of CMB anisotropies in closed FRW models”, Astrophys. J. **538**, 473 (2000), [arXiv:astro-ph/9911177].

[238] S. S. Seahra and W. Hu, “Analytic Description of DGP Perturbations on All Scales”, Phys. Rev. **D82**, 124015 (2010), [arXiv:1007.4242].

[239] A. Cardoso, K. Koyama, S. S. Seahra, and F. P. Silva, “Cosmological perturbations in the DGP braneworld: numeric solution”, Phys. Rev. **D77**, 083512 (2008), [arXiv:0711.2563].

[240] N. Afshordi, G. Geshnizjani, and J. Khoury, “Do observations offer evidence for cosmological-scale extra dimensions?”, JCAP **0908**, 030 (2009), [arXiv:0812.2244].

[241] WMAP, J. Dunkley *et al.*, “Five-Year Wilkinson Microwave Anisotropy Probe

(WMAP) Observations: Likelihoods and Parameters from the WMAP data", Astrophys. J. Suppl. **180**, 306 (2009), [arXiv:0803.0586].

[242] C.-L. Kuo *et al.*, "Improved Measurements of the CMB Power Spectrum with ACBAR", Astrophys. J. **664**, 687 (2007), [arXiv:astro-ph/0611198].

[243] A. C. S. Readhead *et al.*, "Extended Mosaic Observations with the Cosmic Background Imager", Astrophys. J. **609**, 498 (2004), [arXiv:astro-ph/0402359].

[244] K. Grainge *et al.*, "The CMB power spectrum out to l=1400 measured by the VSA", Mon. Not. Roy. Astron. Soc. **341**, L23 (2003), [arXiv:astro-ph/0212495].

[245] The SNLS, P. Astier *et al.*, "The Supernova Legacy Survey: Measurement of Ω_M, Ω_Λ and w from the First Year Data Set", Astron. Astrophys. **447**, 31 (2006), [arXiv:astro-ph/0510447].

[246] A. G. Riess *et al.*, "A Redetermination of the Hubble Constant with the Hubble Space Telescope from a Differential Distance Ladder", Astrophys. J. **699**, 539 (2009), [arXiv:0905.0695].

[247] A. Lewis and S. Bridle, "Cosmological parameters from CMB and other data: a Monte- Carlo approach", Phys. Rev. **D66**, 103511 (2002), [arXiv:astro-ph/0205436].

[248] J. Hamann, S. Hannestad, G. G. Raffelt, and Y. Y. Y. Wong, "Observational bounds on the cosmic radiation density", JCAP **0708**, 021 (2007), [arXiv:0705.0440].

[249] T. H. Jarrett *et al.*, "2MASS Extended Source Catalog: Overview and Algorithms", Astron. J. **119**, 2498 (2000), [arXiv:astro-ph/0004318].

[250] M. F. Skrutskie *et al.*, "The Two Micron All Sky Survey (2MASS)", Astron. J. **131**, 1163 (2006).

[251] SDSS, J. K. Adelman-McCarthy *et al.*, "The Sixth Data Release of the Sloan Digital Sky Survey", Astrophys. J. Suppl. **175**, 297 (2008), [arXiv:0707.3413].

[252] J. J. Condon *et al.*, "The NRAO VLA Sky survey", Astron. J. **115**, 1693 (1998).

[253] K. Koyama and R. Maartens, "Structure formation in the DGP cosmological model", JCAP **0601**, 016 (2006), [arXiv:astro-ph/0511634].

[254] A. Lue, R. Scoccimarro, and G. D. Starkman, "Probing Newton's constant on vast scales: DGP gravity, cosmic acceleration and large scale structure", Phys. Rev. **D69**, 124015 (2004), [arXiv:astro-ph/0401515].

[255] R. E. Smith, C. Hernandez-Monteagudo, and U. Seljak, "Impact of Scale Dependent Bias and Nonlinear Structure Growth on the ISW Effect: Angular Power Spectra", Phys. Rev. **D80**, 063528 (2009), [arXiv:0905.2408].

[256] M. LoVerde and N. Afshordi, "Extended Limber Approximation", Phys. Rev. **D78**, 123506 (2008), [arXiv:0809.5112].

[257] N. Afshordi, "Integrated Sachs-Wolfe effect in Cross-Correlation: The Observer's Manual", Phys. Rev. **D70**, 083536 (2004), [arXiv:astro-ph/0401166].

[258] The 2dFGRS, S. Cole *et al.*, "The 2dF Galaxy Redshift Survey: Power-spectrum analysis of the final dataset and cosmological implications", Mon. Not. Roy. Astron. Soc. **362**, 505 (2005), [arXiv:astro-ph/0501174].

[259] SDSS, N. Padmanabhan *et al.*, "Calibrating Photometric Redshifts of Luminous Red

Galaxies", Mon. Not. Roy. Astron. Soc. **359**, 237 (2005), [arXiv:astro-ph/0407594].

4

$f(R)$ Gravity Models

4.1. Constraints on $f(R)$ gravity from probing the large-scale structure

Lucas Lombriser[1], *Anže Slosar*[2], *Uroš Seljak*[3], *Wayne Hu*[4]

Submitted to Physical Review D, [arXiv:1003.3009]

Abstract

We study cosmological constraints on metric $f(R)$ gravity models that are designed to reproduce the ΛCDM expansion history with modifications to gravity described by a supplementary cosmological freedom, the Compton wavelength parameter B_0. We conduct a Markov chain Monte Carlo analysis on the parameter space, utilizing the geometrical constraints from supernovae distances, the baryon acoustic oscillation distances, and the Hubble constant, along with all of the cosmic microwave background data, including the largest scales, its correlation with galaxies, and a probe of the relation between weak gravitational lensing and galaxy flows. The strongest constraints, however, are obtained through the inclusion of data from cluster abundance. Using all of the data, we infer a bound of $B_0 < 1.1 \times 10^{-3}$ at the 95% confidence level.

4.1.1. Introduction

Cosmic acceleration can either be explained by introducing large amounts of dark energy or considering modifications to gravity such as the addition of a suitable function $f(R)$ of the Ricci scalar to the Einstein-Hilbert action [260–262]. In fact, one may interpret the cosmological constant as being of this kind rather than attributing it to vacuum energy. It has been argued that a valid $f(R)$ model should closely match the ΛCDM expansion history [263, 264]. We specialize our considerations to functions $f(R)$ that exactly reproduce this background and parametrize the class of solutions in terms of its Compton wavelength parameter B_0 [265]. Such $f(R)$ modifications affect gravity at solar-system scales, which are well tested and impose stringent constraints on deviations from general relativity. However, the chameleon effect [266–268] provides a mechanism that allows certain $f(R)$ models to evade solar-system tests (e.g., [263]). The transition required to interpolate between the low curvature of the large-scale structure and the high curvature of the galactic halo sets the strongest bound on the cosmological field ($B_0 \lesssim 10^{-5}$ [263, 269]).

---

[1] Institute for Theoretical Physics, University of Zurich, Winterthurerstrasse 190, CH-8057 Zürich, Switzerland

[2] Brookhaven National Laboratory, Physics Department, Upton NY 11973, USA

[3] Institute for Theoretical Physics, University of Zurich, Winterthurerstrasse 190, CH-8057 Zürich, Switzerland; Physics and Astronomy Department, University of California, and Lawrence Berkeley National Laboratory, Berkeley, California 94720, USA; Ewha University, Seoul 120-750, Korea

[4] Kavli Institute for Cosmological Physics, Department of Astronomy and Astrophysics, Enrico Fermi Institute, University of Chicago, Chicago, Illinois 60637, USA

Independently, strong constraints can also be inferred from the large-scale structure alone. The enhanced growth of structure observed in $f(R)$ gravity models manifests itself on the largest scales of the cosmic microwave background (CMB) temperature anisotropy power spectrum [265], where consistency with CMB data places an upper bound on B_0 of order unity [270]. Cross correlations of the CMB temperature field with foreground galaxies serve as another interesting test of $f(R)$ gravity models [265, 270], tightening the constraint on the Compton wavelength parameter by an order of magnitude (e.g., [271]). However, the currently strongest constraints on $f(R)$ gravity from large scale structures are inferred from the analysis of the abundance of low-redshift X-ray clusters, yielding an improvement over the CMB constraints on the free field amplitude of the Hu-Sawicki [263] ($n = 1$) model of nearly four orders of magnitude [272].

In this paper, we perform an independent analysis of $f(R)$ gravity constraints, focusing on cosmological data only. Our analysis differs from previous studies partially in terms of the theoretical model, the parametrical approach, or data sets implemented. We compare and discuss our results to the constraints of previous analyses. Here, we conduct a Markov chain Monte Carlo (MCMC) study of metric $f(R)$ gravity models that are designed to reproduce the ΛCDM expansion history using data from CMB anisotropies, supernovae distances, the baryon acoustic oscillation (BAO) distances, and the Hubble constant. For observables in the linear regime, we adopt the parametrized post-Friedmann (PPF) framework [273, 274] and its implementation into a standard Einstein-Boltzmann linear theory solver [275] for the theoretical predictions. This framework allows us to include information from the near horizon scales. We also utilize information from the cross correlation between high-redshift galaxies and the CMB through the integrated Sachs-Wolfe (ISW) effect. We further use a probe of the relation between weak gravitational lensing and galaxy flows, as well as data from the abundance of clusters that are identified by overdensities of bright, uniformly red galaxies. Latter yields the tightest constraints on the cosmological parameters, particularly on B_0. We compare these constraints to the results of [272] derived for the Hu-Sawicki model.

In Sec. 4.1.2, we review metric $f(R)$ gravity theory. We present the results of our MCMC study in Sec. 4.1.3 and discuss them in Sec. 4.1.4. Finally, the PPF formalism for $f(R)$ gravity [274] and details about the modifications to the ISWWLL code [276, 277] used for the galaxy-ISW (gISW) cross correlation observations are specified in the appendix.

4.1.2. $f(R)$ gravity

In $f(R)$ gravity, the Einstein-Hilbert action is supplemented by a free function of the Ricci scalar R,

$$S = \frac{1}{2\kappa^2}\int d^4x\sqrt{-g}[R + f(R)] + \int d^4x\sqrt{-g}\mathcal{L}_{\rm m}. \tag{4.1}$$

Here, $\kappa^2 \equiv 8\pi G$ and $\mathcal{L}_{\rm m}$ is the matter Lagrangian, where we have set $c \equiv 1$. Variation with respect to the metric $g_{\alpha\beta}$ yields the modified Einstein equation for metric $f(R)$ gravity,

$$G_{\mu\nu} + f_R R_{\mu\nu} - \left(\frac{f}{2} - \Box f_R\right) g_{\mu\nu} - \nabla_\mu \nabla_\nu f_R = \kappa^2 T_{\mu\nu}, \tag{4.2}$$

where subscripts of R indicate differentiation with respect to the Ricci scalar and the connection is of Levi-Civita type. The modified Friedmann equation is derived in the usual way, i.e., taking the time-time component of Eq. (4.2),

$$H^2 - f_R(H\,H' + H^2) + \frac{f}{6} + H^2 f_{RR} R' = \frac{\kappa^2}{3}\rho, \tag{4.3}$$

where here and throughout the paper primes denote derivatives with respect to $\ln a$.

4.1.2.1. Designer model

The function $f(R)$ can be constructed in a way that it recovers any background history. Given the equation of state of the effective dark energy, $w_{\rm DE}$, one integrates the modified Friedmann equation to obtain the corresponding form of $f(R)$ [265, 278]. It has been pointed out that viable $f(R)$ cosmologies must closely match the ΛCDM expansion history [263, 264]. Here, we focus on flat models and consider modifications to gravity that reproduce the ΛCDM expansion history exactly, i.e., $w_{\rm DE} = -1$, where we neglect contributions from radiation. Note that the restriction to the matter-dominated epoch is well motivated by requiring that the well-tested high-curvature regime reproduces standard phenomenology (e.g., [265]). The ΛCDM background is then given by

$$H^2 = \frac{\kappa^2}{3}(\rho_{\rm m} + \rho_\Lambda). \tag{4.4}$$

Equating it with the matter-dominated Friedmann equation, Eq. (4.3), yields an inhomogeneous second order differential equation for $f(R)$,

$$f'' - \left[1 + \frac{H'}{H} + \frac{R''}{R'}\right] f' + \frac{R'}{6H^2} f = -H_0^2(1-\Omega_{\rm m})\frac{R'}{6H^2}. \tag{4.5}$$

This can be solved numerically with the initial conditions

$$\begin{aligned} f(\ln a_{\rm i}) &= A\,H_0^2 a_{\rm i}^p - 6H_0^2\Omega_\Lambda, & (4.6)\\ f'(\ln a_{\rm i}) &= p\,A\,H_0^2 a_{\rm i}^p, & (4.7) \end{aligned}$$

where $p = (-7+\sqrt{73})/4$ and $a_{\rm i} \sim 0.01$ [265]. A is an initial growing mode amplitude and characterizes a specific solution in the set of functions $f(R)$ that recovers the ΛCDM background. Note that the amplitude of the decaying mode is set to zero in order to not violate constraints in the high-curvature regime. We follow [265] and parametrize our solutions in terms of the Compton wavelength parameter

$$B = \frac{f_{RR}}{1+f_R} R' \frac{H}{H'} \tag{4.8}$$

evaluated at $B_0 \equiv B(\ln a = 0)$ rather than by A. In a Taylor expansion of $f(R)$, the first term corresponds to a cosmological constant, while the second is a rescaling of Newton's constant. With its f_{RR} term, this parametrization therefore captures the essence of the modification. Standard gravity is recovered in the case where $B_0 = 0$. For stability reasons the mass squared of the scalar field f_R must be positive, which implies $B_0 \geq 0$ [265, 279].

4.1.3. Cosmological constraints

We use a variety of cosmological data sets to constrain the $f(R)$ theory of gravity. First we use the CMB anisotropy data from the five-year Wilkinson Microwave Anisotropy Probe (WMAP) [280], the Arcminute Cosmology Bolometer Array Receiver (ACBAR) [281], the Cosmic Background Imager (CBI) [282], and the Very Small Array (VSA) [283]. Next we employ data from the Supernova Cosmology Project (SCP) Union [284] compilation, the measurement of the Hubble constant from the Supernovae and H_0 for the Equation of State (SHOES) [285] program, and the BAO distance measurements of [286]. Furthermore, we take gISW cross correlation observations using the ISWWLL code of [276, 277], the E_G measurement, probing the relation between weak gravitational lensing and galaxy flows, of [287], as well as cluster abundance constraints from the likelihood code of [288] (CA). We quote results with the latter three constraints separately to highlight their impact on the results. For comparison, we also analyze constraints that include the σ_8 measure of the Chandra Cluster Cosmology Project (CCCP) [289].

In Sec. 4.1.3.1, we discuss the predictions for some of these observables for specific values of the Compton wavelength parameter. In Sec. 4.1.3.2, we present the results of a MCMC likelihood analysis, which is conducted with the publicly available COSMOMC [290] package.

4.1.3.1. Cosmological observables

In this section, we illustrate model predictions of the various cosmological observables we use in the constraints. We choose the parameters of the various models that highlight results from the MCMC analysis.

By construction, at high redshifts, the $f(R)$ modifications become negligible, and so we choose a parametrization that separates high-redshift and low-redshift constraints. Specifically we take six high-redshift parameters: the physical baryon and cold dark matter energy density $\Omega_\mathrm{b}h^2$ and $\Omega_\mathrm{c}h^2$, the ratio of sound horizon to angular diameter distance at recombination multiplied by a factor of 100 θ, the optical depth to reionization τ, the scalar tilt n_s, and amplitude A_s at $k_* = 0.002$ Mpc^{-1}.

Since restricting to flat universes, at low redshifts, ΛCDM has no additional parameter, whereas in $f(R)$ gravity, an extra degree of freedom is introduced by the Compton wavelength parameter B_0, where ΛCDM is reproduced in the limit $B_0 \to 0$.

We illustrate predictions from the maximum likelihood ΛCDM model using all of the data (see Table 4.1). For $f(R)$ gravity, where not otherwise specified, we use these ΛCDM best-fit parameters and add nonzero values of B_0 for comparison.

Geometrical measures

The comparison of the magnitudes of high-redshift to low-redshift supernovae yields a relative distance measure. The acoustic peaks in the CMB, the measurement of the local Hubble constant, and the BAO distances additionally provide absolute distance probes which complement the relative distance measure of the supernovae. These probes constrain the background and since our $f(R)$ models are designed to match the ΛCDM expansion history with vanishing effect in the high-curvature regime, they do not generate any tension between the models. For the Hubble constant, we use the SHOES measurement of

$$H_0 = 74.2 \pm 3.6 \text{ km s}^{-1} \text{ Mpc}^{-1}, \tag{4.9}$$

which employs Cepheid measurements to link the low-redshift supernovae to the distance scale established by the maser galaxy NGC 4258. Further, we apply the constraint

$$\Omega_{\rm m} = (0.282 \pm 0.018) \left(\frac{\Omega_{\rm m} h^2}{0.1326} \right)^{0.58} \tag{4.10}$$

from the BAO distance measure of [286] that is obtained from analyzing the clustering of galaxies from the Sloan Digital Sky Survey (SDSS) [291] and the 2-degree Field Galaxy Redshift Survey (2dFGRS) [292]. This measurement yields the tightest constraint on $\Omega_{\rm m}$ and substantially assists in breaking degeneracies with B_0 in the cluster abundance data.

The cosmic microwave background

The CMB probes the geometry of the background history as well as the formation of large-scale structure. The latter manifests itself on the largest scales through the ISW effect from the evolution of the gravitational potential. To predict these effects we implement the PPF modifications described in App. 4.1.A. The incorporation of the PPF formalism into a standard Einstein-Boltzmann linear theory solver yields an efficient way to obtain predictions of $f(R)$ gravity for the CMB. We utilize the PPF modifications to CAMB [293] implemented in Ref. [275], which we configure for $f(R)$ gravity as described by [274].

In Fig. 4.1, we plot the CMB temperature anisotropy power spectrum with respect to angular multipoles ℓ for the best-fit ΛCDM model and the best-fit $f(R)$ gravity model using the Union, SHOES, BAO, and CMB data jointly (see Tables 4.1 and 4.3). Adding an additional freedom from $f(R)$ gravity only yields an insignificant improvement in the fit. Relative to ΛCDM, or equivalently $B_0 = 0$, the growth of structure is enhanced. The ISW effect at the lowest multipoles is decreasing for $B_0 \lesssim 3/2$ [265, 270]. At $B_0 \sim 3/2$, the ISW contribution rises again and turns into a relative enhancement over ΛCDM for $B_0 \gtrsim 3$, ruling out $B_0 \gtrsim 5$ by WMAP data [265, 270].

Due to suppression of $f(R)$ modifications in the high-curvature regime, the CMB acoustic peaks can be utilized as usual to infer constraints on the high-redshift parameters, in particular the physical energy densities of baryonic matter and dark matter as well as the angular diameter distance to recombination.

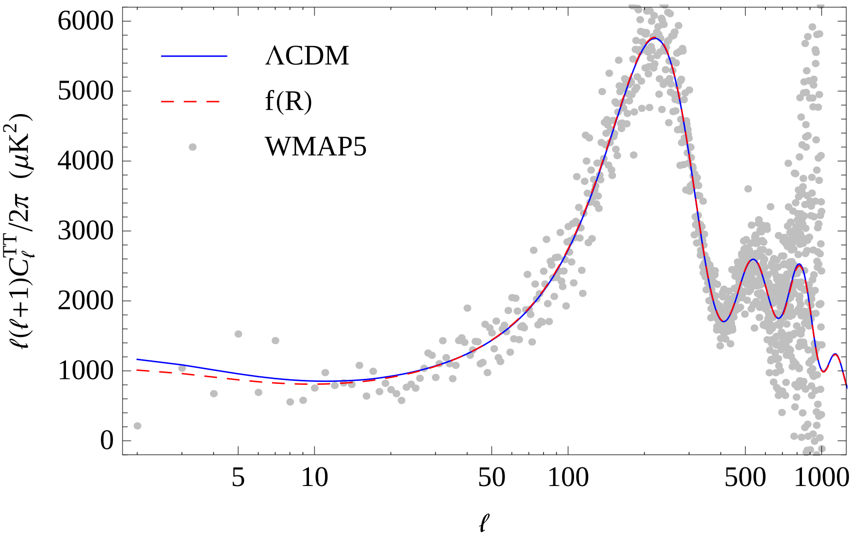

Figure 4.1: Best-fit CMB temperature anisotropy power spectrum for ΛCDM and $f(R)$ gravity from using the Union, SHOES, BAO, and CMB data.

Galaxy-ISW cross correlations

The correlation between galaxy number densities and the CMB anisotropies can be used to isolate the ISW effect in the CMB. Whereas the ISW effect in the CMB is suppressed for $B_0 \lesssim 3$ and enhanced for $B_0 \gtrsim 3$ with respect to $B_0 = 0$, the gISW cross correlation is suppressed for all $B_0 > 0$ and leads eventually to anti-correlations (see Figs. 4.2 and 4.3). This makes the gISW cross correlation interesting for improving constraints (see, e.g., [265, 270]). As was shown in [270], the absence of negative correlations between the CMB and an assortment of galaxy surveys infer a boundary of $B_0 \lesssim 1$. This constraint can be improved by a more rigorous analysis of gISW cross correlations as was performed by, e.g., [271]. This study implements a parametrization for the modifications induced by $f(R)$ gravity that is based on the introduction of an effective scalar degree of freedom in the Einstein-Hilbert action [294, 295] and uses gISW cross correlation data from [296]. Here, we conduct an independent analysis, utilizing the PPF framework and for the calculation of the gISW likelihood, the ISWWLL code of [276, 277], which has turned out to be very useful for constraining infrared modifications of gravity [297–300].

We evaluate the gISW cross correlation in the Limber and quasistatic approximation, as it is done in the ISWWLL code used for the data analysis. The gISW cross correlation in this approximation reads

$$C_\ell^{g_j T} \simeq \frac{3\Omega_\mathrm{m} H_0^2 T_\mathrm{CMB}}{(l+1/2)^2} \int dz f_j(z) H(z) \left[D(a,k) \frac{d}{dz} G(a,k) P(k) \right] \Bigg|_{k=\frac{l+1/2}{\chi(z)}} \quad (4.11)$$

with $z = 1/a - 1$ denoting redshift. Here, $D(a,k)$ is the linear growth rate in the quasistatic regime defined by $\Delta_\mathrm{m}(a,k) = \Delta_\mathrm{m}(1,k)D(a,k)/D(1,k)$, where $\Delta_\mathrm{m}(a,k)$ is the matter density perturbation. $P(k)$ is the matter power spectrum today.

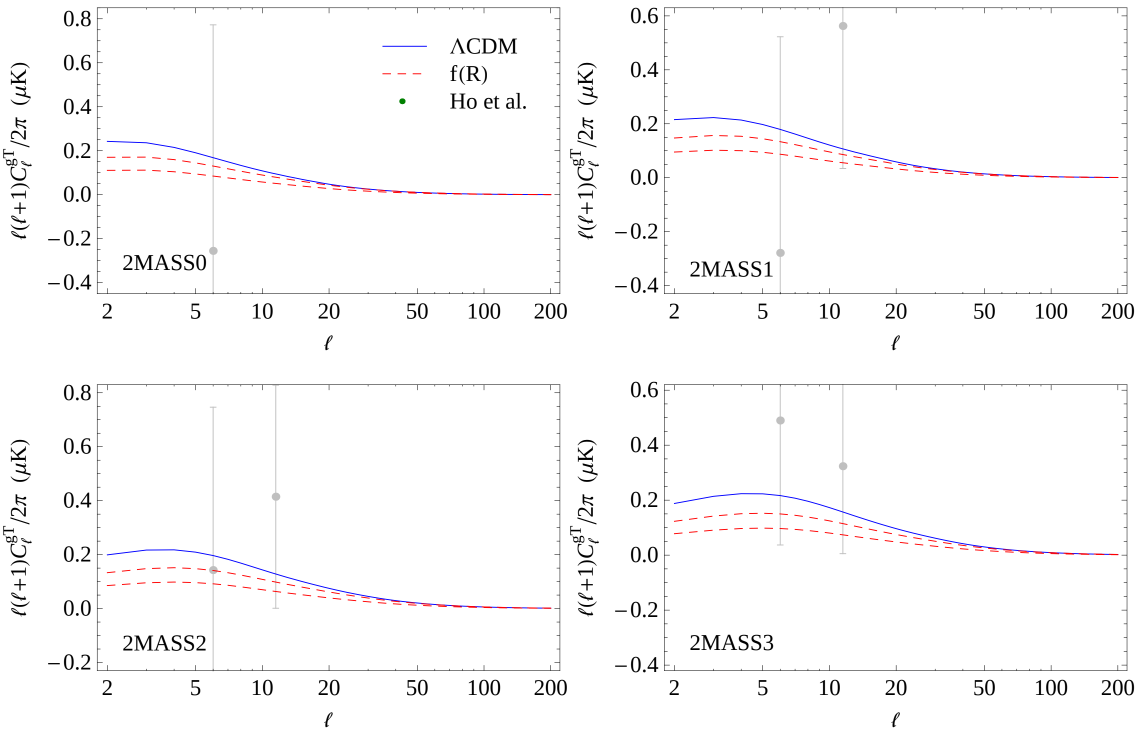

Figure 4.2: Best-fit ΛCDM ($B_0 = 0$) 2MASS gISW cross correlations (blue solid line) for the different galaxy samples, roughly ordered in increasing effective, bias-weighted, redshift. Adding nonzero values for the Compton wavelength parameter (red dashed lines): $B_0 = 0.1$ (top) and $B_0 = 0.5$ (bottom).

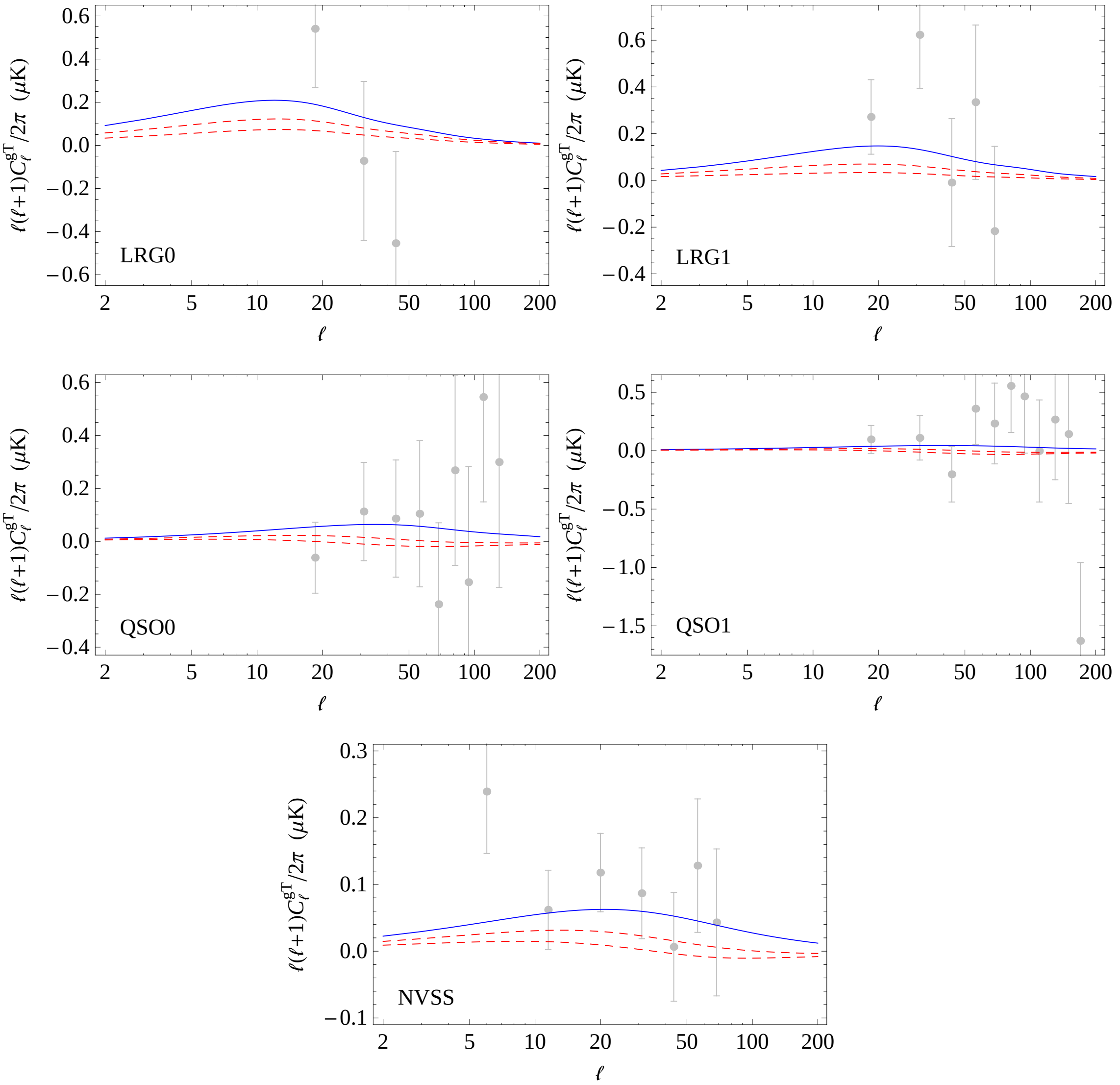

Figure 4.3: Continuation of Fig. 4.2, illustrating the galaxy-ISW cross correlations for the LRG0, LRG1, QSO0, QSO1, and NVSS galaxy samples.

The Limber approximation becomes accurate at the percent level for $\ell \gtrsim 10$. This condition is satisfied by about 90% of the total 42 data points that are used in the ISWWLL code. The data are divided into nine galaxy sample bins j, i.e., 2MASS0-3, LRG0-1, QSO0-1, and NVSS. The function $f_j(z)$ relates the matter density to the observed projected galaxy overdensity with $f_j(z) = b_j(z)\Pi_j(z)$ in the absence of magnification bias. $\Pi_j(z)$ is the redshift distribution of the galaxies and the bias factor $b_j(z)$ is assumed independent of scale (cf. [301]), but dependent on redshift. The code determines $f_j(z)$, among other things, from fitting auto power spectra and cross power spectra between the samples. We refer to App. 4.1.B for more details about the data and the accuracy of the Limber approximation.

Scalar linear perturbations of the Friedmann metric are presented here in longitudinal gauge, i.e.,

$$ds^2 = -(1+2\Psi)dt^2 + a^2(1+2\Phi)d\mathbf{x}^2, \tag{4.12}$$

where $d\mathbf{x}^2$ is the unperturbed spatial line element with curvature $K = 0$. We define $\Phi_- \equiv (\Phi - \Psi)/2$. In the quasistatic regime, we infer

$$\begin{aligned} G(a,k) &= \frac{\Phi_-(a,k)}{\Phi_-(a_\mathrm{i},k)} \frac{\Delta_\mathrm{m}(a_\mathrm{i},k)}{\Delta_\mathrm{m}(1,k)} \frac{1}{a_\mathrm{i}} \\ &\simeq \frac{1}{1+f_R} \frac{D(a,k)}{D(1,k)} \frac{1}{a} \end{aligned} \tag{4.13}$$

from the modified Poisson equation,

$$k^2\Phi_-(a,k) = \frac{1}{2}\frac{\kappa^2}{1+f_R}\frac{H_0^2\Omega_\mathrm{m}}{a}\Delta_\mathrm{m}(a,k), \tag{4.14}$$

requiring that the initial conditions lie well within the high-curvature regime, where general relativity holds. This implies $\Phi_-(a_\mathrm{i},k) \simeq \Phi_-(a_\mathrm{i})$, $D(a_\mathrm{i},k) \simeq D(a_\mathrm{i})$, and $f_R(a_\mathrm{i}) \simeq 0$. We solve the ordinary differential equation

$$\Delta_\mathrm{m}'' + \left(2 + \frac{H'}{H}\right)\Delta_\mathrm{m}' - \frac{3}{2}\frac{1-g(a,k)}{1+f_R}\frac{H_0^2\Omega_\mathrm{m}}{H^2a^3}\Delta_\mathrm{m} = 0 \tag{4.15}$$

for the linear matter density perturbation $\Delta_\mathrm{m}(a,k)$, where $g(a,k)$ is the metric ratio in PPF formalism (see App. 4.1.A). Note that in the limit $B_0 \to 0$, we have $g \to 0$. Therefore, in this limit, Eq. (4.15) recovers the quasistatic ordinary differential equation for the matter overdensity in ΛCDM. We solve Eq. (4.15) with initial conditions at $a_\mathrm{i} \ll 1$, in a regime where general relativity is expected to hold, i.e., $\Delta_\mathrm{m}'(a_\mathrm{i},k) = \Delta_\mathrm{m}(a_\mathrm{i},k)$ with a normalization set by the initial power spectrum. At the scales that are relevant for the gISW cross correlations, the product $D\,dG/dz$ used in Eq. (4.11) is accurately described through solving Eq. (4.15) for Δ_m and using the approximated $G(a,k)$ of Eq. (4.13). We show this by comparing the approximated product to its counterpart from a full derivation within linear perturbation theory (see Figs. 4.4 and 4.5). We take the relations that exactly describe the scalar linear perturbation theory in $f(R)$ gravity for a matter-only universe from Ref. [265].

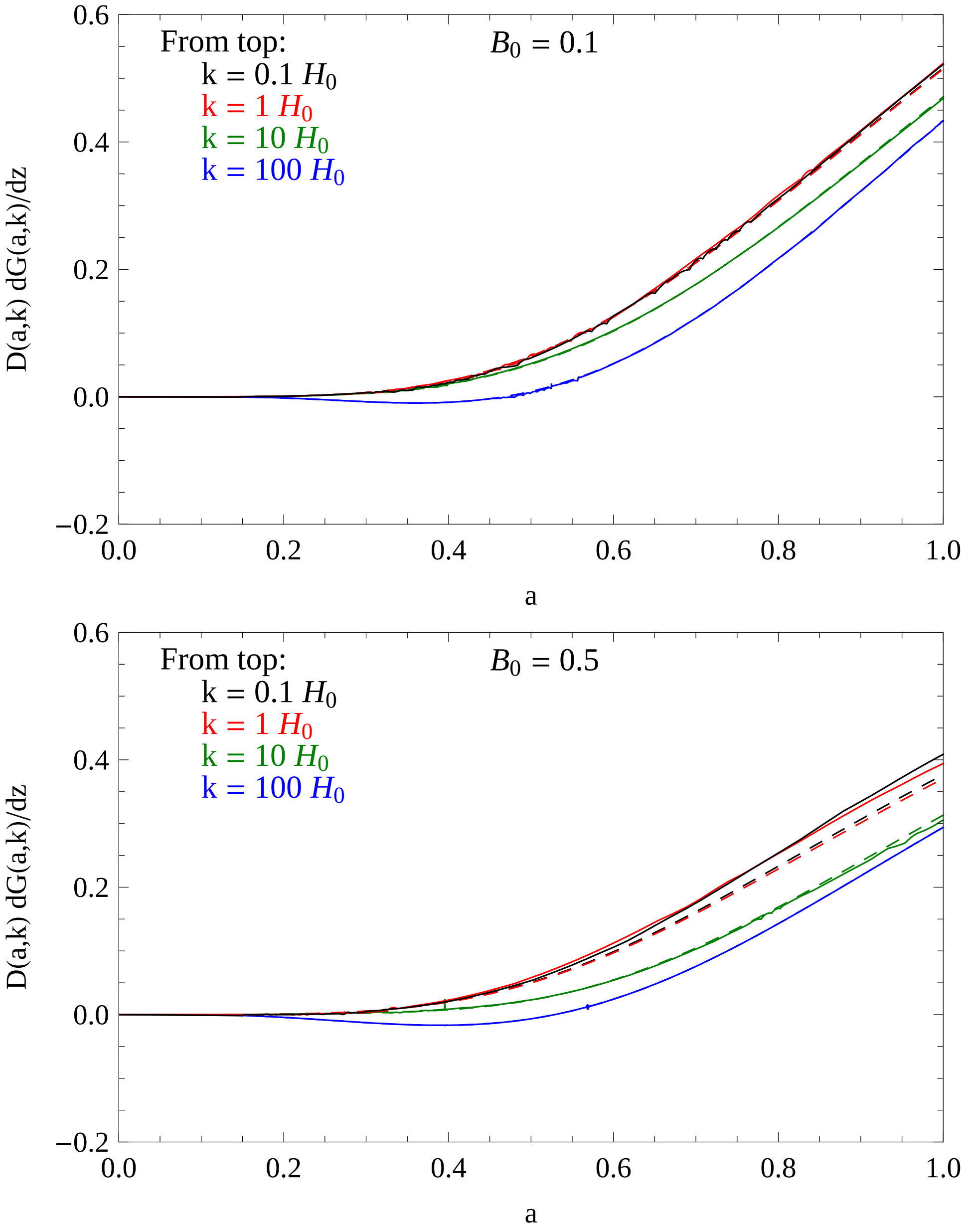

Figure 4.4: Product of the linear density growth rate D and the derivative of the linear potential growth rate G with respect to redshift z. Solid lines are derived from linear perturbation theory, dashed lines are obtained through the approximation described in Sec. 4.1.3.1, using $h = 0.73$ and $\Omega_\mathrm{m} = 0.24$. Note that $H_0 \simeq 3 \times 10^{-4} h$ Mpc^{-1}.

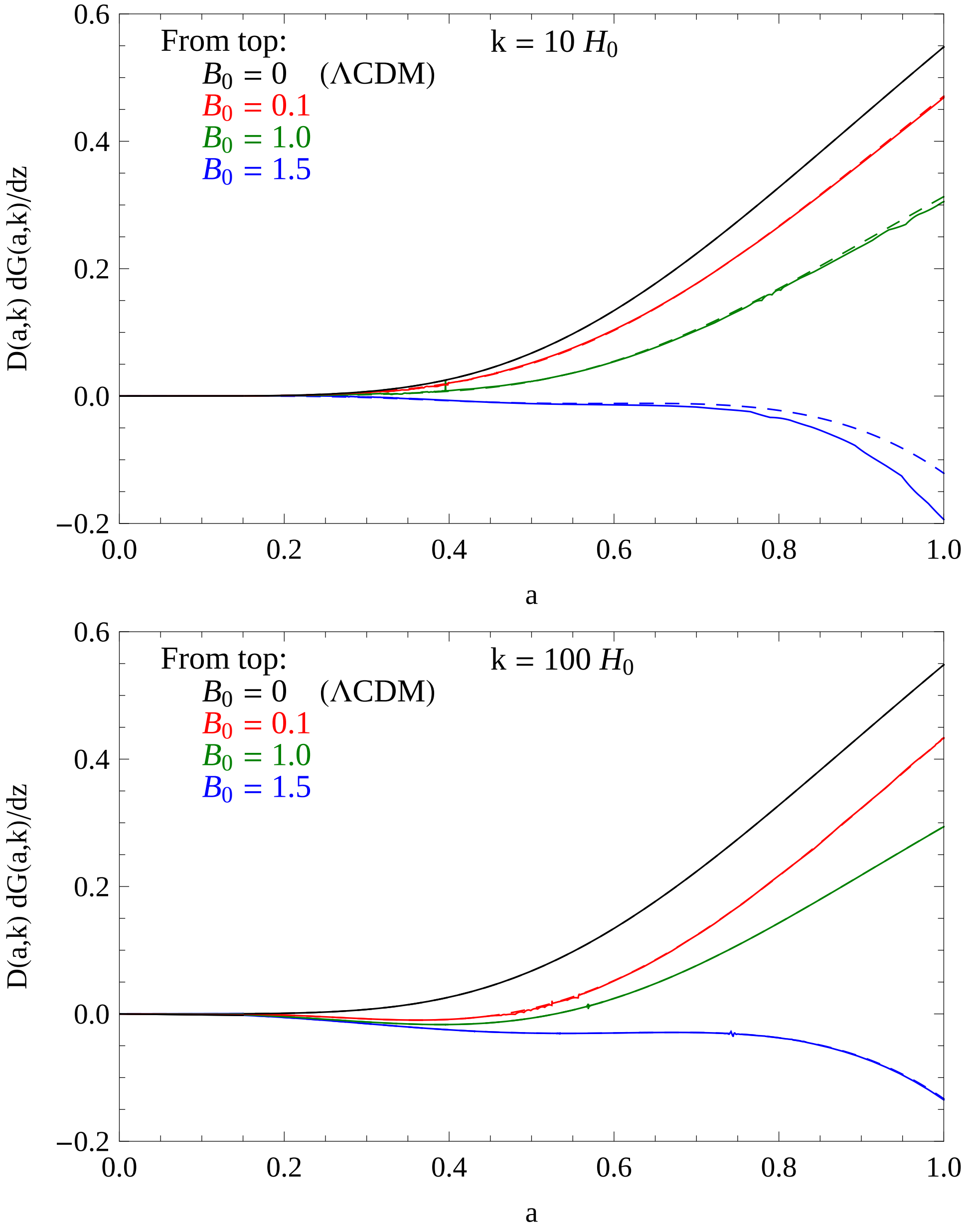

Figure 4.5: Same as Fig. 4.4 but for different values of the Compton wavelength parameter B_0.

Weak gravitational lensing and galaxy flows

The relationship of weak gravitational lensing around galaxies to their large-scale velocities has been proposed as a smoking gun of gravity [302]. The advantage of such a probe lies in its insensitivity to galaxy bias and initial matter fluctuations. The expectation value of the ratio of galaxy-galaxy to galaxy-velocity cross correlations of the same galaxies yields an estimator [302]

$$E_G = \frac{\Omega_{\mathrm{m}}}{(1+f_R)\beta}, \tag{4.16}$$

where $\beta \equiv d\ln\Delta_{\mathrm{m}}/d\ln a$. Recently this quantity has been measured analyzing 70 205 luminous red galaxies [303] from the SDSS [304], yielding $E_G = 0.392 \pm 0.065$ [287] by averaging over scales $R = (10-50)h^{-1}$ Mpc. Note that the E_G measurement is based on spectroscopic LRG samples, whereas the gISW analysis uses photometric LRG samples that do not overlap in redshift. Furthermore, the error on E_G is dominated by uncertainties in lensing and redshift space distortions and most of the signal comes from small scales around $10h^{-1}$ Mpc. The gISW signal is dominated by large scales and most of the error is caused by sampling variance and shot noise of galaxies. Therefore, we can safely neglect correlations between the E_G and gISW data sets.

We calculate Δ_{m} from solving Eq. (4.15), which yields a good approximation to E_G for the scales and Compton wavelength parameters of interest. We illustrate predictions for E_G in Fig. 4.6. The red-dashed lines show the approximated values and crosses indicate check points derived using full linear perturbation theory. At the redshift of the measurement, $z = 0.32$, and in the linear regime of $f(R)$ gravity, Eq. (4.16) is only weakly dependent on scale and shows no k-dependence at all for $B_0 = 0$. Therefore, we only need to evaluate E_G at a representative scale, which we choose here as $k = 0.1h$ Mpc^{-1}. We can then compare this value to the mean E_G observation from [287]. At small values of the Compton wavelength parameter ($B_0 \lesssim 0.01$), a k-dependence shows up for $k \lesssim 0.1h$ Mpc^{-1}. However, the effect is small compared to the error in E_G and is subdominant to the uncertainty in Ω_{m}.

Figure 4.6 demonstrates that the E_G probe has the potential to discriminate between ΛCDM and $f(R)$ gravity even at low values of B_0.

Cluster abundance

Tighter constraints on modified gravity theories and in particular on $f(R)$ gravity than from the linear theory probes can be achieved by testing the weakly to fully nonlinear scales (cf. [272, 305, 306]). We use the abundance of clusters to set our strongest boundary on the possible B_0 values. We employ a preliminary version of the likelihood code of [288], which utilizes constraints from the most massive halos ($M > 10^{13}\ M_{\odot}/h$) inferred from SDSS data. The galaxy-galaxy lensing signal from clusters and groups from the MaxBCG catalog [307] is measured in three cumulative mass bins corresponding to the nominal number densities of groups of 2.5×10^{-7} (Mpc/h)$^{-3}$, 2×10^{-6} (Mpc/h)$^{-3}$, and 1.8×10^{-5} (Mpc/h)$^{-3}$ and in two redshift bins of $z = 0.18$ and $z = 0.25$. This signal is compared to the theoretical predictions based on the mass function calibrated with N-body simulations,

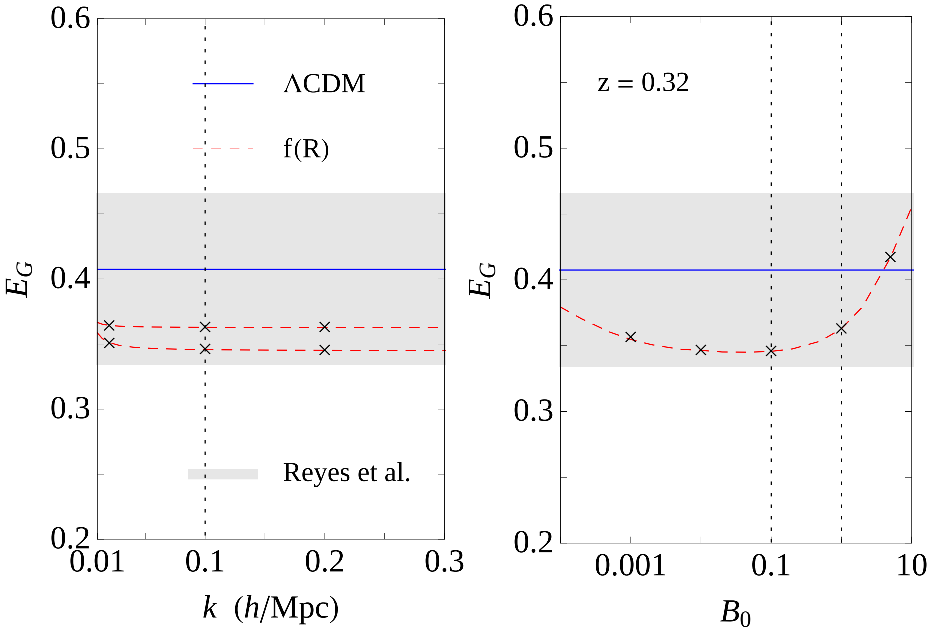

Figure 4.6: Best-fit ΛCDM ($B_0 = 0$) E_G prediction from linear theory (blue solid line). Left panel: adding nonzero values for the Compton wavelength parameter (red dashed lines): $B_0 = 1$ (top) and $B_0 = 0.1$ (bottom). Right panel: E_G at different values of B_0, evaluated at $k = 0.1h$ Mpc^{-1}.

correctly taking into account mass-observable scatter, calibration uncertainties and covariances. We refer to App. 4.1.C for more details.

For comparison, we additionally analyze constraints from applying the σ_8 measurement of [289],

$$\sigma_8 \left(\frac{\Omega_\mathrm{m}}{0.25}\right)^{0.47} = 0.813 \pm 0.013\ (\mathrm{stat}) \pm 0.024\ (\mathrm{sys}), \tag{4.17}$$

inferred from *Chandra* observations of X-ray galaxy cluster samples detected in the *ROSAT* All-Sky Survey by normalizing the mass function at low redshifts. The halos in the sample have masses $M > 10^{12}\ M_\odot/h$. This data was used by [272] to put a constraint of $|f_{R0}| < \left(1.3^{+1.7}_{-0.6}\right) \times 10^{-4}$ ($B_0 \lesssim 10^{-3}$) (95% confidence level) on the Hu-Sawicki [263] $f(R)$ gravity model. The range indicates a ∓9% mass calibration error corresponding to the systematic error in Eq. (4.17). Note that in the likelihood analysis, we add the systematic error in quadrature. The constraint is obtained from using modified forces in the spherical collapse calculations. Using standard spherical collapse instead reduces this number to $|f_{R0}| < 0.4 \times 10^{-4}$ (95% confidence level) [272]. An estimate for the range induced from the mass calibration error can be obtained through scaling from the former result, i.e., $|f_{R0}| \lesssim \left(0.4^{+0.5}_{-0.2}\right) \times 10^{-4}$. This corresponds to an upper bound of $|f_{R0}| \lesssim 1.4 \times 10^{-4}$ at the 95% confidence level of both the statistical and systematic error.

4.1.3.2. Constraints

Our basic cosmological parameter set we use in the MCMC analysis is $P = \{\Omega_\mathrm{b}h^2, \Omega_\mathrm{c}h^2, \theta, \tau, n_\mathrm{s}, \ln[10^{10}A_\mathrm{s}]\}$. On this set we implement the following flat priors: $\Omega_\mathrm{b}h^2 \in (0.01, 0.1)$, $\Omega_\mathrm{c}h^2 \in (0.045, 0.99)$, $\theta \in (0.5, 10)$, $\tau \in (0.01, 0.8)$, $n_\mathrm{s} \in (0.5, 1.5)$, and $\ln[10^{10}A_\mathrm{s}] \in (2.7, 4)$. For $f(R)$ gravity models, where $P \to P \cup \{B_0\}$, we set a flat prior on the free Compton wavelength parameter of $B_0 \in (0, 10)$.

We begin with the analysis of ΛCDM in Tables 4.1 and 4.2. We show constraints of using separately gISW, E_G, CA, and E_G & CA data together with the CMB, SHOES, BAO, and Union measurements, as well as when using all of the data jointly. We also quote maximum likelihood parameters and value. Horizontal lines divide the chain parameters from the derived parameters and the best-fit (maximum) likelihood. Notice the improved constraints for ΛCDM that are obtained by the inclusion of the CA data. This analysis sets the baseline to which adding the $f(R)$ degree of freedom should be measured.

In this paper, we study flat metric $f(R)$ gravity models that reproduce the ΛCDM expansion history. Therefore, the SHOES, BAO, and Union measurements only fix the background and do not distinguish standard from modified gravity. However, they contribute to the breaking of degeneracies that show up in other data sets and help tightening the constraints. When introducing the CMB probes, some additional information becomes available. In fact, we observe that $f(R)$ gravity yields a slightly better fit than flat ΛCDM, which can be attributed to the lowering of the temperature anisotropy power spectrum at small ℓ (see Fig. 4.1), but the improvement in the fit is not at a significant level (see Table 4.3). In contrast to flat ΛCDM, where the inclusion of the gISW data does not yield noticeable improvement on the parameter constraints [276], in the case of $f(R)$ gravity, an order of magnitude improvement on the B_0 constraint is achieved, i.e., $B_0 < 0.42$ at the 95% confidence level. This constraint is in perfect agreement with the independent result of [271], who found an upper bound on the Compton wavelength parameter of $B_0 < 0.4$ at the 95% confidence level, using gISW cross correlations data from [296]. Including the cluster abundance data instead yields another two orders of magnitude improvement over the gISW constraint, i.e., $B_0 < 3.33 \times 10^{-3}$. Here and throughout this section, we quote constraints at the 95% confidence level. If we add either the gISW or E_G data, this bound tightens by a factor of 1.9 or 2.2, respectively. The joint constraint on the Compton wavelength parameters of $B_0 < 1.12 \times 10^{-3}$ (a factor of 3.0) (see Table 4.4) is our main result and is inferred from combining all of the data sets. We therefore found that the gISW and E_G probes are good complementary tests to cluster abundance. In Figs. 4.7 and 4.8, we plot the marginalized likelihood for B_0 and the 2D-marginalized contours for B_0 and $\Omega_{\rm m}$, respectively, with different combinations of the data sets, illustrating this point. It applies particularly to E_G, where bounds on B_0 become looser in the absence of data from cluster abundance. This is what one expects from the trend seen in Fig. 4.6, i.e., for $B_0 \gtrsim 0.1$ the E_G prediction approaches its ΛCDM value and eventually overshoots it.

If we additionally include CCCP to our joint set of data, we obtain a constraint of $B_0 < 0.96 \times 10^{-3}$ or equivalently $|f_{R0}| < 1.65 \times 10^{-4}$. If we take CCCP with neither gISW, E_G, nor CA the constraint becomes $B_0 < 1.83 \times 10^{-3}$ or equivalently $|f_{R0}| < 3.12 \times 10^{-4}$. The constraint is a factor of 2.2 times weaker than what we estimated from the result of [272] when adding the systematic error from mass calibration in the case of standard spherical collapse (see Sec. 4.1.3.1). Note that we have used σ_8 predicted directly by $f(R)$ gravity in Eq. (4.17) rather than constraining the rescaled normalization $\sigma_8^{\rm eff}$ in ΛCDM that matches the halo mass function in $f(R)$ gravity at the pivot mass $M_{\rm eff} = 3.667 \times 10^{14}\ {\rm M}_\odot/h$ ($M = M_{500}$) (cf. [272]). In the case of standard spherical collapse, this leads to an overestimation of $f(R)$ gravity effects on σ_8 of $\sim 2\%$ for $B_0 = 10^{-3}$. The error of the CCCP measurement in Eq. (4.17) is $\sim \pm 3\%$. Also note that the CA data infer a preliminary constraint of [288]

$$\sigma_8 \left(\frac{\Omega_{\rm m}}{0.25} \right)^{0.40} = 0.844 \pm 0.036, \tag{4.18}$$

which is a slightly larger value than in Eq. (4.17) and therefore admits larger values of B_0, i.e., using CCCP instead of CA (without gISW and E_G) tightens the 95% confidence boundary on B_0 by a factor of 1.8. It is also important to keep in mind that the constraint of [272] is inferred for the Hu-Sawicki model that exhibits an enhanced linear growth with respect to the designer model studied here (see, e.g., [308]).

Finally, note that since ΛCDM is reproduced in the limit $B_0 \to 0$, the slightly poorer fits of $f(R)$ gravity with respect to ΛCDM (see Tables 4.3 and 4.4) have to be attributed to sampling errors in the chains.

4.1.4. Discussion

We have performed a MCMC analysis on metric $f(R)$ gravity models that exactly reproduce the ΛCDM expansion history. In addition to geometrical probes from

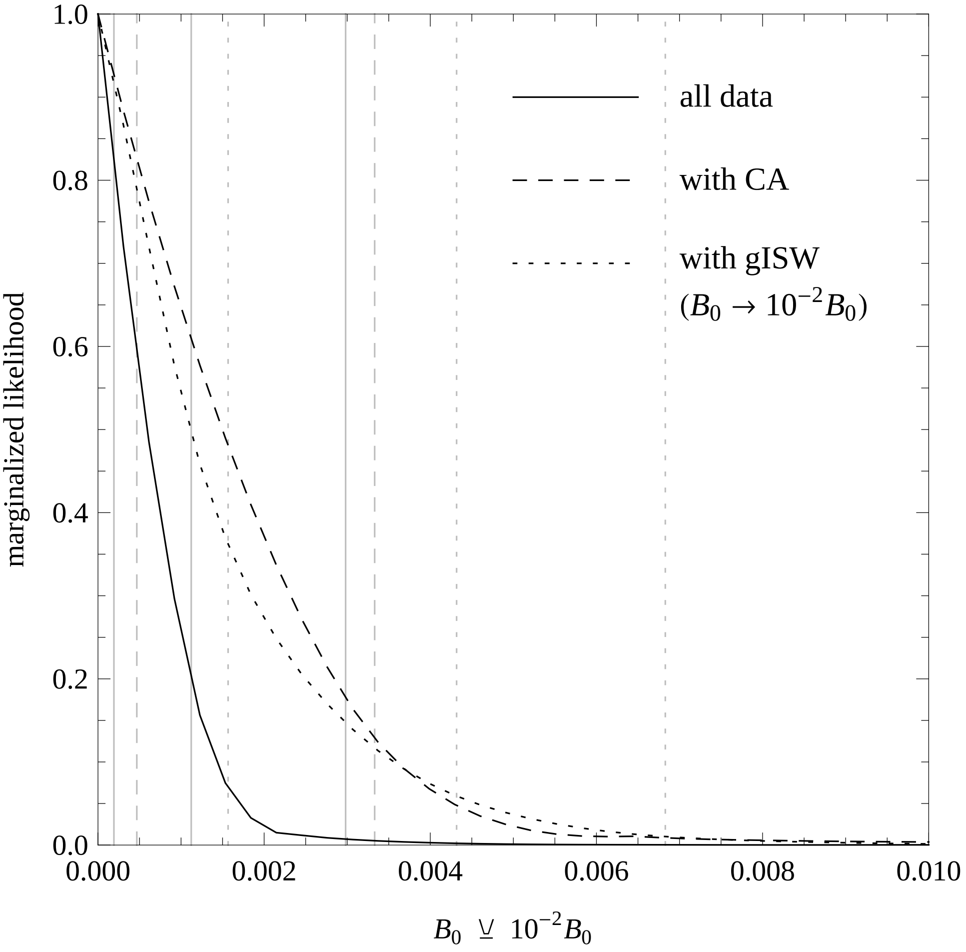

Figure 4.7: Marginalized likelihood for B_0 when using WMAP5, ACBAR, CBI, VSA, Union, SHOES, and BAO in combination with the additional data sets. For gISW, the Compton wavelength parameter is rescaled as $B_0 \to 10^{-2}B_0$, i.e., the constraint is a factor of 10^2 weaker than illustrated. The horizontal lines indicate 68%, 95%, and 99% confidence levels.

Parameters	ΛCDM		ΛCDM (with gISW)		ΛCDM (with E_G)	
$100\Omega_b h^2$	2.235 ± 0.053	2.232	2.235 ± 0.054	2.237	2.235 ± 0.054	2.228
$\Omega_c h^2$	0.1128 ± 0.0036	0.1137	0.1124 ± 0.0036	0.1125	0.1127 ± 0.0037	0.1131
θ	1.0407 ± 0.0026	1.0402	1.0406 ± 0.0027	1.0406	1.0406 ± 0.0027	1.0409
τ	0.082 ± 0.015	0.079	0.084 ± 0.016	0.085	0.082 ± 0.016	0.081
n_s	0.957 ± 0.012	0.955	0.958 ± 0.012	0.956	0.957 ± 0.012	0.957
$\ln[10^{10}A_s]$	3.202 ± 0.038	3.204	3.202 ± 0.038	3.210	3.202 ± 0.039	3.202
Ω_m	0.273 ± 0.016	0.279	0.271 ± 0.016	0.271	0.272 ± 0.016	0.273
H_0	70.4 ± 1.4	69.9	70.6 ± 1.3	70.5	70.5 ± 1.3	70.3
$-2\ln L$	3027.812		3061.630		3027.826	

Table 4.1: Means, standard deviations (left subdivision of columns) and best-fit values (right subdivision of columns) with likelihood for the flat ΛCDM model using data from WMAP, ACBAR, CBI, VSA, Union, BAO, and SHOES (left column). Including one of the gISW (middle column) and E_G data sets (right column).

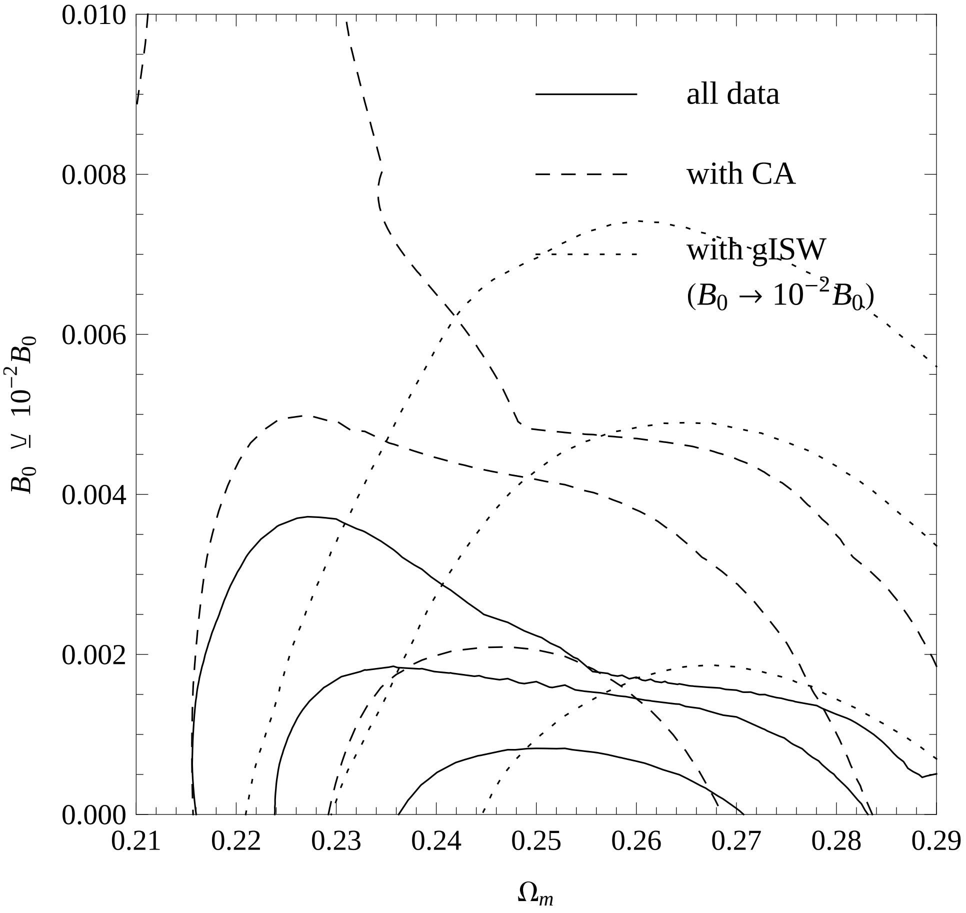

Figure 4.8: Contours of 2D marginalized 68%, 95%, and 99% confidence boundaries using WMAP5, ACBAR, CBI, VSA, Union, SHOES, and BAO in combination with the additional data sets. For gISW, the Compton wavelength is rescaled as $B_0 \to 10^{-2}B_0$, i.e., the constraint is a factor of 10^2 weaker than illustrated. gISW cross correlations favor higher values of Ω_m and break the degeneracy between Ω_m and B_0 seen in the CA data.

Parameters	ΛCDM (with CA)		ΛCDM (with E_G&CA)		ΛCDM (all)	
$100\Omega_\mathrm{b}h^2$	2.228 ± 0.051	2.233	2.229 ± 0.053	2.229	2.231 ± 0.053	2.239
$\Omega_\mathrm{c}h^2$	0.1107 ± 0.0019	0.1112	0.1107 ± 0.0020	0.1112	0.1107 ± 0.020	0.1108
θ	1.0401 ± 0.0025	1.0400	1.0402 ± 0.0025	1.0406	1.0403 ± 0.0026	1.0408
τ	0.081 ± 0.015	0.080	0.081 ± 0.015	0.078	0.082 ± 0.015	0.078
n_s	0.956 ± 0.012	0.957	0.956 ± 0.012	0.956	0.956 ± 0.012	0.957
$\ln[10^{10}A_\mathrm{s}]$	3.195 ± 0.035	3.191	3.195 ± 0.036	3.193	3.196 ± 0.036	3.185
Ω_m	0.2642 ± 0.0099	0.2664	0.2638 ± 0.0098	0.2654	0.2634 ± 0.0098	0.2622
H_0	71.0 ± 1.1	70.8	71.0 ± 1.1	70.9	71.1 ± 1.1	71.3
$-2\ln L$	3032.706		3032.746		3066.240	

Table 4.2: Same as Table 4.1 but including the CA (left column), both E_G and CA (middle column), and all (right column) additional data sets.

Parameters	$f(R)$		$f(R)$ (with gISW)		$f(R)$ (with E_G)	
$100\Omega_\mathrm{b}h^2$	2.223 ± 0.053	2.206	2.225 ± 0.054	2.253	2.224 ± 0.054	2.206
$\Omega_\mathrm{c}h^2$	0.1123 ± 0.0036	0.1109	0.1117 ± 0.0036	0.1133	0.1125 ± 0.0036	0.1131
θ	1.0403 ± 0.0027	1.0392	1.0403 ± 0.0027	1.0416	1.0403 ± 0.0027	1.0394
τ	0.083 ± 0.016	0.082	0.084 ± 0.016	0.090	0.083 ± 0.016	0.083
n_s	0.954 ± 0.012	0.950	0.954 ± 0.012	0.965	0.954 ± 0.013	0.952
$\ln[10^{10}A_\mathrm{s}]$	3.212 ± 0.040	3.215	3.209 ± 0.039	3.200	3.213 ± 0.039	3.221
$100B_0$	< 315	28	< 43.2	0.0	< 319	30
Ω_m	0.272 ± 0.016	0.268	0.269 ± 0.016	0.272	0.273 ± 0.016	0.279
H_0	70.4 ± 1.4	70.4	70.7 ± 1.3	70.7	70.3 ± 1.3	69.6
$10^3\lvert f_{R0}\rvert$	< 350	46	< 69.4	0.0	< 353	51
$-2\Delta \ln L$	-1.104		1.506		-0.696	

Table 4.3: Same as Table 4.1, but for $f(R)$ gravity. $-2\Delta \ln L$ is quoted with respect to the corresponding maximum likelihood flat ΛCDM model. Limits on B_0 and $|f_{R0}|$ indicate the one-sided 1D marginalized upper 95% confidence level. Note that as $B_0 \to 0$ reproduces ΛCDM predictions, the slightly poorer fits of $f(R)$ gravity should be attributed to sampling error in the MCMC runs.

Parameters	$f(R)$ (with CA)		$f(R)$ (with E_G&CA)		$f(R)$ (all)	
$100\Omega_\mathrm{b}h^2$	2.209 ± 0.054	2.204	2.213 ± 0.054	2.235	2.216 ± 0.054	2.210
$\Omega_\mathrm{c}h^2$	0.1064 ± 0.0032	0.1112	0.1073 ± 0.0029	0.1108	0.1076 ± 0.0028	0.1104
θ	1.0390 ± 0.0027	1.0398	1.0392 ± 0.0027	1.0413	1.0394 ± 0.0027	1.0398
τ	0.077 ± 0.016	0.080	0.077 ± 0.015	0.084	0.079 ± 0.015	0.075
n_s	0.953 ± 0.012	0.951	0.954 ± 0.012	0.956	0.954 ± 0.012	0.951
$\ln[10^{10}A_\mathrm{s}]$	3.175 ± 0.0038	3.209	3.179 ± 0.037	3.203	3.182 ± 0.0037	3.193
$100B_0$	< 0.333	0.000	< 0.152	0.000	< 0.112	0.001
Ω_m	0.247 ± 0.014	0.268	0.251 ± 0.012	0.261	0.252 ± 0.012	0.264
H_0	72.2 ± 1.4	70.5	71.9 ± 1.3	71.4	71.9 ± 1.2	70.8
$10^3\lvert f_{R0}\rvert$	< 0.484	0.001	< 0.263	0.000	< 0.194	0.002
$-2\Delta \ln L$	0.802		0.264		0.926	

Table 4.4: Same as Table 4.2, but for $f(R)$ gravity. See also Table 4.3.

supernovae, BAO distance, and Hubble constant measurements, which were used to fix the background, we utilized all of the CMB data, including the lowest multipoles, its correlation with galaxies, the comparison of weak gravitational lensing to large-scale velocities, and the abundance of clusters.

We report a constraint on the Compton wavelength parameter of $B_0 < 1.1 \times 10^{-3}$ at the 95% confidence level from using all of the measurements. This result is substantially driven by data from cluster abundance. However as the data improve, the limits will saturate due to the chameleon effect in massive haloes. gISW measures in combination with the CMB, supernovae, BAO distance, and Hubble constant probes, yield a constraint of $B_0 < 0.42$ (95% confidence level), which is an order of magnitude improvement over using the CMB alone as probe of the growth of large-scale structure in combination with the geometrical measures. This highlights the power of gISW measurements as a linear theory probe to constrain infrared modifications of gravity.

The E_G measurement of the relationship between weak gravitational lensing and galaxy flows does not improve bounds on $f(R)$ gravity on its own. However, when used as a complementary probe to cluster abundance, it contributes substantially to our constraints. This can be attributed to the slow convergence of its prediction toward ΛCDM when $B_0 \to 0$. It is likely that with improved data, the E_G probe will become an important discriminator for gravity models.

Acknowledgments

We would like to thank Fabian Schmidt, Wenjuan Fang, and Tristan Smith for useful discussions and Doug Potter for technical support. We are very grateful to Rachel Mandelbaum for providing preliminary results for the galaxy-galaxy lensing signal from clusters and groups from the MaxBCG catalog. Computational resources were provided on the zBox2, zBox3, and Schrödinger supercomputers at the University of Zurich. This work was supported by the Swiss National Foundation under Contract No. 2000_124835/1, WCU Grant No. R32-2008-000-10130-0, and the U.S. Department of Energy under Contract No. DE-AC02-98CH10886. W.H. was supported by the KICP under NSF contract PHY-0114422, DOE contract DE-FG02-90ER-40560 and the Packard Foundation.

4.1.A. PPF linear theory

Given the expansion history, the PPF framework [273, 274] is defined by three functions and one parameter. From these quantities, the dynamics are determined by conservation of energy and momentum and the Bianchi identities. The defining quantities are $g(a,k)$, which quantifies the effective anisotropic stress of the modifications and distinguishes the two gravitational potentials, $f_\zeta(a)$, which describes the relationship between the matter and the metric on superhorizon scales, and $f_G(a)$, which defines it in the linearized Newtonian regime. The additional parameter c_Γ is the transition scale between the superhorizon and Newtonian behaviors. For $f(R)$ gravity the PPF expressions were developed in [273]. For completeness, we shall review it here.

At superhorizon scales, the metric ratio

$$g_{\mathrm{SH}}(\ln a) = \frac{\Phi + \Psi}{\Phi - \Psi} \tag{4.19}$$

is obtained from solving the differential equation

$$\Phi'' + \left(1 - \frac{H''}{H'} + \frac{B'}{1-B} + B\frac{H'}{H}\right)\Phi' + \left(\frac{H'}{H} - \frac{H''}{H'} + \frac{B'}{1-B}\right)\Phi = 0 \tag{4.20}$$

where $k/(a\,H) \to 0$, and using the relation

$$\Psi = \frac{-\Phi - B\,\Phi'}{1-B}, \tag{4.21}$$

where $k/(a\,H) \to 0$ [273]. This follows from conservation of curvature fluctuation ($\zeta' = 0$) and momentum, considering the superhorizon anisotropy relation $\Phi + \Psi = B\,H'q$ [265], where q is the momentum fluctuation.

In the quasistatic regime, we have $g_{\mathrm{QS}} = -1/3$ and at intermediate scales

$$g(a,k) = \frac{g_{\mathrm{SH}} + g_{\mathrm{QS}}[c_g k/(a\,H)]^{n_g}}{1 + [c_g k/(a\,H)]^{n_g}}, \tag{4.22}$$

where $c_g = 0.71\sqrt{B}$ and $n_g = 2$ [273]. Further, $f_\zeta = -g_{\mathrm{SH}}/3$, $f_G = f_R$ and $c_\Gamma = 1$ [273].

We supply the PPF modified CAMB code [275] with the functions defined above. This gives a good approximation for $B_0 \lesssim 1$. Above this value, the approximation begins to break down at intermediate scales and low redshifts, as we have tested by comparing the metric ratio predicted by the PPF functions and the exact numerical solution for the ordinary differential equations describing scalar linear perturbation theory in $f(R)$ gravity for a matter-only universe. The expressions defining the $f(R)$ scalar linear perturbation theory can be found in [265]. This deviation shows up in the low multipoles of the CMB for high B_0 and partially manifests itself when comparing constraints on B_0 derived from the CMB with the results of [270]. However, when including gISW measures or cluster abundance, the viable values of B_0 lie well within the regime where the approximation holds.

4.1.B. The ISWWLL code for $f(R)$ gravity

We use the publicly available ISWWLL code [276, 277] for our analysis. Note that we have turned off weak lensing contributions in the code, focusing only on the gISW constraints. The 42 data points of gISW cross correlations that are used in the likelihood analysis are collected from the Two Micron All Sky Survey (2MASS) extended source catalog (XSC) [309, 310], the luminous red galaxies (LRGs) and photometric quasars (QSO) of the SDSS [311], and the National Radio Astronomy Observatory (NRAO) Very Large Array (VLA) Sky Survey (NVSS) [312]. They are divided into nine galaxy sample bins j (2MASS0-3, LRG0-1, QSO0-1, and NVSS) based on flux (2MASS) or redshift (LRG and QSO). These data points are a selection of multipole bins from all samples, where the selection is based on the avoidance of nonlinearities and systematic effects from dust extinction, galaxy foregrounds, the thermal Sunyaev-Zel'dovich effect, and point source contamination to affect the gISW cross correlations [276].

In the remainder of App. 4.1.B, we discuss the validity of the Limber approximation and elucidate the function $f_j(z)$ that carries information about the redshift distribution and bias in the context of $f(R)$ gravity.

4.1.B.1. Limber approximation

For $f(R)$ gravity the gISW cross correlations are well described within the approximations given in Sec. 4.1.3.1. The applicability of approximating the product $D\,dG/dz$ in Eqs. (4.11) through (4.15) and (4.13) is a direct consequence of applying the Limber approximation. This can easily be seen from Figs. 4.4 and 4.5 considering the substitution $k \to (\ell + 1/2)/\chi(z)$ at the relevant redshifts. The accuracy of the Limber approximation itself, in the case of ΛCDM, is at the order of 10% at $\ell = 2$ and drops approximately as ℓ^2 at higher ℓ (see, e.g., [301, 313, 314]). Apart from the multipole ℓ, the error depends also on the width of the redshift distribution, which changes only little with $f(R)$ effects. Given the large errors of the currently available data points at low ℓ, we conclude that the Limber approximation is applicable and furthermore very useful since it is numerically faster than an exact integration.

4.1.B.2. Redshift distribution and bias

A further ingredient in the ISWWLL code is the determination of the function $f_j(z)$. In the Markov chain, $f_j(z)$ is recomputed when changing the cosmological parameter values. The methods by which this function is determined differs for each sample, but they are all based on galaxy clustering data.

The 2MASS galaxies are matched with SDSS galaxies in order to identify their redshifts. To obtain the nonlinear power spectrum, the Q model for nonlinearities [292] is applied. Then, the code computes the galaxy power spectrum and fits it to measurements, thereby determining the bias $b(z)$ and Q. Since the required accuracy for the estimation of bias is only at the order of a few tens of percent [276], this processing is also applicable to $f(R)$ gravity. The Q model is also adopted for LRG galaxies, where the redshift probability distribution is inferred with methods described in Ref. [315]. For QSO, first, a preliminary estimate for the redshift distribution is deduced by locating a region of sky with high spectroscopic completeness, but simultaneously maintaining a large area. Taking into account magnification bias and fitting $b_j(z)\Pi_j(z)$ using the quasar power spectrum and quasar-LRG cross power yields the desired shape of $f_j(z)$. Note that in $f(R)$ gravity the relationship between the metric combination sensitive to gravitational redshifts and lensing Φ_- and the density perturbations is modified such that the expression of the lensing window function for magnification effects given in Ref. [276] is rescaled by $(1 + f_R)^{-1} \leq (1 + f_{R0})^{-1} \lesssim 1.1$ for $B_0 \lesssim 1$, where $(1 + f_R)^{-1} \geq 1$. Since this is a small effect and magnification bias is subdominant to bias and redshift distribution, it is save to neglect it. Due to the rather low accuracy requirement, we can furthermore adopt the ΛCDM growth factor in the determination of $b_j(z)\Pi_j(z)$. Finally, the effective redshift distribution of NVSS is obtained from cross correlating with the other samples and $f_j(z)$ is fitted with a Γ distribution.

4.1.C. Cluster abundance in $f(R)$ gravity

The likelihood code of [288] utilizes the halo mass function of Tinker *et al.* [316] at $z = 0.18$, which is described by the functions

$$\frac{dn}{dM} = f(\sigma)\frac{\bar{\rho}_{\rm m}}{M}\frac{d\ln\sigma^{-1}}{dM}, \tag{4.23}$$

where the distribution $f(\sigma)$ is given by

$$f(\sigma) = A\left[\left(\frac{\sigma}{b}\right)^{-a} + 1\right] e^{-c/\sigma^2} \tag{4.24}$$

and

$$\sigma^2 = \int P(k)\hat{W}(k\,R)k^2 dk. \tag{4.25}$$

Here, $\hat{W}$ is the Fourier transform of the real-space top-hat window function of radius R. The free parameters A, a, b, and c at $z = 0.18$ are fitted to ΛCDM simulations in [316]. We define M as the lensing mass, being the more conservative approach than taking it to be the dynamical mass (see [272, 317]). In the large field limit ($B_0 \gtrsim 10^{-3}$), where no chameleon mechanism takes place, these relations provide a reasonable fit to $f(R)$ gravity simulations as well, using the same values for the parameters as in ΛCDM, and correspond to using the Sheth-Tormen [318] halo mass function with spherical collapse predicted by standard gravity (see [272, 319]). Another approach is to alter the spherical collapse calculations, taking care of modified forces [272, 319]. Standard spherical collapse tends to overestimate the $f(R)$ effects, while the opposite occurs for the modified spherical collapse calculations. Given the constraints that can be achieved from the data, we conclude that it is save to assume the large field limit, neglect the chameleon mechanism, and use standard spherical collapse, i.e., using the ΛCDM values for the free parameters in the Tinker *et al.* halo mass function. While choosing modified spherical collapse is the more conservative approach, the standard spherical collapse parameters yield a better fit to the simulations (see [272, 319]). We remind the reader that the 68% confidence level inferred from cluster abundance should be taken with caution since it approaches the small field limit ($B_0 \lesssim 10^{-5}$) and intermediate regime, where chameleon effects appear that cannot be described through Eq. (4.23). A better fit for the halo mass function in $f(R)$ gravity is an objective to future work.

References

[260] S. M. Carroll, V. Duvvuri, M. Trodden, and M. S. Turner, "Is cosmic speed-up due to new gravitational physics?", Phys. Rev. **D70**, 043528 (2004), [arXiv:astro-ph/0306438].

[261] S. Nojiri and S. D. Odintsov, "Modified gravity with negative and positive powers of the curvature: Unification of the inflation and of the cosmic acceleration", Phys. Rev. **D68**, 123512 (2003), [arXiv:hep-th/0307288].

[262] S. Capozziello, S. Carloni, and A. Troisi, "Quintessence without scalar fields", Recent Res. Dev. Astron. Astrophys. **1**, 625 (2003), [arXiv:astro-ph/0303041].

[263] W. Hu and I. Sawicki, "Models of f(R) Cosmic Acceleration that Evade Solar-System Tests", Phys. Rev. **D76**, 064004 (2007), [arXiv:0705.1158].

[264] P. Brax, C. van de Bruck, A.-C. Davis, and D. J. Shaw, "f(R) Gravity and Chameleon Theories", Phys. Rev. **D78**, 104021 (2008), [arXiv:0806.3415].

[265] Y.-S. Song, W. Hu, and I. Sawicki, "The large scale structure of f(R) gravity", Phys. Rev. **D75**, 044004 (2007), [arXiv:astro-ph/0610532].

[266] J. Khoury and A. Weltman, "Chameleon cosmology", Phys. Rev. **D69**, 044026 (2004), [arXiv:astro-ph/0309411].

[267] I. Navarro and K. Van Acoleyen, "f(R) actions, cosmic acceleration and local tests of gravity", JCAP **0702**, 022 (2007), [arXiv:gr-qc/0611127].

[268] T. Faulkner, M. Tegmark, E. F. Bunn, and Y. Mao, "Constraining f(R) gravity as a scalar tensor theory", Phys. Rev. **D76**, 063505 (2007), [arXiv:astro-ph/0612569].

[269] T. L. Smith, "Testing gravity on kiloparsec scales with strong gravitational lenses", (2009), [arXiv:0907.4829].

[270] Y.-S. Song, H. Peiris, and W. Hu, "Cosmological Constraints on f(R) Acceleration Models", Phys. Rev. **D76**, 063517 (2007), [arXiv:0706.2399].

[271] T. Giannantonio, M. Martinelli, A. Silvestri, and A. Melchiorri, "New constraints on parametrised modified gravity from correlations of the CMB with large scale structure", JCAP **1004**, 030 (2010), [arXiv:0909.2045].

[272] F. Schmidt, A. Vikhlinin, and W. Hu, "Cluster Constraints on f(R) Gravity", Phys. Rev. **D80**, 083505 (2009), [arXiv:0908.2457].

[273] W. Hu and I. Sawicki, "A Parameterized Post-Friedmann Framework for Modified Gravity", Phys. Rev. **D76**, 104043 (2007), [arXiv:0708.1190].

[274] W. Hu, "Parametrized Post-Friedmann Signatures of Acceleration in the CMB", Phys. Rev. **D77**, 103524 (2008), [arXiv:0801.2433].

[275] W. Fang, W. Hu, and A. Lewis, "Crossing the Phantom Divide with Parameterized Post-Friedmann Dark Energy", Phys. Rev. **D78**, 087303 (2008), [arXiv:0808.3125].

[276] S. Ho, C. Hirata, N. Padmanabhan, U. Seljak, and N. Bahcall, "Correlation of CMB with large-scale structure: I. ISW Tomography and Cosmological Implications", Phys. Rev. **D78**, 043519 (2008), [arXiv:0801.0642].

[277] C. M. Hirata, S. Ho, N. Padmanabhan, U. Seljak, and N. A. Bahcall, "Correlation of CMB with large-scale structure: II. Weak lensing", Phys. Rev. **D78**, 043520 (2008), [arXiv:0801.0644].

[278] L. Pogosian and A. Silvestri, "The pattern of growth in viable f(R) cosmologies", Phys. Rev. **D77**, 023503 (2008), [arXiv:0709.0296].

[279] I. Sawicki and W. Hu, "Stability of Cosmological Solution in f(R) Models of Gravity", Phys. Rev. **D75**, 127502 (2007), [arXiv:astro-ph/0702278].

[280] WMAP, J. Dunkley *et al.*, "Five-Year Wilkinson Microwave Anisotropy Probe (WMAP) Observations: Likelihoods and Parameters from the WMAP data", As-

trophys. J. Suppl. **180**, 306 (2009), [arXiv:0803.0586].

[281] C.-L. Kuo *et al.*, "Improved Measurements of the CMB Power Spectrum with ACBAR", Astrophys. J. **664**, 687 (2007), [arXiv:astro-ph/0611198].

[282] A. C. S. Readhead *et al.*, "Extended Mosaic Observations with the Cosmic Background Imager", Astrophys. J. **609**, 498 (2004), [arXiv:astro-ph/0402359].

[283] K. Grainge *et al.*, "The CMB power spectrum out to l=1400 measured by the VSA", Mon. Not. Roy. Astron. Soc. **341**, L23 (2003), [arXiv:astro-ph/0212495].

[284] Supernova Cosmology Project, M. Kowalski *et al.*, "Improved Cosmological Constraints from New, Old and Combined Supernova Datasets", Astrophys. J. **686**, 749 (2008), [arXiv:0804.4142].

[285] A. G. Riess *et al.*, "A Redetermination of the Hubble Constant with the Hubble Space Telescope from a Differential Distance Ladder", Astrophys. J. **699**, 539 (2009), [arXiv:0905.0695].

[286] W. J. Percival *et al.*, "Baryon Acoustic Oscillations in the Sloan Digital Sky Survey Data Release 7 Galaxy Sample", Mon. Not. Roy. Astron. Soc. **401**, 2148 (2010), [arXiv:0907.1660].

[287] R. Reyes *et al.*, "Confirmation of general relativity on large scales from weak lensing and galaxy velocities", Nature **464**, 256 (2010.), [arXiv:1003.2185].

[288] U. Seljak, A. Slosar, and R. Mandelbaum *et al.*, in preparation.

[289] A. Vikhlinin *et al.*, "Chandra Cluster Cosmology Project III: Cosmological Parameter Constraints", Astrophys. J. **692**, 1060 (2009), [arXiv:0812.2720].

[290] A. Lewis and S. Bridle, "Cosmological parameters from CMB and other data: a Monte-Carlo approach", Phys. Rev. **D66**, 103511 (2002), [arXiv:astro-ph/0205436].

[291] SDSS, K. N. Abazajian *et al.*, "The Seventh Data Release of the Sloan Digital Sky Survey", Astrophys. J. Suppl. **182**, 543 (2009), [arXiv:0812.0649].

[292] The 2dFGRS, S. Cole *et al.*, "The 2dF Galaxy Redshift Survey: Power-spectrum analysis of the final dataset and cosmological implications", Mon. Not. Roy. Astron. Soc. **362**, 505 (2005), [arXiv:astro-ph/0501174].

[293] A. Lewis, A. Challinor, and A. Lasenby, "Efficient Computation of CMB anisotropies in closed FRW models", Astrophys. J. **538**, 473 (2000), [arXiv:astro-ph/9911177].

[294] E. Bertschinger and P. Zukin, "Distinguishing Modified Gravity from Dark Energy", Phys. Rev. **D78**, 024015 (2008), [arXiv:0801.2431].

[295] G.-B. Zhao, L. Pogosian, A. Silvestri, and J. Zylberberg, "Searching for modified growth patterns with tomographic surveys", Phys. Rev. **D79**, 083513 (2009), [arXiv:0809.3791].

[296] T. Giannantonio *et al.*, "Combined analysis of the integrated Sachs-Wolfe effect and cosmological implications", Phys. Rev. **D77**, 123520 (2008), [arXiv:0801.4380].

[297] L. Lombriser, W. Hu, W. Fang, and U. Seljak, "Cosmological Constraints on DGP Braneworld Gravity with Brane Tension", Phys. Rev. **D80**, 063536 (2009), [arXiv:0905.1112].

[298] R. Bean and M. Tangmatitham, "Current constraints on the cosmic growth history",

Phys. Rev. **D81**, 083534 (2010), [arXiv:1002.4197].

[299] S. F. Daniel and E. V. Linder, "Confronting General Relativity with Further Cosmological Data", Phys. Rev. **D82**, 103523 (2010), [arXiv:1008.0397].

[300] L. Lombriser, "Consistency check of ΛCDM phenomenology", Phys. Rev. **D83**, 063519 (2011), [arXiv:1101.0594].

[301] R. E. Smith, C. Hernandez-Monteagudo, and U. Seljak, "Impact of Scale Dependent Bias and Nonlinear Structure Growth on the ISW Effect: Angular Power Spectra", Phys. Rev. **D80**, 063528 (2009), [arXiv:0905.2408].

[302] P. Zhang, M. Liguori, R. Bean, and S. Dodelson, "Probing Gravity at Cosmological Scales by Measurements which Test the Relationship between Gravitational Lensing and Matter Overdensity", Phys. Rev. Lett. **99**, 141302 (2007), [arXiv:0704.1932].

[303] SDSS, D. J. Eisenstein *et al.*, "Spectroscopic Target Selection for the Sloan Digital Sky Survey: The Luminous Red Galaxy Sample", Astron. J. **122**, 2267 (2001), [arXiv:astro-ph/0108153].

[304] SDSS, D. G. York *et al.*, "The Sloan Digital Sky Survey: technical summary", Astron. J. **120**, 1579 (2000), [arXiv:astro-ph/0006396].

[305] D. Rapetti, S. W. Allen, A. Mantz, and H. Ebeling, "The observed growth of massive galaxy clusters - III. Testing general relativity on cosmological scales", Mon. Not. Roy. Astron. Soc. **406**, 1796 (2010), [arXiv:0911.1787].

[306] S. F. Daniel *et al.*, "Testing General Relativity with Current Cosmological Data", Phys. Rev. **D81**, 123508 (2010), [arXiv:1002.1962].

[307] SDSS, B. Koester *et al.*, "A MaxBCG Catalog of 13,823 Galaxy Clusters from the Sloan Digital Sky Survey", Astrophys. J. **660**, 239 (2007), [arXiv:astro-ph/0701265].

[308] S. Ferraro, F. Schmidt, and W. Hu, "Cluster Abundance in f(R) Gravity Models", Phys. Rev. **D83**, 063503 (2011), [arXiv:1011.0992].

[309] T. H. Jarrett *et al.*, "2MASS Extended Source Catalog: Overview and Algorithms", Astron. J. **119**, 2498 (2000), [arXiv:astro-ph/0004318].

[310] M. F. Skrutskie *et al.*, "The Two Micron All Sky Survey (2MASS)", Astron. J. **131**, 1163 (2006).

[311] SDSS, J. K. Adelman-McCarthy *et al.*, "The Sixth Data Release of the Sloan Digital Sky Survey", Astrophys. J. Suppl. **175**, 297 (2008), [arXiv:0707.3413].

[312] J. J. Condon *et al.*, "The NRAO VLA Sky survey", Astron. J. **115**, 1693 (1998).

[313] M. LoVerde and N. Afshordi, "Extended Limber Approximation", Phys. Rev. **D78**, 123506 (2008), [arXiv:0809.5112].

[314] N. Afshordi, "Integrated Sachs-Wolfe effect in Cross-Correlation: The Observer's Manual", Phys. Rev. **D70**, 083536 (2004), [arXiv:astro-ph/0401166].

[315] SDSS, N. Padmanabhan *et al.*, "Calibrating Photometric Redshifts of Luminous Red Galaxies", Mon. Not. Roy. Astron. Soc. **359**, 237 (2005), [arXiv:astro-ph/0407594].

[316] J. Tinker *et al.*, "Toward a Halo Mass Function for Precision Cosmology: The Limits of Universality", Astrophys. J. **688**, 709 (2008), [arXiv:0803.2706].

[317] F. Schmidt, "Dynamical Masses in Modified Gravity", Phys. Rev. **D81**, 103002

(2010), [arXiv:1003.0409].

[318] R. K. Sheth and G. Tormen, “Large scale bias and the peak background split”, Mon. Not. Roy. Astron. Soc. **308**, 119 (1999), [arXiv:astro-ph/9901122].

[319] F. Schmidt, M. Lima, H. Oyaizu, and W. Hu, “Nonlinear evolution of f(R) cosmologies. III. Halo statistics”, Phys. Rev. **79(8)**, 083518 (2009), [arXiv:0812.0545].

4.2. Cluster density profiles as a test of modified gravity

Lucas Lombriser[5], *Fabian Schmidt*[6], *Tobias Baldauf*[7], *Rachel Mandelbaum*[8], *Uroš Seljak*[9], *Robert E. Smith*[10]

Paper draft

Abstract

General relativity has extensively been probed at solar-system and large, cosmological, scales. We present a new test of the gravitational interactions at the $r \simeq (0.2-20)$ Mpc *scale, i.e., around the virial radius of dark matter halos measured through galaxy-galaxy lensing of maxBCG clusters. Thereby we employ predictions from self-consistent simulations of* $f(R)$ *gravity to find an upper bound on the background field amplitude of* $|f_{R0}| < 0.027$ *at the 1D-marginalized 95% confidence level. Dark-matter-only simulations of the concordance model corresponding to* $|f_{R0}| = 0$ *are consistent with the lensing measurement. However, the fit to the data improves noticeably when parametrizing the effect of the enhancement of the halo density profile induced by* $f(R)$ *gravity by a phenomenological fit with free amplitude* F_0*, neglecting effects from the increased abundance of clusters. This result suggests that employing dark matter particles only in a* Λ*CDM simulation is not sufficient to correctly describe halo profiles at scales of* $r \simeq (1-10)$ Mpc *and that additional effects have to be taken into account.*

4.2.1. Introduction

Modifications of gravity serve as an alternative explanation to the dark energy paradigm for the late-time acceleration of our universe. Such modifications have extensively been tested on solar-system scales (see, e.g., [320]) and at large, cosmological, scales (see, e.g., [321]). Gravity may however also be tested by the structure observed at intermediate scales. In this regime nonlinear gravitational interactions gain on importance and need to be modeled correctly to obtain reliable predictions

---

[5] Institute for Theoretical Physics, University of Zurich, Winterthurerstrasse 190, CH-8057 Zürich, Switzerland

[6] Theoretical Astrophysics, California Institute of Technology M/C 350-17, Pasadena, CA 91125, USA

[7] Institute for Theoretical Physics, University of Zurich, Winterthurerstrasse 190, CH-8057 Zürich, Switzerland

[8] Princeton University Observatory, Peyton Hall, Princeton, NJ 08544, USA

[9] Institute for Theoretical Physics, University of Zurich, Winterthurerstrasse 190, CH-8057 Zürich, Switzerland; Physics and Astronomy Department, University of California, and Lawrence Berkeley National Laboratory, Berkeley, California 94720, USA; Ewha University, Seoul 20-750, Korea

[10] Institute for Theoretical Physics, University of Zurich, Winterthurerstrasse 190, CH-8057 Zürich, Switzerland; Argelander-Institute for Astronomy, Auf dem Hügel 71, D-53121 Bonn, Germany

for both general relativity and its competitors, which in turn can be instrumentalized to infer constraints on the gravitational theories.

To study the nonlinear effects in structure formation, we specialize to a particular gravitational modification, i.e., $f(R)$ gravity. Within this model the Einstein-Hilbert action is supplemented with a free function $f(R)$ of the Ricci scalar R. It has been shown that such models can reproduce the late-time acceleration of the universe without invoking dark energy [322–324]. However, they also produce a stronger gravitational coupling and enhance the growth of structure. $f(R)$ gravity is equivalent to a scalar-tensor theory where the additional degree of freedom is described by the *scalaron* field $f_R \equiv df/dR$ [325, 326]. We parametrize our models by the background value of the scalaron field today $|f_{R0}|$. The f_R field is massive and below its Compton wavelength it enhances gravitational forces by a factor of 4/3. Due to the density dependence of the scalaron's mass, viable $f(R)$ gravity models experience a mechanism dubbed the chameleon effect [327–329] which returns gravitational forces to the standard relations in high-density regions, making them compatible with solar-system tests [330] at $r \lesssim 0.1$ mpc. The transition required to interpolate between the low curvature of the large-scale structure and the high curvature of the galactic halo sets the strongest bound on the background field, $|f_{R0}| < |\Psi| \sim (10^{-6} - 10^{-5})$ [330], i.e., the typical depth of cosmological potential wells. This bound is also required for consistency with strong gravitational lenses [331] at $r \sim (1 - 10)$ kpc. Independently, strong constraints can also be inferred from the large-scale structure ($r \gtrsim 10$ Mpc). The enhanced growth of structure observed in $f(R)$ gravity models manifests itself on the largest scales of the cosmic microwave background (CMB) temperature anisotropy power spectrum [332], where compatibility with CMB data places an upper bound on $|f_{R0}|$ of order unity [333]. Cross correlations of the CMB temperature field with foreground galaxies tighten this constraint by an order of magnitude [332–336]. However, the currently strongest constraints on $f(R)$ gravity models from large-scale structures are inferred from the analysis of the abundance of clusters, yielding an improvement over the CMB constraints of nearly four orders of magnitude [335, 337].

In this paper, we present a new test of gravity at the $r \sim (0.2 - 20)$ Mpc scale, i.e., around the virial radius of dark matter halos measured through the differential excess surface mass density from galaxy-galaxy lensing. N-body simulations of modified gravity scenarios have shown that halo density profiles exhibit a characteristic enhancement at a few virial radii when compared to halo profiles from general relativistic simulations with the same expansion history [338, 339]. In these models, which attempt to explain the acceleration of the universe without dark energy, the modifications to the gravitational force increase towards late times, leading to a pileup of matter in the infall regions of massive halos. In contrast, the inner profiles of halos are less affected since they formed earlier when the force modifications were weak or absent.

Here, we use this effect to constrain the field amplitude $|f_{R0}|$ of the Hu-Sawicki [330] ($n = 1$) $f(R)$ gravity model with measurements around the maxBCG sample, a selection of MaxBCG clusters [340] from the Sloan Digital Sky Survey (SDSS) [341]. We use two methods for comparing $f(R)$ gravity to ΛCDM halo profiles, i.e., by matching clusters by abundance and by averaging over the same halo mass range, respectively. We also place constraints on a phenomenological parameter quantifying first-order effects from the $f(R)$ gravity modifications in the halo density profiles within the fixed mass range scenario. For this purpose we perform a Markov chain Monte Carlo (MCMC) likelihood analysis on the underlying parameter spaces.

In Sec. 4.2.2, we review the Hu-Sawicki $f(R)$ gravity model and the details about the N-body simulations employed to derive the halo properties. We also present our parametrization of the $f(R)$ gravity modified halo density profiles based on the halo model and simulations, and describe our first-order phenomenological approach for the modifications. Section 4.2.3 is devoted to galaxy-galaxy lensing predictions and the constraints on modifications of gravity we can infer from it. We discuss our results in Sec. 4.2.5 and give further details about the halo model predictions for the density profiles in the appendix.

4.2.2. Halo profiles in modified gravity

When gravitational interactions are modified, the growth of structure and thus the distribution of mass, as well as the relation between light deflection and mass distribution can change. Effects of modified gravity on halo properties were studied in the case of $f(R)$ gravity in, e.g., [338, 342] (cf. [343]) and the DGP braneworld scenario in, e.g., [339, 344].

Here, we are in particular interested in the distinctive shapes of halo density profiles under the influence of modifications of the gravitational force. Thereby, we concentrate on Hu-Sawicki [330] $f(R)$ gravity and the nonlinear behavior deduced from N-body simulations of this model [338, 345, 346] (cf. [347]). We shall first review the details about the Hu-Sawicki model and the simulations used. Then we continue by describing our parametrization of $f(R)$ effects on halo density profiles based on the halo model and simulations, and give a phenomenological first-order approach based on a Gaussian fit to the halo profile enhancement observed in the fixed mass range scenario of the $f(R)$ gravity simulations.

4.2.2.1. $f(R)$ gravity

In $f(R)$ gravity, the Einstein-Hilbert action is supplemented by a free function of the Ricci scalar R,

$$S = \frac{1}{2\kappa^2} \int d^4x \sqrt{-g}\,[R + f(R)] + \int d^4x \sqrt{-g}\mathcal{L}_{\rm m}. \tag{4.26}$$

Here, $\kappa^2 \equiv 8\pi G$ and $\mathcal{L}_{\rm m}$ is the matter Lagrangian, where we have set $c \equiv 1$. Variation with respect to the metric $g_{\alpha\beta}$ yields the modified Einstein equations for metric $f(R)$ gravity,

$$G_{\mu\nu} + f_R R_{\mu\nu} - \left(\frac{f}{2} - \Box f_R\right) g_{\mu\nu} - \nabla_\mu \nabla_\nu f_R = \kappa^2 T_{\mu\nu}, \tag{4.27}$$

where the connection is of Levi-Civita type and $f_R \equiv df/dR$ is the additional scalar degree of freedom of the model, characterizing the force modifications.

We specialize our considerations to the functional form [330]

$$f(R) = -m^2 \frac{c_1 \left(R/m^2\right)^n}{c_2 \left(R/m^2\right)^n + 1}, \tag{4.28}$$

where $m^2 \equiv \kappa^2 \bar{\rho}_{\rm m}/3$. The free parameters of the model c_1, c_2, and n can be chosen to reproduce the ΛCDM expansion history and evade solar-system tests [330] through the chameleon mechanism [327–329]. In the high-curvature regime, $c_2^{1/n} R \gg m^2$, Eq. (4.28) simplifies to

$$f(R) = -\frac{c_1}{c_2} m^2 + \frac{f_{R0}}{n} \frac{\bar{R}_0^{n+1}}{R^n}, \tag{4.29}$$

where $\bar{R}_0$ denotes the background curvature today, $\bar{R}_0 = \bar{R}|_{z=0}$, and $f_{R0} \equiv f_R(\bar{R}_0)$. We further infer

$$\frac{c_1}{c_2} m^2 = 2\kappa^2 \bar{\rho}_\Lambda \tag{4.30}$$

from requiring equivalence with ΛCDM when $|f_{R0}| \to 0$ and restrict to models with $n = 1$.

In the quasistatic limit, the trace and time-time component of the modified Einstein equations yield the f_R field equation and Poisson equation for the Newtonian potential $\Psi = \delta g_{00}/(2 g_{00})$, respectively, i.e.,

$$\nabla^2 \delta f_R = \frac{a^2}{3} \left[\delta R(f_R) - \kappa^2 \delta\rho_{\rm m} \right], \tag{4.31}$$

$$\nabla^2 \Psi = \frac{2\kappa^2}{3} a^2 \delta\rho_{\rm m} - \frac{a^2}{6} \delta R(f_R). \tag{4.32}$$

Here, coordinates are comoving, $\delta f_R = f_R(R) - f_R(\bar{R})$, $\delta R = R - \bar{R}$, $\delta\rho_{\rm m} = \rho_{\rm m} - \bar{\rho}_{\rm m}$, and Ψ is in the longitudinal gauge.

If the background field f_{R0} is large compared to the gravitational potentials, we may linearize the field equations via the approximation

$$\delta R \approx \left. \frac{dR}{df_R} \right|_{R=\bar{R}} \delta f_R = 3 \left(\frac{\lambda_{\rm C}}{2\pi} \right)^{-2} \delta f_R, \tag{4.33}$$

where $\lambda_{\rm C}$ is the Compton wavelength of the field at the background. In Fourier space the solution to Eqs. (4.31) and (4.32) within the linearized approximation is

$$k^2 \Psi(\mathbf{k}) = -\frac{\kappa^2}{2} \left\{ \frac{4}{3} - \frac{1}{3} \left[\left(\frac{\lambda_{\rm C}}{2\pi} \frac{k}{a} \right)^2 + 1 \right]^{-1} \right\} a^2 \delta\rho_{\rm m}(\mathbf{k}), \tag{4.34}$$

where $k = |\mathbf{k}|$. For scales $k \gg 2\pi\, \lambda_{\rm C}^{-1} a$, i.e., in the large field limit, this leads to an enhancement of gravitational forces by a factor of 4/3. Computations using Eq. (4.34) are referred to as the *no-chameleon* or *linearized* case [346]. For $|f_{R0}| \ll 1$ the lensing potential and the matter density are related in the usual way. Hence, the combination of Eqs. (4.31) and (4.32) infer that $|\delta f_R| \sim |\Psi|$. In the small field limit, $|f_{R0}| \lesssim 10^{-5}$, the background field becomes small compared to the depth of the gravitational potential, which activates the chameleon mechanism, suppressing non-Newtonian forces. More precisely, $\delta f_R \gg |f_R(\bar{R})|$ and from Eq. (4.31), $\delta R \simeq \kappa^2 \delta\rho_{\rm m}$, which restores the standard Poisson equation in Eq. (4.32). Given that the constraints on $|f_{R0}|$ expected from our lensing data are well inside the linearized regime, we can apply the approximation Eq. (4.34) in the simulations.

4.2.2.2. Simulations

We utilize $f(R)$ gravity simulations to derive relative deviations induced by the modified forces in the halo profiles with respect to the ΛCDM predictions, i.e., $|f_{R0}| = 0$, from the same simulations. We then employ the Zurich Horizon (ZHORIZON) simulations, which provide ΛCDM predictions of higher precision and scale these results with the deviations from the $f(R)$ gravity simulations. Note that we use simulations where the matter density field consists exclusively of dark matter particles, thereafter dark-matter-only (DMO) simulations.

$f(R)$ gravity simulations

Since the expected constraints on $|f_{R0}|$ lie in a regime where the chameleon mechanism is not active and we require sufficient halo statistics, we employ no-chameleon $f(R)$ gravity simulations which solve the linearized f_R field equation, Eq. (4.31), and Eq. (4.34) [338, 345, 346]. Simulations are conducted for $|f_{R0}| = 10^{-2}$, 10^{-3}, 10^{-4}, 0 and $n = 1$. Note that $|f_{R0}| = 0$ corresponds to ΛCDM. Other cosmological parameters are fixed to the values $\Omega_\Lambda = 0.76$, $\Omega_{\rm b} = 0.04181$, $h = 0.73$, $n_{\rm s} = 0.958$, and the initial power in curvature fluctuations $A_{\rm s} = (4.73 \times 10^{-5})^2$ at $k = 0.05$ Mpc^{-1}. The simulations are carried out on 512^3 grid cells with a total of $N_{\rm p} = 256^3$ particles and combined for two different box sizes, $L_{\rm box} = 64h^{-1}$ Mpc, $128h^{-1}$ Mpc.

Halos within the simulation and their associated masses are identified via a spherical overdensity (SO) algorithm (cf. [348]). The particles are placed on the grid by a cloud-in-cell interpolation and counted together within a growing sphere around the center of mass until the required overdensity is reached. The mass of the halo is then defined by the sum of the particle masses contained in the sphere. This process is started at the highest overdensity grid point and hierarchically continued to lower overdensity grid points until all halos are identified. The halos employed for this analysis ($M \gtrsim 10^{14}h^{-1}\ M_\odot$) generally contain more than 10^3 particles.

Concordance model simulations

The ZHORIZON simulations comprise 30 pure dissipationless dark matter N-body simulations of different ΛCDM cosmologies (see Table 4.5), designed for high precision studies of cosmological structures on scales of up to a few $100h^{-1}$ Mpc [349, 350].

The matter density field is sampled by $N_{\rm p} = 750^3$ dark matter particles of total mass $M_{\rm dm} = 5.55 \times 10^{11}h^{-1}\ M_\odot$, in the fiducial case, with a box length of $1.5h^{-1}$ Gpc. For the nonlinear gravitational evolution of the N equal mass particles, the publicly available GADGET-2 code [351] is implemented. In order to avoid two particle collisions, a force softening length of $60h^{-1}$ kpc is employed. The transfer function at redshift $z = 0$ is generated using CMBFAST [352] and rescaled to the

Ω_{m}	Ω_{b}	h	σ_8	n_{s}
0.25	0.04	0.7	0.8	1.00
0.20	0.04	0.7	0.8	1.00
0.30	0.04	0.7	0.8	1.00
0.25	0.04	0.7	0.7	1.00
0.25	0.04	0.7	0.9	1.00
0.25	0.04	0.7	0.8	0.95
0.25	0.04	0.7	0.8	1.05

Table 4.5: Parameter values for the set of ZHORIZON simulations: total and baryonic matter density parameter Ω_{m} and Ω_{b}, respectively, the dimensionless Hubble parameter h, the power spectrum normalization $\sigma_8 = \sigma_8^{\Lambda\mathrm{CDM}}$, and the primordial spectral index n_{s}. The first row indicates the fiducial cosmological parameters inspired by the three-year WMAP best-fit values [356, 357].

initial redshift $z_{\mathrm{i}} = 50$ with the linear growth factor. The power spectrum and the corresponding gravitational potential are determined for each simulation separately. Then, particles are placed on a Cartesian grid of spacing $\Delta x = 2h^{-1}$ Mpc with displacements and initial conditions computed according to second order Lagrangian perturbation theory with the 2LPT code [353, 354].

For each cosmology, we consider only the first four ZHORIZON simulations, each containing 11 snapshots, logarithmically spaced in the expansion factor a from $z = 1$ to $z = 0$, in particular one at $z = 0.23$, and additional six snapshots at $z = (2, 3, 5, 10, 15, 20)$. Thus, our effective volume is $13.5h^{-3}$ Gpc^3. For all snapshots of each simulation, gravitationally bound structures are identified by a Friends-of-Friends[11] (FoF) algorithm [355] with linking length of 0.2 times the mean interparticle spacings. The center of a halo is associated with the minimum of the potential of the particle distribution. Halos of less than 20 particles are rejected, resulting in a halo mass resolution of $M > 1.2 \times 10^{13} h^{-1}\ M_{\odot}$, corresponding to the number density $\bar{n} = 1.8 \times 10^{-5} h^{-1}$ Mpc.

To remove effects from galaxy satellites in the samples, we apply a cylindrical cut in the projected radius at $r_{\mathrm{cut}} = 3r_{\mathrm{v}}$, where r_{v} is the virial radius. This leads to an effective number density of $\bar{n} = 1.43 \times 10^{-5} h^{-1}$ Mpc for scatter $\sigma = 0.4$ (see Sec. 4.2.3.3).

4.2.2.3. Cluster density profiles

We stack the halos identified in the simulations to obtain the average density profile $\delta_\rho(r) = \langle \rho_{\mathrm{h}}(h)/\rho_{\mathrm{m}} - 1\rangle_{\mathrm{h}}$. This is done for each concordance model cosmology (see Table 4.5) and for four different values of scatter σ, i.e., $\sigma = 0, 0.4, 0.6, 0.8$ (see Sec. 4.2.3.3). In Fig. 4.9, we demonstrate effects on the halo profile from varying the cosmological parameters with respect to the fiducial case.

In order to compare the $f(R)$ simulations to observations (see Sec. 4.2.3.2), we consider two cases: a fixed common lower mass limit M_0, derived from the ΛCDM concordance cosmology; and a lower mass limit for $f(R)$ adjusted to match the

---

[11] The FoF code used (B-FOF) was kindly provided by V. Springel.

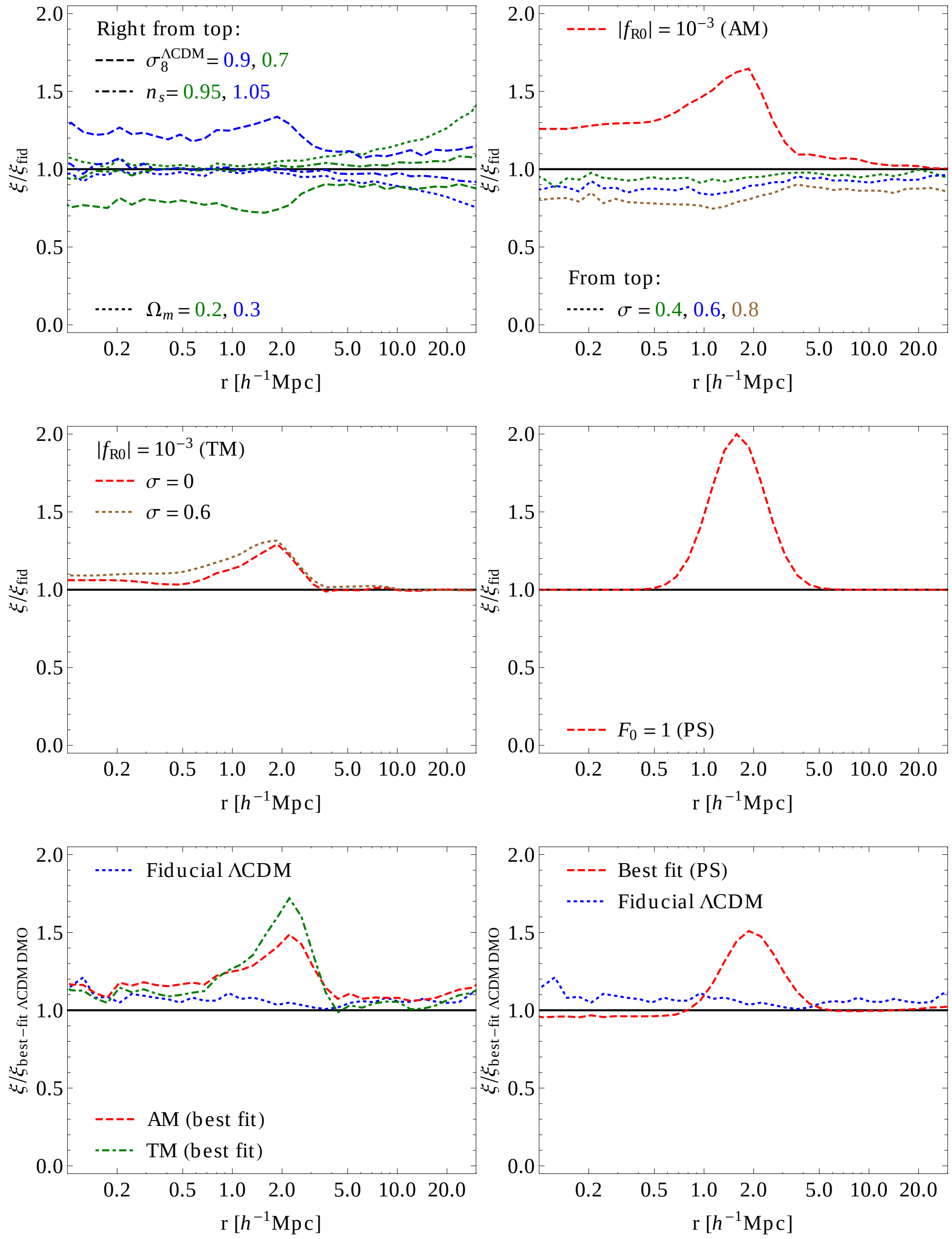

Figure 4.9: Effects on the halo density profile ξ_{hm} from varying the cosmological parameters with respect to the fiducial case. *Upper left*: Different parameter values for $\sigma_8^{\Lambda\text{CDM}}$ (dashed), n_{s} (dot-dashed), and Ω_{m} (dotted). *Upper right*: $|f_{R0}| = 10^{-3}$ for the abundance matched case (dashed) and for the fiducial ΛCDM cosmology with different values of scatter σ (dotted). *Middle left*: $|f_{R0}| = 10^{-3}$ for the threshold matched case with $\sigma = 0$ (dashed) and $\sigma = 0.6$ (dotted). *Middle right*: $F_0 = 1$ for the phenomenological scenario. *Lower left*: Best-fit prediction for ξ_{hm} with respect to the best-fit ΛCDM model prediction. $|f_{R0}| = 10^{-3}$ for the abundance (dashed) and threshold matched case (dot-dashed), respectively, along with the fiducial ΛCDM cosmology (dotted). *Lower right*: Best-fit for the phenomenological scenario (dashed) and fiducial ΛCDM cosmology (dotted).

abundance of tracers, $\bar{n} = 1.8 \times 10^{-5} h^{-1}$ Mpc. Since the mass function of halos is enhanced in $f(R)$ gravity, the $f(R)$ mass threshold is lower in the second case. We adjust the mass limit so that the total number of halos $N_{\rm h}[> M_{0,f(R)}] = \bar{n}\, V_{\rm tot}$ at $z = 0.22$, where $V_{\rm tot}$ is the total simulation volume. In the following we refer to the two scenarios as the threshold matched (TM) and abundance matched (TM) cases, respectively.

If using the same M_0 for both gravity models the effects from a modification of gravity are less severe than when taking into account that massive halos are more abundant in $f(R)$ gravity and matching by abundance. This is in particular evident at the scales $r \lesssim 1 h^{-1}$ Mpc (see Fig. 4.10) and for the amplitude of the peak of the enhancement (see Fig. 4.11). We will study both cases, when taking into account this effect and when neglecting it. We, however, consider the AM case to be the more consistent approach for comparing $f(R)$ gravity to concordance model halos than the TM scenario.

$f(R)$ gravity predictions

We compare $f(R)$ gravity simulations with $|f_{R0}| = 10^{-3}$ to $|f_{R0}| = 0$ to identify the relative deviation induced on the halo profile. In Fig. 4.10, we show the shape of the deviations observed in the AM and TM case, respectively, normalized to unity at the peak.

For interpolation and extrapolation of the simulated profiles, we model the relative deviations of the $f(R)$ gravity halo profiles with respect to their ΛCDM counterparts using the halo model. Thereby, we describe the halo-mass correlation function through a NFW profile with an additional two-halo term for the surrounding mass. The two-halo term is truncated at $r_{\rm v}$, i.e., the halo profile is set to 0 outside of $r_{\rm v}$. This truncation models the peak enhancement in $\xi_{\rm hm}$ observed in the simulations at a few virial radii of the halos (see Figs. 4.10 and 4.11). Both in the AM and TM case, the average halo mass in $f(R)$ gravity is larger than in ΛCDM. Consequently, the virial radius is larger and the NFW profile is truncated at a larger radius, which produces a relative peak to the ΛCDM profile (see Fig. 4.9). Note that a similar but weaker effect may be produced when comparing ΛCDM halos with larger $r_{\rm v}$ to ΛCDM halos with lower $r_{\rm v}$. We can observe this, e.g., in the case of adding mass scatter uncertainty in the halo selection process or changing the power spectrum normalization (see Fig. 4.9).

The overall enhancement observed in the $f(R)$ gravity halo profiles can be attributed to an increase in the linear power spectrum, which is, however, partially cancelled due to a reduced linear bias [338]. The halo-model overpredicts the peak of the enhancement. We therefore apply a fudge factor to correct the amplitude of the enhancement (see Fig. 4.12). We refer to the appendix for more details about the halo-model predictions in $f(R)$ gravity. Figure 4.12 illustrates the halo-model fits to the simulated cluster profiles for $|f_{R0}| = 10^{-3}$.

We parametrize $f(R)$ effects from modified spherical collapse (see App. 4.2.A.1) on the galaxy-matter correlation function by

$$\xi_{\rm hm}^{f(R)}(r) = \left[1 + c(\sigma) A\left(f_{R0}, \sigma_8^{\Lambda\rm CDM}\right) f(r,\sigma)\right] \xi_{\rm hm}^{\Lambda\rm CDM}, \tag{4.35}$$

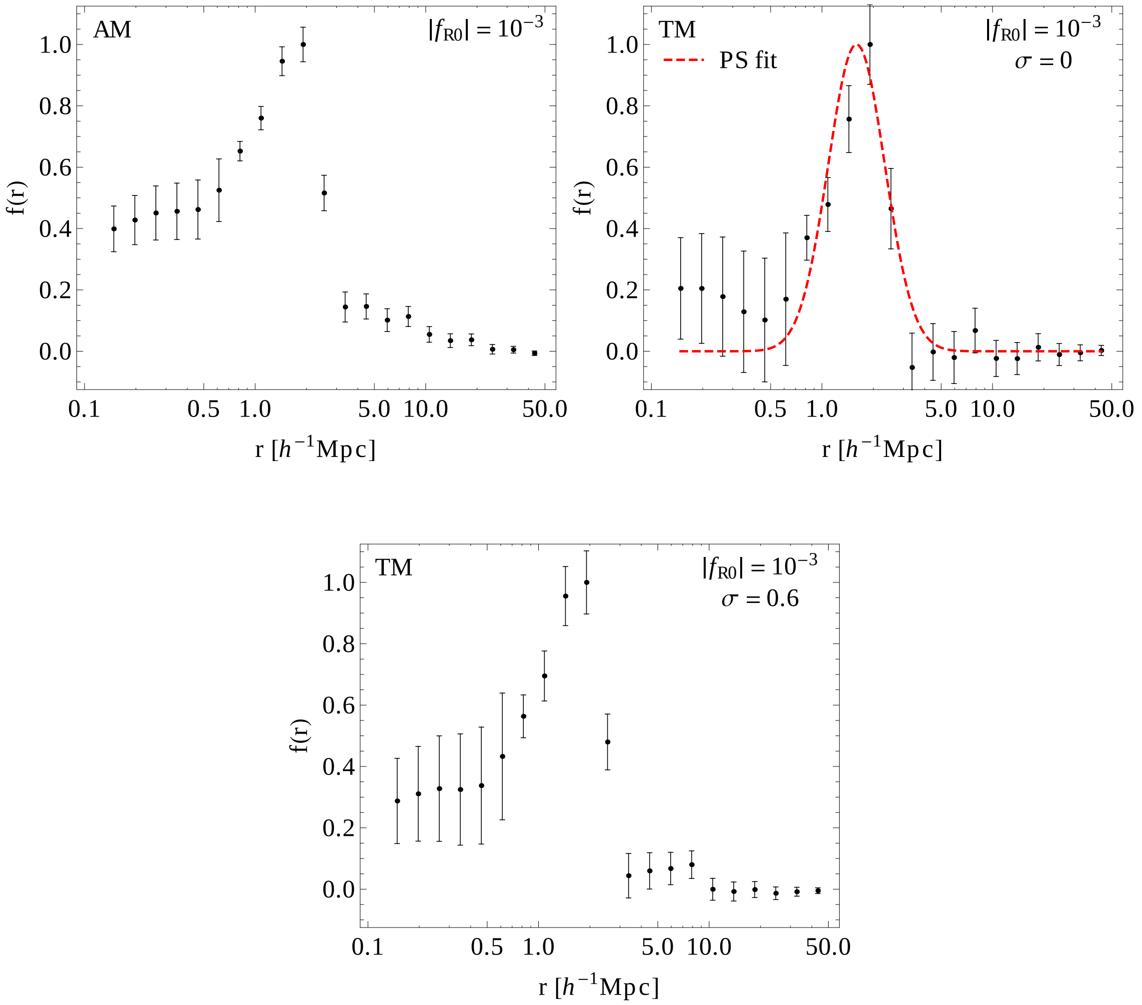

Figure 4.10: The simulated shape of the enhancement $f(r)$ for $|f_{R0}| = 10^{-3}$ in the abundance (upper left panel) and threshold matched case with scatter $\sigma = 0$ (upper right panel) and $\sigma = 0.6$ (lower panel), respectively. The upper right panel also shows the best-fit Gaussian function Eq. (4.40) to the simulation output.

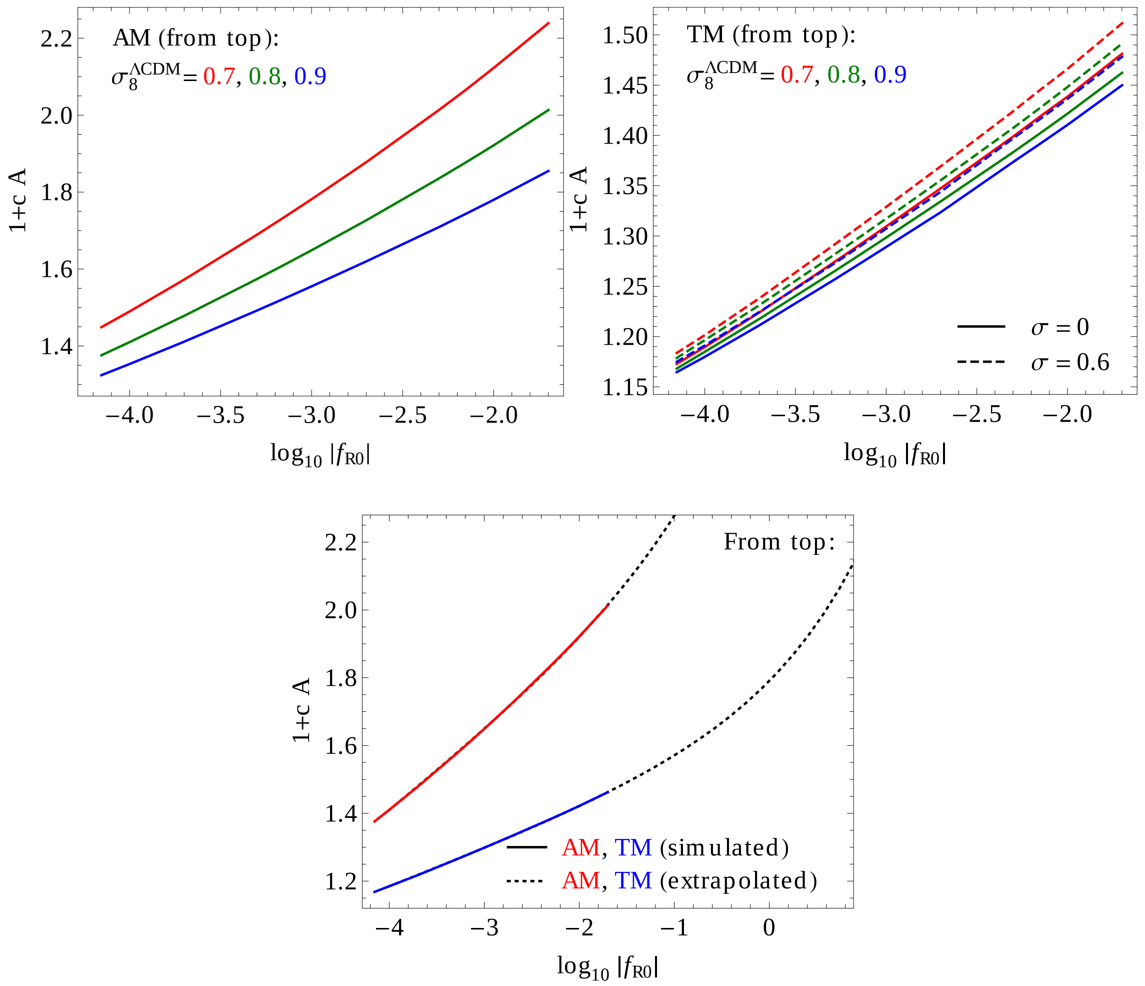

Figure 4.11: The relative enhancement of the peak $1 + c(\sigma)A\left(f_{R0}, \sigma_8^{\Lambda\mathrm{CDM}}\right)$ in the abundance (upper left panel) and the threshold matched case (upper right panel), respectively, as a function of $|f_{R0}|$ for different values of the power spectrum normalization $\sigma_8^{\Lambda\mathrm{CDM}}$ and the mass scatter σ. Effects from scatter can be neglected in the abundance matched case. Note that the enhancement is logarithmically suppressed in $|f_{R0}|$. The lower panel shows the extrapolation of $1 + A\left(|f_{R0}|, \sigma_8^{\Lambda\mathrm{CDM}} = 0.8\right)$ beyond the simulated values of $|f_{R0}|$. The upper and lower curve is the prediction in the abundance and threshold matched case, respectively. In the phenomenological scenario, the lower curve illustrates the correspondence between F_0 and $|f_{R0}|$, i.e., $1 + c\,A = 1 + F_0$.

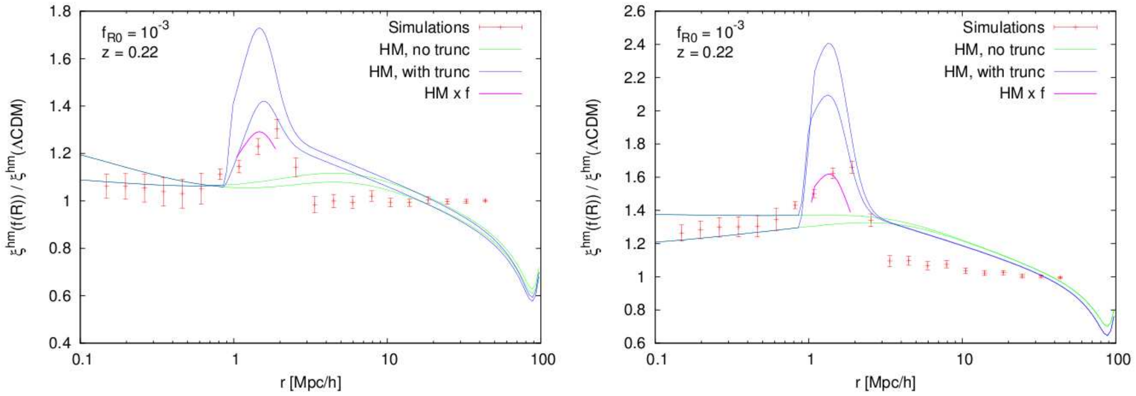

Figure 4.12: Halo-model fit to the simulated cluster density profiles (see appendix). The bump in the halo profile is produced by applying a cut of the one-halo term at the virial radius. The peak enhancement is stronger when using standard forces in the spherical collapse as when accounting for the stronger gravitational attraction observed in $f(R)$ gravity. Applying a fudge factor, the peak amplitude can be matched to simulations.

where c, the amplitude A, and the shape of f are obtained from the halo model and simulations, i.e., the halo model is used to interpolate between and extrapolate beyond the simulated parameter values $|f_{R0}|$ and $\sigma_8^{\Lambda\mathrm{CDM}}$, respectively. $\xi_{\mathrm{hm}}^{\Lambda\mathrm{CDM}}$ refers to the halo-matter correlation inferred from the ZHORIZON simulations. Thereby, $\sigma_8^{\Lambda\mathrm{CDM}}$ denotes the linear power spectrum normalization the $f(R)$ gravity model would have if $|f_{R0}| = 0$, i.e., the σ_8 of the corresponding concordance model. Furthermore, σ is the mass scatter defined in Sec. 4.2.3.3. In the AM case, scatter effects on c and f can be neglected, i.e., f is only a function of r and $c = 0.495$. When choosing same mass ranges, we have $c(\sigma = 0) = 0.716$, $c(\sigma = 0.6) = 0.761$, and $f(r, \sigma = 0) \neq f(r, \sigma = 0.6)$. We illustrate the shape $f(r)$ in Fig. 4.10 and plot the relative enhancement of the peak in Fig. 4.11. We extrapolate A beyond the simulated values of $|f_{R0}|$ (see Sec. 4.2.2.2) by

$$A = a_0(\sigma_8) + a_1(\sigma_8)\, x + a_2(\sigma_8)\, e^x, \tag{4.36}$$

where $x = \log_{10} |f_{R0}|$. This approximation is accurate at the $\lesssim 0.1\%$ level within the range of simulated values of $|f_{R0}|$. For the coefficients we use the fit

$$\begin{aligned} a_i(\sigma_8) &= a_{i0} + a_{i1}\,\sigma_8 + a_{i2}\,\sigma_8^2, && (4.37)\\ a_i(\sigma_8) &= a_{i0} + a_{i1}\,\sigma_8^{-1}, && (4.38)\end{aligned}$$

where $i = 0, 1, 2$, in the AM and TM case, respectively. Note that we used $\sigma_8 = \sigma_8^{\Lambda\mathrm{CDM}}$ in Eqs. (4.36) through (4.38) to simplify notation.

Phenomenology with a Gaussian fit

To first order the effect of modified forces on the halo profile can be described by a simple Gauss function, logarithmically in r, enhancing the standard gravity prediction for both $f(R)$ and DGP gravity (cf. [339, 358]). Here, we focus on the first-order effects on the TM selected $f(R)$ gravity profiles. We fit the relative enhancement produced in the $|f_{R0}| = 10^{-3}$ no-scatter scenario by the amplitude, width, and position of a Gaussian function in $\ln r$ and then take the amplitude F_0 to be the free parameter of the modification, i.e.,

$$\xi_{\text{mod}} = \xi_{\text{GR}} + \xi_+, \tag{4.39}$$

where

$$\xi_+ = F_0 \exp\left[-\frac{1}{2}\left(\frac{\ln r - \mu}{\varsigma}\right)^2\right] \xi_{\text{GR}} = F_0 \bar{\xi}_+. \tag{4.40}$$

The minimal χ^2 for the fit of the fixed mass simulation (see Fig. 4.10) is obtained for $e^{\varsigma} = 1.47 h^{-1}$ Mpc and $e^{\mu} = 1.59 h^{-1}$ Mpc, i.e., $\chi^2_{\text{min}} \simeq 20$.

In the middle panel of Fig. 4.10 we show the ratio of the modified to the ΛCDM ($|f_{R0}| = 0$) simulated density profile for $|f_{R0}| = 10^{-3}$ and the corresponding Gaussian function. We apply this scaling to the cluster profiles measured from the ZHORIZON simulations $\xi_{\text{hm}}^{\Lambda\text{CDM}}$ to test for departures from the standard halo profile predictions. In the following, we refer to this approach as the phenomenological scenario (PS).

Note that by construction F_0 matches the peak height of the enhancement in the threshold matched scenario for

$$F_0 = c(\sigma = 0) A\left(|f_{R0}| = 10^{-3}, \sigma_8^{\Lambda\text{CDM}} = 0.8\right) \simeq 0.30. \tag{4.41}$$

$1 + F_0$ therefore relates to $|f_{R0}|$ via the ordinate of the right panel of Fig. 4.11.

4.2.3. Galaxy-galaxy lensing

We can test the distinct predictions for the halo profile by employing galaxy-galaxy lensing measurements. We start by discussing the details of the galaxy-galaxy lensing observable, in our case, the differential excess surface mass density, i.e., the theoretical predictions, approximations, and interpolations used, as well as the data sets employed, before presenting constraints on the modifications from $f(R)$ gravity.

4.2.3.1. Differential excess surface mass density

Weak lensing serves as a powerful probe of dark matter distributions within our universe. Here, we focus on galaxy-galaxy lensing, which measures the deformation of galaxy images, by a foreground dark matter halo. Quantitatively the effect is described by the average tangential shear γ_t on the background galaxy images, which in turn is used to derive the projected mass distribution of the foreground object. The differential excess surface mass density is determined by [359]

$$\Delta\Sigma_{\text{gm}}(R) = \bar{\Sigma}_{\text{gm}}(R) - \Sigma_{\text{gm}}(R) = \Sigma_{\text{crit}} \langle \gamma_t(R, \phi) \rangle_{\phi}, \tag{4.42}$$

where Σ_{gm} is the projected surface mass density and $R \approx \theta D_l$, the comoving transverse distance between lens and source galaxies with angular separation θ. The indices $\mathcal{I} = \{\text{g}, \text{m}\}$ refer to galaxies and mass, respectively. The mean surface mass density within a circular aperture is given by

$$\bar{\Sigma}_{\text{gm}}(R) = \frac{2}{R^2} \int_0^R \Sigma_{\text{gm}}(R') R' dR', \tag{4.43}$$

and the critical surface mass density is

$$\Sigma_{\mathrm{crit}}(R) = \frac{2c^2}{\kappa^2} \frac{D_{\mathrm{s}}}{D_{\mathrm{ls}} D_{\mathrm{l}} (1+z_{\mathrm{l}})^2}, \tag{4.44}$$

where D_{s}, D_{l}, and D_{ls} denote the angular diameter distance to the source, the lens, and between the lens and the source, respectively. Note that Σ_{crit} is an effective quantity obtained from the stacking of a large amount of foreground and background objects and is dependent on the specific cosmological model (see Sec. 4.2.3.3).

Finally, the projected surface mass density is determined by

$$\Sigma_{\mathrm{gm}}(R) = \frac{2H^2\Omega_{\mathrm{m}}}{\kappa^2} \int_{\mathbb{R}} g_{\mathrm{l}}(\chi) \left[1 + \xi_{\mathrm{hm}}\left(\sqrt{R^2+\chi^2}\right)\right] d\chi, \tag{4.45}$$

where H indicates the Hubble parameter, χ denotes the line of sight, and ξ_{hm} is the halo-matter correlation function determined from the ZHORIZON simulations and Eqs. (4.35) or (4.39). The dependence of the lensing strength on the distribution of the lens mass is contained in the window function $g_{\mathrm{l}}(\chi)$. It is a function of the positions of the lens and the source. The inhomogeneous mass distribution in between contributes to the final distortion. Therefore, $g_{\mathrm{l}}(\chi)$ is taken to be very broad and is defined by the radial distribution of the lens and source samples.

Theoretical predictions

We determine $\Delta\Sigma_{\mathrm{gm}}^{\Lambda\mathrm{CDM}}$ from $\xi_{\mathrm{hm}}^{\Lambda\mathrm{CDM}}$ using Eqs. (4.42) through (4.45) for each concordance model cosmology in Table 4.5. In Fig. 4.13, we plot the prediction of the differential excess surface mass density $\Delta\Sigma_{\mathrm{gm}}$ for the fiducial model and illustrate effects from varying cosmological parameters according to Table 4.5. As our basic grid for $\Delta\Sigma_{\mathrm{gm}}^{\Lambda\mathrm{CDM}}$, we use a four dimensional paraboloid that interpolates between the parameter values of Table 4.5 at each value of the radius r, where we linearly interpolate in $\log r$. We add a further dimension in the case of $f(R)$ gravity or the phenomenological description and based on our halo-model parametrization, for the integration, we use the approximation

$$\Delta\Sigma_{\mathrm{gm}}^{\mathrm{mod}} = \left[1 + \frac{\mathcal{F}}{\mathcal{F}_0} \frac{\Delta\Sigma_{\mathrm{gm}}^{\mathcal{F}_0} - \Delta\Sigma_{\mathrm{gm}}^{\mathrm{fid}}}{\Delta\Sigma_{\mathrm{gm}}^{\mathrm{fid}}}\right] \Delta\Sigma_{\mathrm{gm}}^{\Lambda\mathrm{CDM}} \tag{4.46}$$

for the differential excess surface mass density. Hereby, we set

$$\mathcal{F}\left(\Omega_{\mathrm{m}}, \sigma_8^{\Lambda\mathrm{CDM}}, \sigma, f_{R0}\right) = A\left(f_{R0}, \sigma_8^{\Lambda\mathrm{CDM}}\right), \tag{4.47}$$

where $\mathcal{F}_0$ refers to quantities derived for $|f_{R0}| = 10^{-3}$ and other parameters at their fiducial values, i.e., $\Omega_{\mathrm{m}} = 0.25$, $\sigma_8^{\Lambda\mathrm{CDM}} = 0.8$, $n_{\mathrm{s}} = 1$, and $\sigma = 0$ in the AM and TM cases. $\Delta\Sigma_{\mathrm{gm}}^{\mathcal{F}_0}$ is the corresponding differential excess surface mass density shown in Fig. 4.13. In the TM case $\Delta\Sigma_{\mathrm{gm}}^{\mathcal{F}_0}$ linearly interpolates between the prediction for $\sigma = 0$ and $\sigma = 0.6$. Note that the approximation Eq. (4.46) for the integration of Eq. (4.35), Eqs. (4.42) through (4.45), is valid within $\lesssim 1\%$ accuracy for even the most extreme points of our grid.

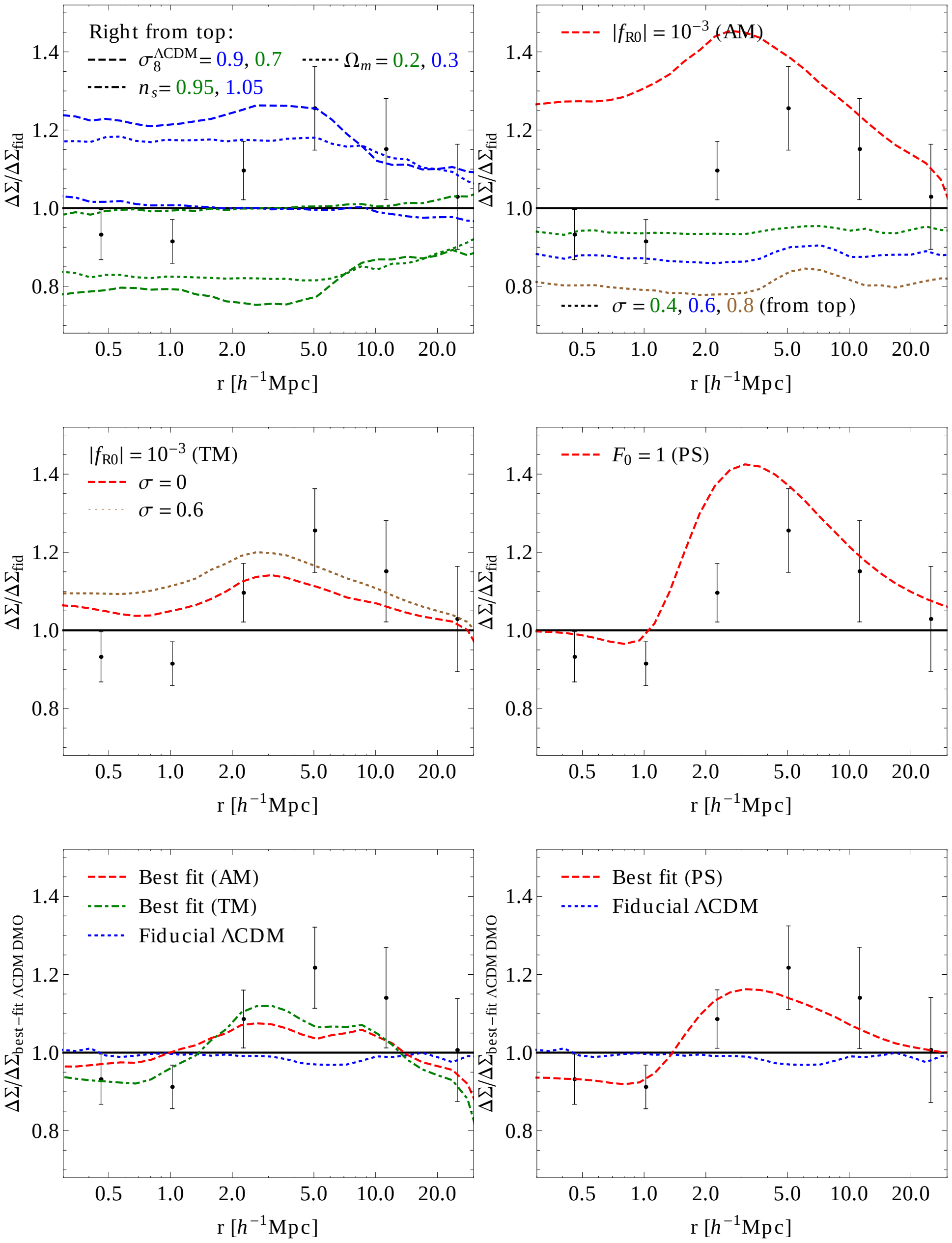

Figure 4.13: Effects on the differential excess surface mass density $\Delta\Sigma_{\mathrm{gm}}$ from varying the cosmological parameters with respect to the fiducial case. *Upper left*: $\sigma_8^{\Lambda\mathrm{CDM}}$ (dashed), n_{s} (dot-dashed), Ω_{m} (dotted). *Upper right*: $|f_{R0}| = 10^{-3}$ for the abundance matched case (dashed) and for the fiducial ΛCDM cosmology with different values of scatter σ (dotted). *Middle left*: $|f_{R0}| = 10^{-3}$ for the threshold matched case with $\sigma = 0$ (dashed) and $\sigma = 0.6$ (dotted). *Middle right*: $F_0 = 1$ for the phenomenological scenario. *Lower left*: Best-fit prediction for the differential excess surface mass density $\Delta\Sigma_{\mathrm{gm}}$ in $f(R)$ gravity in the abundance (dashed) and the threshold (dot-dashed) matched scenarios, as well as for the fiducial ΛCDM model (dotted) with respect to the best-fit concordance model. *Lower right*: Best-fit Gaussian enhancement (dashed) and fiducial ΛCDM model (dotted) with respect to the best-fit concordance model.

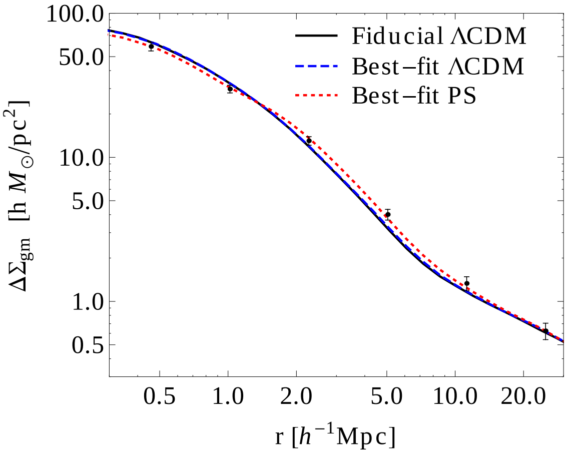

Figure 4.14: Differential excess surface mass density as measured in the maxBCG sample, predicted for the fiducial and best-fit ΛCDM model, respectively, as well as for the best-fit phenomenological scenario. Note that the fiducial and best-fit ΛCDM predictions nearly overlap.

We illustrate the best-fit prediction of the differential excess surface mass density for $f(R)$ gravity with respect to the best-fit prediction of the ΛCDM model in Fig. 4.13. The parameter values for the best-fit models are quoted in Table 4.6.

Comparing Fig. 4.13 and Fig. 4.9, we see that the relative enhancement observed in the halo profiles in $f(R)$ gravity is broadened and propagated to larger radial scales by the operations relating $\xi_{\rm hm}$ to $\Delta\Sigma_{\rm gm}$, i.e., Eqs. (4.42) through (4.45).

4.2.3.2. Observations

We use galaxy-galaxy lensing measurements around the maxBCG sample from the SDSS consisting of 5 891 clusters with background sources. The lens sample relies on 13 823 MaxBCG clusters [340] that are identified by the concentration of galaxies in color-position space using 7 500 square degrees of imaging data from the SDSS. The entire sample is placed into a single redshift slice, i.e., $0.1 < z < 0.3$, and a richness cut in N_{200} is applied to achieve a number density of $\bar{n} = 2 \times 10^{-5} h^{-1}$ Mpc. To remove effects from galaxy satellites in the sample, we apply a cylindrical cut in the projected radius $r_{\rm cut} = 3r_{\rm v}$ with $\Delta z = \pm 0.045$, where a richness-mass relation is used to estimate the virial radii. This removes about a third of the clusters within the sample, of which another third can be attributed to satellite clusters, resulting in a net observed number density of $\bar{n} = 1.4 \times 10^{-5} h^{-1}$ Mpc.

Next we apply three calibration factors to the lensing signal to correct for shear calibration, star/galaxy separation, and photo-z biases in $\Sigma_{\rm crit}$. The first correction is a factor of 1.02 based on STEP2 [360], the second effect is accounted for by a correction factor of 1.01 based on the comparison with COSMOS [361]. The third calibration factor is based on [362] and divided into two redshift slices $z \in (0.1, 0.3)$ and $z \in (0.3, 0.44)$ with correction factors 1.08 and 1.23 at a mean lensing-weighted redshift of $z = 0.21$ and $z = 0.36$, respectively.

Note that error correlations can be neglected and therefore we are only using the diagonal components of the data covariance matrix, restricting to scales $r \gtrsim 0.5h^{-1}$ Mpc for which we can trust the resolution of the simulations in Sec. 4.2.2.2.

4.2.3.3. Systematic effects

The shape of the enhancement effect on the cluster profile $\xi_{\rm hm}$ and the excess surface mass density $\Delta\Sigma_{\rm gm}$ observed in $f(R)$ gravity simulations cannot be reproduced by any reasonable deviations in the parameter values of the fiducial cosmology (see Figs. 4.9 and 4.13). Our comparison of theoretical predictions to the lensing observable is, however, affected by the following systematics.

- *Mass scatter*: We need to account for the fact that the measured masses might not be the true masses. To model the scatter in the mass-richness relation we add a Gaussian scatter to the mass before selecting the halos in the simulation, i.e.,
$$M = \exp\left[\ln(M_0) + \mathcal{N}(0,\sigma)\right], \tag{4.48}$$
where $\mathcal{N}$ is the normal distribution around zero with variance σ^2. We compare $\sigma = 0, 0.4, 0.6, 0.8$ and $\sigma = 0, 0.6$ in the concordance model and $f(R)$ gravity simulations, respectively. In the case of $f(R)$ gravity, the shape and amplitude of the AM profile enhancement $f(r)$ is not affected by variations in σ, however, in the TM scenario it is (see Fig. 4.10). Note that uncertainties from scatter within the concordance model cannot reproduce the profile enhancement seen in $f(R)$ gravity (see Figs. 4.9 and 4.13). We, however, include scatter in our analysis as an additional degree of freedom.

- *Baryons*: In order to understand the formation of galaxies within clusters, it is essential to include the baryonic components. Realistic models comprise mechanisms such as gas cooling, star formation, supernovae feedback, as well as the feedback from supermassive black holes to avoid the overcooling and accumulation of gas in the core of the cluster, the so-called active galactic nucleus (AGN) feedback. AGN outbursts produce shock waves that move the gas from the core to larger radii, i.e., between $r_{\rm v}$ and $2r_{\rm v}$, as was shown in [363] by employing simulations of Virgo-like galaxy clusters. Moreover, due to the AGN feedback, there is a slight adiabatic expansion of the dark matter when compared to DMO simulations [363]. However, we compare these baryonic effects on the cluster profile to the enhancement observed in $f(R)$ gravity and the phenomenological scenario. We conclude that they are qualitatively different in shape [see, e.g., Eq. (4.40)] and smaller in amplitude. Note that baryonic effects on the halo density profile are at the $\lesssim 15\%$ level (cf. [363, 364]), which translates into an error on $\Delta\Sigma_{\rm gm}$ at the $\lesssim 10\%$ level.

- *Intrinsic alignment*: High precision weak lensing measurements may be contaminated by the intrinsic alignment of galaxies (see, e.g., [365]). The correlation of intrinsic alignment and gravitational shear distortion can contribute to the observed ellipticity correlation function and $\Delta\Sigma_{\rm gm}$ at the $\lesssim 10\%$ level [366, 367].

- *Miscentering and satellites*: The cluster centers in the MaxBCG sample are identified by the brightest cluster galaxy (BCG). The true cluster center may, however, be offset due to some physical interference causing the BCG to leave the potential well or photometric redshift errors and limitations to the observational methods (see, e.g., discussion in [368]). The effect causes a suppression of the lensing signal in the inner parts of the halo, which subsequently leads to an underestimation of the cluster mass and the concentration. A miscentered $\Delta\Sigma_{\rm gm}$ can have a bump relative to a correctly centered $\Delta\Sigma_{\rm gm}$, which is, however, located further inwards than the $f(R)$ gravity enhancement (cf. [369]). A similar enhancement around the virial radius can further be introduced by galaxy satellites. To prevent the contamination of the excess surface mass density through satellites, we apply a cylindrical cut in the projected radius at $r_{\rm cut} = 3r_{\rm v}$ in the simulations (see Sec. 4.2.2.2) and the observations (see Sec. 4.2.3.2).

- *Wrong cosmology*: The analysis of lensing requires the assumption of an *a priori* cosmological model to estimate the critical surface mass density $\Sigma_{\rm crit}$ and to convert angles to distances. Within ΛCDM, a wrong prior on the cosmological model produces a radial horizontal shift of $\Delta\Sigma_{\rm gm}$ at the $\lesssim 2\%$ level (see discussion in [370]). Note that the Hu-Sawicki $f(R)$ gravity model matches the ΛCDM background. The inferred distances and systematic error estimates therefore correspond.

- *Simulation systematics*: We compare the halo profiles from the ZHORIZON simulations to the halo profiles of the MILLENNIUM simulations [371], which employ $N = 2160^3$ particles in a 500^3h^{-1} Mpc box. The profiles agree on the scales of interest. We therefore assume that the ZHORIZON simulations have converged for $r \sim (0.2 - 100)h^{-1}$ Mpc. Concordance model clusters are identified here by an FoF halo finder and the $f(R)$ profile enhancement is based on a SO algorithm. The FoF identification tends to link nearby halos, which may cause a contamination of the cluster density profile. Moreover, the shape of the $f(R)$ gravity enhancement on the cluster density profiles $f(r)$ extracted from simulations is affected by statistical uncertainties at the $\lesssim 20\%$ level at small radii with smaller errors on larger scales (see Fig. 4.10). These errors translate into a $\lesssim 10\%$ contamination of the excess surface mass density and dominate over the statistical simulation errors in ZHORIZON and the other simulation uncertainties discussed here. Note that we assume the halo profiles to be given by the mean and tentatively neglect simulation errors in our analysis.

Except for the case of scatter uncertainties, when performing the likelihood analysis on the parameter spaces, we neither model the systematics described above nor include them as additional errors to the measurement, but rather constrain modifications from $f(R)$ gravity on average DMO simulations only. In order to consistently include these systematics, they should not only be carefully analyzed within ΛCDM but also in the context of $f(R)$ gravity, which is beyond the scope of this paper. Note that the described uncertainties sum up to a $\lesssim 15\%$ and $\lesssim 20\%$ error in the predicted excess surface mass density when adding them in quadrature in the concordance model as well as in the phenomenological scenario and in the case of $f(R)$ gravity, respectively. In the following we shall therefore work with the assumptions that the above systematics, exept for the mass scatter, can be neglected and that the observations can correctly be described by the mean of the DMO simulations.

4.2.3.4. Priors from the CMB and distance measures

In order to prevent degeneracies of $|f_{R0}|$ with other cosmological parameters and combinations thereof, we further employ measurements of the background history and the cosmic microwave background. For this purpose, we take the likelihood distribution for the concordance model parameters from the chains of [335]. This analysis uses the CMB anisotropy data from the five-year Wilkinson Microwave Anisotropy Probe (WMAP) [372], the Arcminute Cosmology Bolometer Array Receiver (ACBAR) [373], the Cosmic Microwave Background Imager (CBI) [374], and the Very Small Sky Array (VSA) [375]. It further utilizes data from the Supernova Cosmology Project (SCP) Union [376] compilation, the measurement of the Hubble constant from the Supernovae and H_0 for the Equation of State (SHOES) [377] program generalized by [378], and the BAO distance measurements of [379]. For the description of these observables, in particular for the CMB, a high-redshift parametrization was chosen, constructed from the physical baryon and cold dark matter density $\Omega_{\mathrm{b}}h^2$ and $\Omega_{\mathrm{c}}h^2$, the ratio of sound horizon to angular diameter distance at recombination $\theta/100$, the optical depth to reionization τ, the scalar tilt n_{s}, and amplitude A_{s} at $k_* = 0.002\ \mathrm{Mpc}^{-1}$.

For our analysis we restrict to the parameters that are used for predicting the differential excess surface mass density $\Delta\Sigma_{\mathrm{gm}}$ in Sec. 4.2.3.1, i.e., n_{s} and the derived parameters, the total matter density Ω_{m} and the power spectrum normalization $\sigma_8^{\Lambda\mathrm{CDM}}$. Hence, we marginalize over $\{\Omega_{\mathrm{b}}h^2, \Omega_{\mathrm{c}}h^2, \theta, \tau, \ln[10^{10}A_{\mathrm{s}}]\}$ to obtain a three-dimensional posterior distribution for n_{s}, Ω_{m}, and $\sigma_8^{\Lambda\mathrm{CDM}}$, which serves as our prior within the MCMC analysis.

Note that by construction, at high redshifts, $f(R)$ modifications become negligible, i.e., at large multipoles of the CMB, predictions from $f(R)$ gravity match the predictions from the concordance model. Modifications appear only at low multipoles of the CMB due to the Integrated-Sachs Wolfe effect and lead to constraints on $|f_{R0}|$ of around unity [333]. The background expansion history within the Hu-Sawicki $f(R)$ gravity model matches the one of ΛCDM for $|f_{R0}| \ll 1$ at the accuracy level of current observations. Since we are interested in constraints on $f(R)$ modifications that originate from the halo profile alone, we restrict to the concordance model predictions for comparison with the data described here.

Finally, for scatter σ, we adopt the prior of [380] obtained from requiring consistency between weak lensing and X-ray measurements of the MaxBCG clusters.

4.2.4. Results

We now move to the MCMC likelihood analysis of the cosmological parameter spaces

$$\mathcal{P} = \left\{\Omega_{\mathrm{m}}, \sigma_8^{\Lambda\mathrm{CDM}}, n_{\mathrm{s}}, \sigma, |f_{R0}|\right\} \tag{4.49}$$

Parameter	ΛCDM		AM	
$\Omega_{\rm m}$	0.275 ± 0.011	0.275	0.244 ± 0.010	0.232
$\sigma_8^{\Lambda\rm CDM}$	0.811 ± 0.014	0.803	0.759 ± 0.018	0.733
$n_{\rm s}$	0.957 ± 0.011	0.952	0.964 ± 0.015	0.979
σ	0.448 ± 0.098	0.394	0.61 ± 0.13	0.37
$10^{-2}\lvert f_{R0}\rvert$	$\ldots$		< 2.65	0.10
F_0	$\ldots$		$\ldots$	
$-2\ln L$	10.6		9.1	

Table 4.6: Mean, standard deviations, and best-fit values for the concordance model and $f(R)$ gravity in the abundance matched scenario, respectively. For $|f_{R0}|$ and F_0, we quote 95% 1D-marginalized confidence levels. $-2\ln L$ is calculated for the galaxy-galaxy lensing data including the priors of Sec. 4.2.3.4.

Parameter	TM		PS	
$\Omega_{\rm m}$	0.2414 ± 0.0074	0.2321	0.265 ± 0.010	0.266
$\sigma_8^{\Lambda\rm CDM}$	0.753 ± 0.013	0.733	0.794 ± 0.015	0.790
$n_{\rm s}$	0.967 ± 0.016	0.979	0.956 ± 0.012	0.952
σ	0.450 ± 0.086	0.428	0.46 ± 0.10	0.44
$10^{-2}\lvert f_{R0}\rvert$	< 583	328	$\ldots$	
F_0	$\ldots$		$(0.26, 0.97)$	0.58
$-2\ln L$	6.2		1.9	

Table 4.7: Same as Table 4.6 but for $f(R)$ gravity in the threshold matched and phenomenological scenario, respectively.

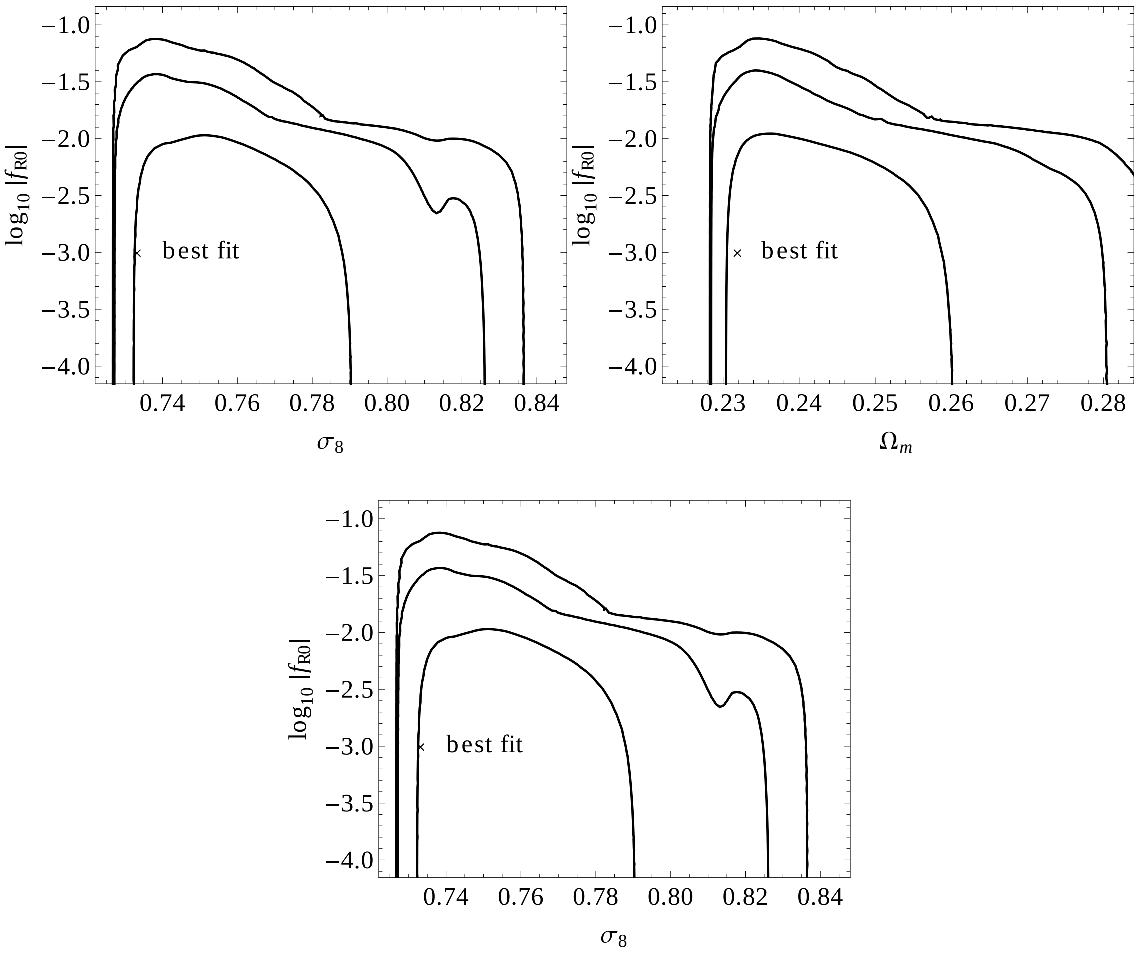

Figure 4.15: 2D-marginalized contour plots for the abundance matched case, showing 68%, 95%, and 99% confidence levels.

and, in the case of the PS enhancement,

$$\mathcal{P}_{\rm Gauss} = \left\{\Omega_{\rm m}, \sigma_8^{\Lambda{\rm CDM}}, n_{\rm s}, \sigma, F_0\right\}, \tag{4.50}$$

where for the concordance model $\mathcal{P}_{\Lambda\rm CDM} = \mathcal{P} \cap \{|f_{R0}| = 0\} = \mathcal{P}_{\rm Gauss} \cap \{F_0 = 0\}$. We implement the following flat priors on the parameters in $\mathcal{P}\backslash\mathcal{P}_{\Lambda\rm CDM}$ and $\mathcal{P}_{\rm Gauss}\backslash\mathcal{P}_{\Lambda\rm CDM}$: $|f_{R0}| \in (0, 10)$, $|f_{R0}| \in (0, 10)$, $|f_{R0}| \in (0, 10^4)$, and $F_0 \in (0, 5)$, for the AM, TM, and PS enhancement, respectively. In addition to the priors from the distance and CMB measurements discussed in Sec. 4.2.3.4, we further employ flat priors on top of the priors on the parameters in $\mathcal{P}_{\Lambda\rm CDM}$: $\Omega_{\rm m} \in (0.05, 0.5)$, $\sigma_8^{\Lambda\rm CDM} \in (0.4, 1.6)$, $n_{\rm s} \in (0.5, 1.5)$, and $\sigma \in (0, 2)$.

The COSMOMC [381] package used for the MCMC likelihood analysis employs the Metropolis-Hastings algorithm [382, 383] for the sampling and the Gelman and Rubin statistic R [384] for testing the convergence. We require $R - 1 < 7 \times 10^{-3}$ for our runs. We summarize our results in Tables 4.6 and 4.7.

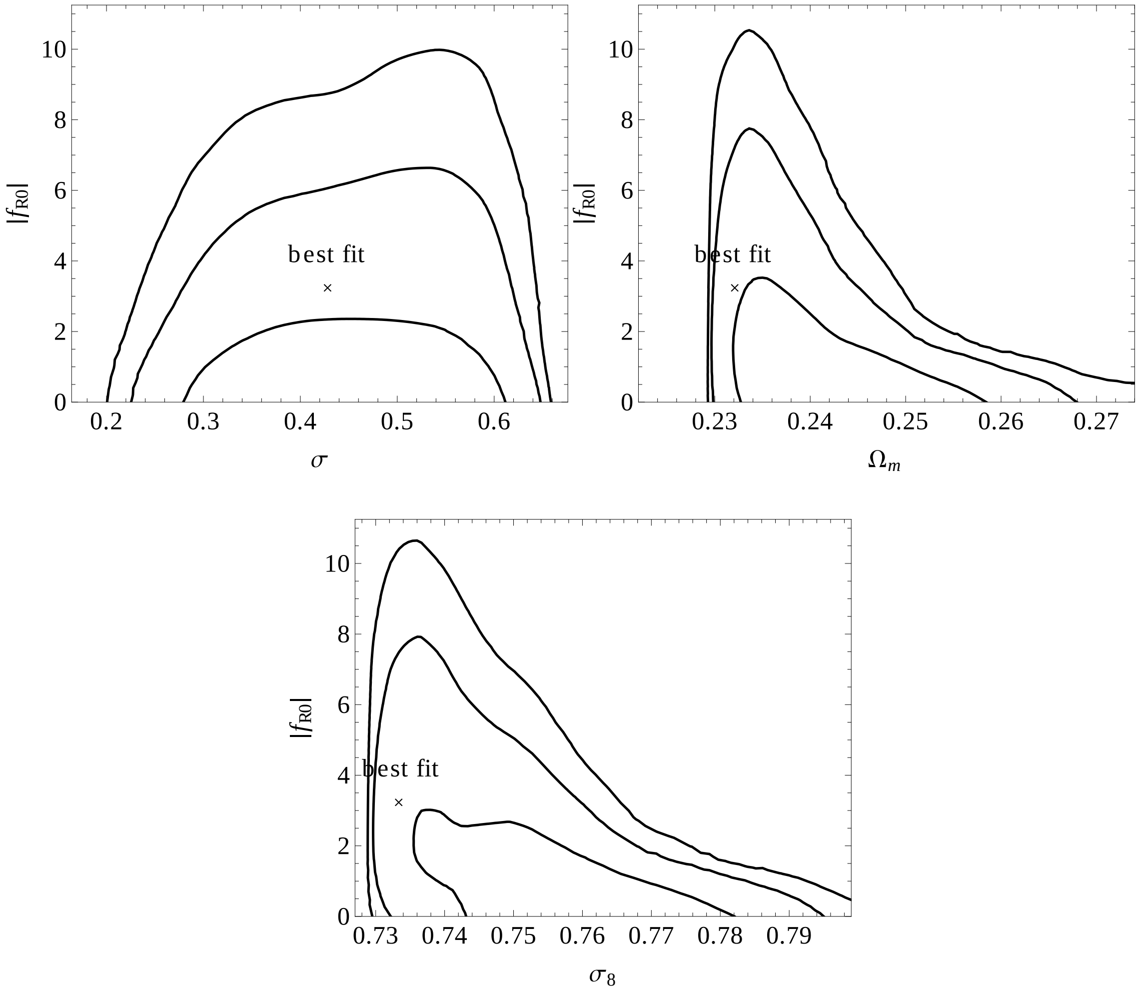

Figure 4.16: Same as Table 4.15 but for the threshold matched case.

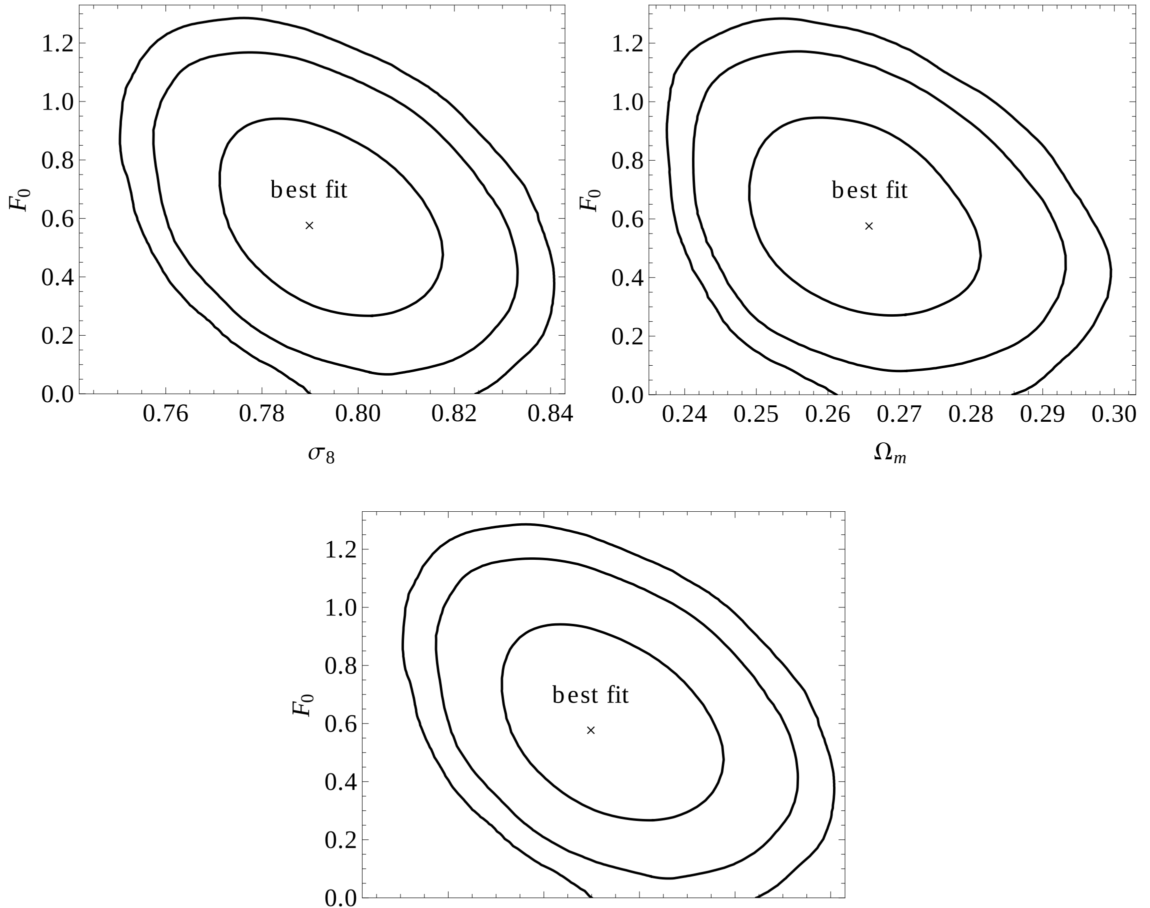

Figure 4.17: Same as Table 4.15 but for the phenomenological enhancement case.

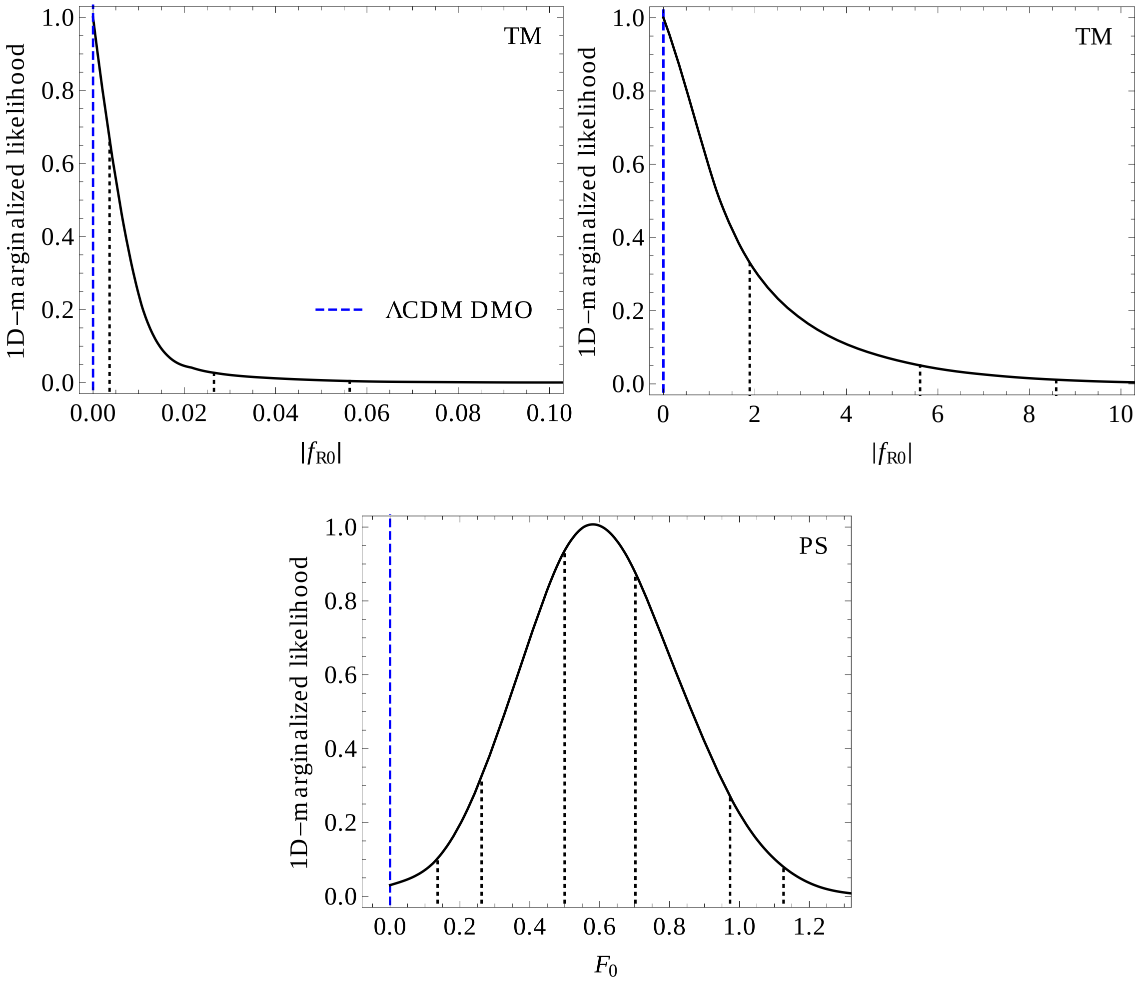

Figure 4.18: 1D-marginalized likelihood. The dotted lines indicate the 68%, 95%, and 99% confidence levels, the dashed line corresponds to the ΛCDM prediction from DMO simulations. *Upper left*: $|f_{R0}|$ in the abundance matched case. *Upper right*: $|f_{R0}|$ in the threshold matched case. *Lower panel*: F_0 in the phenomenological scenario with a Gaussian fit in $\ln r$ to the enhancement in the TM case.

4.2.4.1. Abundance matched case

From Fig. 4.13 it is clear that the relative difference in the $f(R)$ gravity induced enhancement on $\Delta\Sigma_{\rm gm}$ on scales below $r \lesssim 1h^{-1}$ Mpc and above $r \gtrsim 10h^{-1}$ Mpc observed in the AM case leads to a tension that cannot be compensated by adjusting the parameters in $\mathcal{P}$ within the priors given in Sec. 4.2.3.4. This leads to a 1D-marginalized constraint of $|f_{R0}| < 2.7 \times 10^{-2}$ at the 95% confidence level. Note that the prior on the scatter plays an essential role (see Fig. 4.15), i.e., if we were to remove it from the analysis, large scatter would make large $|f_{R0}|$ models viable (see Figs. 4.9 and 4.13) and due to a slow increase of the enhancement A as function of $|f_{R0}|$ (see Fig. 4.11), there would be a rather loose constraint on $|f_{R0}|$. This is what happens in the TM case (see Sec. 4.2.4.2).

Figure 4.15 shows the 2D-marginalized likelihoods for the parameter degeneracies with $|f_{R0}|$ and Fig. 4.18 shows the one-tail 1D-marginalized likelihood for $|f_{R0}|$ when using abundance matching to select the halo mass range.

4.2.4.2. Threshold matched case

In contrary to the AM case, when fixing the mass range equally in the ΛCDM and $f(R)$ gravity model, the discrepancy in the enhancement on $\Delta\Sigma_{\rm gm}$ on scales below $r \lesssim 1h^{-1}$ Mpc and above $r \gtrsim 10h^{-1}$ Mpc is less severe (see Figs. 4.10 and 4.13). This makes large values of $|f_{R0}|$ viable with the galaxy-galaxy lensing data and leads to strong parameter degeneracies (see Fig. 4.16). We obtain an upper bound of $|f_{R0}| < 5.8$. Note that such high values of $|f_{R0}|$ are not consistent with, e.g., measurements of the ISW effect in the CMB [333] and that approximations that are valid for $|f_{R0}| \ll 1$ break down (see Sec. 4.2.3.4).

We illustrate parameter degeneracies with $|f_{R0}|$ in Fig. 4.16. Figure 4.18 shows the one-tail 1D-marginalized likelihood for $|f_{R0}|$ when using the same fixed halo mass range for both the concordance model and the $f(R)$ gravity model.

4.2.4.3. Phenomenological scenario

When modeling the relative enhancement of the TM halo profile in $f(R)$ gravity with a simple Gaussian function in $\ln r$ with width and position fixed to fit the simulation and only considering the amplitude of the Gaussian function F_0 as an additional degree of freedom (see Sec. 4.2.2.3), we end up with a 1D-marginalized constraint of $0.26 < F_0 < 0.97$ at the 95% confidence level (see Fig. 4.18). $F_0 = 0$ corresponds to the ΛCDM model with DMO simulations. $F_0 = 0$ lies even below the lower 1D-marginalized 99% confidendence level, $F_0 < 0.14$. The best fit is obtained for $F_0 = 0.58$ with $-2\Delta \ln L = -8.7$ with respect to the best-fit concordance model. Note that we are neglecting baryonic effects and various other systematics (see Sec. 4.2.3.3). Therefore, this results cannot be interpreted as a detection of modified gravity. We stress, however, that this simple phenomenological approach is well-motivated by results from $f(R)$ gravity simulations and fits the apparent noise in the galaxy-galaxy lensing data remarkably well (see Fig. 4.13 and Table 4.7).

We can estimate the impact the theoretical systematics may have by adding the maximal systematic error of 15% (see Sec. 4.2.3.3) to the measurement errors.

When *not* including the theoretical systematics, we get a $\chi^2_{\rm l} \simeq 10.5, 1.6, 12.2$ for the best-fit concordance model, best-fit PS, and the fiducial ΛCDM model, where $\chi^2_{\rm l}$ is the lensing contribution to χ^2, i.e., $\chi^2 = \chi^2_{\rm l} + \chi^2_{\rm p}$ with $\chi^2_{\rm p}$ coming from the prior (see Sec. 4.2.3.4). If using the same fits with errors that include the maximal estimate of the systematics, we get $\chi^2_{\rm l} = 2.3, 0.4, 2.7$ for the scenarios described above. Hence, the increase in fit of the PS over ΛCDM reduces to $\Delta\chi^2_{\rm l} \simeq -2$, which is not at a significant level anymore. Thus, the increase of the PS fit does not necessarily originate from a modification of gravity but it suggests that DMO ΛCDM simulations are not sufficient for correctly describing the halo density profiles at the scales of $(1-10)$ Mpc.

Figure 4.17 illustrates parameter correlations with F_0 and Fig. 4.18 shows the 1D-marginalized likelihood for the amplitude F_0 when taking a Gaussian enhancement of the concordance model halo profile as a phenomenological approach to describing effects of modifications of gravity. The best-fit parameter values as well as the corresponding $-2\ln L$ are listed in Table 4.7.

4.2.5. Discussion

Modifications of gravity as in the $f(R)$ gravity model under consideration in this paper generically predict departures from the standard growth produced in the concordance model. On the largest, cosmological, scales ($r \gtrsim 10$ Mpc) and on small, solar-system, scales ($r \lesssim 0.1$ mpc) such deviations have extensively been instrumentalized to probe gravity. However, structures on the intermediate scales also offer opportunities to test the gravitational interactions. In this paper, we test modifications of gravity on scales around the virial radius of a cluster, i.e., $r \simeq (0.2-20)$ Mpc. The modification of the Poisson equation leads to a difference in accretion of mass to the virialized dark matter halo. The resulting halos exhibit enhanced density profiles at a few virial radii that offer a unique opportunity for testing gravity. We use the projected mass distribution measured through galaxy-galaxy lensing around maxBCG samples from the SDSS to put constraints on the modifications induced by the Hu-Sawicki $f(R)$ gravity model.

For consistent theoretical predictions, we rely on $f(R)$ gravity and concordance model N-body DMO simulations, where we use two different schemes for relating halos in the models to each other, i.e., by matching the selection of halos by the same abundance threshold (AM) and by using the same fixed halo mass threshold (TM), respectively. Note that massive halos are more abundant in $f(R)$ gravity than within ΛCDM. In the first, more realistic case, modifications from $f(R)$ gravity are more pronounced. In particular the overall amplitude of the enhancement and the difference between the relative enhancement of the differential excess surface mass density at $r \lesssim 1h^{-1}$ Mpc and $r \gtrsim 10h^{-1}$ Mpc is larger. This leads to tighter constraints on the extra degree of freedom of the $f(R)$ gravity model, i.e., the background scalar field strength $|f_{R0}|$. For the AM and TM case, we obtain upper one-tail bounds of $|f_{R0}| < 0.027$ and $|f_{R0}| < 5.8$, respectively, at the 1D-marginalized 95% confidence level, where we consider abundance matching as the more consistent approach for obtaining constraints on $|f_{R0}|$. This places a new independent constraint on $f(R)$ gravity at intermediate scales, where $|f_{R0}| \lesssim 10^{-4}$ and $|f_{R0}| \lesssim (10^{-6}-10^{-5})$ are current bounds inferred from large, cosmological, and solar-system scales, respectively.

We further find consistency of the concordance model with the 1D-marginalized 68% confidence level. However, when we use a Gaussian fit in $\ln r$ for the relative deviations of the halo profiles obtained in the TM $f(R)$ gravity scenario with respect to the DMO simulated halo profiles within the concordance model as a phenomenological approach to classify modifications of gravity, the concordance model forfeits relative performance. We find that DMO simulations predict halo profiles that lie below the 1D-marginalized 99% confidence level of the phenomenological degree of freedom of the Gaussian fit, its amplitude F_0, i.e., $F_0 < 0.14$. This result has to be taken with a grain of salt since we neglected systematic effects arising, e.g, from the influence of the baryonic fluid. However, it suggests that employing dark matter particles only in a ΛCDM simulations is not sufficient to correctly describe halo profiles at the scales of $(1-10)$ Mpc and that additional effects need to be taken into account.

Acknowledgments

We thank Anže Slosar, Bhuvnesh Jain, Darren Reed, Davide Martizzi, Doug Potter, Michael Busha, Jonathan Blazek, Ravi Sheth, Romain Teyssier, and Vincent Desjacques for useful discussions. L.L. thanks the Lawrence Berkeley National Laboratory, the Berkeley Center for Cosmological Physics, and Ewha Womans University for hospitality while parts of this work have been carried out. Computational resources were provided on the Schrödinger supercomputer of the University of Zurich and on the supercomputer of the Institute for the Early Universe at Ewha University. This work was supported by the Swiss National Foundation under Contract No. 2000 124835/1 and WCU Grant No. R32-2008-000-10130-0.

4.2.A. Halo model predictions for the density profiles

For completeness, we shall discuss here how we model the ratio of cluster density profiles in $f(R)$ gravity with respect to their ΛCDM counterparts in Sec. 4.2.2.3. We review the computations of [358] and extend the framework with new parameters to match the theoretical prediction to N-body simulations. First, we discuss how spherical collapse is modified by the enhanced forces experienced in $f(R)$ gravity. Then, we give a halo model prediction for the $f(R)$ gravity and ΛCDM cluster density profiles, which we use to determine the ratios illustrated in Fig. 4.10. Applying a fudge factor for the amplitude of the peak of the enhancement, we can use the halo model to interpolate between and extrapolate beyond simulated cosmological parameter values.

4.2.A.1. Modified spherical collapse

The continuity and Euler equation for a pressureless fluid of nonrelativistic matter,

$$\dot{\delta} + \frac{1}{a}\nabla \cdot (1+\delta)\mathbf{v} = 0, \tag{4.51}$$

$$\dot{\mathbf{v}} + \frac{1}{a}(\mathbf{v}\cdot\nabla)\mathbf{v} + H\mathbf{v} = -\frac{1}{a}\nabla\Psi, \tag{4.52}$$

respectively, can be combined to yield a second-order differential equation for the overdensity δ, i.e.,

$$\ddot{\delta} + 2H\,\dot{\delta} - \frac{\partial_{x^i}\partial_{x^j}}{a^2}\left[(1+\delta)v^i v^j\right] = \frac{\nabla\cdot(1+\delta)\nabla\Psi}{a^2}. \tag{4.53}$$

Here, dots indicate partial differentiation with respect to t, $\mathbf{v}$ is the velocity field and Ψ is the Newtonian potential, where spatial coordinates are comoving. The density perturbation shall be approximated by a top-hat distribution for determining the velocity field such that $\mathbf{v} = A(t)\mathbf{r}$. Using Eq. (4.51), Eq. (4.53) becomes

$$\ddot{\delta} + 2H\dot{\delta} - \frac{4}{3}\frac{\dot{\delta}^2}{1+\delta} = \frac{1+\delta}{a^2}\nabla^2\Psi. \tag{4.54}$$

The system closes with Eqs. (4.31) and (4.32). Mass conservation implies

$$\dot{M} = \frac{4\pi}{3}\frac{\partial}{\partial t}\left[r^3\bar{\rho}_{\mathrm{m}}(1+\delta)\right] = 0, \tag{4.55}$$

which applied to Eq. (4.54) yields

$$\frac{\ddot{r}}{r} = -\frac{\kappa^2}{6}\left[\bar{\rho}_{\mathrm{m}} + (1+w)\bar{\rho}_{\mathrm{eff}}\right] - \frac{1}{3a^2}\nabla^2\Psi \tag{4.56}$$

when describing additional contributions to the background expansion history through an effective dark energy term $\bar{\rho}_{\mathrm{eff}}$.

There are two limiting cases that relate $\nabla^2\Psi$ to $\delta\rho_{\mathrm{m}}$, which become apparent in the Poisson equation, Eq. (4.34), and may be parametrized as [358]

$$\frac{\ddot{r}}{r} = -\frac{\kappa^2}{6}\left[\bar{\rho}_{\mathrm{m}} + (1+3w)\bar{\rho}_{\mathrm{eff}}\right] - \frac{\kappa^2}{6}(1+F)\delta\rho_{\mathrm{m}}, \tag{4.57}$$

where $F = 1/3$ and $F = 0$ corresponds to the *modified spherical collapse* and *standard spherical collapse* scenario with enhanced and standard gravitational forces, respectively.

From Eq. (4.55), we have

$$\delta = \left(1 + \frac{a_{\mathrm{i}}}{a}y\right)^{-3}(1+\delta_{\mathrm{i}}) - 1, \tag{4.58}$$

where δ_{i} is the initial density perturbation at a_{i} and $y = r_{\mathrm{i}}^{-1}(r - r_{\mathrm{i}}a_{\mathrm{i}}^{-1}a)$. This implies a turn around at $r' = 0$ ($y' = -a/a_{\mathrm{i}}$) and collapse at $r = 0$ ($y = -a/a_{\mathrm{i}}$).

For a ΛCDM background expansion with $w = -1$ and $\bar{\rho}_{\mathrm{eff}} = \rho_\Lambda = 3H_0^2\Omega_\Lambda/\kappa^2$, Eq. (4.57) becomes

$$\begin{aligned} y'' + \frac{H'}{H}y' &= -\frac{1}{2}\frac{\Omega_{\mathrm{m}}a^{-3} - 2\Omega_\Lambda}{\Omega_{\mathrm{m}}a^{-3} + \Omega_\Lambda}y \\ &\quad -\frac{1}{2}\frac{\Omega_{\mathrm{m}}a^{-3}}{\Omega_{\mathrm{m}}a^{-3} + \Omega_\Lambda}(1+F)\left(y + \frac{a}{a_i}\right)\delta. \end{aligned} \tag{4.59}$$

The linearized combination of Eqs. (4.51) and (4.52)

$$\delta'' + \left(2 + \frac{H'}{H}\right)\delta' - \frac{3}{2}(1+F)\delta = 0 \tag{4.60}$$

imply that during matter domination $\delta \propto a^{1+p}$ with

$$p = -\frac{5}{4} + \frac{5}{4}\sqrt{1 + \frac{24}{25}F}. \tag{4.61}$$

Hence, assuming that the initial conditions for Eq. (4.60) lie well within the matter dominated regime, we have

$$y_\mathrm{i} = 0 \tag{4.62}$$

$$y'_\mathrm{i} = -\frac{1}{3}(1+p)\delta_\mathrm{i}. \tag{4.63}$$

Taking $\Omega_\mathrm{m} = 0.24$, for the linear overdensity extrapolated to the collapse, this yields $\delta_\mathrm{c} = 1.673$ and $\delta_\mathrm{c} = 1.692$ for $F = 0$ and $F = 1/3$, respectively [358].

The virial theorem states that

$$T = -\frac{1}{2}W + W_\Lambda, \tag{4.64}$$

where T is the kinetic energy and the potential energies are given by [358, 385]

$$W = -\frac{3}{5}(1+F)\frac{G\,M^2}{r}, \tag{4.65}$$

$$W_\Lambda = -\frac{\kappa^2}{10}\bar{\rho}_\mathrm{eff} M\, r^2. \tag{4.66}$$

Consider the ratio of the virial radius to the turn-around radius $s = r_\mathrm{v}/r_\mathrm{max}$ and the ratio

$$\eta = \frac{2\bar{\rho}_\mathrm{eff}}{(1+F)\rho_\mathrm{m}}, \tag{4.67}$$

where ρ_m is the matter density at turn-around. Energy conservation then requires

$$\begin{aligned} W(r_\mathrm{max}) + W_\Lambda(r_\mathrm{max}) &= T(r_\mathrm{v}) + W(r_\mathrm{v}) + W_\Lambda(r_\mathrm{v}) \\ &= \frac{1}{2}W(r_\mathrm{v}) + 2W_\Lambda(r_\mathrm{v}), \end{aligned} \tag{4.68}$$

which yields the equation

$$2\eta\, s^3 - (\eta + 2)s + 1 = 0. \tag{4.69}$$

The virial density is defined as the ratio between the overdensity at the virial radius and the average density at the end of collapse, i.e., $\Delta_\mathrm{v} = \rho_\mathrm{m}(r_\mathrm{v})/\bar{\rho}_\mathrm{m}(r = 0)$. For a ΛCDM background with $\Omega_\mathrm{m} = 0.24$ and collapse today, we have $\Delta_\mathrm{v} = 390$ and $\Delta_\mathrm{v} = 309$ for $F = 0$ and $F = 1/3$, respectively [358].

4.2.A.2. Halo model approach for the density profile

Consider the variance $\sigma(M)$ of the linear density field convolved with a top-hat filter of radius R, where $M = 4\pi\, r^3 \bar{\rho}_{\rm m}/3$ and $\bar{\rho}_{\rm m} = 3H_0^2 \Omega_{\rm m} a^{-3}/\kappa^2 \simeq 2.77468 \times 10^{11}\, \Omega_{\rm m} h^2 a^{-3}$ $\mathrm{M}_\odot/\mathrm{Mpc}^3$,

$$\sigma^2(R) = \int \frac{d^3k}{(2\pi)^3} \left|\hat{W}(k\,R)\right|^2 P_{\rm L}(k) \tag{4.70}$$

with the Fourier transform of the real-space top-hat window function of radius R,

$$\hat{W}(k\,R) = 3\left[\frac{\sin(k\,R)}{(k\,R)^3} - \frac{\cos(k\,R)}{(k\,R)^2}\right] \tag{4.71}$$

and linear matter power spectrum $P_{\rm L}(k)$. The peak threshold is defined by $\nu = \delta_{\rm c}/\sigma(M_{\rm v})$, where $M_{\rm v}$ is the virial mass. We use the Sheth-Tormen prescription [386] of the mass function, which defines the comoving number density of halos per logarithmic interval in the virial mass $M_{\rm v}$ by

$$n_{\ln M_{\rm v}} \equiv \frac{dn}{d\ln M_{\rm v}} = \frac{\bar{\rho}_{\rm m}}{M_{\rm v}} f(\nu) \frac{d\nu}{d\ln M_{\rm v}}, \tag{4.72}$$

where

$$\nu\, f(\nu) = A\sqrt{\frac{2}{\pi} a\,\nu^2}\left[1 + (a\,\nu^2)^{-p}\right] e^{-a\,\nu^2/2}. \tag{4.73}$$

Within the concordance model, $a \simeq 0.75$, $p \simeq 0.3$, $\delta_{\rm c} \simeq 1.673$, and A is chosen such that $\int d\nu f(\nu) = 1$.

The cluster profile or halo-matter correlation function $\xi_{\rm hm}(r)$ can be modeled by a two- and one-halo contribution yielding [358, 387]

$$\xi_{\rm hm}(r) = b_{\rm L}(M_{\rm v}) \int \frac{d^3k}{(2\pi)^3} I(k) P_{\rm L}(k) e^{-i\mathbf{k}\cdot\mathbf{x}} + \frac{\rho_{\rm NFW}(r)}{\bar{\rho}_{\rm m}}, \tag{4.74}$$

where $b_{\rm L}(M_{\rm v})$ is the linear bias given by

$$b_{\rm L}(M_{\rm v}) = 1 + \frac{a\,\nu^2 - 1}{\delta_{\rm c}} + \frac{2p}{\delta_{\rm c}\left[1 + (a\,\nu^2)^p\right]} \tag{4.75}$$

and $\rho_{\rm NFW}(r)$ is the Navarro-Frenk-White (NFW) [388] profile with

$$\rho_{\rm NFW}(r) = \frac{\rho_{\rm s}}{\frac{r}{r_{\rm s}}\left(1 + \frac{r}{r_{\rm s}}\right)^2}. \tag{4.76}$$

Here, $r_{\rm s}$ is the scale radius of the halo defined through the concentration $c_{\rm v} \equiv r_{\rm v}/r_{\rm s} = 9(M_*/M_{\rm v})^{0.13}$ and M_* is given by $\sigma(M_*) = \delta_{\rm c}$. The normalization $\rho_{\rm s}$ is given by

$$M_{\rm v} = 4\pi \int_0^{r_{\rm v}} \rho_{\rm NFW}(r) r^2 dr, \tag{4.77}$$

i.e., $\rho_{\rm s}^{-1} = 4\pi\, M_{\rm v}^{-1} r_{\rm s}^3\, [\ln(1+c_{\rm v}) - c_{\rm v}/(1+c_{\rm v})]$. Finally,

$$I(k) = \int d\ln M_{\rm v}\; n_{\ln M_{\rm v}} \frac{M_{\rm v}}{\bar{\rho}_{\rm m}} y(k, M_v) b_{\rm L}(M_{\rm v}), \tag{4.78}$$

with $y(k, M) = \hat{\rho}_{\rm NFW}(k)/N$, where $\hat{\rho}_{\rm NFW}(k)$ is the Fourier transform of a NFW density profile truncated at $r_{\rm v}$, i.e.,

$$\begin{aligned} \hat{\rho}_{\rm NFW}(k) &= \frac{\rho_{\rm s} r_{\rm s}^3}{2\pi^2} \Big[\cos(r_{\rm s}k) \left\{ {\rm Ci}[k(r_{\rm s}+r_{\rm v})] - {\rm Ci}(r_{\rm s}k) \right\} \\ &\quad + \sin(r_{\rm s}k) \left\{ {\rm Si}[k(r_{\rm s}+r_{\rm v})] - {\rm Si}(r_{\rm s}k) \right\} \\ &\quad - \frac{\sin(k\, r_{\rm v})}{k(r_{\rm s}+r_{\rm v})} \Big], \end{aligned} \tag{4.79}$$

with Si and Ci being the sine and cosine trigonometric integrals, respectively, and

$$N \equiv \lim_{k\to 0} \hat{\rho}_{\rm NFW}(k) = \frac{\rho_{\rm s} r_{\rm s}^3}{2\pi^2} \left[\ln\left(\frac{r_{\rm s}+r_{\rm v}}{r_{\rm s}} \right) - \frac{r_{\rm v}}{r_{\rm s}+r_{\rm v}} \right]. \tag{4.80}$$

Tuncation at $r = r_{\rm v}$ produces the enhancement of the cluster density profile at $(0.5-5)h^{-1}$ Mpc observed in Fig. 4.9. Note that in the case of standard spherical collapse, this enhancement is stronger than when applying a modified spherical collapse. In order to match the peak height to simulations, corrections for the peak amplitude obtained in the modified spherical collapse scenario are done via a fixed fudge factor $c_{\rm p}$, which is $c_{\rm p} = 0.44$ in the TM case and $c_{\rm p} = 0.4$ in the AM case (see Fig. 4.12). We may furthermore multiply the two-halo term with a factor of $c_{\rm 2h} = 0.85$ to match the halo-model prediction to the simulated halo profile at $r \gtrsim 8$ Mpc/h. For peak corrections in the standard spherical collapse scenario see Sec. 4.2.2.3.

References

[320] C. M. Will, "The confrontation between general relativity and experiment", Living Rev. Rel. **9**, 3 (2005), [arXiv:gr-qc/0510072].

[321] B. Jain and J. Khoury, "Cosmological Tests of Gravity", Annals Phys. **325**, 1479 (2010), [arXiv:1004.3294].

[322] S. M. Carroll, V. Duvvuri, M. Trodden, and M. S. Turner, "Is cosmic speed-up due to new gravitational physics?", Phys. Rev. **D70**, 043528 (2004), [arXiv:astro-ph/0306438].

[323] S. Nojiri and S. D. Odintsov, "Modified gravity with negative and positive powers of the curvature: Unification of the inflation and of the cosmic acceleration", Phys. Rev. **D68**, 123512 (2003), [arXiv:hep-th/0307288].

[324] S. Capozziello, S. Carloni, and A. Troisi, "Quintessence without scalar fields", Recent Res. Dev. Astron. Astrophys. **1**, 625 (2003), [arXiv:astro-ph/0303041].

[325] A. A. Starobinsky, "Spectrum of relict gravitational radiation and the early state of the universe", JETP Lett. **30**, 682 (1979).

[326] A. A. Starobinsky, “A new type of isotropic cosmological models without singularity”, Phys. Lett. **B91**, 99 (1980).

[327] J. Khoury and A. Weltman, “Chameleon cosmology”, Phys. Rev. **D69**, 044026 (2004), [arXiv:astro-ph/0309411].

[328] I. Navarro and K. Van Acoleyen, “f(R) actions, cosmic acceleration and local tests of gravity”, JCAP **0702**, 022 (2007), [arXiv:gr-qc/0611127].

[329] T. Faulkner, M. Tegmark, E. F. Bunn, and Y. Mao, “Constraining f(R) gravity as a scalar tensor theory”, Phys. Rev. **D76**, 063505 (2007), [arXiv:astro-ph/0612569].

[330] W. Hu and I. Sawicki, “Models of f(R) Cosmic Acceleration that Evade Solar-System Tests”, Phys. Rev. **D76**, 064004 (2007), [arXiv:0705.1158].

[331] T. L. Smith, “Testing gravity on kiloparsec scales with strong gravitational lenses”, (2009), [arXiv:0907.4829].

[332] Y.-S. Song, W. Hu, and I. Sawicki, “The large scale structure of f(R) gravity”, Phys. Rev. **D75**, 044004 (2007), [arXiv:astro-ph/0610532].

[333] Y.-S. Song, H. Peiris, and W. Hu, “Cosmological Constraints on f(R) Acceleration Models”, Phys. Rev. **D76**, 063517 (2007), [arXiv:0706.2399].

[334] T. Giannantonio, M. Martinelli, A. Silvestri, and A. Melchiorri, “New constraints on parametrised modified gravity from correlations of the CMB with large scale structure”, JCAP **1004**, 030 (2010), [arXiv:0909.2045].

[335] L. Lombriser, A. Slosar, U. Seljak, and W. Hu, “Constraints on f(R) gravity from probing the large-scale structure”, (2010), [arXiv:1003.3009].

[336] A. Hojjati, L. Pogosian, and G.-B. Zhao, “Testing gravity with CAMB and CosmoMC”, (2011), [arXiv:1106.4543].

[337] F. Schmidt, A. Vikhlinin, and W. Hu, “Cluster Constraints on f(R) Gravity”, Phys. Rev. **D80**, 083505 (2009), [arXiv:0908.2457].

[338] F. Schmidt, M. Lima, H. Oyaizu, and W. Hu, “Nonlinear evolution of f(R) cosmologies. III. Halo statistics”, Phys. Rev. **D79(8)**, 083518 (2009), [arXiv:0812.0545].

[339] F. Schmidt, “Cosmological Simulations of Normal-Branch Braneworld Gravity”, Phys. Rev. **D80**, 123003 (2009), [arXiv:0910.0235].

[340] SDSS, B. Koester *et al.*, “A MaxBCG Catalog of 13,823 Galaxy Clusters from the Sloan Digital Sky Survey”, Astrophys. J. **660**, 239 (2007), [arXiv:astro-ph/0701265].

[341] SDSS, K. N. Abazajian *et al.*, “The Seventh Data Release of the Sloan Digital Sky Survey”, Astrophys. J. Suppl. **182**, 543 (2009), [arXiv:0812.0649].

[342] A. Borisov, B. Jain, and P. Zhang, “Spherical Collapse in f(R) Gravity”, (2011), [arXiv:1102.4839].

[343] M. C. Martino, H. F. Stabenau, and R. K. Sheth, “Spherical Collapse and Modified Gravity”, Phys. Rev. **D79**, 084013 (2009), [arXiv:0812.0200].

[344] F. Schmidt, “Self-Consistent Cosmological Simulations of DGP Braneworld Gravity”, Phys. Rev. **D80**, 043001 (2009), [arXiv:0905.0858].

[345] H. Oyaizu, “Non-linear evolution of f(R) cosmologies I: methodology”, Phys. Rev. **D78**, 123523 (2008), [arXiv:0807.2449].

[346] H. Oyaizu, M. Lima, and W. Hu, "Non-linear evolution of f(R) cosmologies II: power spectrum", Phys. Rev. **D78**, 123524 (2008), [arXiv:0807.2462].

[347] G.-B. Zhao, B. Li, and K. Koyama, "N-body Simulations for f(R) Gravity using a Self-adaptive Particle-Mesh Code", Phys. Rev. **D83**, 044007 (2011), [arXiv:1011.1257].

[348] A. Jenkins *et al.*, "Mass function of dark matter halos", Mon. Not. Roy. Astron. Soc. **321**, 372 (2001), [arXiv:astro-ph/0005260].

[349] R. E. Smith, "Covariance of cross-correlations: towards efficient measures for large-scale structure", Mon. Not. Roy. Astron. Soc. **400**, 851 (2009), [arXiv:0810.1960].

[350] R. E. Smith, C. Hernandez-Monteagudo, and U. Seljak, "Impact of Scale Dependent Bias and Nonlinear Structure Growth on the ISW Effect: Angular Power Spectra", Phys. Rev. **D80**, 063528 (2009), [arXiv:0905.2408].

[351] V. Springel, "The cosmological simulation code GADGET-2", Mon. Not. Roy. Astron. Soc. **364**, 1105 (2005), [arXiv:astro-ph/0505010].

[352] U. Seljak and M. Zaldarriaga, "A Line of Sight Approach to Cosmic Microwave Background Anisotropies", Astrophys. J. **469**, 437 (1996), [arXiv:astro-ph/9603033].

[353] R. Scoccimarro, "Transients from Initial Conditions: A Perturbative Analysis", Mon. Not. Roy. Astron. Soc. **299**, 1097 (1998), [arXiv:astro-ph/9711187].

[354] M. Crocce, S. Pueblas, and R. Scoccimarro, "Transients from Initial Conditions in Cosmological Simulations", Mon. Not. Roy. Astron. Soc. **373**, 369 (2006), [arXiv:astro-ph/0606505].

[355] M. Davis, G. Efstathiou, C. S. Frenk, and S. D. M. White, "The evolution of large-scale structure in a universe dominated by cold dark matter", Astrophys. J. **292**, 371 (1985).

[356] WMAP, D. N. Spergel *et al.*, "First Year Wilkinson Microwave Anisotropy Probe (WMAP) Observations: Determination of Cosmological Parameters", Astrophys. J. Suppl. **148**, 175 (2003), [arXiv:astro-ph/0302209].

[357] WMAP, D. N. Spergel *et al.*, "Wilkinson Microwave Anisotropy Probe (WMAP) three year results: Implications for cosmology", Astrophys. J. Suppl. **170**, 377 (2007), [arXiv:astro-ph/0603449].

[358] F. Schmidt, M. V. Lima, H. Oyaizu, and W. Hu, "Non-linear Evolution of f(R) Cosmologies III: Halo Statistics", Phys. Rev. **D79**, 083518 (2009), [arXiv:0812.0545].

[359] G. Squires and N. Kaiser, "Unbiased Cluster Lens Reconstruction", Astrophys. J. **473**, 65 (1996), [arXiv:astro-ph/9512094].

[360] R. Massey *et al.*, "The Shear TEsting Programme 2: Factors affecting high precision weak lensing analyses", Mon. Not. Roy. Astron. Soc. **376**, 13 (2007), [arXiv:astro-ph/0608643].

[361] R. Massey *et al.*, "COSMOS: 3D weak lensing and the growth of structure", Astrophys. J. Suppl. **172**, 239 (2007), [arXiv:astro-ph/0701480].

[362] R. Nakajima *et al.*, in preparation.

[363] R. Teyssier, B. Moore, D. Martizzi, Y. Dubois, and L. Mayer, "Mass distribution in galaxy clusters: the role of Active Galactic Nuclei feedback", Mon. Not. Roy. Astron.

Soc. **414**, 195 (2011), [arXiv:1003.4744].

[364] D. Martizzi, R. Teyssier, and B. Moore, "The formation of the brightest cluster galaxies in cosmological simulations: the case for AGN feedback", (2011), [arXiv:1106.5371].

[365] J. Blazek, M. McQuinn, and U. Seljak, "Testing the tidal alignment model of galaxy intrinsic alignment", JCAP **1105**, 010 (2011), [arXiv:1101.4017].

[366] C. M. Hirata *et al.*, "Intrinsic galaxy alignments from the 2SLAQ and SDSS surveys: luminosity and redshift scalings and implications for weak lensing surveys", Mon. Not. Roy. Astron. Soc. **381**, 1197 (2007), [arXiv:astro-ph/0701671].

[367] J. Blazek *et al.*, in preparation.

[368] R. Mandelbaum, U. Seljak, T. Baldauf, and R. E. Smith, "Precision cluster mass determination from weak lensing", Mon. Not. Roy. Astron. Soc. **405**, 2078 (2010), [arXiv:0911.4972].

[369] S. Hilbert and S. D. M. White, "Abundances, masses and weak-lensing mass profiles of galaxy clusters as a function of richness and luminosity in ΛCDM cosmologies", Mon. Not. Roy. Astron. Soc. **404**, 486 (2010), [arXiv:0907.4371].

[370] T. Baldauf, R. E. Smith, U. Seljak, and R. Mandelbaum, "An algorithm for the direct reconstruction of the dark matter correlation function from weak lensing and galaxy clustering", Phys. Rev. **D81**, 063531 (2010), [arXiv:0911.4973].

[371] V. Springel *et al.*, "Simulating the joint evolution of quasars, galaxies and their large-scale distribution", Nature **435**, 629 (2005), [arXiv:astro-ph/0504097].

[372] WMAP, J. Dunkley *et al.*, "Five-Year Wilkinson Microwave Anisotropy Probe (WMAP) Observations: Likelihoods and Parameters from the WMAP data", Astrophys. J. Suppl. **180**, 306 (2009), [arXiv:0803.0586].

[373] C.-L. Kuo *et al.*, "Improved Measurements of the CMB Power Spectrum with ACBAR", Astrophys. J. **664**, 687 (2007), [arXiv:astro-ph/0611198].

[374] A. C. S. Readhead *et al.*, "Extended Mosaic Observations with the Cosmic Background Imager", Astrophys. J. **609**, 498 (2004), [arXiv:astro-ph/0402359].

[375] K. Grainge *et al.*, "The CMB power spectrum out to l=1400 measured by the VSA", Mon. Not. Roy. Astron. Soc. **341**, L23 (2003), [arXiv:astro-ph/0212495].

[376] Supernova Cosmology Project, M. Kowalski *et al.*, "Improved Cosmological Constraints from New, Old and Combined Supernova Datasets", Astrophys. J. **686**, 749 (2008), [arXiv:0804.4142].

[377] A. G. Riess *et al.*, "A Redetermination of the Hubble Constant with the Hubble Space Telescope from a Differential Distance Ladder", Astrophys. J. **699**, 539 (2009), [arXiv:0905.0695].

[378] B. A. Reid, L. Verde, R. Jimenez, and O. Mena, "Robust Neutrino Constraints by Combining Low Redshift Observations with the CMB", JCAP **1001**, 003 (2010), [arXiv:0910.0008].

[379] W. J. Percival *et al.*, "Baryon Acoustic Oscillations in the Sloan Digital Sky Survey Data Release 7 Galaxy Sample", Mon. Not. Roy. Astron. Soc. **401**, 2148 (2010), [arXiv:0907.1660].

[380] E. Rozo *et al.*, “Constraining the Scatter in the Mass-Richness Relation of maxBCG Clusters With Weak Lensing and X-ray Data”, Astrophys. J. **699**, 768 (2009), [arXiv:0809.2794].

[381] A. Lewis and S. Bridle, “Cosmological parameters from CMB and other data: a Monte- Carlo approach”, Phys. Rev. **D66**, 103511 (2002), [arXiv:astro-ph/0205436].

[382] N. Metropolis, A. W. Rosenbluth, M. N. Rosenbluth, A. H. Teller, and E. Teller, “Equation of state calculations by fast computing machines”, J. Chem. Phys. **21**, 1087 (1953).

[383] W. K. Hastings, “Monte Carlo sampling methods using Markov chains and their applications”, Biometrika **57**, 97 (1970).

[384] A. Gelman and D. B. Rubin, “Inference from Iterative Simulation Using Multiple Sequences”, Statist. Sci. **7**, 457 (1992).

[385] O. Lahav, P. B. Lilje, J. R. Primack, and M. J. Rees, “Dynamical effects of the cosmological constant”, Mon. Not. Roy. Astron. Soc. **251**, 128 (1991).

[386] R. K. Sheth and G. Tormen, “Large scale bias and the peak background split”, Mon. Not. Roy. Astron. Soc. **308**, 119 (1999), [arXiv:astro-ph/9901122].

[387] A. Cooray and R. K. Sheth, “Halo models of large scale structure”, Phys. Rept. **372**, 1 (2002), [arXiv:astro-ph/0206508].

[388] J. F. Navarro, C. S. Frenk, and S. D. M. White, “The Structure of Cold Dark Matter Halos”, Astrophys. J. **462**, 563 (1996), [arXiv:astro-ph/9508025].

Curriculum Vitae

Personal Information

Lucas LOMBRISER
Born 12 April 1982 in Zürich ZH, Switzerland
Citizen of Trun GR, Switzerland

Education

2008–2011	Doctoral candidate in Theoretical Physics (Dr. sc. nat.) at the Institute for Theoretical Physics, University of Zurich, Switzerland *Thesis*: Confronting Theories of Gravity with Large-Scale Structures (*advisor*: Prof. Dr. Uroš Seljak) Employed since March 2008, enrolled since HS 2008
2002–2008	Diploma studies in Physics (Dipl. Phys. ETH equiv. MSc ETH) with subject in Theoretical Physics at ETH Zurich, Switzerland *Thesis*: Testing Modifications of General Relativity with Cosmological Observations (*supervisor*: Prof. Dr. Uroš Seljak)
1999–2000	Exchange year (Honorary High School Diploma) at Champlain Valley Union High School, Hinesburg VT, USA
1995–2002	Gymnasium (Matura, Typus C) at Kantonsschule Chur, Graubünden, Switzerland

Academic Experience

2008–2011	Research and teaching assistant at the Institute for Theoretical Physics, University of Zurich, Switzerland
2010	Research visitor at Lawrence Berkeley National Laboratory and Berkeley Center for Cosmological Physics, University of California, USA
2009	Research visitor at Berkeley Center for Cosmological Physics, University of California and Lawrence Berkeley National Laboratory, USA
2006–2007	Undergraduate teaching assistant at Department of Mathematics, ETH Zurich, Switzerland
2006	Internship at CERN and Institute for Particle Physics, ETH Zurich, Switzerland